Chemo-hygro-thermo-mechanical model for simulation of corrosion induced damage in reinforced concrete

Von der Fakultät Bau- und Umweltingenieurwissenschaften
der Universität Stuttgart zur Erlangung der Würde
eines Doktor-Ingenieurs (Dr.-Ing.)
genehmigte Abhandlung

Vorgelegt von
Filip Oršanić
aus Karlovac, Kroatien

Hauptberichter: Prof. Dr.-Ing. habil. Joško Ožbolt
Mitberichter: Prof. Dr.-Ing. Christoph Gehlen
Mitberichter: Prof. Dr.-Ing. Gojko Balabanić
Mitberichter: Prof. Dr.-Ing. Jan Hofmann

Tag der mündlichen Prüfung: 04.02.2015

Institut für Werkstoffe im Bauwesen der Universität Stuttgart
2015

ACKNOWLEDGEMENTS

First and foremost, I would like to thank my guide Prof. Joško Ožbolt, who had invited me to work with him on the subject of modelling corrosion induced damage in reinforced concrete at the Institute of Construction Materials in Stuttgart. His immense and vast expertise in the field of computational and fracture mechanics, with his impeccable work ethics and continuous strive for knowledge, have been a continuous inspiration during my research. His numerous advices, comments and encouragements have made this work possible and I would like to express my sincerest gratitude for all his help.

Furthermore, I would like to thank Prof. Gojko Balabanić, whose many insights in the field of non-mechanical transport processes have been of invaluable worth for the completion of this thesis. I am also grateful to Prof. Christoph Gehlen and Prof. Jan Hofmann for their insightful comments which have contributed to the final form of the here presented work.

The project of simulating corrosion induced damage in reinforced concrete was funded by the German Research Foundation DFG. Their support is greatly acknowledged.

I am immensely grateful to my two friends and former work colleagues at IWB, Dr. Josipa Bošnjak and Marina Stipetić. Josipa has gone above and beyond in helping me with many of the work and non-work related problems. Her always encouraging advices, solution driven attitude and positive outlook on life will always be remembered and cherished. Marina has been a truly great and supportive friend, helping me to overcome many of the obstacles during my stay at IWB. Thank you both for the unforgettable 4 years working together and the numerous coffee breaks.

I am deeply thankful to my good friend Dr. Akanshu Sharma, who was always ready to offer assistance and advice during our technical discussions. Thomas Rauscher has been a great friend and colleague, proofing my german reports and organizing countless squash matches. Furthermore, I am grateful to my dear friends Natalija Bede, Daniela Ruta, Emiliano Sola, Baris Irhan and Kaipei Tian for all the time spent together at IWB.

I owe a very special thanks to Dr. Christian Fischer, who has offered an unlimited access to his research, needed for the verification of the here presented model. Kind help of Simone Reeb and Dana Ullmann in regard to sorption isotherms is greatly appreciated. Dr. Goran Periškić and Dr. Marija Kušter have been helpful with the introduction to the FE code of the chemo-hygro-thermo-mechanical model.

I would also like to thank Sylvia Choynacki for helping me with the administrative things at IWB and for improving my unimprovable german conversational skills. Help

provided by the IWB staff (Gisela Baur, Regina Jäger, Olga Weber, Simone Stumpp) is greatly appreciated. Monika Werner has been highly helpful with the literature research, finding every book and paper needed.

Furthermore, I would like to thank my friends Katarina Ćuk, Martina Krznarić, Mario Martinčić, Mario Zelenika, Matej Fonović and Stefan Kolnik for all the fun moments spent together in Baden-Würtemberg.

Above all, my deepest appreciation goes out to my family. My brother Matija, sister-in-law Ivana and my little nephew Luka have been a constant rock while working on this thesis and I am truly grateful for their presence in my life.

At last, I would like to express my deepest gratitude to my mother Miljenka and father Tomislav. Without their unconditional love, continuous support and endless encouragement I wouldn't be able to come so far. This thesis is dedicated to them.

Stuttgart, February 2015
Filip Oršanić

ABSTRACT

Reinforced concrete (RC) elements exposed to chloride induced corrosion have a shortened service life which presents a major challenge for durability of structures. The extensive costs of repair heighten the importance of developing a model as a numerical assessment tool of corrosion induced damage effects. A three dimensional (3D) chemo-hygro-thermo-mechanical (CHTM) model has been recently developed (Ožbolt et al. 2010, 2011). The model is implemented into a finite element code and is capable of predicting the non-mechanical processes before and after depassivation of steel, for both un-cracked and cracked concrete elements.

Here presented work is a further development of the model, focused on predicting the rate of rust production and the corresponding damage (cracking and spalling) of the concrete cover surrounding the embedded steel bars. The extent of the damage and its progress in time are highly dependent on the ingress of corrosion products into pores and cracks. Therefore, the transport of corrosion products is incorporated into the model as a convective diffusion problem. The expansion of rust and the subsequent compressive pressure on the cover is taken into account by developing one-dimensional corrosion contact elements. To ensure a realistic simulation of the corrosion induced damage, the model couples the mechanical with the non-mechanical processes, and vice versa.

Validation of the CHTM model's ability for simulating corrosion induced damage is performed on concrete specimens with a single embedded reinforcement bar and for multi-rebar cases, without and with stirrups. Comparison of the numerical results with the existing experimental data shows that the model is capable of realistically capturing the damage of the concrete cover and its effects on the mechanical properties of the investigated RC elements.

Hysteretic moisture model for concrete is a further addition to the CHTM model. It accounts for the hysteretic behaviour of concrete which is characterized by the ability to contain different degrees of water saturation for the same value of relative humidity, at a constant temperature. Hence, the water content values are highly dependent on the exposure to cyclic wetting and drying conditions.

The hysteretic moisture model is validated directly through existing experimental studies by verifying the calculated scanning curves and the distribution of relative humidity, i.e. the water content in concrete, respectively. The importance of incorporating the moisture hysteresis in the CHTM model is demonstrated by comparing the experimentally and numerically obtained distribution of chloride ions in concrete specimens exposed to cyclic wetting and drying conditions.

KURZFASSUNG

Eine der wesentlichen Aspekte der Dauerhaftigkeit von Bauwerken stellt die chloridinduzierte Korrosion dar, die die Lebensdauer von Stahlbetonelementen beeinträchtigt. Relativ hohe Instandsetzungskosten zeigen den Nutzen, den ein numerisches Modell zur Bewertung der korrosionsinduzierten Schäden darstellt. Ein dreidimensionales (3D) Chemo-Hygro-Thermo-Mechanisches (CHTM) Modell wurde kürzlich entwickelt (Ozbolt et al. 2010,2011). Das Modell ist im FE Code implementiert und in der Lage, die nicht-mechanischen Prozesse vor und nach der Depassivierung des Stahles, sowohl für ungerissenen als auch für gerissenen Beton, vorherzusagen.

Die vorliegende Arbeit stellt eine Weiterentwicklung des Modells dar, wobei ein besonderer Augenmerk auf der Korrosionsrate und der dazugehörigen Schädigung der Betondeckung (Risse und Abplatzungen) liegt. Umfang und Zeitentwicklung der Schädigung sind stark vom Transport der Korrosionsprodukte in Rissen und Poren abhängig. Aus diesem Grund wird dieser Transport als ein konvektiv-diffusiver Prozess in dem CHTM Modell implementiert. Die Ausdehnung der Korrosionsprodukte und die daraus folgende Druckkraft auf die Betondeckung werden mithilfe von eindimensionalen Korrosions-Kontaktelementen berücksichtigt. Ein wesentliches Merkmal des Modells liegt in der vollständigen Kopplung der mechanischen und nicht-mechanischen Prozesse, die zu einer realitätsnahen Simulation beiträgt.

Das Modell wird anhand der vorhandenen Versuche an Stahlbetonelementen mit einem und mehreren Bewehrungsstäben („multi-rebar“) sowie mit und ohne Bügel validiert. Es wird gezeigt, dass das vorgestellte Modell die wichtigsten Aspekte der korrosionsinduzierten Schädigung des Betons und die Auswirkungen dieser Schädigung auf die mechanischen Eigenschaften der Stahlbetonelemente realistisch erfasst.

Ferner wird das CHTM Modell erweitert, um die Hysterese der Feuchte im Beton zu berücksichtigen. Das Hysteresemodell beschreibt die Eigenschaft des Betons, unterschiedliche Wassergehalte bei gleicher relativer Feuchtigkeit (für konstante Temperatur) aufzuweisen. Demzufolge ist der Wassergehalt stark von der zyklischen Benetzung und Trocknung abhängig.

Die Validierung des Modells erfolgt anhand vorhandener Versuchsergebnisse. Die empirische Definition der Zwischenkurven („scanning curves") führt zu realitätsnahen Ergebnissen. Es wird weiterhin gezeigt, dass das Modell den Wassergehalt- und die Feuchteverteilung realistisch abbilden kann. Das Modell ist in der Lage, die experimentell beobachtete Verteilung der Chloride im Beton unter zyklischer Benetzung und Trocknung realistisch abzubilden. Diese Ergebnisse veranschaulichen die Bedeutung des Hysteresemodells für die Transportprozesse.

CONTENTS

LIST OF INDICES

Literature review

i	current density	[A/m^2]
i_0	exchange current density	[A/m^2]
z	number of the transferred charge	[-]
α_{barr}	measure of free energy barrier symmetry	[-]
Φ	electric potential	[V]
Φ_0	equilibrium electric potential	[V]
F	Faradey's constant	[C/mol]
R	universal gas constant	[J/Kmol]
T	absolute temperature	[K]
β	Tafel curve slope	[V/dec]
C_o	oxygen concentration	[kg/m^3]
C_o^{surf}	oxygen concentration at the electrode surface	[kg/m^3]
$i_{c,dif}$	limiting diffusion current density	[A/m^2]
D_o	oxygen diffusion coefficient	[m^2/s]
n	outward normal to the steel bar surface	[-]
$i_{init.}$	initial current density	[A/m^2]
t	time	[s]
C	corrosion constant dependant on the pore saturation, pH, cover thickness and permeability	[s^{-1}]
$C_{c,tot}$	total chloride content near the steel's surface	[kg/m^3]
r_C	ohmic resistance of concrete	[Ω]
f	slag correction factor depending on the binder type	[-]
$C_{cond,90}$	90 day chloride conductivity index value	[S/m]
c_{cov}	concrete cover depth	[m]
$i_{corr,rep}$	annually representative current density	[A/m^2]
i_{corr}^{site}	in situ measured current density	[A/m^2]
$i_{corr}^{\max}$	maximum current density value	[A/m^2]
Φ^{anode}	anodic potential	[V]
$\Phi^{cathode}$	cathodic potential	[V]
u_w^{anode}	amount of capillary water at anode	[$m^3_{H_20}/m^3_{con}$]
$u_w^{cathode}$	amount of capillary water at cathode	[$m^3_{H_20}/m^3_{con}$]
C_f	concentration of ferrous hydroxide	[kg/m^3]

$\Phi_{O_2}^0$	standard half-cell potential of oxygen (cathodic equilibrium potential)	[V]
Φ_{Fe}^0	standard half-cell potential of iron (anodic equilibrium potential)	[V]
β_a, β_c	Tafel slopes of the anodic and cathodic reactions	[V/dec]
$i_a,\ i_c$	anodic and cathodic current densities	[A/m^2]
$i_{0a},\ i_{0c}$	anodic and cathodic exchange current densities	[A/m^2]
R_{con}	concrete resistivity	[Ωm]
R_s	steel resistivity	[Ωm]
$R_{p,a}, R_{p,c}$	anodic and cathodic polarization resistances	[Ω]
J_r	rate of the rust production	[kg/m^{2}s]
M	molar mass	[kg/mol]
S_{ink}	residual degree of pore saturation	[-]
P_c^*	probability of pore interconnection	[-]
ϕ_a, ϕ_d	adsorption and desorption relative humidities	[-]
$H(\phi_a, \phi_d)$	integral function in the IPM model	[-]

Chemo-hygro-thermo-mechanical model

$\mathbf{j}_w$	vector of the specific water discharge	[$m^3_{H_20}/m^2_{con}s$]
$\mathbf{v}_w$	vector of the mean water velocity	[m/s]
K_w	unsaturated hydraulic conductivity	[m/s]
θ_w	volume fraction of pore water	[$m^3_{H_20}/m^3_{con}$]
Ψ	capillary potential	[m]
D_w	water diffusivity	[m^2/s]
ρ_w	water density	[kg/m^3]
D_0	limiting magnitude term	[m^2/s]
$\overline{\theta}_w$	reduced water content	[-]
θ_{wi}	initial water content	[$m^3_{H_20}/m^3_{con}$]
θ_{wd}	saturated water content	[$m^3_{H_20}/m^3_{con}$]
$\mathbf{j}_{o,diff}$	vector of the diffusive flux of oxygen	[kg/m^{2}s]
$\mathbf{j}_{o,conv}$	vector of the convective flux of oxygen	[kg/m^{2}s]
$\mathbf{j}_o$	vector of the total flux of oxygen	[kg/m^{2}s]
h	relative humidity	[-]
p_{cp}	porosity of the hardened cement paste	[-]

p_c	concrete porosity	[-]
a/c	aggregate/cement ratio	[-]
w/c	water/cement ratio	[-]
ρ_c	density of cement	[kg/m^3]
ρ_a	density of aggregate	[kg/m^3]
$\mathbf{j}_c$	vector of the total flux of chloride ions	[kg/m^{2}s]
C_c	concentration of free chloride dissolved in pore solution	[kg/m^3]
D_c	chloride diffusion coefficient	[m^2/s]
$D_{c,ref}$	reference value of D_c evaluated at standard conditions	[m^2/s]
C_{cb}	concentration of bound chlorides	[kg/m^3]
k_r	chloride binding rate coefficient	[s^{-1}]
α	constant - chloride binding process	[-]
U	activation energy of chloride diffusion process	[J/mol]
λ	thermal conductivity	[W/mK]
c	heat capacity per unit mass of concrete	[J/(K kg)]
ρ_{con}	mass density of concrete	[kg/m^3]
W	internal source of heating	[W/m^3]
N	shape functions	[-]
α_{TR}	heat transfer coefficient	[W/m^{2}K]
Q	number of oxygen molecules reduced per unit surface of cathode and per unit time	[mol/m^2 s]
j_o^c , j_o^a	oxygen diffusion flux at the anode and cathode surface	[kg/m^2 s]
j_{fh}	rate of $Fe(OH)_2$ production	[mol/m^2 s]
k_c, k_a	constants (stoichiometry of electrochemical reactions)	[kg/C]
$\mathbf{j}_i$	vector of the flux of ions	[mol/m^2 s]
$\mathbf{i}$	vector of the electric current density	[A/m^2]
σ	electrical conductivity of concrete	[Ω^{-1}m^{-1}]
C_{ob}	oxygen concentration at surface of concrete element exposed to seawater	[kg/m^3]
S_w	water saturation	[-]
J_r	rate of rust production	[kg/m^{2}s]
m_r	mass of hydrated red rust	[kg]
A_r	surface of the steel reinforcement	[m^2]
Δt	time interval	[s]
R	amount of corrosion products per volume of pore solution	[kg/m^3]
D_r	corrosion products diffusion coefficient	[m^2/s]

σ	stress	[N/mm^2]
ε	strain	[-]
σ^V	volumetric stress	[N/mm^2]
ε^V	volumetric strain	[-]
K	bulk modulus	[N/mm^2]
ε_{ij}	total strain tensor for concrete	[-]
ε_{ij}^m	mechanical strain tensor	[-]
ε_N	normal component of the microplane strain	[-]
ε_D	deviatoric component of the microplane strain	[-]
ε_V	volumetric component of the microplane strain	[-]
ε_{Tr}	tangential component of the microplane strain	[-]
S	sphere surface area	[m^2]
φ	discontinuity function in the microplane model	[-]
σ_N	normal component of the microplane stress	[N/mm^2]
σ_D	deviatoric component of the microplane stress	[N/mm^2]
σ_V	volumetric component of the microplane stress	[N/mm^2]
σ_{Tr}	tangential component of the microplane stress	[N/mm^2]
δ_{ij}	Kronecker delta (operator)	[-]
ν	Poisson's coefficient	[-]
E	macroscopic E modulus	[N/mm2]
f_t	macroscopic tensile strength	[N/mm2]
f_c	macroscopic compressive strength	[N/mm2]
G_f	macroscopic fracture energy (tension)	[N/mm2]
G_c	macroscopic fracture energy (compression)	[N/mm^2]
Δl_r	inelastic radial expansion of corrosion contact elements	[m]
ρ_r	density of rust	[kg/m^3]
ρ_s	density of steel	[kg/m^3]
E_r	elastic modulus of rust	[N/mm^2]

Hysteretic moisture model for concrete

u	water to dry mass of concrete ratio	[kg_{H_20}/kg_{con}]
w	moisture content per m^3 of concrete	[kg_{H_20}/m^3_{con}]
$\mathbf{j}_{w,mass}$	vector of the moisture flux	[kg/m^{2}s]
δ_v	water vapour permeability	[s]

$p_{v,sat}$	saturation pressure	[Pa]
ξ	moisture capacity	$[kg_{H_20}/m^3_{con}]$
β_{hum}	surface humidity transfer coefficient	[m/s]
h_s	relative humidity at the exposed concrete surface	[-]
h_{env}	relative humidity of the ambient air	[-]
a_0	reference permeability at 25 ºC	[s]
$f_1(h)$	function which reflects the moisture transfer within the adsorbed water layers	[-]
h_c	transition humidity	[-]
ϑ	temperature	[ºC]
ξ_{hys}	moisture capacity, i.e. the slope of the scanning curve	[-]
ξ_a	moisture capacity calculated from the main adsorption isotherm	$[kg_{H_20}/m^3_{con}]$
ξ_d	moisture capacity calculated from the main adsorption isotherm	$[kg_{H_20}/m^3_{con}]$
w_a	moisture content calculated from main adsorption curve	$[kg_{H_20}/m^3_{con}]$
w_d	moisture content calculated from main desorption curve	$[kg_{H_20}/m^3_{con}]$
w_0	initial moisture content	$[kg_{H_20}/m^3_{con}]$
Δh	change in the relative humidity	[-]
$\mathbf{j}_{c,diff}$	vector of the diffusive flux of chloride ions	$[kg/m^2s]$
$\mathbf{j}_{c,conv}$	vector of the convective flux of chloride ions	$[kg/m^2s]$
$\mathbf{j}_{w,vol}$	vector of the specific water discharge	$[m^3_{H_20}/m^2_{con}s]$

1 INTRODUCTION

1.1 Motivation and context of research

1.1.1 Corrosion induced damage in reinforced concrete structures

Corrosion induced damage of concrete is a major problem for durability of reinforced concrete (RC) elements exposed to severe climate conditions. The onset of corrosion can be caused by carbonation of the concrete cover or by reaching a critical concentration of free chloride ions in the vicinity of the reinforcement bar. Here presented work is focused on damage due to the chloride induced corrosion.

Reinforced concrete structures in maritime environment such as bridges, oil platforms or structures treated with de-icing salts during winter periods show a great vulnerability to corrosion processes (Tuutti 1993; Cairns 1998). Damage is usually exhibited in the form of cracking and spalling of the concrete cover which reduces the mechanical properties of reinforced concrete elements, leading to a shorter serviceability (Figure 1.1). Also, due to corrosion the bar's cross-section area is reduced, which has negative implications on the bearing capacity of the RC. Additionally, as a consequence of the pitting effect (Cairns et al. 2005; Apostolopoulos & Papadakis 2008), ductility and bond properties of reinforcement can be significantly reduced (Tuutti 1993; Fischer 2012). Damage due to the chloride induced corrosion in RC structures exerts relatively large costs of repair. Approximately 300 million euros were spent in 2004 for the maintenance of highway bridges in Germany (Jacob 2008). Roughly 40 % of the costs were due to repair of concrete bridges, damaged mostly through chloride contamination and the subsequent corrosion induced damage.

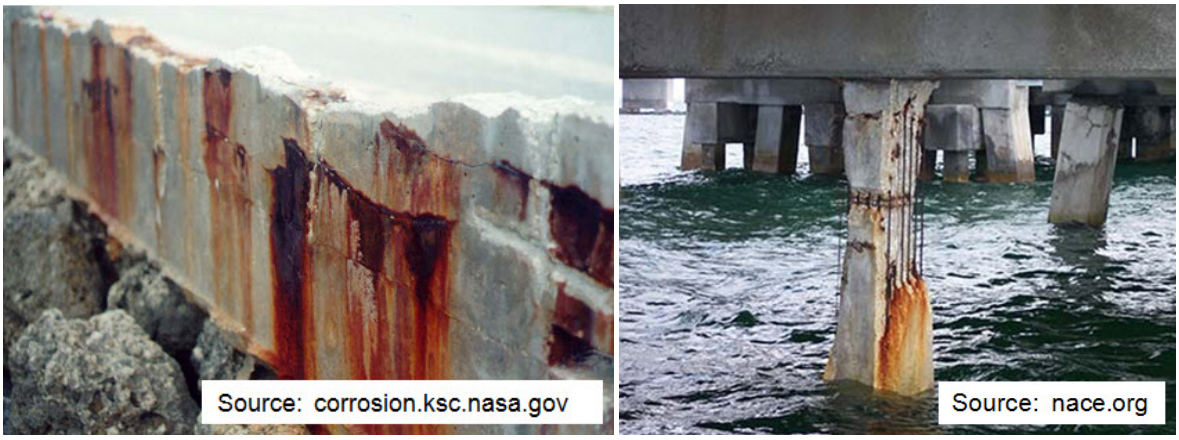

Figure 1.1 Examples of the corrosion induced damage in reinforced concrete elements: cracking and staining of a seawall near the Kennedy Space Centre (left); extensive damage of the bridge piling due to reinforcement corrosion (right)

Therefore, it is of great significance to develop a numerical model for simulating the electrochemical processes and mechanical damage of the concrete cover due to corrosion of reinforcement. The main advantage of having a realistic model for simulating chloride induced corrosion is not only its ability to investigate a possible onset and progression of damage in older RC structures with the inadequate thickness of the concrete cover, but also its application as an engineering tool in the process of structural design.

To understand which conditions should be imposed on a model in order to be considered reliable, the main mechanisms and the processes related to corrosion should be identified.

Relatively high pH values (12 to 13) of the pore solution around the embedded steel bars, create a passive surface film, i.e. a very thin oxide layer which reduces the corrosion rate to an insignificant level of 0.1 μm per year (Foley 1975). With this layer being damaged or depassivated the corrosion rate increases up to 1000 times (ACI-222 2001).

Damage can be caused by mechanical action (too high tensile stress), or can appear because of non-mechanical effects (temperature, shrinkage, etc.) or be induced by corrosion of reinforcement. Depassivation of the protective layer can occur by reaching a critical concentration of free chloride ions near the reinforcement bar surface (Figure 1.2a) or as a consequence of carbonation of the concrete cover which then directly reduces the pH value of the surrounding pore solution (Tuutti 1993; Glass & Buenfeld 1995; Sandberg et al. 1995). In the case of the latter the corrosion is occurring over a large area of the reinforcement steel, as the carbonation front penetrates into the concrete cover depth. Depassivation and subsequent corrosion due to the chloride attack is characterized by smaller anodic regions, which is more severe due to higher corrosion rate.

The mechanism of the protective film breakdown by chlorides is a very complex problem due to the challenging task of investigating the processes on the atomistic scale. It is mostly believed that in the case of a thicker oxide layer the chloride ions are positioned at weak spots in the film structure, causing ionic defects and therefore increasing ionic transport (ACI-222 2001). Once these locations in the film structure have been formed, the corrosion process can start and continue in a progressive manner.

The corrosion of steel in concrete is an electrochemical process with two half-cell reactions. At the anodic site the electrons are being produced (Figure 1.2b), i.e. iron is being oxidized to form ferrous ions:

$$Fe \rightarrow Fe^{2+} + 2e^{-} \tag{1.1}$$

Free electrons are consumed by oxygen at the cathodic site in the presence of water and form hydroxyl ions OH^- (Figure 1.2b):

$$2H_2O + O_2 + 4e^- \rightarrow 4OH^- \quad (1.2)$$

The hydroxyl ions are then transported to the anodic site where they react with the ferrous ions forming the iron(II)-hydroxide (Figure 1.2c):

$$Fe^{2+} + 2OH^- \rightarrow Fe(OH)_2 \quad (1.3)$$

Further reactions and production of corrosion products depend on the environmental conditions and available chemical reactants. Newly formed rust products have a greater volume than steel. The increase of volume can vary from 2 to 6 times depending on the product that was formed (Fischer 2012). One of the possible occurring reactions is the production of iron(III)- hydroxide or red rust in the presence of oxygen and water (Figure 1.2d):

$$4Fe(OH)_2 + O_2 + 2H_2O \rightarrow 4Fe(OH)_3 \quad (1.4)$$

Here discussed model is calibrated with the assumption of dominantly produced red rust around the reinforcement bar, which has a volume increase of 4 times compared to steel.

Production of corrosion products around the reinforcement bar exerts a pressure on the surrounding concrete cover causing cracking of the protective concrete layer (Figure 1.2e). With the development of cracks the process of corrosion becomes progressive with the chloride ions now penetrating much faster through the cracks and subsequently depassivating new regions of the steel bar.

Rate of rust production is proportional to the corrosion current density. Therefore, to predict the progress of the corrosion induced damage it is important to calculate the current density in the corrosion unit. Generally, calculation of corrosion current density depends upon following physical, electrochemical and mechanical processes: (1) transport of capillary water, oxygen and chloride through the concrete cover; (2) immobilization of chloride in the concrete; (3) transport of OH- ions through electrolyte in concrete pores; (4) cathodic and anodic polarization; (5) transport of corrosion products into pores and cracks and (6) damage of concrete due to mechanical and non-mechanical actions (Bažant 1979a).

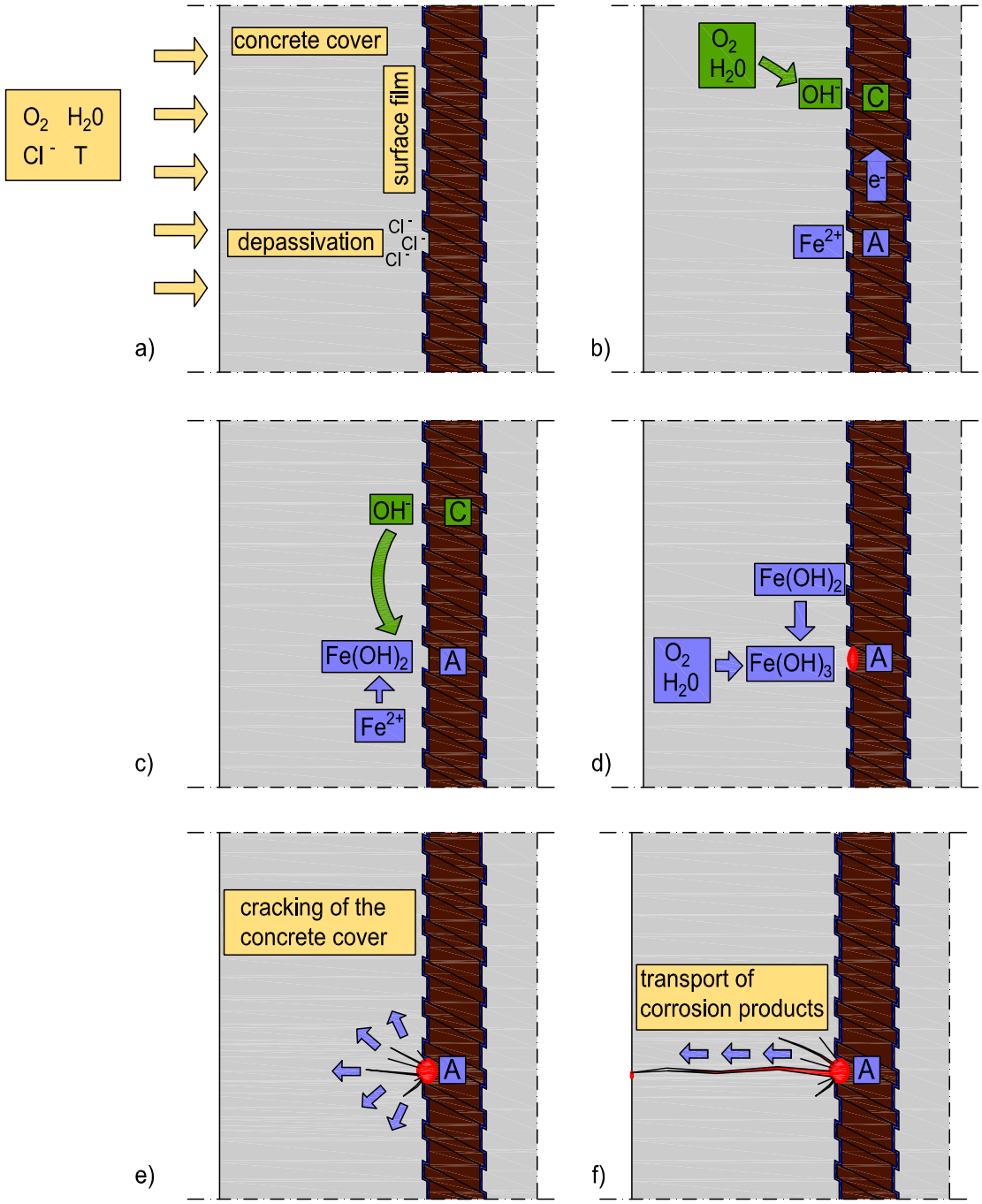

Figure 1.2 Illustration of the corrosion processes in reinforced concrete: (a) ingress of oxygen, water, heat and chlorides in the concrete cover and depassivation of the protective surface film; (b) oxidation of iron (anode) and forming of hydroxyl ions (cathode); (c) forming of ferric(II)-hydroxide (anode); (d) production of iron(III)-hydroxide or red rust (anode); (e) cracking of the concrete cover; (f) transport of corrosion products into the generated cracks

Recent experiments (Wong et al. 2010; Fischer 2012) have shown that a relatively large amount of corrosion products is transported into pores and subsequently generated cracks (Figure 1.2f). The phenomenon needs to be accounted for in a model attempting to simulate the process of corrosion induced damage. With the soluble species being transported away from the corroded steel-concrete interface, the pressure of the expanding products decreases and the occurrence of damage is

progressing in a more moderate way. Transport of corrosion products in cracked concrete and its effect on the corrosion-induced damage has been scarcely addressed in the literature, i.e. most of the state-of-the-art corrosion models do not account for the transport of soluble species. The main problem in defining such models is quantifying the controlling parameters for the rust distribution (Wong et al. 2010; Fischer 2012).

Currently, there are a number of models in literature, which are able to simulate processes before and after depassivation of reinforcement in uncracked concrete (Bažant 1979a; Page et al. 1981; Tuutti 1993; Balabanić et al. 1996a, 1996b; Zhang & Gjørv 1996; Andrade et al. 1997; Martin-Perez 1999; Thomas & Bamforth 1999; Glass & Buenfeld 2000). For computational model to be considered realistic, chemo-hygro-thermo processes have to be coupled with mechanical processes, and also vice versa. The localization of damage (cracking) is a characteristic response of structures made of quasi-brittle materials, such as concrete, subjected to mechanical or non-mechanical loading. Computational modelling of damage in concrete is still a challenging task, especially its interaction with transport processes in concrete. Presently, there are only a limited number of coupled 3D chemo-hygro-thermo-mechanical models capable of realistically simulating corrosion processes in cracked concrete (Ishida et al. 2009; Marsavina et al. 2009; Ožbolt et al. 2010, 2011).

The 3D chemo-hyrgo-thermo mechanical (CHTM) model for concrete has been recently developed (Ožbolt et al. 2010, 2011). It is implemented into a 3D FE code and the results of numerical studies show that the model is able to realistically simulate non-mechanical and mechanical processes and their interaction before (Ožbolt et al. 2010) and after depassivation of reinforcement (Ožbolt et al. 2011).

Here presented work is a further extension of the recently developed 3D CHTM model for concrete. The rate of rust production and the corresponding mass of red rust, which are dependent on the calculated anodic current density, are implemented into the model. The corresponding compressive pressure on the surrounding concrete cover due to the build up of red rust at the depassivated anodic regions, is accounted for by implementing 1D corrosion contact elements. These elements, which are radially placed around the bar, are able to account for the inelastic strains due to the expansion of corrosion products. Subsequently, by reaching the tensile strength of the surrounding concrete, the cracking of the cover occurs. The mechanical part of the model is based on the microplane model with relaxed kinematic constraints (Ožbolt et al. 2001).

The distribution of corrosion products into the pores and corrosion induced cracks is incorporated in the model as a convective-diffusion problem. By accounting for the transport of rust, the corrosion induced damage is less pronounced and hence the onset of the first visible crack on the concrete surface is predicted more realistically. It should be noted that at this stage of the model development, the parameters

governing the distribution of rust are taken more in a qualitative sense. To quantitate their values requires comprehensive experimental tests, which are currently not available in the literature.

The 3D CHTM model's application for predicting corrosion induced damage is investigated for concrete specimens with a single embedded rebar. The validation is shown on a simple reinforced concrete beam. To further quantitatively verify and calibrate the 3D CHTM model, the experiments on the beam-end specimens by Fischer (2012) are numerically replicated. The specimens, which are used to investigate the bond behaviour of the embedded reinforcement bars, were first exposed to accelerated corrosion conditions. The rebars were subsequently pulled out of the specimens for different levels of corrosion exposure. Hence, the 3D chemo-hygro-thermo mechanical model is used to simulate the aggressive corrosion process and the corresponding cracking of the concrete cover. Additionally, the influence of the anodic-cathodic configuration on the bar's surface and the distribution of corrosion products into the cracks is investigated. The pull-out capacity of the reinforcement bar, which is numerically obtained for different degrees of corrosion damage, is compared with the experimental results. The predicted crack patterns and the reduction of the pull-out capacity demonstrate that the model is able to successfully simulate the coupling of the electrochemical processes with the mechanical damage and vice versa.

Further on, the cracking of the RC elements reinforced with multiple rebars placed in close proximity of each other is investigated. Experiments by Dong et al. (2011) are simulated to validate the model's ability to account for the complex development of the corrosion crack patterns. The results of the numerical analyses show that the model is capable to adequately assess the damage in multi-rebar cases, but also the importance of determining the distribution of anodic and cathodic regions on the steel bar's surface.

The robustness of the model is investigated by analysing the corrosion induced cracking on specimens reinforced with both rebars and stirrups. This presents a complicated scenario for simulating the electrochemical processes and for validating the mechanical part of the model. The experimental data by Dong et al. (2011) and Fischer (2012) are used to verify the 3D CHTM model. In the case of the former, a complex crack pattern is realistically captured by the numerical simulation. In the case of the latter, a similar trend of the pull-capacity is accounted for with the progressive corrosion induced damage.

1.1.2 Hysteretic moisture behaviour of concrete

Transport processes important for the onset and progression of corrosion in concrete are highly dependent on the pore moisture content. With the change of the environmental relative humidity (RH), the relative pore pressure is correspondingly changing and hence, affecting the water content in the concrete pores.

Unsaturated conditions in a concrete specimen have a strong influence on the distribution of chlorides. Convective flux of chloride ions due to moisture transport becomes more dominant compared to a slower, diffusive flux. Hence, the ingress of chlorides is more pronounced compared to the chloride attack under saturated conditions (Ababneh et al. 2003). Furthermore, exposure to wetting and drying cycles can result in characteristic "peak" chloride profiles along the concrete depth (Saetta et al. 1993; Polder & Peelen 2002; Fenaux 2013), with the peak value of the total chloride content being translated away from the exposed surface.

Likewise, the electric conductivity of concrete is strongly dependant on the pore water content. Therefore, accounting for the changing RH conditions plays an important role in calculating the corrosion current density and the subsequent rate of rust production (Gjørv et al. 1977; Tuutti 1982).

Concrete, as a porous material, exhibits hysteretic behaviour. Assuming isothermal conditions, the water content can differ for the same relative humidity, depending on the specimen's dynamic moisture loading history (Mualem 1974; Hansen 1986; Pedersen 1990; Xi et al. 1994; Baroghel-Bouny 2007; Ranaivomanana et al. 2011; Bažant & M. Bažant 2012; Derluyn et al. 2012). For a constant air temperature and constant relative humidity, equilibrium conditions can be obtained in a concrete specimen, i.e. the pore pressure in the specimen will be approximately the same as the RH of the ambient air. The connection between the equilibrium relative humidity and the experimentally measured water content is given by a point on the isotherm curve (Hansen 1986). Usually in the experiments for determining the isotherm curves, very small or thin specimens are used to quickly reach the equilibrium state, for a step-like increase or decrease of the ambient RH (Baroghel-Bouny 2007). The main adsorption curve is obtained by plotting the values of the water content for each increase of the RH, starting from a completely dry specimen. Similarly, starting from conditions of absolute saturation and incrementally decreasing the RH of the ambient air, the main desorption curve can be plotted.

As mentioned before, porous materials as concrete have different moisture values for the same RH, depending on the loading history. Therefore, the sorption curves differ from each other at a constant temperature, with the position of the desorption curve always being above the adsorption isotherm (Figure 1.3).

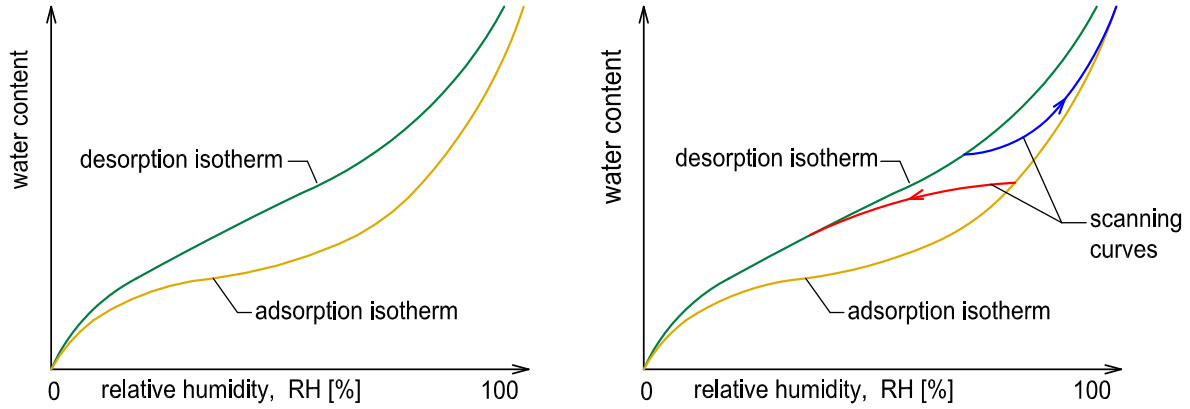

Figure 1.3 Illustration of the main adsorption and desorption curves (left) and the scanning curves (right) for a cementitious material

The hysteretic behaviour of a cementitious material for cases where the conditions change periodically from drying to wetting conditions is described with the so-called scanning curves (Figure 1.3). They are positioned between the main adsorption and desorption curve which are acting as envelopes (Hansen 1986; Pedersen 1990; Baroghel-Bouny 2007).

One of the aims of here presented work is to incorporate the complex behaviour of concrete under changing moisture conditions into the 3D chemo-hygro-thermo-mechanical model. It is important to note that in the previous model definition, the distribution of water content was described as transport of capillary water in terms of volume fraction of pore water by Richards' equation (Ožbolt et al. 2010, 2011). Implementation of hysteretic moisture behaviour of concrete presents a further development of the model with the ability to account for the cyclic environmental moisture conditions (drying-wetting) and its effects on transport processes.

The main adsorption and desorption curves are given as input data. The model explicitly calculates the distribution of relative humidity in concrete and then indirectly determines the moisture content based on the sorption curves. By knowing the position on the isotherm curve from a previous computational time step, a new distribution of the relative pore pressure can be calculated for the current boundary conditions. Subsequently, the corresponding water content is established from a new location on the isotherm curve. In the case of static moisture conditions, i.e. constant wetting or drying, the analysis is following the input main adsorption or desorption curve. This is valid only for the assumption that the initial starting condition (previously wetted or dried concrete) corresponds to the boundary environmental condition (wetting or drying).

With the dynamic moisture conditions, i.e. with the change from wetting to drying or vice versa, the scanning curves need to be determined. They are calculated empirically by using the formulas developed by Pedersen (1990). They differ from the

main adsorption or desorption curves and behave in a loop-like manner depending on the number of wetting and drying cycles.

The implemented scanning curves are verified by simulating the experiments of Baroghel-Bouny (2007). To give more insight into the relative humidity and water content distribution in concrete exposed to wetting and drying cycles, the experiments of Dong et al. (2011) are simulated. The numerically obtained results show that the model is capable of realistically calculating the complex hysteretic moisture behaviour under numerous wet and dry cycles.

For the case of concrete specimens exposed to chloride attack in a dynamic moisture environment, chloride profiles along the concrete cover depth are analysed and compared to the experimental results (Polder & Peelen 2002). The analysis amplifies the importance of the hysteretic moisture behaviour of concrete in the CHTM model. The predicted "peak" chloride profiles can only be accounted for by exposure to cyclic wetting and drying conditions at the specimen's surface.

1.2 Research objectives

The objectives of the here presented thesis are:

1. Extend the 3D chemo-hygro-thermo-mechanical (CHTM) model to simulate the damage in RC elements due to expansion of corrosion products around the reinforcement bars.

2. Implement the rate of rust production and develop the 1D corrosion contact elements for encompassing the inelastic expansion of rust products.

3. Account for the transport of corrosion products in the CHTM model.

4. Validate the implemented phenomena in the CHTM model through comparison with experimental results for single and multi rebar cases.

5. Analyse the influence of size and position of the anodic and cathodic regions on the corrosion induced damage.

6. Investigate the influence of transport of corrosion products on the corrosion induced damage.

7. Investigate the influence of corrosion induced damage on the pull-out capacity of the reinforcement bar.

8. Validate the developed CHTM model for specimens reinforced with both, rebars and stirrups.

9. Account for the hysteretic behaviour of concrete in the CHTM model, in order to accommodate the dynamic moisture conditions, i.e. the exposure to wetting and drying cycles.

10. Validate the hysteretic moisture model for concrete and its effect on transport of chlorides through experimental results.

1.3 Scope of research

Here presented work is focused on the numerical analyses of the non-mechanical and mechanical processes important for the development of corrosion induced damage. Experimental results from other researchers are used to validate the presented 3D CHTM model.

Emphasis of the numerical analyses is on the processes after the depassivation of reinforcement bars. Specifically, the anodic and cathodic regions were chosen upfront and kept unchanged throughout the calculation, which is an assumption made to simplify already complicated processes. This is not a limitation of the CHTM model, which is able to simultaneously calculate the processes before and after depassivation, but rather an approach chosen due to time and CPU requirements that such calculations would require.

Certain input parameters for the hysteretic moisture behaviour of concrete and for the transport of corrosion products have approximate values due to very complicated methods for their experimental measurement. Although their values are inside the permitted boundaries mentioned in the literature, they should be taken more in a qualitative sense.

2 LITERATURE REVIEW

2.1 Modelling corrosion induced damage of reinforced concrete

Corrosion induced damage is a major limiting factor for the durability of reinforced concrete structures, causing progressive damage to the concrete cover and embedded steel bars. The corrosion process in concrete is usually divided into two phases (fib 2006): (i) initiation and (ii) propagation phase (Figure 2.1). The initiation phase is defined as a time period characterised by the ingress of aggressive substances through the concrete cover. The protective oxide film on the bar surface becomes damaged by reaching a critical concentration of chloride ions in the vicinity of the steel surface or by carbonation of the protective concrete cover. The depassivation of the protective surface layer marks the start of the active corrosion process or the propagation phase. During this period the electrochemical reactions are occurring at the anodic and cathodic half-cells. The expansive volume of the corrosion products at the anodic regions causes cracking and spalling of the concrete cover. Further on, the loss of reinforcement cross section leads to the reduction of the structure load bearing capacity.

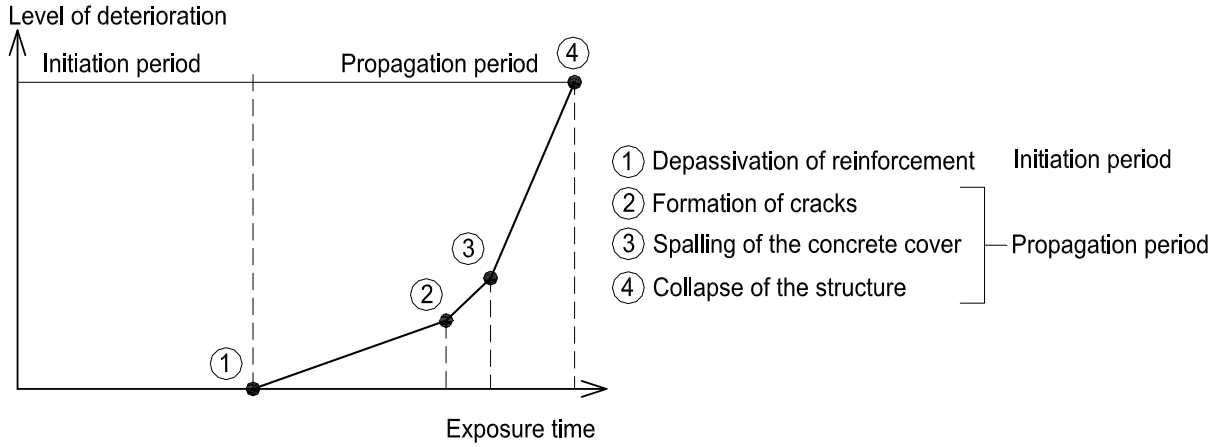

Figure 2.1 Initiation and propagation period with the corresponding deterioration levels for a reinforced concrete structure exposed to corrosion (FIB 2006)

Modelling corrosion induced damage of concrete during the propagation phase is a highly challenging task. It requires not only a realistic modelling approach for the electrochemical reactions and the rate of rust production, but also a proper assessment of the mechanical and transport properties of the corrosion products. Further on, the non-mechanical processes need to be coupled with the mechanical behaviour of concrete in order to properly evaluate the influence of damage (cracks) on the kinetics of the investigated reactions.

One of the most important parameters in determining the behaviour of active corrosion processes is the current density, i (Liu & Weyers 1998; Otieno et al. 2011). The rate of rust production is highly dependent on the values of the current density at

the anodic sites. Therefore, the model's ability to realistically determine the corrosion induced damage (cracks) is directly related with its competence to properly assess the current densities for different environmental conditions.

The reactions (Eq. 1.1-1.3) of the corrosion cell indicate that the values of the current density are governed by the processes, which can also be described as resistances in a simplified corrosion electrical circuit (Figure 2.2) (Raupach 1996; Balafas & Burgoyne 2010):

- the iron oxidation at the anodic half-cell , i.e. anodic resistance (R_a)
- the oxygen and water supply at the cathodic half-cell, i.e. cathodic resistance (R_c)
- the hydroxyl ions transport through the concrete pore water (electrolyte), i.e. concrete resistance (R_{con})

The flow of the electric charge will be blocked if one of the resistances is infinite (Balafas & Burgoyne 2010). The propagation phase cannot start if the passive protective film surrounding the steel bar is not damaged ($R_a \rightarrow \infty$). Absence of oxygen at the cathodic regions ($R_c \rightarrow \infty$), which is a characteristic of the underwater concrete structures, stops the active corrosion process. Completely dried out concrete lacks not only the medium for the transport of hydroxyl ions ($R_{con} \rightarrow \infty$), but also the reactant needed for the cathodic half-cell reaction ($R_c \rightarrow \infty$). Steel resistance ($R_s \approx 0$) can be neglected compared to previously mentioned resistances.

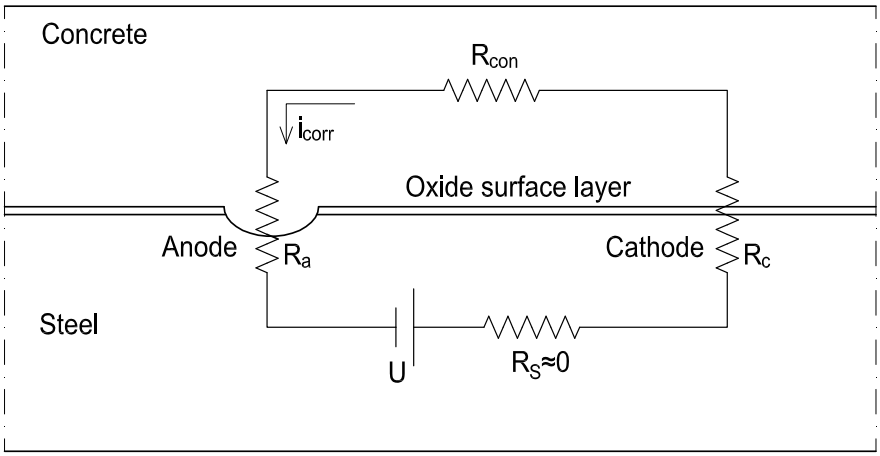

Figure 2.2 Resistances in a simplified electrical circuit (Raupach 1996)

Rate of rust production and the corresponding properties of corrosion products should be properly taken into account when modelling corrosion induced damage. The connection between the current density and the production rate of the resulting corrosion products should be established. Mechanical properties of the produced rust need to be given as an model input parameter to accommodate the expansive nature of the rust and its effects on the cracking and spalling of concrete cover.

Recent experiments (Wong et al. 2010; Fischer 2012) have demonstrated the importance of incorporating the transport of corrosion products into the pores and cracks around the reinforcement bar. Without accounting for this phenomena, the models are unrealistic and overestimate results in terms of the first crack appearance and the extent of damage. Governing model parameters for simulating the corrosion induced damage in reinforced concrete are addressed in the following sections.

2.1.1 Transport processes before depassivation of reinforcement

The emphasis of the here presented work is on the processes after the depassivation of steel in concrete. Hence, a comprehensive overview of the state of the art in regard to developing the 3D CHTM model for the initiation phase can be found in Kušter (2013).

Deterministic modelling approach of the initiation phase, in a chloride aggressive environment, requires a realistic and comprehensive description of chloride ions ingress through the concrete cover, taking into account the effects of possible concrete damage (cracks). Therefore, the transport of free and bound chloride ions, water, oxygen and distribution of heat in concrete need to be accounted for in a model predicting the depassivation of reinforcement (Page et al. 1981; Zhang & Gjørv 1996; Andrade et al. 1997; Martin-Perez 1999; Thomas & Bamforth 1999; Glass & Buenfeld 2000).

Furthermore, the non-mechanical processes have to be coupled with the mechanical behaviour of concrete as the cracking of the concrete cover accelerates the ingress of chlorides (Ishida et al. 2009; Marsavina et al. 2009; Ožbolt et al. 2010; Bentz et al. 2013; Kušter 2013; Šavija et al. 2013a). Modelling of chloride transport in unsaturated concrete presents a further challenge due to a dominant moisture transport of chloride ions (Saetta et al. 1993; Ababneh et al 2003; Sleiman et al. 2012). Additionally, there is a very limited number of models in the literature capable of predicting the chloride profiles in concrete exposed to cyclic wetting and drying conditions (Meijers et al 2005; Fenaux 2013).

Distribution of water content in unsaturated concrete can be described as a single phase flow model of pore water by using Richards equation, which presents a generalized Darcy equation (Richards 1931; Bear & Bachmat 1990; Kumar 2010). Furthermore, the moisture content in concrete can be expressed in terms of pore relative humidity and requires determining the concrete sorption curves (Bažant & Najjar 1972, Xi et al. 1993). Concrete subjected to dynamic moisture conditions (cyclic wetting and drying) exhibits a pronounced hysteretic moisture behaviour, i.e. the water content values are highly dependent on the moisture loading history. Hysteretic moisture model for concrete in here presented work is developed as a further extension of the 3D CHTM model, applicable for modelling processes before

and after depassivation. Due to the complexity of the aforementioned problem, a detailed literature review is presented in separate Section 2.2.

2.1.2 Electric potential and polarization

Corrosion of steel reinforcement in concrete is an electrochemical process which includes the cathodic and anodic half-cell reactions (Eq. 1.1-1.2). Each half-cell reaction has a standard potential measured at equilibrium in regard to a reference electrode (usually a hydrogen electrode) under standard conditions (25 °C) (Callister & Rethwisch 2012). Oxidation of iron at the anodic site and the oxygen reduction at the cathodic region have a standard potential of 0.440 V and 0.401 V, respectively (Ang & Chen 2009; Callister & Rethwisch 2012).

The change of the half-cell standard potential from its equilibrium value due to the generated electric current is called polarization and the corresponding change value is called overpotential. Two types of polarization have an important effect on the kinematics of the corrosion cell: the activation and the concentration polarization. Both contributions to the electric overpotential should be accounted for in the models simulating corrosion induced damage in concrete.

Activation polarization presents a change of corrosion cell potential due to the overcoming of the activation energy of electrochemical reactions. This energy barrier is related to the slowness of the charge-transfer process occurring on the surface of electrodes (Stolten 2010). Effect of the activation polarization on the current density is described by the Butler-Volmer equation (McCafferty 2010):

$$i = i_0 \left[\exp\left(\frac{\alpha_{barr} z F}{RT} (\Phi - \Phi_0) \right) - \exp\left(\frac{-(1-\alpha_{barr}) n F}{RT} (\Phi - \Phi_0) \right) \right] \tag{2.1}$$

where i_0 is the exchange current density (A/m^2), z is the number of transferred charge, α_{barr} is a dimensionless parameter as a measure of free energy barrier symmetry , Φ is the electric potential (V), Φ_0 is the equilibrium electric potential (V), F and R are Faradey's and universal gas constants, respectively, and T is the absolute temperature (K). For higher values of overpotential $(\Phi - \Phi_0)$ the last term in Eq. 2.1, presenting the rate of the reverse reaction, becomes negligible (Newman & Thomas-Alyea 2004). By plotting the current density as a function of the relatively higher overpotential values, in a semi-log scale, the linear Tafel curves are obtained (McCafferty 2010). For this linear region, the Tafel equation can be derived from Equation 2.1:

$$(\Phi - \Phi_0) = \frac{2.303RT}{\alpha nF} \log \frac{i}{i_0} = \beta \log \frac{i}{i_0} \tag{2.2}$$

where β is the slope of the Tafel curve.

Concentration polarization is the potential difference due to the changes in the reactant's concentration at the electrode-electrolyte interface (Böckris et al. 2000). The supply shortage of the reacting species at the electrode's surface causes the decrease of the equilibrium potential and is termed as the concentration overpotential. Cathodic half-cell reaction, i.e. the reduction of oxygen at the cathodic sites (Eq. 1.1) is therefore dependent on the process of oxygen diffusion to the cathode surface. The relation between the concentration overpotential $(\Phi - \Phi_0)$ and the limiting oxygen supply in the case of the cathodic reaction can be written as follows (McCafferty 2010):

$$(\Phi - \Phi_0) = \frac{2.303RT}{4F} \log \frac{C_o^{surf}}{C_o} \tag{2.3}$$

where C_o^{surf} and C_o are the concentrations of dissolved oxygen at the electrode surface and in the bulk of the electrolyte (kg/m^3), respectively.

2.1.3 Electrical resistivity of concrete

Electrical resistivity of concrete or its reciprocal value (electrical conductivity of concrete) is a significant factor for determining the values of current density and consequently the amount of corrosion induced damage (Liu 1996; Martin-Perez 1999; Bertolini et al. 2004). The current density increases with higher values of the electrical conductivity. Hence, it is necessary for a model to incorporate different parameters which have an influence on the change of the electrical conductivity. During the propagation phase, the flow of ions is introduced in the concrete pores surrounding the rebar. The resistance to this flow presents the electrical resistivity of concrete which is influenced by the concrete porosity, the degree of water pore saturation and the composition of the pore solution (Bentur & Diamond 2005).

The higher value of the concrete water-cement ratio increases not only the total pore volume of concrete, but also the connectivity and the size of the pores (Van Mier 1996; Bertolini et al. 2004). Hence, the electrical resistivity decreases with the increase of the w/c ratio (Gjørv et al. 1977; Tuutti 1993).

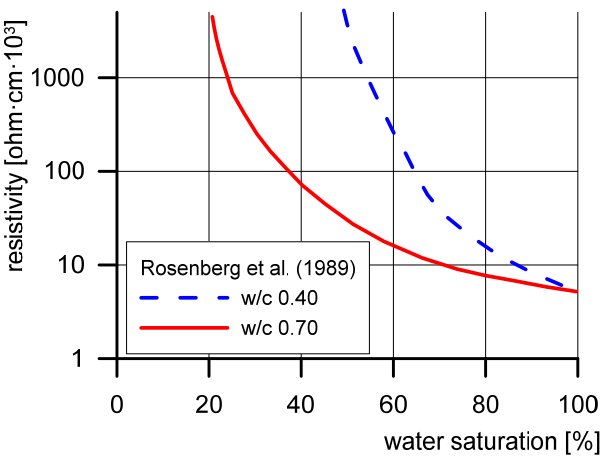

Figure 2.3 Electrical resistivity of concrete as a function of water saturation for the water-cement ratio of 0.40 and 0.70 (Rosenberg et al. 1989)

Degree of water saturation has a major influence on the values of the current density. Experimental measurements have shown that the decrease of the water saturation from a fully saturated concrete to relatively low values of saturation can increase the electrical resistivity up to approximately three orders of magnitude (Figure 2.3) (Gjørv et al. 1977; Rosenberg et al. 1989; Tuutti 1993). The values of electrical conductivity of concrete measured by (Gjørv et al. 1977) are given in Table 2.1 as a function of water saturation for w/c ratios of 0.4 and 0.7.

Table 2.1 Values of electrical conductivity of concrete as a function of water saturation for w/c ratios 0.4 and 0.7 (Gjørv et al. 1977)

Electrical conductivity σ ($10^{-3}\ \Omega^{-1}m^{-1}$)											
Saturation (%)	40	45	50	55	60	65	70	75	80	85	90
w/c = 0.40	0.03	0.07	0.20	0.25	0.53	0.75	1.00	2.00	6.00	10.0	11.2
w/c=0.70	1.0	1.81	2.75	3.0	4.28	8.70	9.52	10.5	11.5	12.5	13.5

Higher values of the chloride ion concentration in the pore solution can decrease the electrical resistivity to a certain extent (Browne 1980). This is an indirect effect due to the hygroscopic nature of chlorides which can influence the retainment of water in concrete. Further on, the carbonation of the concrete cover can increase the electrical resistivity (Bertolini et al. 2004). This is usually explained by the decrease in the concrete porosity as the expansion of the solid volume occurs with the formation of the calcium carbonate (Chi et al 2002).

Osterminski et al. (2012) provided extensive and detailed experimental data with emphasis on the long term behaviour of the electrical resistivity of concrete, taking into account the effects of cement type (ordinary Portland cement and blast furnace

slag cement), w/c ratio (0.45, 055 and 0.65), external humidity distribution and cover depths. As expected, a higher w/c ratio resulted in increasing the sensitivity of concrete to external moisture fluctuations. The slag cement exhibited not only a higher electrical resistivity compared to Portland cement, but also a continuous increase over a long period of time (up to 13 years) due to a ongoing hydration of the slag component. In comparison, the Portland cement showed no significant changes in electrical resistivity after approximately 3 years. Furthermore, an extensive approach for quantifying the electrical resistivity of concrete was presented in the probabilistic, engineering model for predicting the corrosion of steel reinforcement by Osterminski & Schieβl (2012). The approach is based on measuring the reference value of the electrical resistivity for concrete elements (28 days after casting) and on quantifying the factors which take into account the testing method of the reference value, humidity, chloride content, carbonation, temperature and cement hydration (Osterminski & Schieβl 2012, von Greve-Dierfeld & Gehlen 2012).

2.1.4 Oxygen supply at cathodic regions

Oxygen supply at cathodic regions is a hindering factor for the rate of corrosion reactions, as mentioned in Section 2.1.2. The value of the current density is limited by the availability of the dissolved oxygen in the electrolyte needed as a reactant for the cathodic reaction (Eq. 1.2). Consumption of oxygen causes the oxygen concentration at the steel-concrete interface to be less compared to the concentration in the concrete bulk. At higher levels of water saturation the oxygen arriving at the cathode is instantaneously consumed. Hence, an interface diffusion layer ensues, governed by the oxygen concentration gradient (Böckris et al. 2000). Under such conditions the maximum possible current density is equal to the limiting diffusion current density $i_{c,dif}$ of the oxygen reduction which can be calculated by combining the Faraday's law and the Fick's first law of diffusion (McCafferty 2010), as follows:

$$i_{c,dif} = zFD_o \left.\frac{\partial C_O}{\partial n}\right|_{cathode} \tag{2.4}$$

where z is the number of electrons transferred in the cathodic reaction (z = 4), F is the Faraday's constant, D_o is the oxygen diffusivity coefficient (m^2/s), C_o is the oxygen concentration per volume of pore water (kg/m^3) and n is the normal to the cathode surface.

It is therefore important for a model simulating corrosion induced damage to couple the transport of oxygen in concrete with the ongoing electrochemical reactions. The main parameters influencing the oxygen distribution in concrete is the degree of water saturation (Page & Treadaway 1982; Broomfield 2002) and the concrete

quality, i.e. the water-cement ratio (Tuutti 1982). Kobayashi & Shuttoh (1991) investigated the influence of concrete pore saturation on the oxygen diffusivity coefficient and obtained values which were 15 times higher when the saturation dropped down from 80% to 40%. Similarly, Sudjono & Seki (2000) determined that the value of the oxygen diffusivity coefficient dropped significantly for saturation values over 80%. Values of oxygen diffusivity coefficient determined by Tuutti (1982), as a function of water saturation, are given in Table 2.2 for concrete with w/c ratio of 0.40 and 0.70.

Huet et al. (2007) and Hussain & Ishida (2010) developed comprehensive models for simulating transport of both dissolved and gaseous oxygen phases through the concrete porous media. Further on, the oxygen consumption at the cathodic site is incorporated in the models as a direct influence on the current density of the corrosion cell. Although the models present an elaborate contribution for simulating the oxygen supply in reinforced concrete during an active corrosion process, the application of the models was presented only on one dimensional cases. Additionally, determining a number of the model input parameters is a challenging task in regard to lack of available experimental data. The influence of damage (cracks) on oxygen distribution is not incorporated in the models which can have a significant influence on the corrosion rate.

Table 2.2 Values of oxygen diffusivity for concrete as a function of water saturation for w/c ratios 0.4 and 0.7 (Tuutti 1982)

Oxygen diffusivity D_o (10^{-8} m^2/s)											
Saturation (%)	40	45	50	55	60	65	70	75	80	85	90
w/c = 0.40	2.75	2.15	1.55	1.30	1.20	1.00	0.75	0.45	0.30	0.20	0.13
w/c=0.70	10.7	10.2	9.30	9.00	8.00	7.50	6.00	5.00	3.50	2.50	1.50

2.1.5 Current density

With respect to their approach for determining current density, the models for simulation of corrosion induced damage can be divided in two main groups. Empirical models define direct formulas for calculating the corrosion rate based on numerous experimental data, while the mathematical models specify a set of complex partial differential equations which need to be numerically solved.

2.1.5.1 Empirical models for defining the current density

Yalcyn & Ergun (1996) performed accelerated corrosion tests on concrete cylinder specimens and measured the influence of chloride and acetate ions on the current density. The measurements were performed by using linear polarization resistance (LPR) method and by determining the half-cell potentials (Yalcyn & Ergun 1996). The experiments were conducted for a period of 90 days and from the experimental data the following equation was obtained:

$$i = i_{init} e^{-Ct} \tag{2.5}$$

where i is the current density at certain time t, i_{init} is the initial current density and C is a constant (s^{-1}) dependant on the pore saturation, pH value, cover thickness and permeability. The constant was calibrated from the experiments. The main disadvantage of the model lies in its calibration that was based on the accelerated corrosion tests conducted on uncracked concrete specimens in a relatively short period of time. With only one type of concrete mixture investigated, the model application is very limited and not realistic for natural corrosion conditions.

Liu & Weyers (1998) conducted a large scale experimental program with 44 uncracked bridge slabs exposed to outdoor conditions lasting up to 5 years. Different parameters were varied: the concrete cover, water to binder ratios, the cement content and the addition of NaCl in the concrete mixture. The current densities were measured using the LPR technique. From the statistical analysis of the results a non-linear regression curve was obtained:

$$i = 0.0092 \exp(8.37 + 0.618 \ln(1.69 C_{c,tot}) - 3034(T^{-1}) - 0.0015 r_C + 2.35 t^{-0.215}) \tag{2.6}$$

where $C_{c,tot}$ is the total chloride content near the steel's surface (kg/m^3), T is the temperature near the reinforcement (K), r_C is the ohmic resistance of the concrete cover (ohm) and t is the time expressed in years. Although Liu & Weyers (1998) model presents a more elaborated attempt for determining current density, it should be noted that its application in a 3D structural applications is not clear due to the fact that the model doesn't encompass the ability to assess the geometrical effects, i.e. the influence of the concrete cover, the different anodic-cathodic configuration on the steel bar or the number and spacing of multiple rebars and stirrups. Also, some researchers have reported (Balafas & Burgoyne 2010) that for the start of the propagation phase the model gives unrealistically high values of i.

Scott (2004) experimentally measured the current densities for cracked beam specimens with crack widths of 0.2 and 0.7 mm. Different parameters were varied:

concrete covers, water to binder ratios and binder types. An empirical formula for current density was obtained by calibrating it with the experimental data:

$$i = \left(1.43 \frac{C_{cond,90}}{f} + 0.02 \right) e^{\left[(40 - c_{\text{cov}}/20) 1.2 (C_{cond,90}/f)^3 \right]} \tag{2.7}$$

where f is the slag correction factor depending on the binder type, $C_{cond,90}$ is the 90 day chloride conductivity index value (mS/cm) and c_{cov} is the concrete cover depth in mm. Although the current densities were measured on cracked specimens, the crack width is not incorporated in the model as an input parameter. Additionally, the specifics of the test setup and the difficulties in determining the chloride conductivity index values limit the application of the model to a narrow set of scenarios.

Martinez & Andrade (2009) have proposed three ways to determine an annually representative current density $i_{corr,rep}$. The value can be obtained by integrating the on-site measured current density curve as a function of a longer period of time and then dividing the integral value with time expressed in years. If there is no possibility to measure the time development of the current density, Martinez & Andrade (2009) have proposed approximate values corresponding to the exposure classes of Eurocode 2:DIN EN 1992. The third approach consists of individual short term in situ measurements of the current density i_{corr}^{site} and the corresponding resistivity. The drilled samples from the investigated site are then conditioned to 85% of relative humidity (for structural elements protected from the rain) or vacuum water saturated (for non sheltered structural elements) and subsequently the minimum resistivity is measured. By plotting the in situ current density values as a function of resistivity, the maximum current value $i_{corr}^{\max}$ can be extrapolated from the measured minimum resistivity. Finally, the representative current density value can be calculated as:

$$i_{corr,rep} = \frac{i_{corr}^{site} + i_{corr}^{\max}}{2} \tag{2.8}$$

Martinez & Andrade (2009) model presents a simplified engineering approach for determining the current density whose accuracy largely depends on the extent of the experimental measurements.

2.1.5.2 Mathematical models for defining the current density

Mathematical models for modelling of corrosion induced damage in concrete represent a complex set of coupled partial differential equations (PDE) for describing processes before and/or after depassivation of reinforcement. The current density in mathematical models is usually calculated from the distribution of the electric

potential Φ ,i.e. from the potential gradient $\nabla\Phi$ and from the known values of the electrical conductivity of concrete. The PDE describing the corrosion processes are solved by using a suitable numerical method (finite element method, finite difference method etc.).

Bažant (1979a) developed a highly sophisticated model able to model processes before and after depassivation of steel. Taking into account the Nernst equation for concentration polarization, the anodic and cathodic potentials are calculated, respectively:

$$\Phi^{anode} = 0.357 - 0.0296 \log u_w^{anode} + 0.0296 \log C_f \quad (2.9a)$$

$$\Phi^{cathode} = 1.187 - 0.0148 \log u_w^{cathode} + 0.0148 \log C_o \quad (2.9b)$$

where u_w^{anode} and $u_w^{cathode}$ are amounts of capillary water at anode and cathode, respectively ($m^3_{H_20}/m^3_{con}$), C_f is the concentration of ferrous hydroxide $Fe(OH)_2$ per cubic meter of concrete (kg/m^3) and C_o is the oxygen concentration per cubic meter of concrete (kg/m^3). Considering only the concentration polarization presents a valid assumption only for highly saturated concrete, such as submerged RC elements. Oxygen diffusivity decreases with higher values of water saturation (Gjørv et al. 1977). Hence, the oxygen supply at the cathodic regions becomes a limiting factor for the kinetics of the electrochemical reactions. For relatively lower values of the water content, in cases of elements subjected to periodical wetting and drying conditions, the contribution of the activation polarization should be included in defining the overall polarization of the corrosion half-cells (Kranc & Sagüés 1997; Martin-Perez 1999; Otieno et al. 2011).

Kranc & Sagüés (1997) developed a detailed model for simulating corrosion induced damage, based on the approach of Walton & Sagar (1986) and Harker et al. (1987) who used Butler-Volmer kinetics to calculate uniform corrosion of radioactive waste metal canisters encircled by a concrete layer. They proposed that the kinetics of the anodic reaction, i.e. dissolution of iron, is only controlled by the activation polarization. On the other hand, the polarization at the cathodic regions is a combination of activation and concentration polarization effects. The later takes into account the possible reduction of the oxygen supply due to the higher values of water saturation. Subsequently, the calculated anodic and cathodic potential are used as boundary conditions for solving the Laplace's equation of the electric potential Φ in concrete:

$$\nabla^2 \Phi = 0 \quad (2.10)$$

Further on, the current density is calculated from the Ohm's law by determining the gradient of the electric potential and the corresponding electrical conductivity of

concrete. By taking into account, not only the activation polarization, but also the limiting factor of oxygen supply at the cathodic sites, the model of Kranc & Sagüés (1997) model gives a more realistic approach for modelling of corrosion current density.

Isgor (2001) model, similarly to Kranc & Sagüés (1997), solves Eq. 2.10 by determining the boundary conditions from polarization of the cathodic and anodic regions. The cathodic site are assumed to polarize as a combination of activation and concentration polarization, while the anodic sites only as activation polarization. The boundary conditions at the anodic and cathodic sites are obtained (Stern & Geary (1957) as follows:

$$\Phi^{anode} = \Phi^0_{Fe} + \beta_a \log \frac{i_a}{i_{0a}} \tag{2.11a}$$

$$\Phi^{cathode} = \Phi^0_{O_2} + \beta_c \log \frac{i_c}{i_{0c}} - \frac{2.303RT}{zF} \log \frac{i_{c,dif}}{i_{c,dif} - i_c} \tag{2.11b}$$

where Φ^0_{Fe} and $\Phi^0_{O_2}$ are the standard half-cell potentials of iron and oxygen (V), β_a and β_c are the Tafel slopes of the anodic and cathodic reactions, i_{0a} and i_{0c} are the anodic and cathodic exchange current densities (A/m^2) and i_L is the limiting current density (A/m^2). Similarly to approaches from Bažant (1979a) and Kranc & Sagüés (1997), the model's challenge lies in determining the anodic and cathodic distributions on the reinforcement bar surface.

In Raupach & Gulikers (1999) model, the macro-cell current density is calculated by using the Ohm's law in a simplified electrical circuit (Figure 2.2). Hence, the potential difference between the cathodic and anodic site is divided with the circuit equivalent resistance and the following is obtained:

$$i = \frac{\Phi^0_{O_2} - \Phi^0_{Fe}}{R_{p,c} + R_{con} + R_{p,a} + R_s} \tag{2.12}$$

where Φ^0_{Fe} and $\Phi^0_{O_2}$ are anodic and cathodic equilibrium potentials, respectively, R_{con} and R_s are the concrete and steel electrical resistances (Ω), $R_{p,a}$ and $R_{p,c}$ are the anodic and cathodic polarization resistances calculated by using Butler-Volmer kinetics (Ω). The main drawback of the model is its limited application in regard to positioning the anodic and cathodic sites for a complicated reinforcement geometry and multi-rebar cases.

Maruya et al. (2007) model combines the micro- and macro-cell corrosion approaches for calculating the corrosion current density. The macro-cell circuit occurs between the anodic and cathodic regions separated at a certain distance, while the micro-cell circuit consists of anode and cathode at a negligible distance. In the first part of the model, anode and cathode are assigned to each element of the discretized steel bar (Figure 2.4a) with the assumption that there is no interaction between separate elements. Hence, the half-cell potential and the current density for each micro-cell circuit are calculated at the intersection point of the corresponding anodic and cathodic polarization curves (Maruya et al. 2007), which relate the electric potential with the anodic or cathodic current density (Bertolini et al. 2004), respectively. The anodic polarization curve is dependent on the ratio of chloride and hydroxyl ion concentration, while the cathodic polarization curve is a function of the oxygen concentration at the rebar surface. In the second part of the model, the macro-cell circuit can be established between any two separate electrodes with different micro-cell potentials. The half-cell potentials and current density of the macro-cell circuit are calculated by taking into account the distance between the electrodes, concrete electrical resistivity and the Tafel slopes of the macro-cell polarization curves (Maruya et al. 2007). Due to the presence of larger number of electrodes along the bar, all of the macro-cell circuits between the element with a lowest micro-cell potential (anode) and the rest of the elements (cathodes) need to be analysed (Figure 2.4b) .

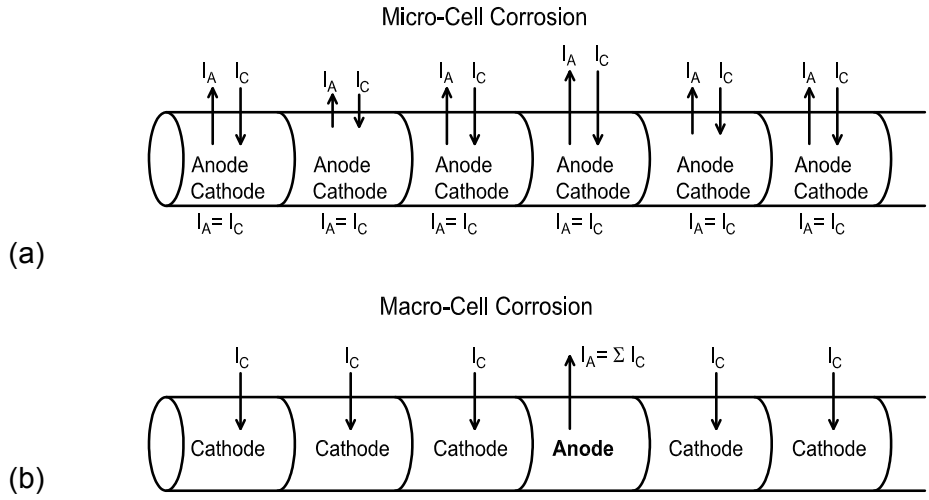

Figure 2.4 Micro-cell (a) and macro-cell (b) modelling approach by Maruya et al (2007)

Although the model presents a very detailed attempt in calculating the current density, the actual values of the anodic and cathodic polarization curves for the micro-cell corrosion and the Tafel slopes of the macro-cell circuit are given as empirical equations. Hence, the values are highly dependent on the corresponding test setups used for their determination. Additionally, a complex reinforcement configuration presents a challenging task for determining the current density as the interaction between each element in the macro-cell circuit needs to be considered.

2.1.6 Corrosion products

2.1.6.1 Types of corrosion products

Types of corrosion products forming around the depassivated regions of steel reinforcement in concrete are significantly influenced by the availability of water and oxygen, but also by the chloride concentration around the steel-concrete interface (Šavija et al. 2013b). Usually, corrosion products are a mix of different hydroxides, oxides and even complex chemical compounds containing chlorides and sulfates (Jamali et al. 2013). Their content and ratios are highly affected by the environmental conditions. Correspondingly, their effect on the cracking of the concrete cover can differ greatly depending on their volume increase compared to steel. The relative volume increase varies from 1.70 up to the value of 6 (Fischer 2012). Different types of rust products which can form during the corrosion process are listed in Table 2.3. The data from Table 2.3 illustrate the importance of different rust products forming around the reinforcing bars for the analytical models. Obviously, the input model parameters should be calibrated according to the dominant environmental conditions influencing the rust production.

Table 2.3 Corrosion products and their volume increase in comparison with steel

Corrosion product	Chemical formula	Relative volume increase compared to steel
Iron oxide	FeO	1.70
Hematite	1/2 Fe_20_3	2.00
Magnetite	1/3 Fe_20_3	2.10
Geothite	α-FeOOH	2.91
Lepidocrocite	γ-FeOOH	3.03
Akagenite	β-FeOOH	3.48
Ferrous hydroxide	$Fe(OH)_2$	3.60
Ferric hydroxide	$Fe(OH)_3$	4.00
Hydrated ferric hydroxide	$Fe(OH)_3$, $3H_2O$	6.15

2.1.6.2 Rate of rust production

Rate of rust production at the depassivated regions of the reinforcement bars is dependent on the anodic current density. In certain models (Bažant 1979a; Andrade et al. 1993; Martin-Perez 1999) this relationship is considered to be linear and based on the following: (i) the Faraday's law and (ii) the stoichiometry of the electrochemical reactions. Hence, the rate of the rust production J_r (kg/m^{2}s) at the anode is proportional to the anodic current density and to the equivalent mass (M/z) of the corrosion product:

$$J_r = \frac{i_a M}{F z} \tag{2.13}$$

where i_a is the anodic current density, F is the Faraday's constant , z is the valency of the reaction and M is the molar mass of the corresponding corrosion product.

Liu & Weyers (1998) proposed an empirical model in which the rate of rust production decreases with time as a consequence of the increasing thickness of the rust layer. As the layer becomes thicker, the iron ionic diffusion distance increases and the rate of rust production should decrease. The disadvantage of the model is that it gives unrealistically high values at the beginning of the depassivation phase. Balafas & Burgoyne (2010) have therefore proposed that the rust production should follow the Faraday's linear law at the start of the corrosion process, but should change to the Liu & Weyers (1998) model at the later phase. The problem with such approach is the uncertainty in choosing the proper value of the parameter, which governs the reduction of the corrosion rate and which Liu & Weyers (1998) determined empirically by calibration with the experimental results. Hence, the model cannot be used as a proper prediction tool without knowing in advance the results of the corrosion induced damage.

2.1.6.3 Mechanical properties of corrosion products

Experimental data on the mechanical properties of corrosion products is scarcely available in the literature. Therefore, many numerical models for simulating the corrosion induced damage in concrete estimate the mechanical properties, especially the value of the elastic modulus of corrosion products. For example, Molina et al. (1993) assumed that the properties of rust are similar to those of liquid water and the value of 12 N/mm^2 is assumed for the modulus. On the other hand, in the numerical model developed by Bhargava et al. (2005), the relatively high value of the steel modulus of elasticity was taken as the input mechanical parameter for the corrosion products. In the numerical work of Suda et al (1993) the value of 100 N/mm^2 or higher was proposed.

Experimental and numerical analysis by Caré et al. (2008) determined the value of the modulus of elasticity to be equal to 130 N/mm^2. The value was calculated by conducting the accelerated corrosion tests and measuring the radial displacement at the steel-concrete interface by using digital image correlation. The displacements were taken as the input data for the analytical model of a hollow cylinder subjected to inner and outer pressures and subsequently the Young's modulus was calibrated.

Müller and Bohner (2012) obtained the elastic modulus of rust based on an extensive experimental study and a subsequent numerical analysis. The experiments were focused on measuring the tangential strains on the surface of concrete cylinders with

a single rebar exposed to aggressive environmental conditions. The corresponding tangential strains were additionally obtained on a set of hollow concrete cylinders with embedded thin-walled copper tubes by controlling the pressure of the hydraulic fluid in the tube. The value of 30000 N/mm^2 was calibrated by predicting the measured tangential strains with a 2D numerical model of the concrete cylinder. The model loading function was defined as a uniform increase of the embedded steel bar radius, determined from the hollow cylinder experimental and numerical data

In recent experimental results by Zhao et al. (2012), the elastic modulus of corrosion products was measured directly by performing the cyclic low-compression tests on a series of flaky rust samples taken from naturally corroded reinforcement exposed to marine environment. The apparent Young's modulus was determined to be 165 N/mm^2. The experimentally obtained result is dependent on the local environmental conditions, therefore the value of 100 N/mm^2 was proposed (Zhao et al. 2012) as the input elastic modulus for corrosion products.

2.1.6.4 Influence of the porous zone for accommodating the corrosion products

It is well known from the literature (Wong et al. 2010; Michel et al. 2011; Angst et al. 2012) that corrosion products penetrate the concrete pores and voids around the depassivated regions of the reinforcement bars. This can to a certain extent mitigate the expansive pressure of rust on the surrounding concrete cover. The penetration of the rust products into the pores is a complex process dependant on the corrosion rate, the pore solution and the convective and diffusive aspects of the soluble species (Jamali et al. 2013).

Determining the diffusion coefficient of the corresponding soluble species in concrete is a challenging task and there is currently no available information in the literature. The diffusion coefficient of the ferric ion (Fe^{3+}) in uncracked concrete with a w/c ratio of 0.4 is given in Castellote et al. (1999). The measured results give an approximate orienting range from 2.57×10^{-14} up to 7.81×10^{-16} m^2/s. The data showed a relatively large discrepancy and the diffusion coefficient values of the ferrous species were not addressed. Further on, assuming such low value of the diffusivity coefficient results in a relatively small amount of rust being transported into the pores and voids of uncracked concrete.

A number of numerical models (Molina et al. 1993; Liu & Weyers 1998; Bhargava et al. 2005; El Maaddawy & Soudki 2007; Chernin & Val 2011; Lu et al. 2011) incorporated this effect by assuming a "ring" zone around the embedded bars, which can accommodate the penetrating products. The models assume that the diffusive or porous zone has a uniform thickness around the reinforcement bar and the pressure can only be exerted on the concrete after filling the zone with rust products. The main

drawback of such models, as stated in Jamali et al. (2013), is not only the uncertainty of choosing the thickness, but also the assumption of their uniform distribution around the bar.

The zone thickness is usually assumed between 10 to 20 μm (Liu & Weyers 1998; El Maaddawy & Soudki 2007; Lu et al. 2011) by fitting the numerical results with the experimental data of the accelerated corrosion tests. Hence, this value can be interpreted as a fitting parameter which cannot be used for natural corrosion conditions. Further on, the experimental investigations (Wong et al. 2010; Michel et al. 2011) have shown not only that the corrosion products penetrate much deeper into the concrete pores (even up to 180 μm), but also that the ingress is to a large extent non-uniformly distributed around the bar. Therefore the assumption of the uniform diffusion zone is highly idealized and simplified compared to the actual experimental observations.

2.1.6.5 Transport of corrosion products into the cracks

Recent experimental investigations (Wong et al. 2010; Fischer 2012) have shown that a significant amount of rust products penetrates into the corrosion induced cracks (Figure 2.5). Fischer (2012) observed that the amount of the rust distributed in cracks can reach up to 50 % of the totally produced corrosion products around the embedded reinforcement bar. Therefore, the transport of rust products into the cracks has a strong influence on the development of damage by reducing the expansion pressure on the surrounding concrete. This effect is largely neglected in all empirical and mathematical models for simulation of corrosion induced damage.

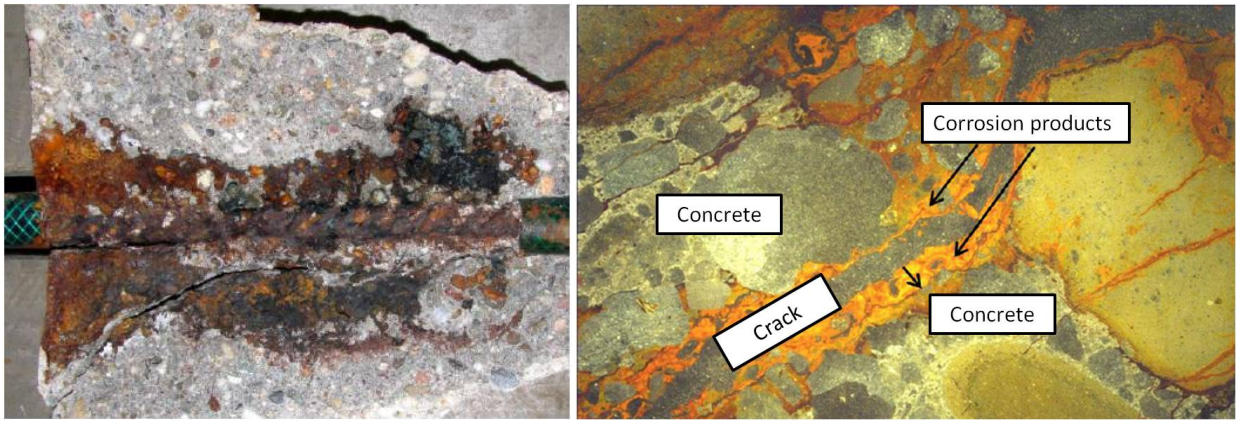

Figure 2.5 Penetration of corrosion products into the cracks (left) and the corresponding microscopic image (right) of the damaged concrete region observed in experiments by Fischer (2012)

Recently, Tran et al. (2011) developed a model based on the Rigid-Body-Spring method with 3D Voronoi particles in which the above mentioned reduction effect is implemented by continuously measuring the developing crack widths and crack volumes. The model doesn't account for the chemo-hygro-thermo reactions and

therefore assumes that certain steel regions uniformly corrode as a time independent process. Regarding the corrosion induced cracks, Tran et al. (2011) assumed that the cracked volume is completely filled when the crack width reaches the limiting value of 0.1 mm. By reaching this value, the pressure is uniformly reduced around the bar depassivated region. Subsequently, a "half" model (only the half of the bar circumference being depassivated) is used to replace the initial depassivated area around the whole circumference.

These assumptions oversimplify the effect of rust distribution by choosing the limiting crack width of 0.1 mm with no gradual ingress of products into the cracks. The cracked volume is completely and instantaneously filled by reaching this limiting value, which leads to a sudden and unrealistic uniform reduction of the expansive pressure over the whole depassivated region. Moreover, the change of the depassivated region from the whole to the half model presents an inconsistent approach in regards to the actual electrochemical processes occurring during the corrosion of reinforcement bar.

Grassl et al. (2014) developed a hydro-mechanical lattice model for corrosion induced cracking of concrete in which the rust layer is modelled as a fluid. The model is based on two coupled dual lattices used for fluid mass (rust) transport and mechanical response, respectively. The cracking of the mechanical elements gives an increase in the conductivity of the corresponding transport elements, while the fluid pressure in the transport part of the model induces additional stress in the mechanical elements. Although, the model presents a valuable addition for investigating the effects of rust transport into cracks, the lack of modelling of the electrochemical processes presents a shortcoming of the model.

2.1.7 Geometrical influences

2.1.7.1 Concrete cover thickness

Thickness of the concrete cover has a significant influence on the progress of the corrosion cell reactions and on the corrosion induced damage (cracks). The increase of the cover not only prolongs the initiation time for the chloride ions to reach and depassivate the steel surface, but also reduces the availability of oxygen for the cathodic half-cell reaction in cases of high water saturation (Bertolini et al. 2004).
Further on, a thicker concrete cover can take up higher values of the compressive pressure due to the expansion of corrosion products (Morinaga 1990). Hence, the observation of the first visible surface crack is delayed with increase of the concrete cover thickness. This is in agreement with the numerical results of many models which incorporate the thickness directly as a model parameter (Bažant 1979a; Liu & Weyers 1998; Lu et al. 2011).

2.1.7.2 Reinforcement bar diameter

The increase of the bar diameter with a constant concrete cover leads to a larger area of the steel surface being exposed to corrosion and subsequently a larger amount of expansive corrosion products is being produced (Williamson & Clark 2000). Therefore, the time needed for cracking to occur decreases with a higher rebar diameter. These results are in agreement with most of the models (Andrade et al. 1993; Rodriguez et al. 1996; Alonso et al. 1998; Lu et al. 2011) simulating corrosion induced damage. Some models (Bažant 1979b; Morinaga 1990; Liu & Weyers 1998) are showing unrealistic results which predict an increase of the cracking time with a higher diameter and a constant cover. These predictions suggest a certain weakness of the formulation. It is interesting to note that with the increasing values of the concrete cover to diameter ratio, all of the models predict more time needed for the cracking of the cover (Al-Harthy et al. 2011).

2.1.7.3 Spacing of the reinforcement bars (Multi-rebar cases)

Recent experiments (Ahmed et al. 2007; Dong et al. 2011) under accelerated corrosion conditions of the multi-rebar concrete specimens indicated a significant influence of the rebar spacing on the development of crack patterns in concrete. Multi-rebars are present in realistic reinforced concrete structural elements and it is therefore necessary to investigate if a model is capable to simulate the corrosion induced damage for these cases. Bažant (1979b) has directly incorporated the rebar spacing as a model input parameter, while the other analytical and empirical models do not consider the spacing explicitly. For most of the empirical models which are experimentally calibrated on concrete specimens with a single bar, this presents a major drawback (Jamali et al. 2013).

Tran (2012) conducted a numerical parametric study in the case of the multi-rebar specimen by using the Rigid-Body-Spring Method with 3D Voronoi particles. He concluded that the rebar spacing is an important factor in predicting the corrosion induced damage due to the possibility of the concrete cover delamination. The internal cracks which form between the rebars before the appearance of the surface cracks can play a significant role in causing this type of concrete cover failure (Tran 2012).

2.1.7.4 Influence of stirrups

In the experiments of Dong et al. (2011) the influence of stirrups on the corrosion induced damage was investigated. The crack patterns obtained for a multi-rebar case with and without stirrups showed a major effect of the shear reinforcement on the crack propagation. This is largely neglected in validating the available corrosion models for reinforced concrete and there is currently no available information in the

literature regarding the numerical analysis for such complex cases. Models attempting to simulate the corrosion induced damage in the presence of stirrups require not only a robust mathematical formulation for determining the current density, but also a reliable mechanical model capable of realistically predicting damage in concrete as a quasi-brittle material.

2.2 Hysteretic moisture behaviour of concrete

Concrete as an adsorbent porous media exhibits hysteretic moisture behaviour which directly influences the transport processes responsible for the degradation of mechanical properties of reinforced concrete elements (chloride induced corrosion, carbonation, freezing and thawing cycles etc.). The behaviour is characterised with ability of the porous material to contain different degrees of water saturation for the same value of the relative humidity (RH), at a constant temperature. Hence, the water content values are highly dependent on the moisture loading history, i.e. on the exposure to cyclic wetting and drying.

Numerous experiments (Powers & Brownyard 1946; Feldman & Sereda 1964; Hansen 1986; Anderberg 2004; Baroghel-Bouny 2007; Nielsen 2007) on concrete and cement pastes showed with the pronounced hysteresis in cases of lower and higher values of relative humidity. Curve obtained by decreasing RH in a step-like manner from a fully saturated specimen at a constant temperature is called a desorption isotherm. Similarly, adsorption curve is determined by gradually increasing the RH from a completely dry specimen and subsequently measuring the equilibrium water content (Hansen 1986). The desorption and adsorption isotherms define the boundaries for the hysteresis loop while the different paths between them are termed as scanning curves (Hansen 1986; Pedersen 1990).

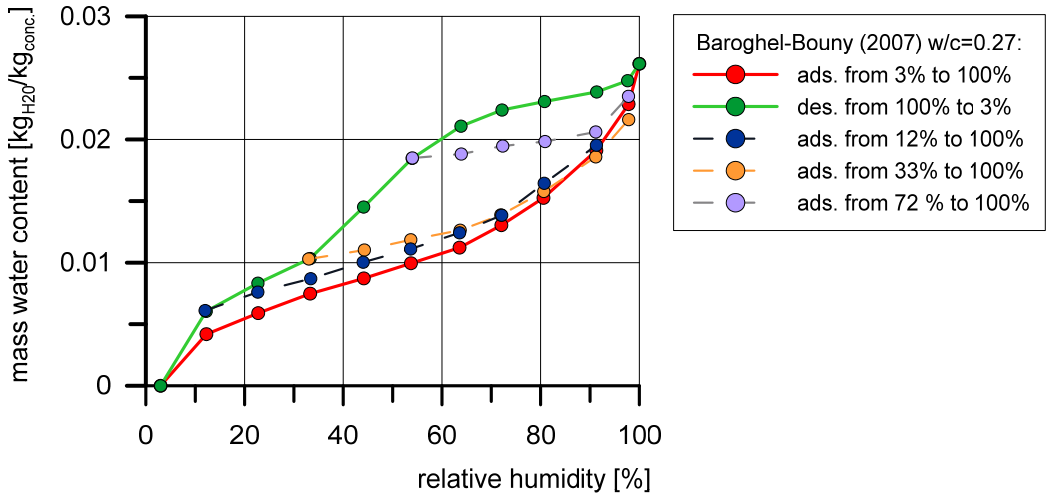

Figure 2.6 Desorption and adsorption isotherms (100% - 3% RH and 3% - 100% RH, respectively) and scanning curves within various RH ranges for concrete with a w/c ratio of 0.27 determined by Baroghel-Bouny (2007)

The extensive experiments done by (Baroghel-Bouny 2007) give a detailed insight to the shape and the behaviour of the sorption isotherms (Figure 2.6). The main disadvantage of such experiments is that they are time consuming due to obtaining equilibrium moisture conditions in specimens for every RH increment of the surrounding air (Derluyn et al. 2012). Hence, only a limited number of hysteretic loops is usually determined. Developing a numerical model which can be used for

analysing the water content for numerous wetting and drying cycles, present an important aspect for predicting the deterioration of concrete.

The experimental results for the main desorption and adsorption curves for different concrete types can be found in the literature (Hansen 1986; Baroghel-Bouny 2007; Nielsen 2007) with the water-cement ratio being the main parameter. Although, certain attempts for cataloguing the sorption curves are available (Hansen 1986), the isotherms should be experimentally obtained for each investigated concrete mixture due to the fact that the additives and admixtures can significantly influence the resulting values.

It is important to note that the experimentally determined sorption curves are obtained for a constant ambient temperature which is usually kept around 20°C. There is little information in the literature about the influence of temperature on the sorption isotherms. In the experiments by Poyet (2009) the desorption isotherm data for the concrete with the w/c ratio of 0.43 was determined for the temperatures of 30°C and 80°C (Figure 2.7). It can be seen that the desorption curve significantly changes its shape from a straight line to a nonlinear curve. Hence, the loss of water is more pronounced at higher temperatures with the decreasing relative humidity.

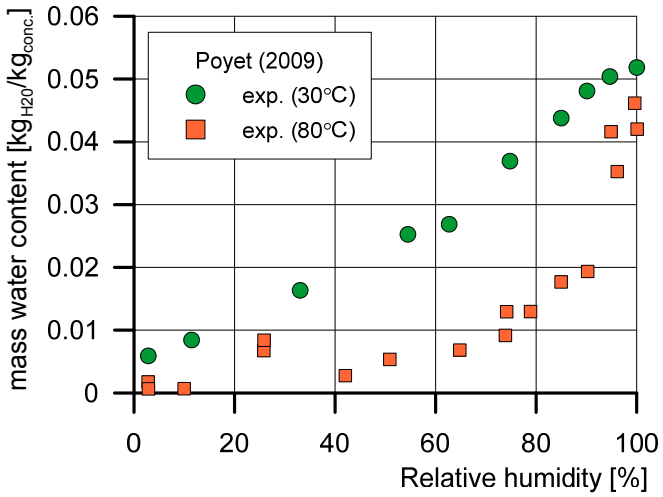

Figure 2.7 Experimentally obtained (Poyet 2009) first desoprtion curves data (w/c=0.43) for 30 ºC and 80 ºC

2.2.1 Mechanism behind the moisture hysteresis in concrete

Completely dried concrete specimen exposed to ambient air with a certain relative humidity, increases its mass due to the water molecules attaching themselves to the outer and inner pore surfaces. The governing type of interaction between the molecules and the concrete surface are the weak van der Waals forces (Åhs 2007). The molecules will continue to accumulate until the equilibrium conditions are reached, i.e. the amount of water molecules attaching and leaving the surface is the

same. The process of accumulation of water molecules on the surface is called adsorption, while the opposite mechanism is termed desorption.

With the increase of RH, further amounts of water molecules are being attached to the already present adsorbate and thus forming a thin liquid like film on the exposed surface (Åhs 2007). There are a couple of models describing the process of adsorbate accumulation on an already existing adsorbate layer, such as Langmuir model (Langmuir 1916) for monolayer adsorption or the BET (Brunauer–Emmett–Teller) model (Brunauer et al. 1938) for multi-layer adsorption.

In smaller concrete pores, usually between 1.4nm and 1μm (Powers & Brownyard 1946), the accumulated water curves on the pore walls and at a certain RH a concave meniscus is formed connecting the adjacent pore walls (Figure 2.8). Saturation pressure above a concave surface is less than above a flat surface (McArthur & Spalding 2004), which leads to water molecules condensing on the formed water meniscus surface. Process of water condensation on a curved meniscus is called capillary condensation and becomes a dominant binding mechanism for RH above 45% (Åhs 2007; Baroghel-Bouny 2007).

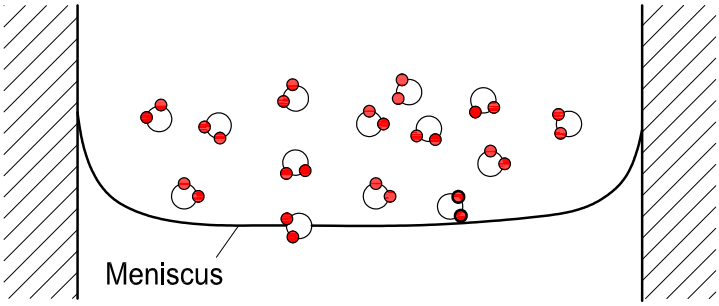

Figure 2.8 Illustration of the concave meniscus forming in the pores (Åhs 2007)

A completely saturated specimen exposed to an ambient air with a lower RH loses its mass during the process of desorption. The filled pores gradually lose the water molecules due to the lower RH in the adjacent surrounding and subsequently, the menisci develop inside of the pores. With the development of the menisci, the air bubbles spontaneously form due to the lower hydrostatic pressure inside of the pores. The water content corresponding to the air bubble volume is transported towards the surface (Fagerlund 1999). Further on, as the drying continues the pore pressure above the curved meniscus surface becomes higher than the saturation pressure. This leads to the breaking of the meniscus but at a lower RH than the value needed for its forming (Åhs 2007).

As mentioned in the previous section, the adsorption and the desorption curves at a constant temperature do not coincide. Hence, these isotherms define the hysteretic moisture behaviour of concrete. Currently, there is not a unique agreement in the literature for the main mechanism causing the hysteresis.

According to Baroghel-Bouny (2007) one of the possible mechanisms is the difference between the capillary condensation and evaporation due to the shape of the pores, possible different curvatures at the liquid-vapour interface (meniscus) or by the ink-bottle effect, i.e. the multi-scale ink-bottle effect (Jennings 2000). The ink-bottle effect (Brunauer 1943; Maekawa et al. 2008) describes a phenomena in the case of larger pores connected to pores with a much smaller radii. During the drying process the water in the bigger pores becomes trapped as long as the smaller pores are saturated with water (Figure 2.9). According to Bažant & M. Bažant (2012), the ink-bottle effect is only valid for higher relative humidity values due to the smaller percentage of the water liquid phase in the total evaporable water content. Further on, Baroghel-Bouny (2007) mentions also a possibility of certain kinetic effects which can impede the equilibrium conditions and therefore contribute to the hysteresis.

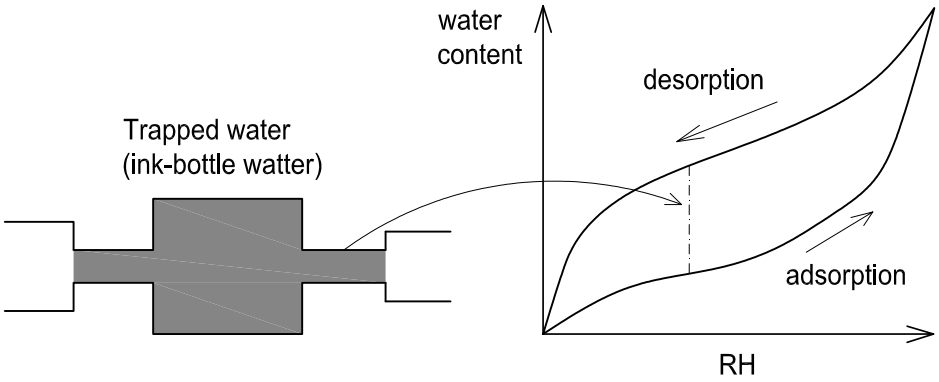

Figure 2.9 Illustration of the trapped (ink-bottle) water in the pores connected to pores with a much smaller radius (Maekawa et al. 2008). During the desorption process the ink-bottle water can be affected only if the water in the smaller pores is dried out.

Feldman & Sereda (1968) proposed that the hysteresis effect, at lower ranges of RH, can be contributed to the changes in the nanopore structure. Specifically, the removal of the interlayer water which is strongly bound to the C-S-H gel, causes the nanopores to collapse. Bažant & M. Bažant (2012) strongly objects to this theory as it predicts very large macroscopic deformations which are not experimentally observed for shrinkage caused by drying of concrete. Further on, Bažant & M. Bažant (2012) state that this theory also contradicts the experimental findings for the second desorption isotherm being very close to the first one (Baroghel-Bouny 2007), which should not be the case if the nanopores have collapsed.

Hall et al. (1995) suggested that the hysteresis can be contributed to the new hydration of the unreacted cement and its corresponding swelling which damages the existing pore structure. Bažant & M. Bažant (2012) criticize this approach due to the absence of the hydration process for the relative humidities below 70-85 % and also since it cannot explain the previously mentioned second desorption isotherm.

In a recent work, Bažant & M. Bažant (2012) proposed a mechanism of the snap-through instabilities for the hysteresis effect in the range of relative humidities below 80%. Misfit pressures arising from the molecular forces around the irregular nanopore geometry provide the local energy barriers which prevent the passage of the adsorbate-vapour interface. With the change of the vapour pressure, the interface remains pinned at the heterogeneity until a snap-through instability occurs (M. Bažant & Bažant 2012). This is analogues to the snap-through buckling of arches and shells which causes the energy dissipation. The instabilities generate the path-dependant "non-uniqueness" of the adsorbate layers and the dynamic jumps of the water content in nanopores. The hysteresis effect ensues as the snap-through instabilities follow different paths during the adsorption and desorption processes. It is important to note that the mechanism is pore-width dependent and cannot function in pores wider than 3nm (Bažant & M. Bažant 2012).

2.2.2 Modelling the moisture hysteresis in concrete

Modelling the hysteretic moisture behaviour of concrete is a challenging task due to the nanoscale mechanisms responsible for its occurrence. The approaches found in the literature are usually oriented towards pore network modelling with the ink-bottle effect (Espinosa & Franke 2006; Ishida et al. 2007; Ranaivomanana et al. 2011) or towards the independent domain theory (Everett 1955; Derluyn et al. 2012).

A model by Ranaivomanana et al. (2011), based on the approach of Ishida et al. (2007), takes the hysteresis into account by assuming a certain pore size distribution in which the drying at a given RH occurs only if the affected pores are connected to the already dry network. As the RH decreases, the probability of the saturated pores being connected to the dry pore network becomes higher. If the relative humidity decreases from a value of h_1 to h_2, the model assumes that only the pores whose radii is affected by these RH values, i.e. pores with radii between $r_1 = r(h_1)$ and $r_2 = r(h_2)$ are partially saturated and are subjected to drying. The connectivity of the pores to the dry network with a radius greater than r_2 is dependent on the probability of interconnection of these pores, $P_c^*(r > r_2)$. Thus, the residual degree of saturation S_{ink} for pores with radii greater than r_2 is directly dependent on the connectivity and is calculated as follows (Ranaivomanana et al. 2011):

$$S_{ink} = 1 - P_c^*(r > r_2) \tag{2.13}$$

For the increase of RH from a value of h_1 to h_3, the pores with a size between r_1 and r_3 belonging to the dry network, are instantaneously filled with water. The water content in pores, with a radius greater than r_3, remains constant. Although the model

presents a very thorough and comprehensive approach for modelling the hysteresis, its application is very limited because it requires modelling of the pore size distribution and its interconnectivity. Further on, the ink-bottle effect cannot be considered as the only mechanism governing the hysteretic moisture behaviour of concrete, as mentioned in Section 2.2.1.

Model developed by Derluyn et al. (2012) is based on the independent domain theory (Everett 1955). According to the theory, a porous material is described with a number of domains or sorption sites which behave independently. A sorption site is defined in a triangular Preisach-Mayergoyz (PM) space (Preisach 1935; Mayergoyz 1985) by (ϕ_a, ϕ_d) where ϕ_a and ϕ_d are the relative humidities during the adsorption and desorption process, respectively. An example of the relative humidity loading history for a specimen and its representation in the PM space with the corresponding sorption curves is taken from Derluyn et al. (2012) and shown in Figure 2.10. The region with filled sorption sites (marked grey) is usually bordered by a staircase line after a certain loading history.

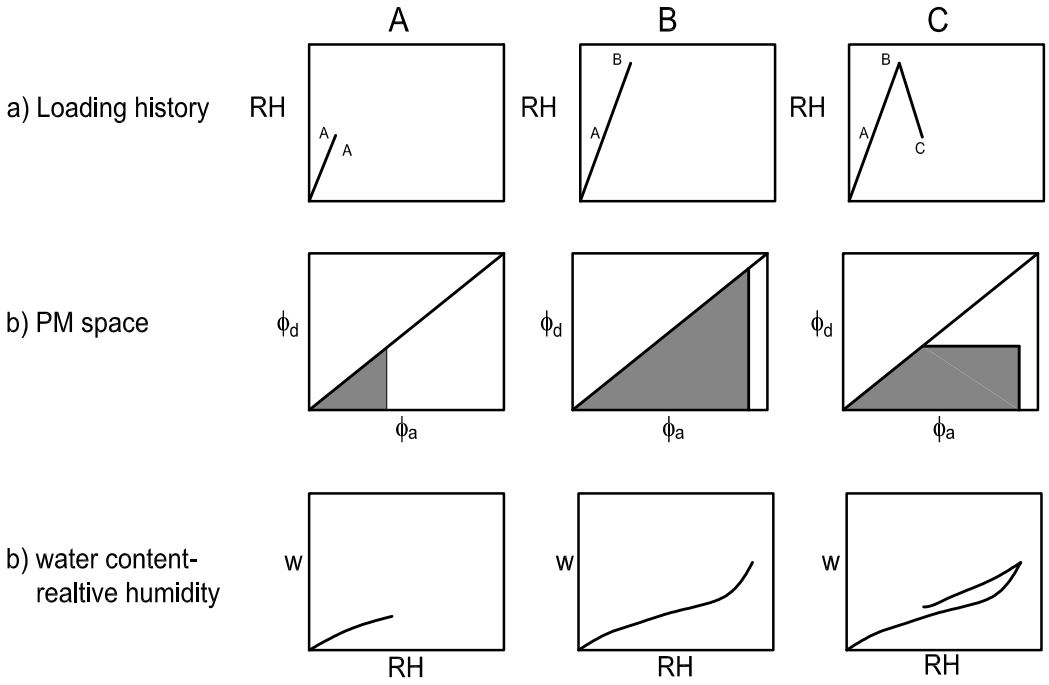

Figure 2.10 Example of the environmental RH loading history (a), the corresponding representation in the PM space (b) and the corresponding water content as a function of relative humidity (c) (Derluyn et al. 2012)

The moisture content in the integrated PM approach (IPM) by Derluyn et al. (2012) is calculated from the integral function $H(\phi_a, \phi_d)$ defined over the PM space and obtained from the experimental data. The moisture content M for a certain relative humidity value ϕ in the loading history is determined as follows:

$$M(\phi) = \sum_{i=1}^{m} H(\phi_{ai}, \phi_{di}) - \sum_{i=1}^{n} H(\phi_{ai}, \phi_{di+1}) \tag{2.14}$$

where m and n are the number of vertical and horizontal boundaries, respectively, describing the right-side staircase border in the PM space. Seven parameters are required for the definition of the integral function $H(\phi_a, \phi_d)$. These can be obtained from the experimental data: main adsorption and desorption curve and the corresponding scanning curves. The parameter values have to be chosen such that the *H*-function is monotonically increasing with increasing ϕ_a and decreasing ϕ_d (Figure 2.11).

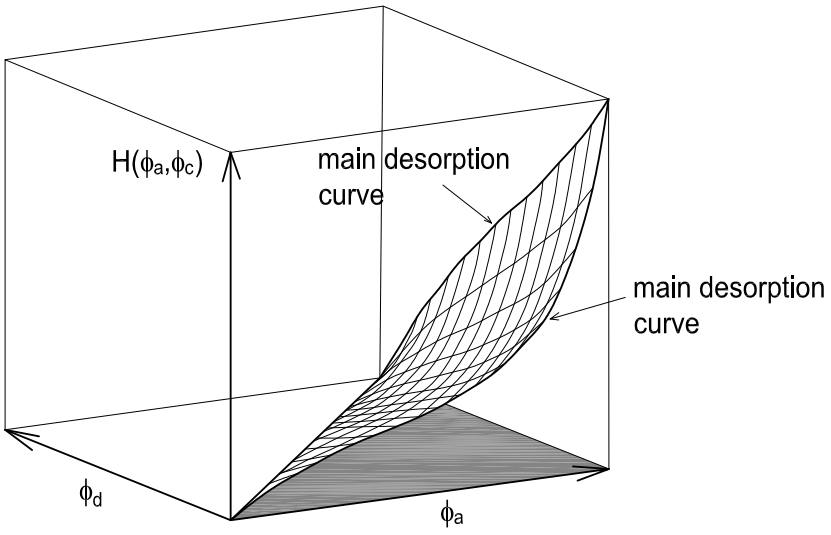

Figure 2.11 Depiction of the $H(\phi_a, \phi_d)$ function defined over the IPM space (Derluyn et al. 2012)

Derluyn et al. (2012) model presents a numerically applicable approach for simulating the exposure of concrete to drying and wetting conditions due to the implicit implementation of the hysteresis phenomena through the *H*-function. The drawback of the model is that it requires extensive experimental data to properly define the curved surface of the function $H(\phi_a, \phi_d)$,i.e. the behaviour of the scanning curves between the main adsorption and desorption curve (Figure 2.11).

3 CHEMO-HYGRO-THERMO-MECHANICAL MODEL (CHTM MODEL)

A surface layer of ferric oxide covers and protects the embedded steel bar in concrete. With this layer being damaged or depassivated the corrosion of reinforcement in concrete can be activated. Depassivation of the protective layer can occur by reaching a critical concentration of free chloride ions near the reinforcement bar surface or as a consequence of carbonation of concrete (Tuutti 1993; Glass & Buenfeld 1995; Sandberg et al. 1995). In the here presented work only the chloride type of corrosion is investigated as the most severe one.

Corrosion of steel in concrete is an electrochemical process dependent on electrical conductivity of concrete and steel surfaces, presence of electrolyte in the concrete and the concentration of dissolved oxygen in the pore water near the reinforcement (Glassstone 1964; Bažant 1979a; Page & Treadaway 1982). The developed 3D chemo-hygro-thermo-mechanical model couples the above mentioned physical and electrochemical processes with the mechanical behaviour of concrete (damage).

The model is able to realistically predict the processes before (Ožbolt et al. 2010) and after (Ožbolt et al. 2011, 2012a, 2014) depassivation of steel reinforcement in concrete It is important to note that the distribution of water and chlorides in concrete, described in the following section, yields realistic results for submerged elements or elements being continuously exposed to sea waves, i.e. elements in the so called "splash" zone (Ožbolt et al. 2010, 2011). A further development of the model in regard to moisture distribution and chloride convective transport for concrete elements exposed to cyclic wetting and drying conditions is given in Section 4.

Although the emphasis of the here presented work is on the corrosion induced damage due to the processes after depassivation, description of the complete 3D chemo-hygro-thermo-mechanical model is given to provide a comprehensive overview of the modelling approach.

3.1 Non-mechanical processes before depassivation of reinforcement

3.1.1 Transport of capillary water

Due to the fact that concrete is in practice rarely saturated, permeability is not a suitable parameter to describe the transport of capillary water through the concrete. At complete saturation, the suction exerted by concrete is reduced to zero therefore ″extended″ Darcy equation to formulate unsaturated flow is employed (Bear & Bachmat 1990) :

$$\mathbf{j}_w = K_w(\theta_w)\mathbf{F}_c(\theta_w) \tag{3.1}$$

where $\mathbf{j}_w = \theta_w \mathbf{v}_w$ is the specific water discharge, $\mathbf{v}_w$ is the mean water velocity (m/s), K_w is the unsaturated hydraulic conductivity (m/s), $\mathbf{F}_c$ is the capillary force and θ_w is the volume fraction of pore water ($m^3_{H_2 0}/m^3_{con}$). Capillary force can be expressed as the gradient of capillary potential:

$$\mathbf{F}_c = -\nabla\Psi(\theta_w) \tag{3.2}$$

so that the ″extended″ Darcy equation can be written as:

$$\mathbf{j}_w = -K_w(\theta_w)\nabla\Psi(\theta_w) \tag{3.3}$$

As the capillary potential depends on the volumetric moisture content, equation 3.3 reads:

$$\mathbf{j}_w = -D_w(\theta_w)\nabla\theta_w \tag{3.4}$$

where

$$D_w(\theta_w) = K_w(\theta_w)\frac{\partial\Psi}{\partial\theta_w} \tag{3.5}$$

is the water diffusivity (m^2/s).

The mass balance equation for pore water, without source or sink terms, becomes:

$$\frac{\partial(\theta_w\rho_w)}{\partial t} = -\nabla\cdot(\theta_w\rho_w\mathbf{v}_w) = -\nabla\cdot(\rho_w\mathbf{j}_w) \tag{3.6}$$

where ρ_w is the density of water. Substituting (3.4) into (3.6), under assumption that $\rho_w = const$, it follows:

$$\frac{\partial\theta_w}{\partial t} = \nabla\cdot\left[D_w(\theta_w)\nabla\theta_w\right] \tag{3.7}$$

Equation (3.7) describes transport of capillary water in terms of volume fraction of pore water in aged concrete. Capillary water diffusivity is a function of moisture content (Leech et al. 2003):

$$D_w(\theta_w) = D_0 e^{n\bar{\theta}_w} \tag{3.8}$$

where D_0 = 2.2x10^{-14} m^2/s is the limiting magnitude term, $\bar{\theta}_w = (\theta_w - \theta_{wi})/(\theta_{wd} - \theta_{wi})$ is reduced water content, θ_{wi} and θ_{wd} are initial and saturated water content, respectively, and n = 6.4 is the shape term.

3.1.2 Transport of oxygen

Transport of oxygen through concrete will be considered as convective diffusion problem. Oxygen dissolved in the pore water is transported through concrete by molecular diffusion and convection as a consequence of capillary suction and moisture diffusion.

The macroscopic flux $\mathbf{j}_{o,diff}$, due to molecular diffusion of oxygen is expressed as:

$$\mathbf{j}_{o,diff} = -D_o(\theta_w)\nabla C_o \tag{3.9}$$

where C_o is the oxygen concentration in pore solution (kg$_{oxygen}$ / m^3$_{pore\ solution}$) and $D_o(\theta_w)$ is the effective oxygen diffusion coefficient (m^2/s). The macroscopic flux $\mathbf{j}_{o,conv}$, due to capillary suction and moisture diffusion is expressed as:

$$\mathbf{j}_{o,conv} = C_o \mathbf{v}_w \tag{3.10}$$

The total mass flux of oxygen, $\mathbf{j}_o$ takes the form:

$$\mathbf{j}_o = C_o \mathbf{v}_w - D_o(\theta_w)\nabla C_o \tag{3.11}$$

The mass balance for oxygen in the pore water is given as (Bear & Bachmat 1990):

$$\frac{\partial(\theta_w C_o)}{\partial t} = -\nabla \cdot (\theta_w \mathbf{j}_o) \tag{3.12}$$

and inserting expression (3.11) into the balance equation (3.12), it follows:

$$\frac{\partial(\theta_w C_o)}{\partial t} = -\nabla \cdot \theta_w (C_o \mathbf{v}_w - D_o(\theta_w)\nabla C_o) \tag{3.13}$$

By combining (3.13) and volume balance equation (3.6), under assumption that ρ_w = const, the equation which describes transport of oxygen through concrete before depassivation of reinforcement is obtained as:

$$\theta_w \frac{\partial C_o}{\partial t} = D_w(\theta_w)\nabla\theta_w\nabla C_o + \nabla\cdot\left[\theta_w D_o(\theta_w)\nabla C_o\right] \tag{3.14}$$

The effective oxygen diffusion coefficient (m^2/s) is dependent on pore relative humidity h (Isgor & Razaqpur 2006), as indicated in the following expression:

$$D_o(h) = 1.92\times10^{-6}\, p_{cp}(1-h)^{2.2} \tag{3.15}$$

in which p_{cp} is the porosity of hardened cement paste and is expressed as (Burkan Isgor & Razaqpur 2004):

$$p_{cp} = p_c\left(\frac{1+\frac{a}{c}\frac{\rho_c}{\rho_a}}{1+\frac{w}{c}\frac{\rho_c}{\rho_w}}\right) \tag{3.16}$$

where p_c is the concrete porosity, a/c = aggregate / cement ratio, w/c = water / cement ratio, ρ_c, ρ_a and ρ_w are the densities of cement, aggregate and water, respectively.

3.1.3 Transport of chloride ions

Transport of chloride ions through concrete, before steel depassivation, is also considered as a convective diffusion problem and the total mass flux of chloride ions, $\mathbf{j}_c$ analogous to expression (3.11) may be written as:

$$\mathbf{j}_c = C_c\mathbf{v}_w - D_c(\theta_w, T)\nabla C_c \tag{3.17}$$

where C_c is the concentration of free chloride dissolved in pore solution ($kg_{Cl^-}/m^3_{\text{pore solution}}$), T is temperature and $D_c(\theta_w, T)$ is the effective chloride diffusion coefficient (m^2/s).

Due to the fact that part of the chlorides can be bound into cement hydration products, the balance equation for chloride ions in concrete is given by:

$$\frac{\partial(\theta_w C_c)}{\partial t} = -\nabla\cdot(\theta_w \mathbf{j}_c) - \frac{\partial C_{cb}}{\partial t} \tag{3.18}$$

where C_{cb} is the concentration of bound chlorides ($\mathrm{kg_{Cl^-}}$ / $\mathrm{m^3}$ of concrete).

By combining (3.18) and volume balance equation (3.6), under assumption that $\rho_w = const$, the equation that describes transport of chloride ions through concrete before depassivation of reinforcement is:

$$\theta_w \frac{\partial C_c}{\partial t} = D_w(\theta_w)\nabla\theta_w\nabla C_c + \nabla\cdot\left[\theta_w D_c(\theta_w, T)\nabla C_c\right] - \frac{\partial C_{cb}}{\partial t} \tag{3.19}$$

Mathematical model of chloride binding mechanism by hardened cement paste is given as:

$$\frac{\partial C_{cb}}{\partial t} = k_r(\alpha C_c - C_{cb}) \tag{3.20}$$

where k_r is the binding rate coefficient ($\mathrm{s^{-1}}$), $\alpha = 0.7$ is constant and shows that there exists a linear relation between concentration of bound and free chloride and also that there is a limit value for bound chloride (Saetta et al. 1993). The dependence of chloride diffusion coefficient on water content and temperature is expressed as:

$$D_c(\theta_w, T) = D_{c,ref}\left[1 + \frac{(1-h(\theta_w))^4}{(1-h_c)^4}\right]^{-1}\cdot\exp\left[\frac{U}{R}\left(\frac{1}{T_{ref}} - \frac{1}{T}\right)\right] \tag{3.21}$$

where $D_{c,ref}$ is a reference value of D_c evaluated at standard conditions, h_c = 0.75, $h(\theta_w)$ expresses dependence of relative humidity on pore water content in concrete according to the adsorption isotherm of a BSB model (Saetta et al. 1993), U is the activation energy of chloride diffusion process (44.6 kJ/mol for *w/c* = 0.5), R is universal gas constant and T_{ref} = 296 K.

3.1.4 Heat transfer in concrete

The equation which describes temperature distribution in solid reads:

$$\lambda\Delta T + W(T) - c\rho_{con}\frac{\partial T}{\partial t} = 0 \tag{3.22}$$

where λ is thermal conductivity (W/(mK)), c is heat capacity per unit mass of concrete (J/(K kg)), ρ_{con} is mass density of concrete (kg/m^3) and W is internal source of heating (W/m^3).

3.1.5 Finite element formulation of the governing equations before depassivation of steel

To solve the system of partial differential equations using the finite element method for domain Ω, the strong forms of equations described in chapters 3.1.1-3.1.4 need to be rewritten into the weak form. The weak form of the partial differential equations which govern the transport of capillary water and oxygen through concrete, chloride ingress into the concrete, binding of chloride by the hardened cement paste and heat transport in concrete is obtained by employing the Galerkin weighted residual method:

$$
\begin{aligned}
&\left[P_{\theta_w}\right]\left\{\dot{\theta}_w\right\}+\left[K_{\theta_w}\right]\left\{\theta_w\right\}=\{0\}\\
&\left[P_{C_O}\right]\left\{\dot{C}_O\right\}+\left[K_{C_O}\right]\left\{C_o\right\}=\{0\}\\
&\left[P1_{C_c}\right]\left\{\dot{C}_c\right\}+\left[P1_{C_{cb}}\right]\left\{\dot{C}_{cb}\right\}+\left[K_{C_c}\right]\left\{C_c\right\}=\{0\}\\
&\left[P2_{C_{cb}}\right]\left\{\dot{C}_{cb}\right\}+\left[P2_{C_c}\right]\left\{\dot{C}_c\right\}+\left[P3_{C_{cb}}\right]\left\{C_{cb}\right\}=\{0\}\\
&\left[C_T\right]\left\{\dot{T}\right\}+\left(\left[K\right]+\left[H\right]\right)\left\{T\right\}=\left\{R\right\}
\end{aligned}
\tag{3.23}
$$

with:

$$
\begin{aligned}
&\left[P_{\theta_w}\right]=\int_{\Omega}\left[N\right]^T\left[N\right]d\Omega;\ \left[K_{\theta_w}\right]=\int_{\Omega}D_w(\theta_w)\left[\nabla N\right]^T\left[\nabla N\right]d\Omega\\
&\left[P_{C_O}\right]=\int_{\Omega}\theta_w\left[N\right]^T\left[N\right]d\Omega\\
&\left[K_{C_O}\right]=\int_{\Omega}\theta_w D_o(\theta_w)\left[\nabla N\right]^T\left[\nabla N\right]d\Omega-\int_{\Omega}D_w(\theta_w)\nabla\theta_w\left[N\right]^T\left[\nabla N\right]d\Omega\\
&\left[P1_{C_c}\right]=\int_{\Omega}\theta_w\left[N\right]^T\left[N\right]d\Omega;\ \left[P2_{C_c}\right]=\int_{\Omega}k_r\alpha\left[N\right]^T\left[N\right]d\Omega\\
&\left[K_{C_c}\right]=\int_{\Omega}\theta_w D_c(\theta_w,T)\left[\nabla N\right]^T\left[\nabla N\right]d\Omega-\int_{\Omega}D_w(\theta_w)\nabla\theta_w\left[N\right]^T\left[\nabla N\right]d\Omega\\
&\left[P1_{C_{cb}}\right]=\int_{\Omega}\left[N\right]^T\left[N\right]d\Omega;\ \left[P2_{C_{cb}}\right]=\int_{\Omega}-\left[N\right]^T\left[N\right]d\Omega\\
&\left[P3_{C_{cb}}\right]=\int_{\Omega}-k_r\left[N\right]^T\left[N\right]d\Omega;\ \left[C_T\right]=\int_{\Omega}c\rho\left[N\right]^T\left[N\right]d\Omega\\
&\left[K\right]=\int_{\Omega}\lambda_r\left[\nabla N\right]^T\left[\nabla N\right]d\Omega;\ \left[H\right]=\int_{\Gamma}\alpha_{TR}\left[N\right]^T\left[N\right]d\Gamma\\
&\left[R\right]=\int_{\Omega}W(T)\left[N\right]^T d\Omega+\int_{\Gamma}\alpha_{TR}\left[N\right]^T T_M d\Gamma
\end{aligned}
\tag{3.24}
$$

where $[N]$ is the column matrix of shape functions that connects the volume fraction of pore water in concrete θ_w, mass concentration of oxygen in pore water C_o, mass concentration of free chloride in pore water C_c, concentration of bound chloride in concrete C_{cb} and temperature T with their nodal values; α_{TR} is the transfer coefficient and T_M is the temperature of the media in which the surface of concrete is exposed to.

The numerical analysis is incremental. In each time step Δt partial differential equations are solved simultaneously and it is assumed, while solving the non-mechanical part of the problem, that the mechanical properties are constant. This means that the non-mechanical properties of concrete are controlled by mechanical properties (damage) from the end of the previous time step.

3.2 Non-mechanical processes after depassivation of reinforcement

The corrosion of steel is activated with the depassivation of reinforcement in concrete. The non-mechanical processes important for the propagation stage of steel corrosion are: (1) Mass sinks of oxygen at steel surface due to cathodic and anodic reaction, (2) The flow of electric current through pore solution and (3) The cathodic and anodic potential.

3.2.1 Oxygen consumption

The oxygen molecules approaching the cathode surface are being reduced to OH^- ions which carry the electric current through the pore solution. The number of ions produced per unit surface of cathode and per unit time (electric current density i_c (A/m^2)) is equal to:

$$i_c = -FzQ \tag{3.25}$$

where F = 96486.7 C/mol is Faraday's constant, z = 4 is the number of hydroxyl ions in the oxygen reduction reaction (Eq. 1.2) and Q is the number of oxygen molecules reduced per unit surface of cathode and per unit time (mol/m^2 s). The oxygen diffusion flux at the cathode surface, j_o^c (kg/m^2s) can be calculated as follows:

$$j_o^c = D_o(S_w, p_c)\left.\frac{\partial C_o}{\partial n}\right|_{cathode} \tag{3.26}$$

where n is the outward normal to the cathode surface. A balanced condition is established between the approaching and reacting oxygen molecules, that is:

$$j_o^c = D_o(S_w, p_c)\left.\frac{\partial C_o}{\partial n}\right|_{cathode} = Q \tag{3.27}$$

or

$$D_o(S_w, p_c)\left.\frac{\partial C_o}{\partial n}\right|_{cathode} = -\frac{1}{Fz}i_c = k_c i_c \tag{3.28}$$

where after converting moles into kg, k_c = 8.29×10^{-8} kg/C.

Similar analogy is applied to the anodic sites, so it can be written:

$$i_a = j_{fh}Fz \tag{3.29}$$

where i_a (A/m^2) is the current density at the anode surface, j_{fh} (mol/m^2 s) is the rate of $Fe(OH)_2$ production and z = 2. According to Eq. 1.4 the rate of oxygen consumption on the anode is given as follows:

$$j_o^a = -\frac{32}{359.4} j_{fh} = -0.089\, j_{fh} \tag{3.30}$$

or

$$D_o(S_w, p_c) \frac{\partial C_o}{\partial n}\bigg|_{anode} = -0.089 \frac{1}{Fz} i_a = -k_a i_a \tag{3.31}$$

where after converting moles into kg, k_a = 4.14x10^{-8} kg/C.

3.2.2 Flow of electric current through electrolyte

The mechanism of the ionic transport in solution can be described by the Nernst - Planck equation (Bertolini et al. 2004). In the here presented model, a simplified version o the Nernst -Planck equation is used in which the chemical activity effects are neglected. This is assumed in order to keep the mathematical derivation of equations governing the electric current passing through the electrolyte in the concrete pores as simple as possible. The flux of various ions, $\mathbf{j}_i$ (mol/m^2 s) through electrolyte in the concrete pores can be described by the following equation (Newman & Thomas-Alyea 2004):

$$\mathbf{j}_i = -z_i \gamma_i F C_i \nabla \Phi - D_i \nabla C_i + C_i \mathbf{v} \tag{3.32}$$

where index i refers to various ions, γ is mobility of ions, C is concentration of ions, Φ is electric potential, D is diffusivity of ions and $\mathbf{v}$ is flow velocity of electrolyte. The first term in Eq. 3.32 is related to migration of ions in electric field and the second and the third terms are related to diffusion and convection, respectively. The electric current through the electrolyte is a result of motion of charged particles and it can be written as:

$$\mathbf{i}_i = F \sum_i z_i \mathbf{j}_i \tag{3.33}$$

or taking into account the Eq. 3.32:

$$\mathbf{i}_i = -F^2 \nabla \Phi \sum_i z_i^2 \gamma_i C_i - F \sum_i z_i D_i \nabla C_i + F \mathbf{v} \sum_i z_i C_i \tag{3.34}$$

With the assumptions of the electrical neutrality of the system and the uniform ions concentration, the second and the third term are equal to zero and Eq. 3.34 can be rewritten as follows:

$$\mathbf{i} = -\sigma(S_{w,} p_c)\nabla \Phi \qquad \text{with: } \sigma(S_{w,} p_c) = -F^2 \sum_i z_i^2 \gamma_i C_i \tag{3.35}$$

where $\mathbf{i}$ (A/m^2) is vector of the electric current density, σ is electrical conductivity of concrete dependant on degree of water saturation of concrete and concrete porosity.

If the electrical neutrality is accounted for and the electrical conductivity of concrete is assumed as uniformly distributed, the equation of electrical charge conservation (Newman & Thomas-Alyea 2004) reads:

$$\nabla \mathbf{i} = 0 \tag{3.36}$$

By substituting Eq. 3.35 into Eq. 3.36 and by assuming that the electrical conductivity is uniformly distributed, the following equation is given:

$$\nabla^2 \Phi = 0 \tag{3.37}$$

For a given boundary conditions, the solution of the Laplace's equation (Eq. 3.37) determines the distribution of electric potential and by using Eq. 3.35 the corrosion current density can be calculated.

3.2.3 Polarization of anode and cathode

In the present model the kinetics of reaction at the anode surface can be estimated according to Butler – Volmer kinetics as follows (Martin-Perez 1999):

$$i_a = i_{0a} e^{2.3(\Phi - \Phi_{0a})/\beta_a} \tag{3.38}$$

where i_a is the anodic current density (A/m^2), i_{0a} is the exchange current density of the anodic reaction (A/m^2), Φ is electric potential in pore solution near reinforcement surface (V), Φ_{0a} is the anodic equilibrium potential (V) and β_a is the Tafel slope for anodic reaction (V/dec). Equation 3.38 assumes that the reaction at the anode is only influenced by activation polarization. For the cathodic reaction it is assumed that it is subjected to both activation and concentration polarization. Hence, the kinetics at the cathode site are given by:

$$i_c = i_{0c} \frac{C_o}{C_{ob}} e^{2.3(\Phi_{0c} - \Phi)/\beta_c} \tag{3.39}$$

where i_c is the cathodic current density (A/m^2), i_{0c} is the exchange current density of the cathodic reaction (A/m^2), C_{ob} is oxygen concentration at the boundary surface of the investigated concrete specimen (kg/m^3), Φ_{0c} is the cathodic equilibrium potential (V) and β_c is the Tafel slope for cathodic reaction (V/dec).

3.2.4 Rate of rust production and distribution of corrosion products

Rate of rust production J_r (kg/m^{2}s) and mass of hydrated red rust per related surface (A_r) of rebar m_r (kg), respectively, are calculated as (Martin-Perez 1999):

$$\begin{aligned} J_r &= 5.536\times10^{-7}\, i_a \\ m_r &= J_r \Delta t A_r \end{aligned} \tag{3.40}$$

where Δt is time interval in which the corrosion is taking place and A_r is the corresponding surface of the steel reinforcement. The coefficient of proportionality between the anodic current density i_a and rate of rust production J_r is calculated using the stoichiometry of chemical reactions and Faraday's law (Martin-Perez 1999; Ožbolt et al. 2011, 2012a, 2012b).

Recent experimental investigations (Wong et al. 2010; Fischer 2012) have shown that the penetration of corrosion products into the pores and their relatively large ingress through the corrosion induced cracks around the bar, has a significant effect on the development of corrosion induced damage. The influence can be summarized as: (1) The distribution of rust and radial pressure over the anodic surface is not uniform and (2) Damage due to expansion of products is less pronounced.

The distribution of corrosion product (red rust) R into the pores and through the cracks in concrete has been mathematically formulated as a convective diffusion problem:

$$\theta_w \frac{\partial R}{\partial t} = \nabla \cdot \left[\theta_w D_r \nabla R\right] + D_w(\theta_w)\nabla\theta_w \nabla R \tag{3.41}$$

in which D_r is the diffusion coefficient (m^2/s) of corrosion product. It is important to note that Equation 3.41 does not directly describe the transport of red rust, but rather the distribution of the rust formed in the concrete pores and cracks as a consequence of soluble species (which can dissolve in concrete pore solution and subsequently migrate in the pores and cracks) reacting with oxygen in the pore water (Wong et al. 2010).

Currently, the above mentioned process of transport of corrosion products is considered more in a qualitative sense. Detailed experimental investigations needed for the quantitative calibration of the model are currently not available (Wong et al. 2010; Fischer 2012). Therefore, a further development of the model is needed in the context of experimentally measuring the transported amount of corrosion products into the cracks and then using this data for the adjustment of the model parameters.

3.2.5 Finite element formulation of governing equations after depassivation of steel

The strong form of the partial differential equations, important for the processes after depassivation of steel, must be rewritten in the weak form. The weak form of partial differential equation which governs the transport of oxygen through concrete and Laplace's equation for electric potential is carried out by employing the Galerkin weighted residual method as follows:

$$[A_o]\{C_o\} + [B_o]\left\{\frac{dC_o}{dt}\right\} = \{f_o\} \tag{3.42a}$$

$$[A_o]\{\Phi\} = \{0\} \tag{3.42b}$$

with:

$$\begin{aligned} [A_o] &= \int_{\Omega} \theta_w D_o(S_{w,} p_{con}) [\nabla N]^T [\nabla N] d\Omega - \int_{\Omega} D_w(\theta_w) \nabla \theta_w [N]^T [\nabla N] d\Omega \\ [B_o] &= \int_{\Omega} \theta_w [N]^T [N] d\Omega \end{aligned} \tag{3.42c}$$

$$\begin{aligned} [f_o] &= -k_c i_c \int_{\Gamma} [N] d\Gamma \quad cathodic\ surface \\ [f_o] &= -k_a i_a \int_{\Gamma} [N] d\Gamma \quad anodic\ surface \end{aligned} \tag{3.42d}$$

$$[A_\Phi] = \int_{\Omega} [\nabla N]^T [N] d\Omega \tag{3.42e}$$

where [*N*] is the column matrix of shape functions that connects the mass concentration of dissolved oxygen in pore water and electric potential with their nodal values and Γ is the reinforcement surface.

Equations 3.42a and 3.42b represent a system of coupled and highly nonlinear equations. They are linearized, decoupled and solved iteratively by employing the direct integration method of implicit type. In the first iteration a small initial current is assumed for the entire concrete solid. The iterative procedure consists of following steps:

(I) Knowing the boundary conditions at the electrode surface, calculated from Eq. 3.38 and 3.39, electric potential is calculated by solving Eq. 3.42b. (II) Electric current density is calculated from Eq.3.35 and used for the calculation of the right side of Eq. 3.42d. (II) Distribution of oxygen is calculated by solving Eq. 3.42a. (IV) Maximum residual of electric potential and oxygen are calculated based on the Euclidian norm. If the residuals are smaller than in advance prescribed tolerance, a new time step is taken. Otherwise, the iteration steps 1 to 4 are repeated.

3.3 Direct integration method

As mentioned in Sections 3.1.5 and 3.2.5, the weak forms of equations for simulation of processes before and after depassivation need to be solved as a transient, i.e. time dependant problem. Direct integration method is used which solves the equations for discrete time step Δt.

The application of the direct integration method is presented here through Eq. 3.42a, describing the distribution of oxygen in concrete after the start of depassivation. By using the generalized trapezoidal rule, the connection between two states of oxygen distribution $\{C_o\}_{\mathrm{n}}$ and $\{C_o\}_{\mathrm{n+1}}$ separated by a time interval of Δt can be defined by (Cook et al. 1998) :

$$\{C_o\}_{n+1} = \{C_o\}_n + \left\{\left(1-\beta^*\right)\{\dot{C}_o\}_n + \beta^*\{\dot{C}_o\}_{n+1}\right\} \tag{3.43}$$

where the value of β^* can be chosen for an interval from 0 to 1. Eq. 3.42a can be rewritten for time t, i.e. for the state of oxygen distribution $\{C_o\}_{\mathrm{n}}$ and then multiplied with $\left(1-\beta^*\right)$ which gives the following (Cook et al. 1998):

$$\left(1-\beta^*\right)\left([A_o]\{C_o\}_n + [B_o]\{\dot{C}_o\}_n\right) = \left(1-\beta^*\right)\{f_o\}_n \tag{3.44}$$

The same can be done for the state of oxygen distribution $\{C_o\}_{\mathrm{n+1}}$, but the equation is in this case multiplied with β:

$$\beta\left([A_o]\{C_o\}_{n+1} + [B_o]\{\dot{C}_o\}_{n+1}\right) = \beta\{f_o\}_{n+1} \tag{3.45}$$

By adding Eq. 3.44 and 3.45 and inserting the expression for the time derivative of $\{\dot{C}_o\}_{n+1}$ or $\{\dot{C}_o\}_n$ from Eq. 3.43, the following is obtained:

$$\frac{1}{\Delta t}\left(\left[B_o\right]+\beta^*\left[A_o\right]\right)\left\{C_o\right\}_{n+1}=\left(\frac{1}{\Delta t}\left[B_o\right]-(1-\beta^*)\left[A_o\right]\right)\left\{C_o\right\}_n + \left(1-\beta^*\right)\left\{f_o\right\}_n+\beta^*\left\{f_o\right\}_{n+1} \tag{3.46}$$

For nonlinear problems the only unconditionally stable form of Eq. 3.46 is achieved by choosing the value of β^* equal to 1 (Cook et al. 1998). In this way the direct integration method is termed as an implicit method and Eq. 3.46 can be rewritten as:

$$\frac{1}{\Delta t}\left(\left[B_o\right]+\left[A_o\right]\right)\left\{C_o\right\}_{n+1}=\frac{1}{\Delta t}\left[B_o\right]\left\{C_o\right\}_n+\left\{f_o\right\}_{n+1} \tag{3.47}$$

In this way the distribution of oxygen $\{C_o\}_{\mathrm{n+1}}$ for a new time increment Δt is solved by knowing the distribution from a previous step $\{C_o\}_{\mathrm{n}}$ and calculating the current values of the matrices $\left[A_o\right]$ and $\left[B_o\right]$.

3.4 Chemo-hygro-thermo-mechanical coupling

The governing equilibrium equation for the mechanical behaviour of a continuous body in the case of static loading condition reads:

$$\nabla\left[D_m\left(u,\theta_w,T\right)\nabla u\right]+\rho b=0 \tag{3.48}$$

in which D_m is material stiffness tensor, ρb is specific volume load and u is displacement field. In the mechanical part of the model the total strain tensor ε_{ij} is decomposed into mechanical strain ε_{ij}^{m}, thermal strain, hygro strain ε_{ij}^{w} (swelling – shrinking) and strain due to expansion of corrosion products ε_{ij}^{corr}:

$$\varepsilon_{ij}=\varepsilon_{ij}^{m}+\varepsilon_{ij}^{T}+\varepsilon_{ij}^{w}+\varepsilon_{ij}^{corr} \tag{3.49}$$

The mechanical strain component can be decomposed into elastic, plastic and damage parts. It is used to calculate the effective stress increments (stress in the solid phase of concrete matrix) and macroscopic stresses increment from the microplane model for concrete (Ožbolt et al. 2001) as a constitutive law .

3.4.1 Microplane model with relaxed kinematic constraint

The constitutive law employed for concrete in this work is microplane model with relaxed kinematic constraint (Ožbolt et al. 2001). The model utilizes the strength of both macroscopic and microscopic models and therefore is known to provide results in very good agreement with the experiments (Ožbolt et al. 1999). The model is able to realistically describe micro-structural phenomena such as cohesion, friction and aggregate interlock.

Contrary to classical macroscopic type of constitutive laws, which are based on tensorial invariants of stresses and strains, in the microplane model the material response is calculated based on the monitoring of stresses and strains in a number of predefined directions. Integrating microplane stresses in a thermodynamically consistent way, it is possible to calculate macroscopic stress tensor from a known macroscopic strain tensor. The constitutive framework is similar to discrete type of the models (e.g. random particle model) with the difference that the model is formulated in the framework of continuum. The physical concept behind the microplane model was already discussed at the beginning of last century by Taylor (1938). The microplanes may be imagined to represent damage planes or weak planes in the microstructure, such as those that exist at the contact between

aggregate and the cement matrix or slip planes in the theory of plasticity as shown in Figure 3.1 (Ožbolt et al. 2001).

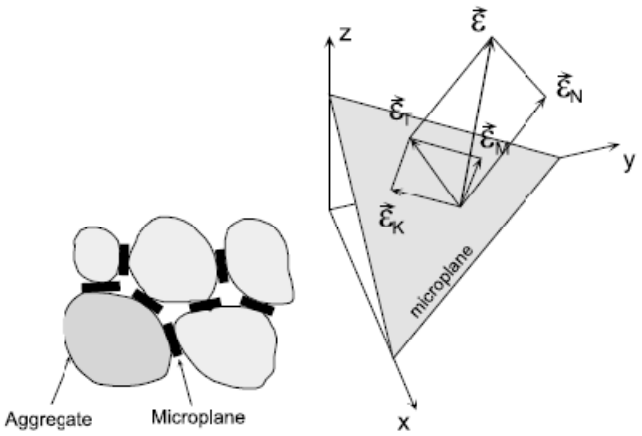

Figure 3.1. Microplane model: Idealized contact planes (left) and decomposition of the total macroscopic strain tensor on the microplane (Ožbolt et al. 2001) (right)

Generally, in macroscopic models the macroscopic strain tensor is related to a macroscopic stress tensor through a constitutive relationship valid at macro level. In the microplane model the macroscopic strain tensor at each integration point is projected into a number of microplanes in normal and shear directions, which characterize the material behaviour.

In the model each microplane is defined by its unit normal vector components n_i. Microplane strains are assumed to be the projections of macroscopic strain tensor ε_{ij} (kinematic constraint). Normal (σ_N, ε_N) and two shear stress-strain components (σ_K, σ_M, ε_K, ε_M) are considered on the microplane. To realistically model concrete, the normal microplane stress and strain components have to be decomposed into volumetric and deviatoric parts ($\sigma_N = \sigma_V + \sigma_D$, $\varepsilon_N = \varepsilon_V + \varepsilon_D$). Unlike the most microplane formulations for concrete, which are based on the kinematic constraint approach, to prevent unrealistic model response for dominant tensile load, in this model kinematic constraint is relaxed (Ožbolt et al. 2001).

Figure 3.2 shows the implementation of the model at the 3D FE level. As shown, for a 3D solid finite element having eight integration points, the macroscopic strain tensor is for each integration point first projected to the microplane and then decomposed into normal and shear microplane directions. Uniaxial stress-strain relations on each microplane are then employed to determine the respective microplane stress components. Finally, using the principle of virtual work, a numerical integration over all microplanes is performed to determine the macroscopic stress tensor.

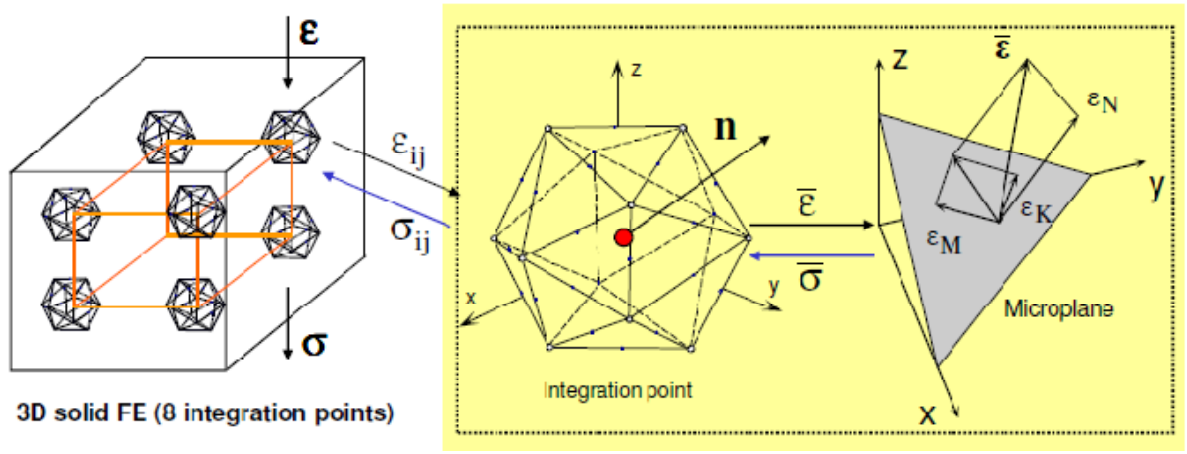

Figure 3.2. Concept of microplane model (Ožbolt et al. 2001)

At the integration point, the number of microplanes considered can have any natural number as a value. Obviously, larger number of microplanes will produce more accurate results but at the same time will need much higher computational effort. A good balance between the computational time and accuracy can be obtained by considering 21 microplanes for the symmetric part of the unit radius sphere, as shown in Figure 3.2. The major advantage of the model is that, since microplanes with different spatial orientations have been considered, the tensorial invariant restrictions are automatically fulfilled and they need not be directly enforced.

Based on the micro-macro work conjugancy of volumetric-deviatoric split and using in advance defined microplane stress-strain constitutive laws, the macroscopic stress tensor is calculated as an integral over all possible predefined microplane orientations:

$$\sigma_{ij}=\sigma_V\delta_{ij}+\frac{3}{2\pi}\int_S\left[\sigma_D\left(n_in_j-\frac{\delta_{ij}}{3}\right)+\frac{\sigma_K}{2}\left(k_in_j+k_jn_i\right)+\frac{\sigma_M}{2}\left(m_in_j+m_jn_i\right)\right]dS \tag{3.50}$$

where S = the surface of the unit radius sphere, δ_{ij} = Kronecker delta and k_i and m_i = directions of shear microplane components.

To account for large strains and large displacements, Green-Lagrange finite strain tensor is used. Furthermore, to account for the loading history of concrete, the co-rotational Cauchy stress tensor is employed. For more detail see Bažant et al. (2000) and Ožbolt et al. (2001).

3.4.2 One-dimensional corrosion contact elements

One-dimensional corrosion contact elements are employed to account for the inelastic strains due to the expansion of corrosion products. They are placed radially around the reinforcement bar surface and their main function is to simulate the contact between reinforcement and the surrounding concrete. These contact elements can take up only shear forces in direction parallel to reinforcement axis and compressive forces perpendicular to the adjacent surface of the reinforcement. The inelastic radial expansion due to corrosion Δl_r is calculated as:

$$\Delta l_r = \frac{m_r}{A_r}\left(\frac{1}{\rho_r} - \frac{0.523}{\rho_s}\right) \tag{3.51}$$

where ρ_r = 1.96×10^3 (kg/m^3) and ρ_s = 7.89×10^3 (kg/m^3) are densities of rust and steel, respectively, 0.523 is the ratio between the mass of steel (m_s) and the corresponding mass of rust (m_r) over the related surface of reinforcement A_r that corresponds to the contact element. Note that the ratio between densities of steel and rust is here assumed to be 4, which approximately corresponds to red rust (Bažant 1979a; Cornell & Schwertmann 1996; Liu 1996). However, this value depends on the type of the corrosion products and can vary from 2 to 6. The stiffness of the rust layer is assumed to be E_r = 100 MPa (Zhao et al. 2012). In the model it is represented by the axial stiffness of the corrosion contact elements. The shear resistance of the contact elements, defined by the bond-slip relationship, is used to model the bond between deformed steel reinforcement and concrete.

The contact elements are introduced in order to model the interface zone between concrete and deformed steel reinforcement bar, however, the interaction between axial and tangential resistance is not accounted for. The elements are embedded in the interface layer, i.e. in the layer composed of hexahedral elements, with a negligible stiffness (Fichtner 2011), radially placed around the rebar surface (Figure 3.3a).The hexahedral interface elements are used to calculate the surface area of the rebar which corresponds to the corrosion contact element.

As mentioned before, no tensile stresses can be transferred in the radial direction (no cohesion is assumed) and the compressive resistance is assumed to be linear elastic (Figure 3.3b). The typical bond-slip relationship (Figure 3.3c) is obtained from pull-out experiments of un-corroded concrete reinforcement bars from well confined concrete specimen (Lettow 2006). It is assumed that for confined conditions the bond-slip relationship is not affected by the corrosion of reinforcement.

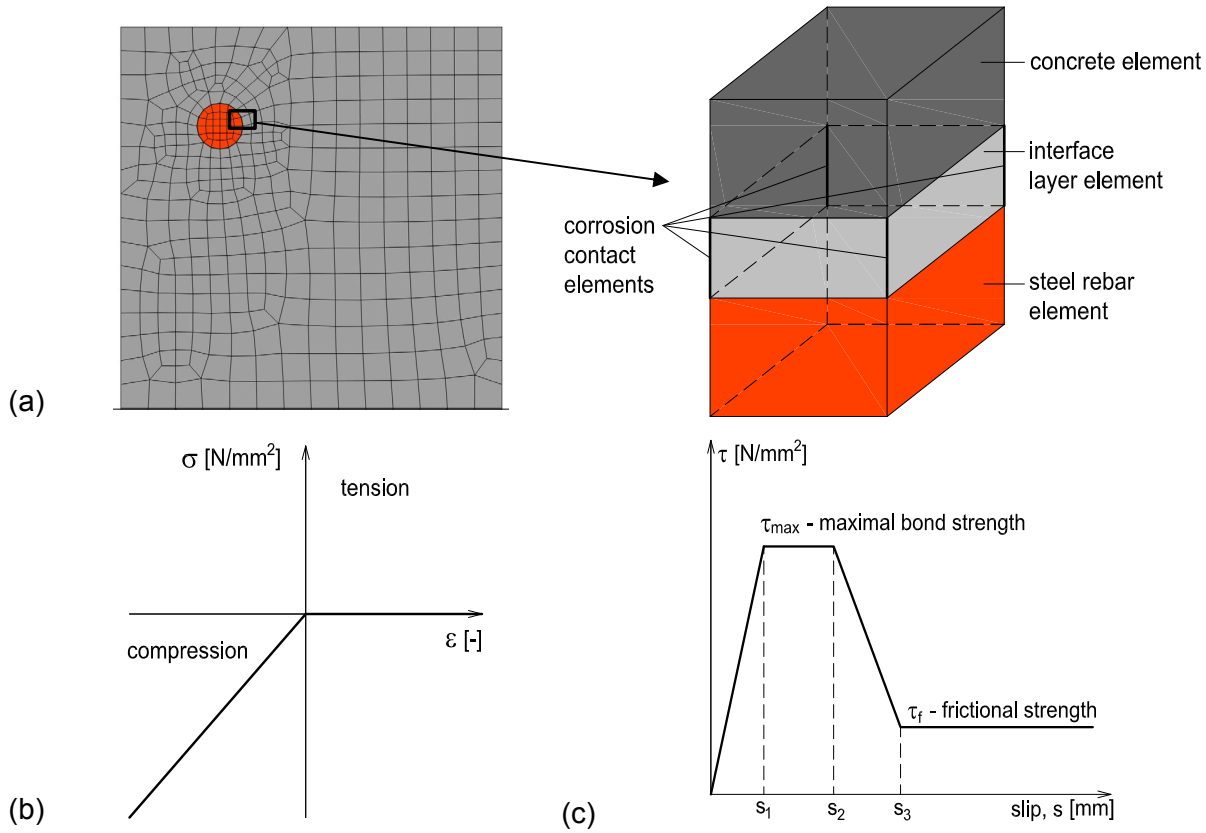

Figure 3.3. Illustration of the 1D corrosion contact element's implementation in a 3D finite element model (a); axial (b) and shear (c) resistance behaviour of the corrosion contact elements

3.4.3 Numerical implementation

The equilibrium equation 3.48 is solved by employing the Newton-Raphson iterative scheme. In the finite element analysis cracks are treated in a smeared way, i.e. smeared crack approach is employed. To avoid mesh size dependency the simple crack band approach is employed as a regularization method (Oh & Bažant 1983). The crack band theory assumes that the crack (damage) is localized in a crack band such that the specific fracture energy consumed by concrete inside the band corresponds to concrete fracture energy. In the finite element analysis the band corresponds to a row of finite elements. The width of the band is equal to the effective element size *h*. The crack width (opening) is calculated by multiplying maximum principal strain, which is perpendicular to the direction of crack propagation, with the element size *h*. For more detail see Ožbolt et al. (2001) and (Ožbolt & Reinhardt 2002).

It should be pointed out that the coupling between mechanical and non-mechanical processes is not performed in explicit sense. It is implicitly accounted for through the incremental finite element analysis and continuous update of mechanical and non mechanical concrete properties. For instance, the inelastic expansion strains of the

corrosion contact elements, calculated from the produced mass of red rust (Eq. 3.51), causes cracking of the surrounding concrete.

On the other hand, the damage (cracks) calculated by using the microplane model (Ožbolt et al. 2001) influences the non mechanical processes through the continuous update of the model parameters, i.e. the diffusivity coefficients which are formulated as damage dependent. Data related to these dependencies are not available in the literature, due to a challenging task of measuring effects of the cracked concrete on the non mechanical processes related to the corrosion of the embedded steel reinforcement. Therefore, the shape of the model curve describing the diffusivity dependency on the crack width is based on the experimental results for water permeability in cracked and fully saturated concrete (Wang et al. 1997; Aldea et al. 2000) shown in Figure 3.4. It can be seen that by reaching a critical crack width ($c_{w,c}$ = 0.2), the permeability increases up to its maximum value, that is up to three orders of magnitude greater than its initial value. For further increase of the crack width (open crack), permeability is assumed to be constant due to the numerical reasons. For more detail see Ožbolt et al. (2010).

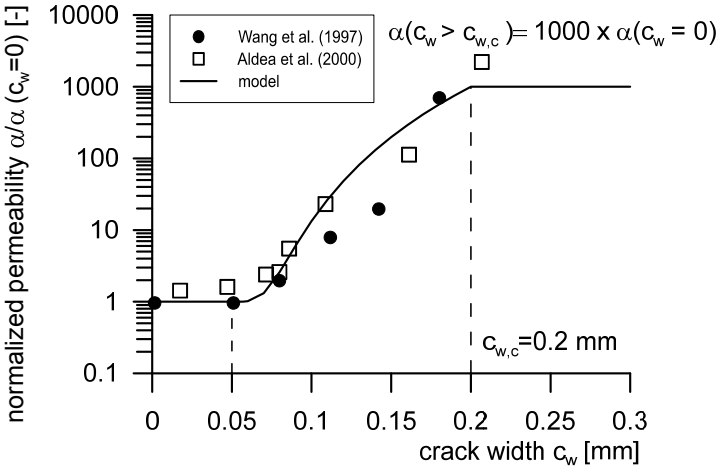

Figure 3.4. Normalized water permeability of concrete as a function of crack width

3.5 Numerical algorithm

The flow diagram of the numerical algorithm used for the incremental transient FE analysis of the processes related to the corrosion of steel reinforcement in concrete is presented in Figure 3.5. The non-mechanical and mechanical processes are solved for each time step. The used material characteristics, finite element mesh and initial and boundary conditions present the model input data.

At the start of each time increment Δt, the model checks if the depassivated steel regions are available. In the case when the steel surface of the investigated rebar is not depassivated, only the distribution of water, oxygen, heat and chlorides is

calculated for the concrete specimen. When the depassivation occurs by reaching a critical chloride concentration near the steel surface or by imposing a certain anode-cathode distribution at the start of the calculation, the processes related to the active corrosion are additionally calculated: electric potential, current density, oxygen consumption at the electrodes, the rate of rust production and the distribution of rust in the cracks and pores. It is important to note that the material parameters as a function of mechanical damage (cracks) from a previous step, are constantly being evaluated and updated before starting the analysis of the non-mechanical processes for the current time increment.

After obtaining results of the non-mechanical processes, the nonlinear static analysis is performed using the microplane model for the same time step. The loading can consist of the external static loads and/or the radial pressure due to expansion of corrosion products around the rebars, which is carried out by calculating the inelastic expansion of the implemented corrosion contact elements. The result of the nonlinear static analysis is the distribution of stresses and strains of an investigated specimen.

After the static analysis is performed, procedure is repeated for a new time step $t = t + \Delta t$ or if a final time period is reached, the calculations are terminated.

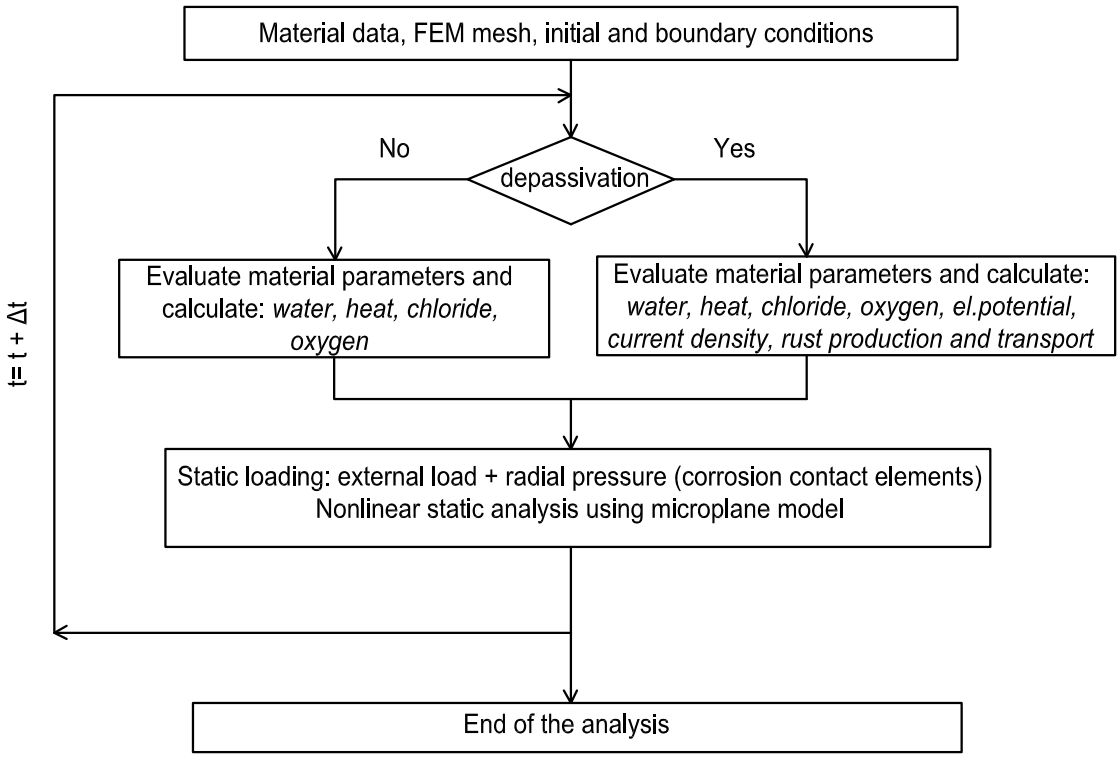

Figure 3.5. Flow diagram of the model's numerical algorithm

4 HYSTERETIC MOISTURE MODEL FOR CONCRETE

In the CHTM model discussed in the previous section it was assumed that for wetting and drying conditions, the transport of water is controlled by a single sorption curve. As discusses in Section 2.2, such assumption is not realistic because concrete exhibits significant hysteretic moisture behaviour. When accounting for hysteresis, the processes to be modelled are the same except that the so called "h" formulation is used, i.e. the moisture content is expressed in terms of relative vapour pressure h.

Concrete elements exposed to natural climate conditions are subjected to periodic changes of the ambient relative humidity (RH), which is defined as the ratio of the partial vapour pressure to the saturated vapour pressure of air at a certain temperature. As the air humidity rises, the corresponding relative humidity in concrete is getting higher and the moisture content is subsequently rising. Similarly, with decreasing RH, concrete is getting drier. The amount of moisture content in concrete for the corresponding RH and temperature of the ambient air, can be obtained from the isotherm curves, which are not same for drying and wetting conditions.

The moisture content can be described as: the water to dry mass ratio, u, the moisture content per m^3 of concrete, w,or as the degree of saturation, S_w (Hansen 1986). In the case of water to dry mass ratio, water content is determined by weighing a concrete specimen, m_{wet}, and then subsequently drying it at 105 °C until the mass is constant, m_{dry}. The water to dry mass ratio or mass water content in kg_{water} / $kg_{concrete}$ is determined as follows:

$$u = \frac{m_{wet} - m_{dry}}{m_{dry}} \tag{4.1}$$

The moisture content w per m^3 of concrete (kg_{water} / $m^3_{concrete}$) can be calculated from the water to dry mass ratio, u, by knowing the mass density of the concrete specimen, ρ_{con} (Hansen 1986):

$$w = \rho_{con}\, u \tag{4.2}$$

The degree of saturation S_w is defined as the ratio of the moisture content to the maximal amount of moisture which material can contain after spontaneous water suction.

4.1.1 Moisture transport

During wetting and drying cycles is assumed that concrete is exposed only to changes in relative humidity, so the macroscopic liquid flow is not included. Transport of moisture through the concrete is described as a vapour transport, which means that for nonsaturated concrete at uniform temperature, moisture flux $\mathbf{j}_{w,mass}$ (kg/m^{2}s) may be expressed as (Kwiatkowski et al 2009):

$$\mathbf{j}_{w,mass} = -\delta_v(h) p_{v,sat} \nabla h \tag{4.3}$$

where h is relative humidity (dimensionless), $\delta_v(h)$ is water vapour permeability (s) and $p_{v,sat}$ is water vapour saturation pressure (Pa). The mass conservation condition is

$$\frac{\partial w(h)}{\partial t} = \frac{\partial w(h)}{\partial h}\frac{\partial h}{\partial t} = \nabla \cdot (\delta_v(h) p_{v,sat} \nabla h) \tag{4.4}$$

where t is time (s), w is moisture content ($\mathrm{kg_{H_20}/m^3_{con}}$) and $\frac{\partial w}{\partial h} \equiv \xi$ is the moisture capacity (derivative of the sorption isotherm).

The main adsorption and desorption isotherms for the investigated concrete are taken as model input data from the experimentally obtained results. If the water content from the input isotherm data is defined in terms of mass water content, u ($\mathrm{kg_{water}}$ / $\mathrm{kg_{concrete}}$), the moisture capacity can be introduced into Eq. 4.4 by accounting for the density of concrete in kg/m^3, ρ_{con} :

$$\frac{\partial w(h)}{\partial h} = \rho_{con}\frac{\partial u(h)}{\partial h} \tag{4.5}$$

and the Eq. 4.4 can be rewritten in the following form:

$$\rho_{con}\frac{\partial u(h)}{\partial h}\frac{\partial h}{\partial t} = \nabla(\delta_v(h) p_{v,sat} \nabla h) \tag{4.6}$$

The boundary conditions are defined on the exposed surface as follows:

$$\mathbf{n}\,\mathbf{j}_{w,mass} = \beta_{hum}\left(h_s - h_{env}\right) \tag{4.7}$$

where $\mathbf{n}$ is the unit vector normal to the exposed surface, β_{hum} is the surface humidity transfer coefficient (m/s), h_s is the value of the relative humidity at the exposed concrete surface and h_{env} is the given relative humidity of the ambient air.

4.1.2 Water vapour permeability

Values of water vapour permeability $\delta_v(h)$ for unsaturated concrete are taken from Bažant & Kaplan (1996) according to the following expression:

$$\delta_v(h) = a_0 f_1(\mathrm{h}) \tag{4.8}$$

where a_0 is the reference permeability at 25 ºC. For a mature paste, values range from 10^{-10} to 10^{-14} (s) (Neville 1973; Bažant 1975). Function $f_1(h)$ reflects the moisture transfer within the adsorbed water layers and according to Bažant & Najjar (1972) it is estimated as follows:

$$f_1(h) = \alpha + \frac{1-\alpha}{1+\left(\frac{1-h}{1-h_c}\right)^4} \tag{4.9}$$

where h_c ≈ 0.75 and α ≈ 0.05 at 25 °C.

According to Ochs et al. (2008) the saturation pressure $p_{v,sat}$ can be calculated in a temperature range from 0 ºC to 109.9 ºC with the following expression:

$$p_{sat,v} = 610.8 \cdot e^{\frac{17.08085 \cdot \vartheta}{234.175+\vartheta}} \tag{4.10}$$

where ϑ is the temperature in ºC.

4.1.3 Empirical model for determining the scanning curves

The solution of differential equation 4.4, i.e. 4.6, gives the distribution of relative humidity, not the content of water in the capillary pores. As the transport of moisture in concrete is a slow process, the different phases of water in the pores of concrete remain almost in thermodynamic equilibrium at any time (Bažant & Najjar 1972), and the content of free water can be determined using sorption isotherms that relate the relative humidity and content of evaporable water at a constant temperature. However, it is known that for materials such as concrete, there are different curves

that relate the relative humidity and free water in the pores during adsorption (wetting) and desorption (drying). In other words, the hysteresis loops are observed during wetting and drying cycles. Thus, for the more accurate calculation of the moisture distribution in the concrete a proper mathematical model of hysteresis phenomenon in cycles of wetting and drying is required.

For hysteretic material, such as concrete, the moisture capacity is determined by the slope of the scanning curves which are located between the main adsorption and desorption isotherms. A simple empirical model, proposed by Pedersen (1990), is used to determine the slope of the scanning curve for the adsorption conditions:

$$\xi_{hys,a} = \frac{0.1\left(w - w_a\right)^2 \xi_d + \left(w - w_d\right)^2 \xi_a}{\left(w_d - w_a\right)^2} \tag{4.11}$$

and for the desorption conditions:

$$\xi_{hys,d} = \frac{\left(w - w_a\right)^2 \xi_d + 0.1\left(w - w_d\right)^2 \xi_a}{\left(w_d - w_a\right)^2} \tag{4.12}$$

where ξ_{hys} is the moisture capacity, i.e. the slope of the scanning curve at a given relative humidity, $\xi_a = \frac{\partial w_a}{\partial h}$ is the moisture capacity at a given relative humidity calculated from the main adsorption isotherm, $\xi_d = \frac{\partial w_d}{\partial h}$ is the moisture capacity at a given relative humidity calculated from the main desorption isotherm, w is the current moisture content, w_a and w_d are moisture contents calculated from main adsorption and desorption curves corresponding to the current relative humidity.

Equation 4.11 is used in 4.4 (4.6) when the water content is rising compared to two previous time steps. Correspondingly, equation 4.12 is employed when the water content is decreasing compared to the two previous time steps.

The water content during scanning between the main adsorption and desorption isotherms is determined by the following relation:

$$w = w_0 + \xi_{hys} \cdot \Delta h \tag{4.13}$$

where w_0 is the initial moisture content and Δh is the change in the relative humidity which equals the difference between the humidity at time $j+1$ and j, at a spatial point i.

4.1.4 Chloride convective diffusion

The transport of chlorides is formulated here same as in Section 3.1.3, except that the convective flux of chloride ions needs to be expressed in terms of relative vapour pressure. When the concrete surface is exposed to drying and wetting, besides the diffusion contribution to the transport of chloride, the contribution due to water ingress (convection) must be taken into account. Therefore, transport of chloride ions through concrete, before steel depassivation, will be considered as convective diffusion. Free chloride ions in pore water are transported through concrete by diffusion and convection as consequence of moisture transport. The macroscopic flux of chloride $\mathbf{j}_{c,diff}$, due to diffusion is expressed as:

$$\mathbf{j}_{c,diff} = -D_c(\theta_w, T)\nabla C_c \tag{4.14}$$

where C_c is the concentration of free chloride dissolved in pore water (kg_{Cl^-} / m^3 of pore solution), $\theta_w = w/\rho_w$ is the volume fraction of pore water (m^3 of water / m^3 of concrete), ρ_w is density of water, T is temperature and $D_c(\theta_w, T)$ is the effective chloride diffusion coefficient (m^2/s). The macroscopic flux of chloride $\mathbf{j}_{c,conv}$, due to moisture transport is expressed as:

$$\mathbf{j}_{c,conv} = C_c \mathbf{v}_w \tag{4.15}$$

where $\mathbf{v}_w$ is the mean water velocity (m/s). Thus, the total mass flux of chloride ions, $\mathbf{j}_c$, takes the form:

$$\mathbf{j}_c = C_c \mathbf{v}_w - D_c(\theta_w, T)\nabla C_c \tag{4.16}$$

Due to the fact that part of the chlorides can be bound into cement hydration products, the balance equation for chloride ions in concrete is given by (Bear & Bachmat 1990):

$$\frac{\partial(\theta_w C_c)}{\partial t} = -\nabla \cdot (\theta_w \mathbf{j}_c) - \frac{\partial C_{cb}}{\partial t} \tag{4.17}$$

where C_{cb} is the concentration of bound chloride (kg_{Cl^-} / m^3 of concrete). By inserting expression (4.17) into equation (4.16), it follows:

$$\frac{\partial(\theta_w C_c)}{\partial t} = -\nabla \cdot (\theta_w C_c \mathbf{v}_w - \theta_w D_c(\theta_w, T)\nabla C_c) - \frac{\partial C_{cb}}{\partial t} \tag{4.18a}$$

or

$$\theta_w \frac{\partial C_c}{\partial t} = -\nabla \cdot (C_c \mathbf{j}_{w,vol} - \theta_w D_c(\theta_w, T) \nabla C_c) - \frac{\partial C_{cb}}{\partial t} \tag{4.18b}$$

where $\mathbf{j}_{w,vol} = \theta_w \mathbf{v}_w = \frac{\delta_v(h)}{\rho_w} p_{v,sat} \nabla h$ denotes specific water discharge (volume of pore water per unit area of concrete per unit time). Under assumption that $\rho_w = const$, the mass balance for pore water, without source or sink terms, can be written as:

$$\frac{\partial \theta_w}{\partial t} = -\nabla \cdot \mathbf{j}_{w,vol} \tag{4.19}$$

By combining (4.18b) and balance equation (4.19) we obtain the equation that describes transport of chloride ions through concrete:

$$\theta_w \frac{\partial C_c}{\partial t} = \left(\frac{\delta_v(h)}{\rho_w} p_{v,sat} \nabla h \cdot \nabla C_c \right) + \nabla \cdot \left(\theta_w D_c(\theta_w, T) \nabla C_c \right) - \frac{\partial C_{cb}}{\partial t} \tag{4.20}$$

Mathematical model of chloride binding mechanism by hardened cement paste is given as:

$$\frac{\partial C_{cb}}{\partial t} = k_r (\alpha C_c - C_{cb}) \tag{4.21}$$

where k_r is the binding rate coefficient, $\alpha = 0.7$ is constant and shows that there exists a linear relation between concentration of bound and free chloride and also that there is a limit value for bound chloride (Saetta et al. 1993). The dependence of chloride diffusion coefficient on water content and temperature is expressed as:

$$D_c(\theta_w, T) = D_{c,ref} f_1(h(w)) f_2(T) = D_{c,ref} \left[1 + \frac{\left(1 - h(w)\right)^4}{\left(1 - h_c\right)^4} \right]^{-1} \exp\left[\frac{U}{R} \left(\frac{1}{T_{ref}} - \frac{1}{T} \right) \right] \tag{4.22}$$

where $D_{c,ref}$ is a reference value of D_c evaluated at standard conditions, h_c = 0.75, $h(w)$ expresses dependence of relative humidity on pore water content in concrete according to the model of sorption isotherms, U is the activation energy of chloride diffusion process (44.6 kJ/mol for *w/c* = 0.5), R is universal gas constant and T_{ref} = 296 K.

4.1.5 Numerical implementation

The strong forms of the equations describing the distribution of relative humidity and chloride ions in concrete, respectively, are rewritten into the weak form by using the Galerkin weighted residual method as follows:

$$\left[C_h\right]\left\{\frac{\partial h}{\partial t}\right\}+\left[K_h\right]\{h\}=\left[F_h\right] \tag{4.23}$$

$$\begin{aligned}&\left[P1_{C_{cb}}\right]\left\{\dot{C}_{cb}\right\}+\left[K_{C_c}\right]\{C_c\}=\{0\}\\&\left[P2_{C_{cb}}\right]\left\{\dot{C}_{cb}\right\}+\left[P2_{C_c}\right]\left\{\dot{C}_c\right\}+\left[P3_{C_{cb}}\right]\{C_{cb}\}=\{0\}\end{aligned} \tag{4.24}$$

with

$$\begin{aligned}&\left[C_h\right]=\int_{\Omega}\frac{\partial w}{\partial h}\left[N\right]^T\left[N\right]\,d\Omega^T\\&\left[K_h\right]=\int_{\Omega}\left(\delta_v(h)p_{v,sat}\right)\left[\nabla N\right]^T\left[\nabla N\right]d\Omega+\int_{\Gamma}\beta\left[N\right]^T\left[N\right]d\Gamma\\&\left[F_h\right]=\int_{\Gamma}\beta h_{env}\left[N\right]^T\left[N\right]d\Gamma\\&\left[P1_{C_c}\right]=\int_{\Omega}\theta_w\left[N\right]^T\left[N\right]d\Omega;\ \left[P2_{C_c}\right]=\int_{\Omega}k_r\alpha\left[N\right]^T\left[N\right]d\Omega\\&\left[K_{C_c}\right]=\int_{\Omega}\theta_w D_c(\theta_w,T)\left[\nabla N\right]^T\left[\nabla N\right]d\Omega-\int_{\Omega}\frac{\delta_v(h)}{\rho_w}p_{v,sat}\nabla h\cdot\left[N\right]^T\left[\nabla N\right]d\Omega\\&\left[P1_{C_{cb}}\right]=\int_{\Omega}\left[N\right]^T\left[N\right]d\Omega;\ \left[P2_{C_{cb}}\right]=\int_{\Omega}-\left[N\right]^T\left[N\right]d\Omega\\&\left[P3_{C_{cb}}\right]=\int_{\Omega}-k_r\left[N\right]^T\left[N\right]d\Omega;\ \left[C_T\right]=\int_{\Omega}c\rho\left[N\right]^T\left[N\right]d\Omega\end{aligned} \tag{4.25}$$

where $\left[N\right]$ is the column matrix of shape functions which relates relative humidity values h in concrete, mass concentration of free chloride in pore water C_c, mass concentration of bound chloride in concrete C_{cb} with their nodal values and Γ is the concrete surface exposed to environmental conditions. Equations 4.23 and 4.24 are solved, the same as discussed in Section 3, i.e. by using the direct integration method of implicit type.

5 VALIDATION OF THE 3D CHTM MODEL: SINGLE REBAR CASE

5.1 Single rebar case without the influence of stirrups

5.1.1 Unloaded beam-end specimen

Further extensions of the 3D chemo-hygro-thermo-mechanical model, i.e. the calculation of the rate of rust productions from the anodic current density and the implementation of the 1D corrosion contact elements to simulate the inelastic expansion of the products, are tested on a simple example of the beam-end concrete specimen. Note that the water content is assumed to be uniformly distributed and constant in the specimen. Therefore, the hysteretic moisture model for concrete is not implemented for this case. The specimen geometry and parameters relevant for the calculation of processes after depassivation of steel are chosen according to the model presented in Ožbolt et al. (2011), which validated the 3D CHTM model for calculating the values of current density as a function of concrete saturation. Although there are no available experimental data in regard to concrete cover cracking of the investigated specimen geometry, the predicted corrosion induced damage is verified in the context of time to critical crack appearance on the concrete surface (Thoft-Christensen 2000).

Segment of an unloaded concrete beam-end is subjected to aggressive environmental conditions. The beam rectangular cross-section is reinforced with four steel bars (diameter ϕ= 10 mm) in each corner with a concrete cover of 25 mm (Figure 5.1). The length of the investigated beam section is 205 mm.

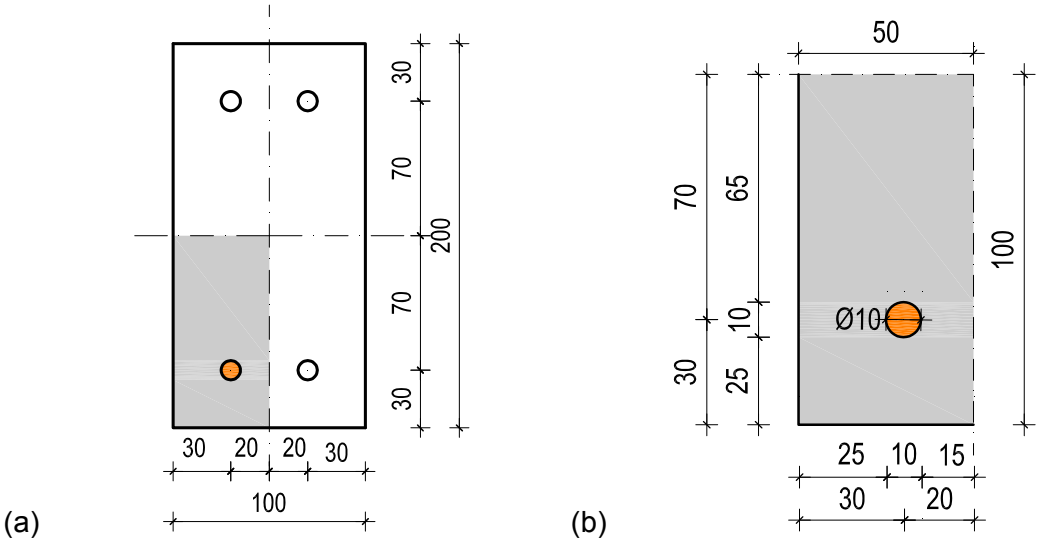

Figure 5.1. Geometry of the RC beam's cross-section (a) and the detail of quarter of the cross-section (b) (all in mm)

Due to the symmetry conditions only a quarter of the beam is modelled with only one rebar (Figure 5.2). The FE discretization is performed employing eight node solid elements for the concrete and the reinforcement bar. The 1D corrosion contact elements are radially distributed around the bar with 16 contact elements in each cross-section. They are placed in the interface layer with thickness of 0.1 mm.

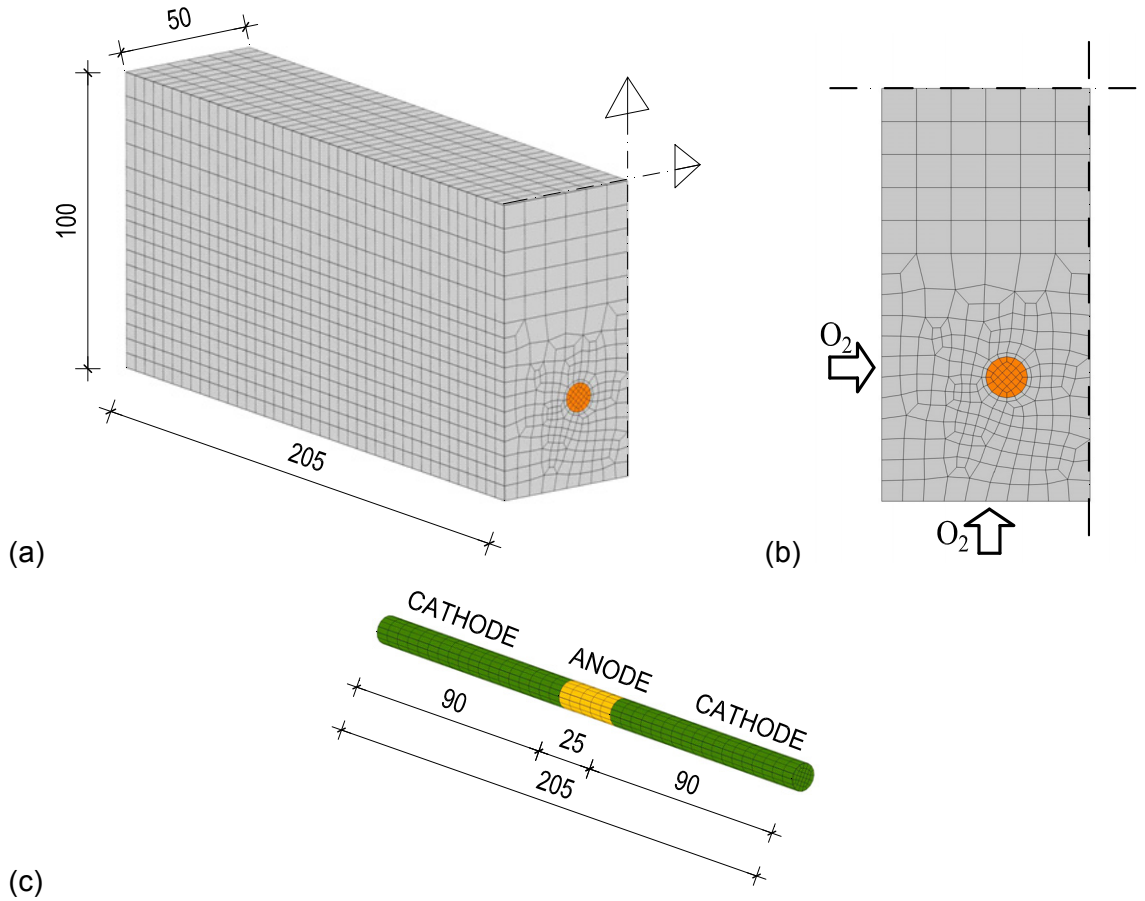

Figure 5.2. FE discretization of the investigated beam (a); cross-section of the analysed quarter of the cross-section (b); anodic and cathodic distribution along the reinforcement (c) (in mm)

It is assumed that at the start of the analysis, the reinforcement bar is already depassivated, hence the processes before depassivation of reinforcement are not calculated. The distribution of cathode and anode on the surface of the reinforcement is taken as shown in Figure 5.2c. The anode is assumed to be active at the middle of the reinforcement bar, with the length of 2.5 bar diameter. The whole circumference of the bar is assumed to be depassivated in the anodic region. The rest of the reinforcement surface is taken as cathode.

Due to the emphasis on the modelling of processes after depassivation, only the following is calculated: distribution of oxygen, electric potential, current density, corrosion rate, expansion of corrosion products and damage due to the expansion and transport of corrosion products. The analysis is performed for un-cracked good quality concrete (water-cement ratio, w/c = 0.4) assuming water saturation of 55%. The saturation of the entire specimen is assumed to be constant and equal to the

boundary conditions. For the initial and boundary oxygen conditions, the value of 0.0085 kg / m^3 of concrete is assumed, same as in Ožbolt et al. (2011). Mechanical properties of concrete, steel and rust used in the analysis are summarized in Table 5.1.

Table 5.1 Mechanical parameters used in the model

Parameter	Value
Modulus of elasticity of concrete, E_c (N/mm^2)	25000.0
Poisson's ratio of concrete, ν_c	0.18
Tensile strength of concrete, f_t (N/mm^2)	2.00
Uniaxial compressive strength of concrete , f_c (N/mm^2)	25.0
Fracture energy of concrete, G_f (J/m^2)	80.0
Modulus of elasticity of steel, E_s (N/mm^2)	200000.0
Poisson's ratio of steel, ν_s	0.33
Modulus of elasticity of rust, E_r (N/mm^2)	100.0
Volume expansion factor of rust, $\alpha_r = \rho_s / \rho_r$	4.0

The parameters relevant for the calculation of electric potential, consumption of oxygen and rust distribution are presented in Table 5.2. They approximately correspond to parameters for severe splash environmental condition (Ožbolt et al. 2011).

Table 5.2 Parameters used in the numerical simulations

Parameter	Value
Anodic exchange current density, i_{0a} (A/m^2)	1.875×10^{-4}
Cathodic exchange current density, i_{0c} (A/m^2)	6.25×10^{-6}
Anodic equilibrium potential, Φ_{0a} (V vs. SCE)	-0.780
Cathodic equilibrium potential, Φ_{0c} (V vs. SCE)	0.160
Tafel slope for anodic reaction, β_a (V/dec)	0.06
Tafel slope for cathodic reaction, β_c (V/dec)	0.160
Diffusivity coefficient of rust, D_r (m^2/s)	2.2×10^{-16}

5.1.1.1 Results and discussion

Damage (cracks) due to the corrosion of steel reinforcement (maximum principal strains) 750 days after depassivation of steel are shown in Figure 5.3a, while the Figure 5.3b shows the distribution of corrosion products in cracks at the same time period. The crack is plotted in terms of maximum principal strains on undeformed specimens with the red (dark) zone corresponding to the crack opening of 0.20 mm or larger.

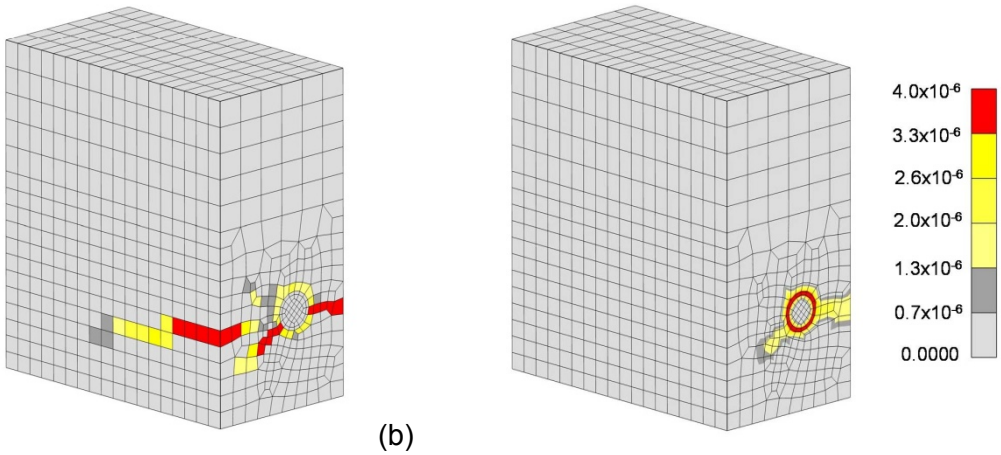

(a) (b)

Figure 5.3 Damage (cracks) due to the corrosion of steel reinforcement, 750 days (~2 years) after depassivation of steel (a); Distribution of corrosion products in cracks 750 days (~2 years) after depassivation of steel (in kg) (b)

The thickness of the rust layer around the reinforcement bar, corresponding to the first crack observed on the concrete surface (crack width of 0.05 mm), is approximately 0.10 mm. This is observed 220 days after depassivation of reinforcement (start of the analysis). The critical crack width of 0.20 mm on the beam surface is first observed 610 days after depassivation of steel, which is in agreement with the predicted time to critical cover cracking according to Thoft-Christensen (2000).

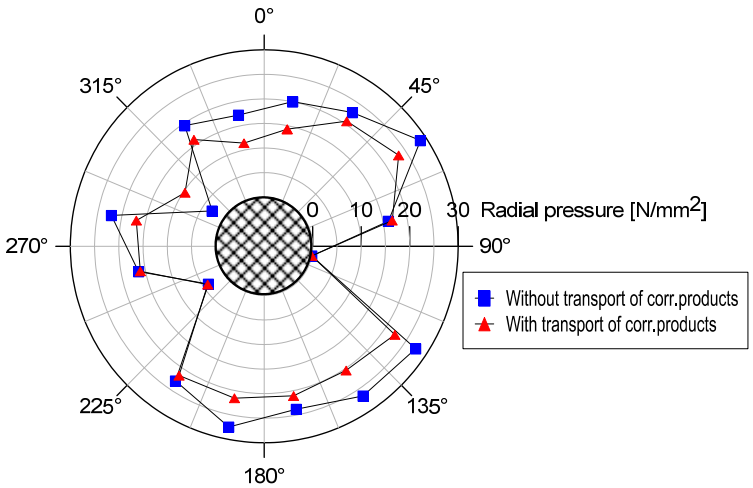

Figure 5.4 Distribution of radial pressure at the reinforcement surface 360 days after depassivation of steel

The distribution of radial pressure at the reinforcement surface, at the anode-cathode transition zone (maximal corrosion rate), 360 days after depassivation of reinforcement, is presented in Figure 5.4. It is shown that the pressure is not radial-symmetrically distributed over the surface of reinforcement. Moreover, radial pressure is becoming lower at regions where the corrosion induced cracks are generated. With the transport of corrosion products being accounted for, the accumulated rust products are transported in the cracks and therefore reducing the pressure on the surrounding concrete.

5.1.2 Pull-out capacity of corroded beam-end specimen

The experimental results obtained by Fischer (2012) present valuable data for validation and calibration of numerical model for simulation of corrosion induced damage and its effects on the behaviour of RC elements. Therefore, these results are used to verify the proposed 3D chemo-hygro-thermo-mechanical model. Investigated are the generated crack patterns and crack widths due to the corrosion induced damage, as well as their influence on the pull-out capacity of the rebars. The hysteretic moisture behaviour of concrete is not investigated for the beam-end specimen, i.e. the water content is assumed to be constant and uniformly distributed in the specimens.

5.1.2.1 Test setup and experimental conditions

The main aim of the experiments performed by Fischer (2012) was to investigate the influence of the corrosion induced damage on the bond behaviour of the embedded steel bars. Series of beam-end specimens were chosen according to Chana (1990), where the specimen geometry was optimized in order to prevent yielding of reinforcement and to exclude the influence of neighbouring bars on each other while the pull-out test is conducted in each separate corner (see Figure 5.5).

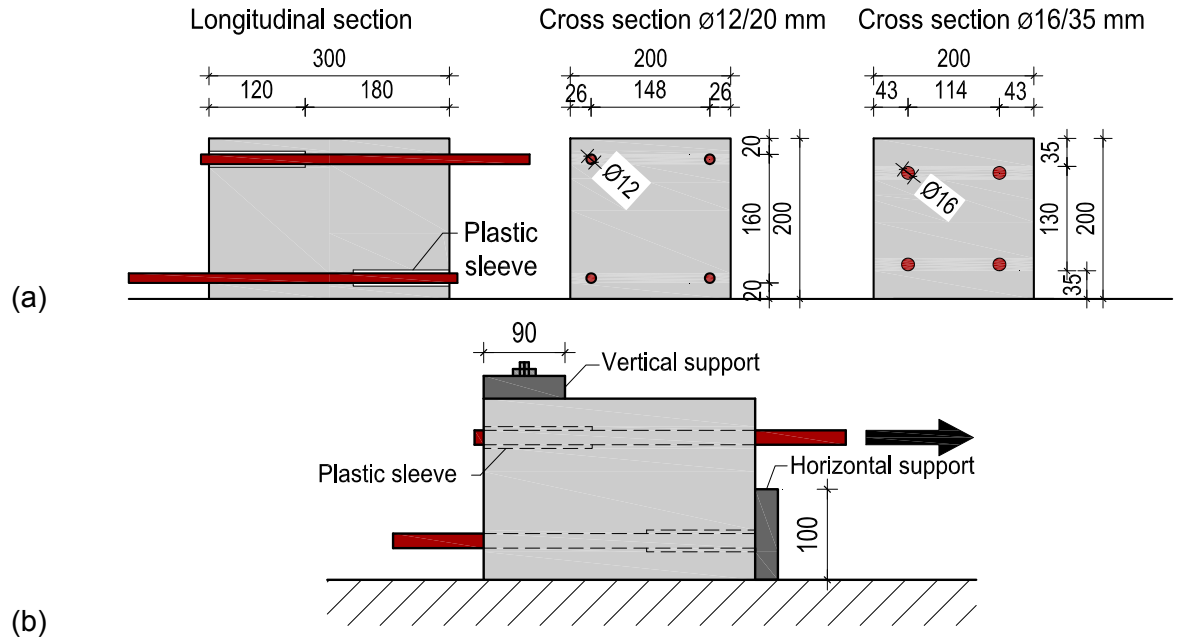

Figure 5.5 Geometry of the beam-end specimen (a) and pull-out loading condition (b)

The specimens were first exposed to aggressive environmental conditions, which caused the corrosion of the embedded reinforcement bar and subsequently the reinforcement was pulled out from the specimen. Only two specimen types without stirrups, with four bars arranged in corners, were studied by the test method proposed by Chana (1990). The cross-section in both cases was 200 x 200 mm^2. For

the first specimen type, the diameter of the reinforcement bar was 12 mm with a concrete cover of 20 mm (ϕ12/20 mm) and for the second, the bar diameter of 16 mm with a cover of 35 mm (ϕ16/35 mm) was used (Figure 5.5a). The total embedment length of the reinforcement in both cases was 180 mm, whereas the rest of the length was isolated with a plastic sleeve (Figure 5.5a). The height of the support placed on the pull-out face was 100 mm. To prevent the lifting of the specimen another support was placed on the rear part of the top surface over a length of 90 mm (Figure 5.5b).

The experiments were carried out under accelerated corrosion, which approximately corresponds to the severe splash natural conditions. In order to accelerate the corrosion process, a potential of +500 mV NHE was applied between the rebars (anodes) and two platinised titanium meshes (cathodes), one at each side of the specimen. The two longitudinal sides of each specimen were wetted twice a day with 1 % chloride solution for 1 to 3 minutes. The resulting current densities for the bar diameter d = 12 mm were approximately i_{corr} = 20-25 μA/cm^2. For the bar diameter d = 16 mm, the values of i_{corr} = 15-20 μA/cm^2 were obtained.

5.1.2.2 Finite element discretization and model input parameters

In the analysis it is assumed that certain length sections of the bar are activated as anode (depassivated) at the start of the analysis, i.e. the processes before depassivation of reinforcement are not computed. This predefined position of anode and cathode (Figure 5.6a), assuming initially un-cracked concrete, is kept unchanged during the computation. In this way only the electric potential, current density, distribution of oxygen, cracking of concrete and distribution of corrosion products are calculated after depassivation. Note that the application of the model for computation of processes before depassivation of reinforcement can be found in Ožbolt et al. (2010).

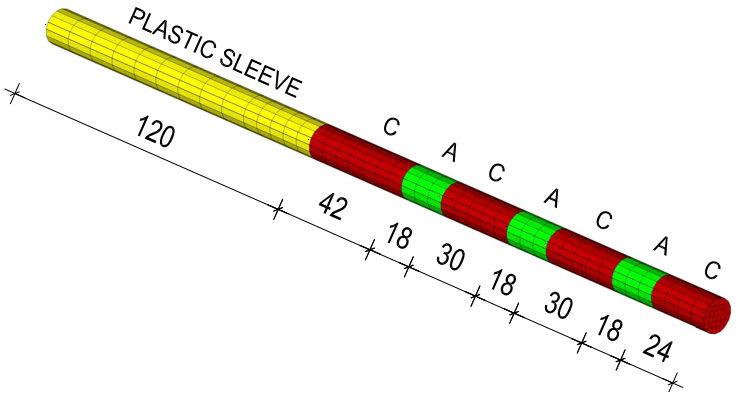

(a)

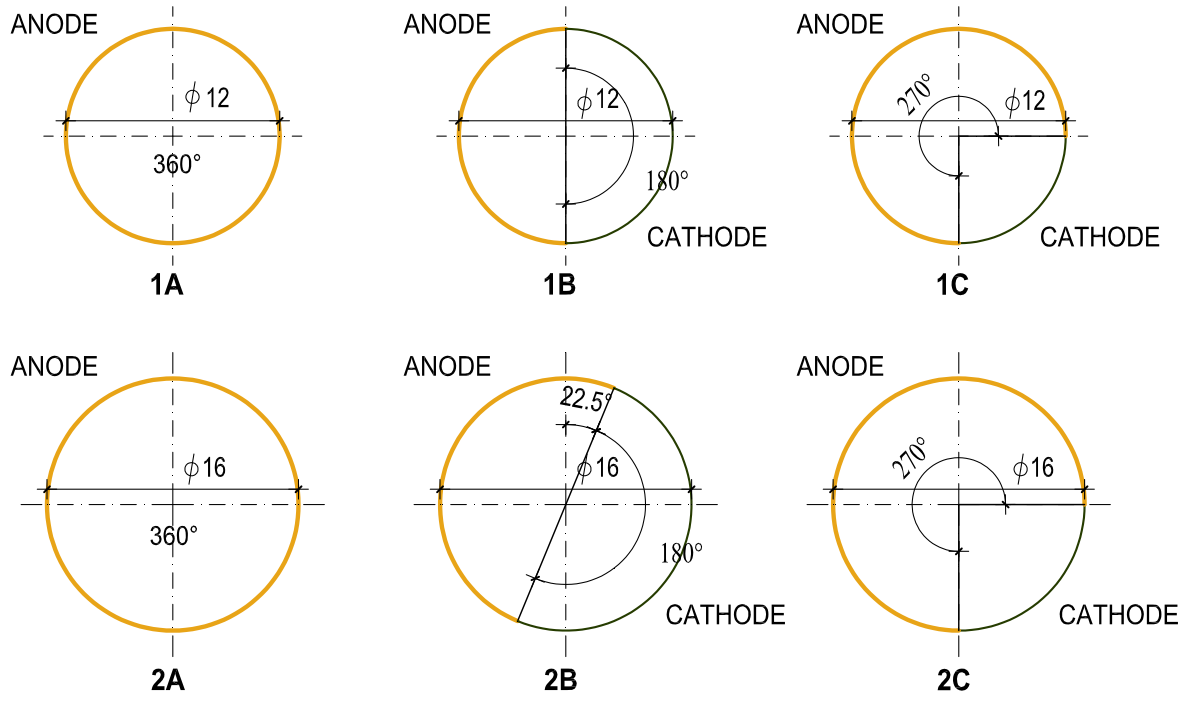

(b)

Figure 5.6 Assumed anodic and cathodic regions: (a) along the length and (b) along the cross-section of the reinforcement bar

One of the aims of the here presented study is to investigate the influence of the anodic region distribution in the cross-section of the reinforcement bar. Therefore, for each specimen (reinforcement diameter), three configurations of the anodic surface over the circumference are assumed (Figure 5.6b): (A) anode over the entire circumference, (B) over the half of the circumference and (C) over the 3/4 of the circumference. For case B, two additional positions are studied, with the vertical symmetry axis and with the symmetry axis inclined at 22.5° with respect to the vertical axis. In the following, these types will be addressed in accordance with Figure 5.6b , e.g. type 1A is the first case (ϕ12/20 mm) with the cross-section configuration in which the anodic region is assumed along the whole surface of the reinforcement circumference.

For the computation of the transport processes after depassivation of reinforcement, it is assumed that the water saturation is constant over the entire volume of the specimen (S_w = 50%). The initial concentration of oxygen in concrete is taken the same as the concentration on the exposed concrete surfaces and is equal to 0.0085 kg of dissolved oxygen / m^3 of pore solution. Oxygen diffusivity and electrical conductivity of concrete are chosen for a good quality concrete with water-cement ratio, w/c = 0.4 (Tables 2.1 and 2.2) The parameters relevant for the calculation of electric potential, consumption of oxygen and rust distribution are summarized in Table 5.3. They approximately correspond to parameters for severe splash environmental condition (Ožbolt et al. 2010, 2011). In the experiment the corrosion was accelerated and was approximately 5 times faster than the highest corrosion rate observed in nature. However, the model used in the analysis results in relatively

high corrosion rates under natural conditions. Therefore, the model parameters (saturation of 50%) are chosen such that the corrosion induced damage in real time (after 7 years) corresponds to the experimentally obtained damage under accelerated conditions (after 6 months).

Table 5.3. Parameters used in the numerical simulations

Parameter	Value
Faraday's constant, F (C/mol)	96486.7
Anodic exchange current density, i_{0a} (A/m^2)	1.875×10^{-4}
Cathodic exchange current density, i_{0c} (A/m^2)	6.25×10^{-6}
Anodic equilibrium potential, Φ_{0a} (V vs. SCE)	-0.780
Cathodic equilibrium potential, Φ_{0c} (V vs. SCE)	0.160
Tafel slope for anodic reaction, β_a (V/dec)	0.06
Tafel slope for cathodic reaction, β_c (V/dec)	0.160
Diffusivity coefficient of rust, D_r (m^2/s)	2.2×10^{-16}

The diffusivity coefficient D_r is determined by taking into account the values mentioned in Section 2.1.6.4 and by calibrating the model predictions with the experimental results obtained by Fischer (Fischer 2012). At this stage of the model development the value of diffusivity coefficient is taken in a qualitative sense. Further experimental investigations are needed in order to make a more accurate calibration of the parameter.

Table 5.4. Mechanical properties used in the analysis

Parameter	Value
Modulus of elasticity of concrete, E_c (N/mm^2)	25000.0
Poisson's ratio of concrete, ν_c	0.18
Tensile strength of concrete, f_t (N/mm^2)	3.0
Uniaxial compressive strength of concrete , f_c (N/mm^2)	41.0
Fracture energy of concrete, G_f (J/m^2)	90.0
Modulus of elasticity of steel, E_s (N/mm^2)	200000.0
Poisson's ratio of steel, ν_s	0.33
Modulus of elasticity of rust, E_r (N/mm^2)	100.0
Volume expansion factor of rust, $\alpha_r = \rho_s / \rho_r$	4.0

Mechanical properties of concrete, steel and rust are summarized in Table 5.4. Because of the complexity of the model and in order to reduce the computational

time, only half of the specimen is simulated (Figure 5.7a). In the case of the second specimen, the width of the modelled section is taken 10 mm wider than the symmetry plane to accommodate for a bigger bar diameter and a deeper concrete cover, while analyzing the pull-out resistance (Figure 5.7b). Eight-node solid 3D finite elements are used to model the concrete and the reinforcement bar.

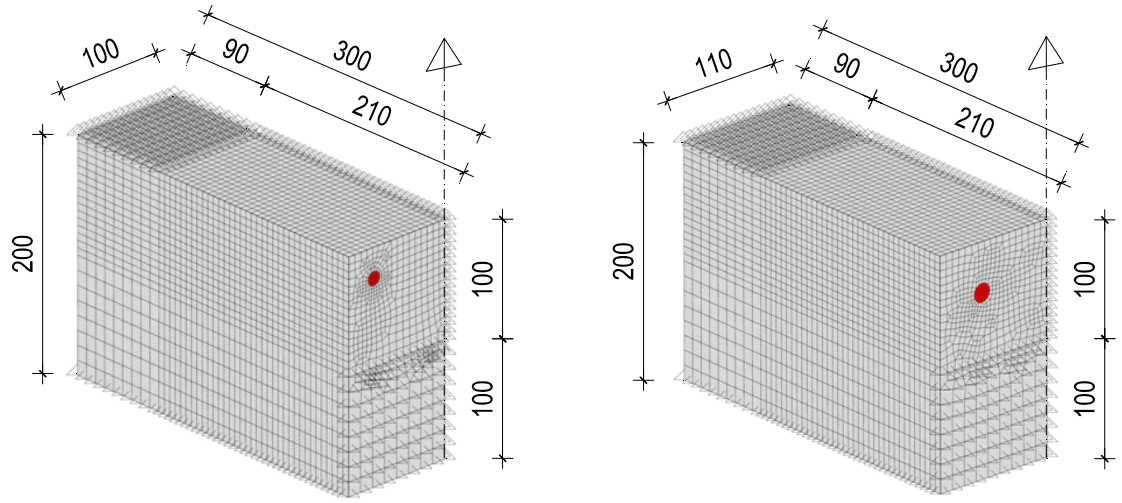

(a) (b)

Figure 5.7 Model geometry (all in mm) in the case of the first (a) and (b) the second specimen

To simulate the expansion due to the formation of corrosion products, 1D radially oriented corrosion contact finite elements are used with a length of 0.1 mm. The radial compressive resistance is assumed to be linear elastic and shear resistance controlled by the bond-slip relationship. The bond-slip constitutive laws of the contact elements used for both specimen types (ϕ12 / 20 mm and ϕ16 / 35 mm) are shown in Figure 5.8, where τ_{max} is the total bond strength and τ_f is the frictional strength. These constitutive laws correspond to the average bond-slip resistance of the reinforcement bars pulled out from the concrete block with no influence of edges (Lettow 2006).

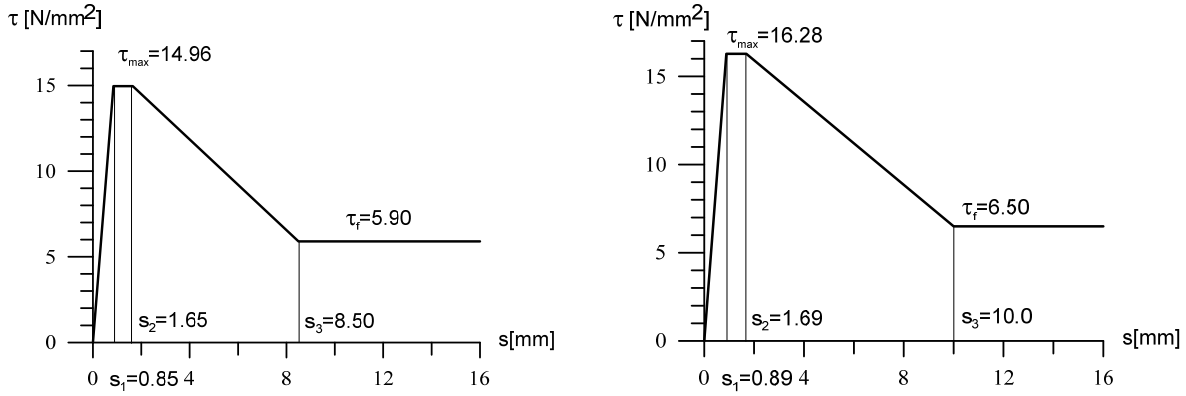

(a) (b)

Figure 5.8 Bond-slip constitutive law for: (a) the first specimen (ϕ12 / 20 mm) and (b) the second specimen (ϕ16 / 35 mm)

5.1.2.3 Influence of the position of anode and cathode on the corrosion induced damage

The numerical analysis is focused on the corrosion-induced damage of concrete. Therefore, the processes during the initiation phase are not computed, i.e. it is assumed that at the start of the analysis, the reinforcement bar is depassivated. Furthermore, the continuous formation of new anodic regions after depassivation of reinforcement would be a too demanding task in combination with computing current density, corrosion rate and damage of concrete. To further simplify the problem, it is assumed that in the propagation phase, the position of cathode and anode remains constant. The experimental results (Fischer 2012) indicated that a significant amount of rust was found in the corrosion-induced cracks. Therefore, the transport of corrosion products through cracks is also accounted for in the numerical analysis. Since the corrosion rate in the experiments was accelerated by the factor of approximately 5 times compared to the natural corrosion rate (severe splash conditions), only the total amount of corrosion products and not their time evolution can be compared with numerical results.

Experimentally observed and numerically predicted crack patterns in the mid cross section of the specimen, 7 years after depassivation of reinforcement, are shown in Figures 5.9 and 5.10 for cases 1A-C and 2A-C, respectively. Note that in the following paragraphs, the cracks (red zones) are plotted on undeformed specimens in terms of maximal principal strains. The critical strain ε_{cr} is calculated as $\varepsilon_{cr} = w_{cr} / h$ and corresponds to the critical crack opening w_{cr}, which is assumed to be 0.10 mm, i.e. red zones correspond to locations where the maximal principal strain is equal to or larger than the critical strain. For the first specimen (ϕ12 / 20 mm), the cases 1A and 1C lead to a similar crack formation pattern around the reinforcement bar, whereas type 1B gives a somewhat better agreement with the experimental crack pattern (Fischer 2012). Although the best agreement with the experimental crack pattern is obtained for the case 1B as seen from Figure 5.9, it can be concluded that for relatively small bar diameter and small concrete cover, the crack pattern is not strongly influenced by the assumed positions of cathode and anode. For the second specimen (ϕ16 / 35 mm), the configuration type 2B shows a crack pattern that fits nicely with the damage observed in the experiments, in which only one visible crack was noticed on the side of the free surface of the concrete specimen. When considering the whole circumference as depassivated (type 2A), the concrete surrounding the bar is fully cracked and the average crack width on the side surface is larger compared to the type 2B. The type 2C, with 3/4 of the circumference being assumed as anode, generates an additional crack on the upper surface of the specimen. The results indicate that with increase of bar diameter and concrete cover, the crack pattern becomes more sensitive to the size and position of cathode and anode.

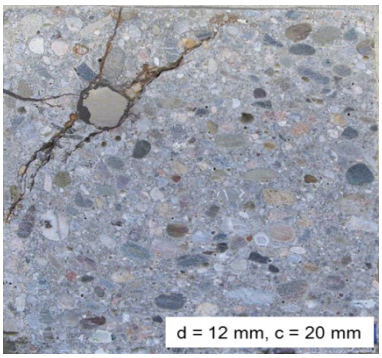

Test results for ϕ12/20 mm (Fischer 2012)

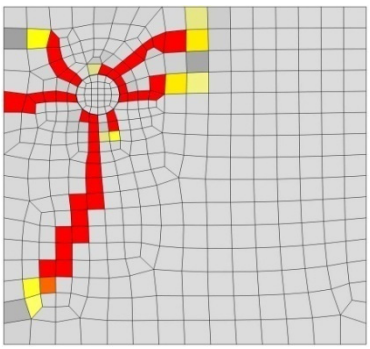

1A -after 7 years

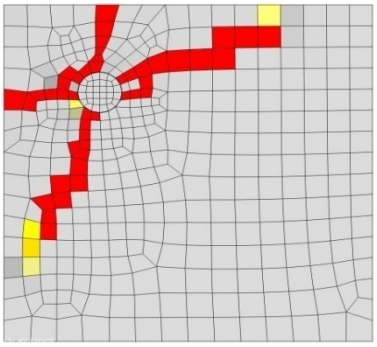

1B -after 7 years

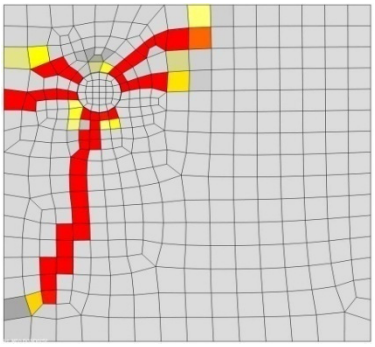

1C -after 7 years

Figure 5.9 Comparison of the crack patterns in the cross section at the beam's mid-span for the cases 1A-C with the experimental results

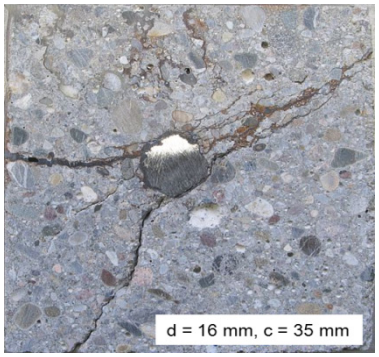

Test results for ϕ16/35 mm (Fischer 2012)

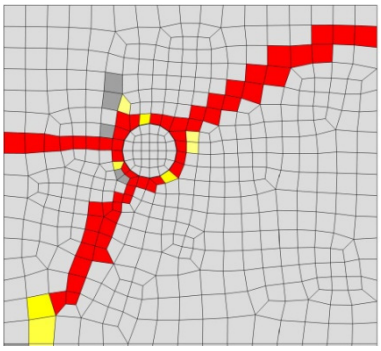

2A -after 7 years

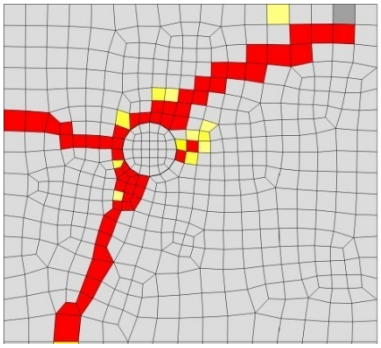

2B -after 7 years

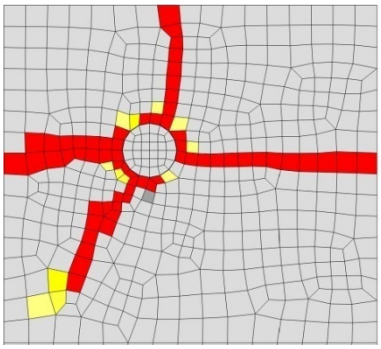

2C -after 7 years

Figure 5.10 Comparison of the crack patterns in the cross section at beam's mid-span for the cases 2A-C with the experimental results

In Figure 5.11, the distribution of radial pressure as a consequence of expansion of corrosion products is plotted for the cases 1B and 2B. The pressure is shown in the anode-cathode transition zone. As expected, the pressure is not axial-symmetrically distributed over the surface of the reinforcement. For smaller diameter and smaller concrete cover (ϕ12 / 20 mm), maximal radial pressure of approximately 40 MPa is observed. For larger diameter and larger concrete cover (ϕ16 / 35 mm), the maximal radial pressure is higher and it reaches approximately 55 MPa. In both cases, the maximal pressure is obtained approximately 1.5 years after corrosion initiation.

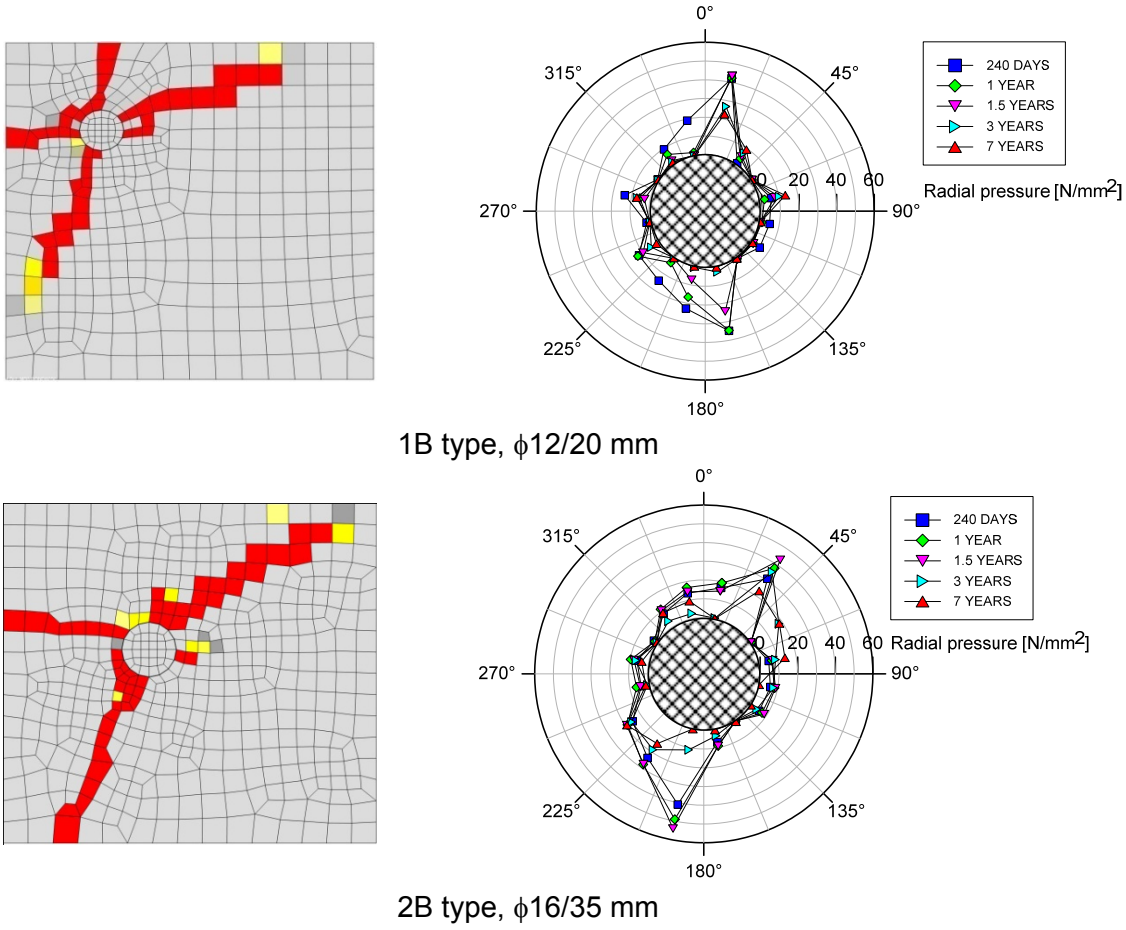

1B type, ϕ12/20 mm

2B type, ϕ16/35 mm

Figure 5.11 Distribution of radial pressure and corresponding crack pattern

5.1.2.4 Distribution of oxygen, electric potential and current density

After depassivation of reinforcement (propagation phase), the corrosion rate is strongly influenced by distribution of water and oxygen. For instance, if the supply of oxygen is not sufficient at the cathodic regions as mentioned in Section 2.1.4 , the corrosion process will slow down and eventually stop.

In the present numerical investigations, the water saturation is assumed to be constant during the corrosion phase (S_w = 50%). However, the distribution of oxygen

depends on the corrosion rate, which is in turn dependent on mechanical properties of concrete (cracking). More cracking provides a better oxygen supply and consequently leads to a higher corrosion rate. In the following, the influence of cracking on the distribution of oxygen, electric potential and current density is studied.

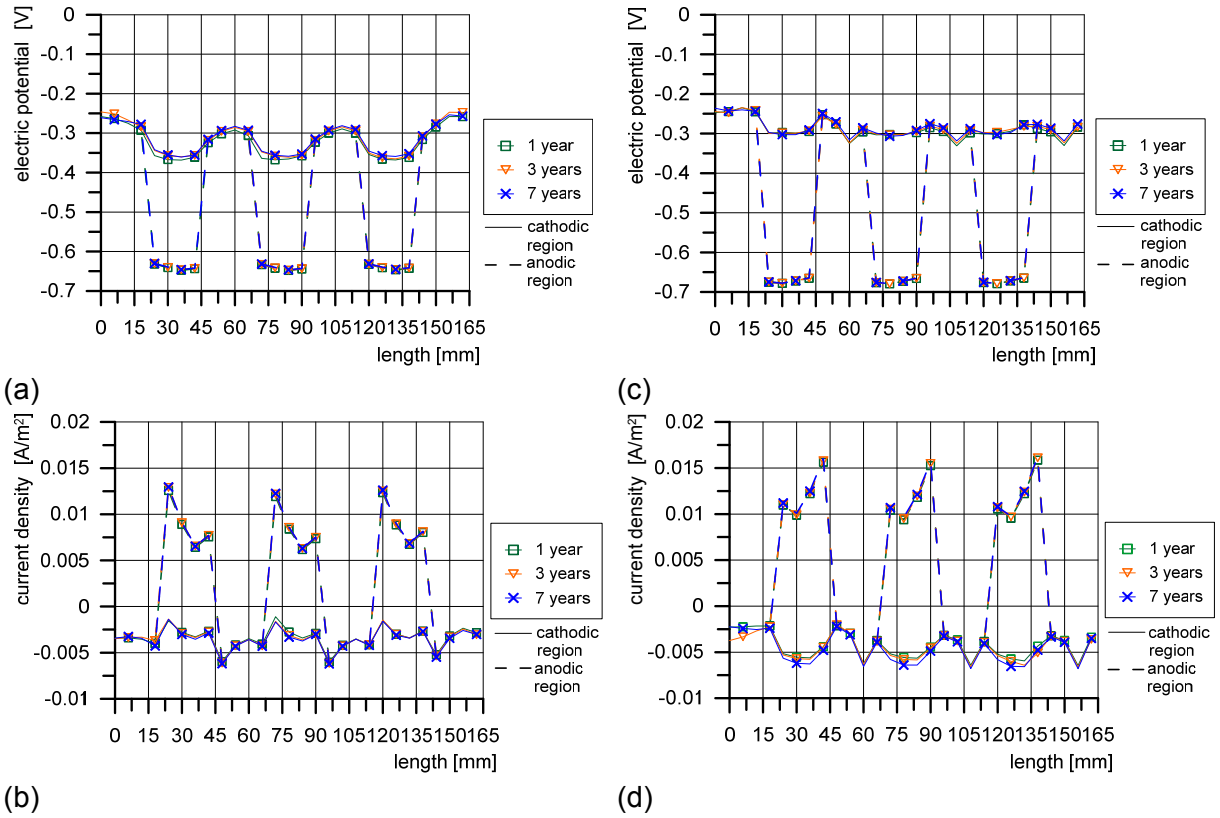

Figure 5.12 Time dependant distribution of the average electric potential and current density for the type 1B (a,b) and the type 2B (c,d) along the reinforcement bar

The distribution of electric potential (V), current density (A/m^2) and oxygen (kg/m^3 of pore solution) along the 162 mm length of the reinforcement bar, starting from the pull-out surface, are shown in Figures 5.12 - 5.14, respectively. Plotted are average values over the corresponding cathodic and anodic regions in the cross-sections of the bar. The distribution of the current density and electric potential along the length of the bar (Figure 5.12) shows that the highest electric potential and current density is predicted in the cathode-anode transition zone.

Similarly as observed by Ožbolt et al. (2011), it can be noticed that the opening of cracks, which are occurring later with the forming of a thick enough rust layer, has a small effect on the electric potential and current density. This is a consequence of the assumed constant water saturation and is also due to the fact that the position and size of the anode and cathode along the bar (Figure 5.6) is not changing during the corrosion phase.

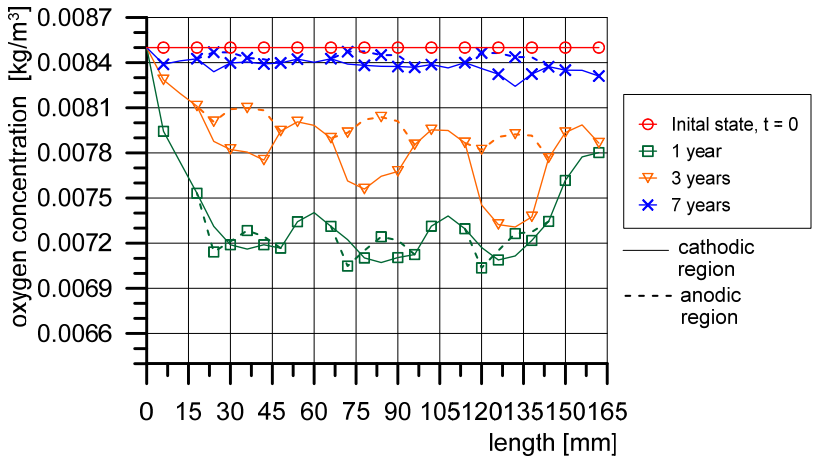

Figure 5.13 Time dependant distribution of average oxygen concentration for the type 1B

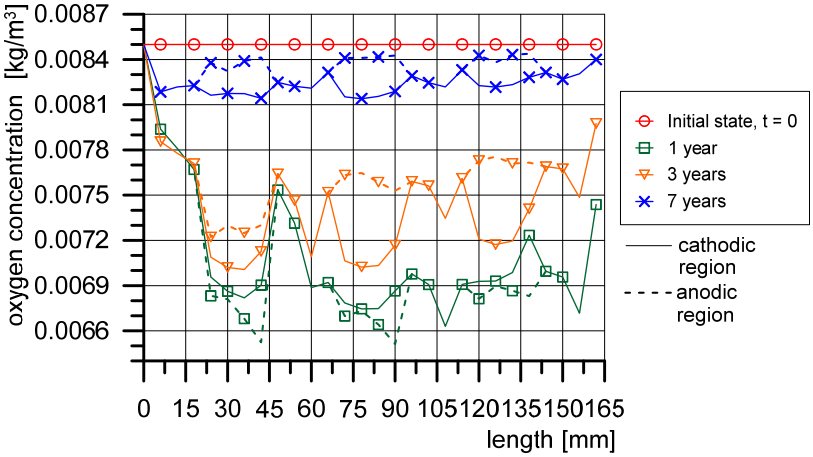

Figure 5.14 Time dependant distribution of average oxygen concentration for the type 2B

The distribution of oxygen concentration along the reinforcement bar is shown in Figures 5.13 and 5.14. It demonstrates significant effect of the corrosion induced damage and the importance of coupling the transport processes with mechanical properties of concrete. The consumption of oxygen reaches its maximum soon after the start of the analysis (depassivation) and remains approximately constant until the first surface crack appears. In the case of the second specimen (ϕ16 / 35 mm) the reduction of oxygen content at the anodic-cathodic transition zone is higher than for the specimen with the concrete cover of 20 mm (ϕ12 / 20 mm). This can be explained by the thicker concrete cover, which causes a slower supply of oxygen from the free surface of un-cracked concrete, but partly also by the larger anodic surface of reinforcement bar. With the opening of the surface crack(s) the flow of oxygen rises and consequently the concentration of oxygen at the reinforcement surface, 7 years after depassivation, is almost identical to the values at the beginning of the corrosion process. The results for the specimen 1B (ϕ12 / 20 mm) show that the increase of oxygen concentration is faster compared to the specimen 2B (ϕ16 / 35 mm), which can also be attributed to the thinner concrete cover.

Figures 5.13 - 5.14 illustrate a difference in oxygen concentration profiles at anodic and cathodic regions of the same bar cross sections. This is clearly shown in Figure 5.15 where the average cathode and anode oxygen concentration are plotted as a function of time for 1B and 2B cases, respectively, in the cross-section of the anode-cathode transition zone at 24 mm distance from the pull-out surface of the specimen. The anodic region shows a higher consumption of oxygen at the beginning of the corrosion process. Due to the accumulation of the corrosion products in this area which causes damage, the effect of cracking on oxygen distribution is faster compared to the cathodic regions. These areas (cathodes) are further away from the cracked concrete elements and therefore the increased ingress of oxygen through the cracks is being manifested more slowly.

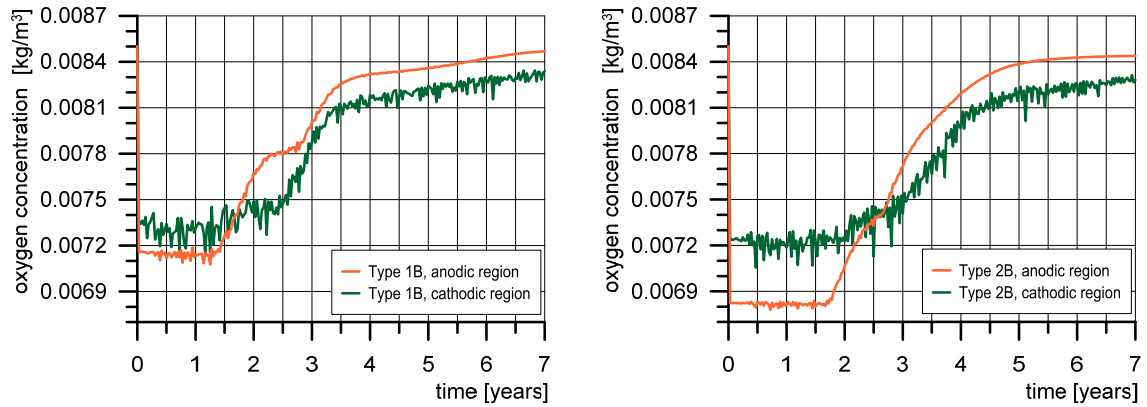

Figure 5.15 Time dependant distribution of oxygen in the cross-section at the anode-cathode transition zone for: type 1B (a) and type 2B (b)

5.1.2.5 Influence of the corrosion induced damage on the pull-out capacity

One of the objectives of the here presented study is to investigate the effect of corrosion induced damage on the pull-out capacity of the reinforcement. Similar as in experiments (Fischer 2012), the bars are pulled out from the specimens for different levels of corrosion: t = 0 (reference - no corrosion), 1, 3, 5 and 7 years, respectively. Typical crack patterns after the pull-out failure (specimen type 1B) obtained in the experiment and the analysis for t = 0 (reference), 1 and 7 years are shown in Figure 5.16. As expected, the failure is due to the splitting of concrete cover and not to the pull-out of the reinforcement bar. The same failure mode and similar crack patterns for different corrosion rates were observed in the experimental tests of Fischer (2012) (see Figure 5.16a).

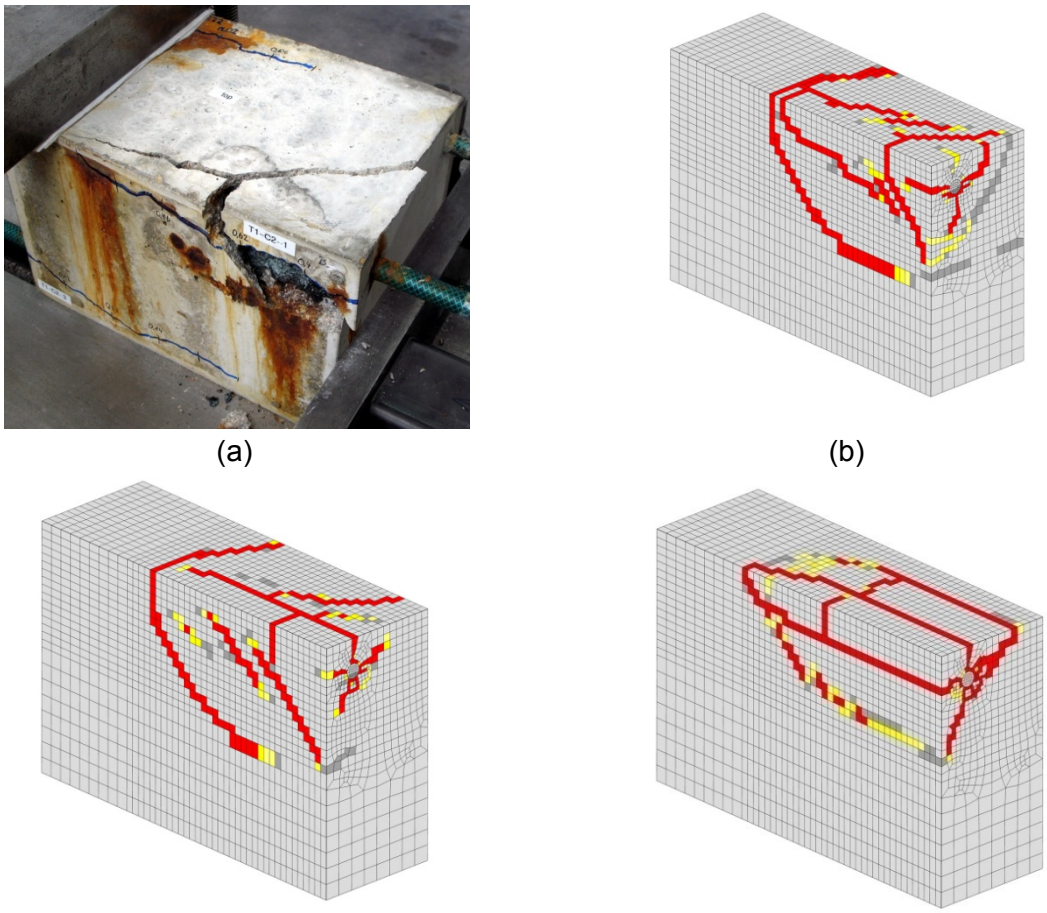

(a) (b)

(c) (d)

Figure 5.16 Typical pull-out failure mode for specimen type 1B: (a) Fischer (2012) corresponds approximately to t = 7 years of the analysis; (b) analysis, (reference) t =0; (c) analysis, t = 1 year and (d) analysis t = 7 years

The predicted and experimentally measured relative decrease of the bond resistance is plotted in Figure 5.17a,b as a function of the average corrosion penetration of the reinforcement bar, x_{corr}. The corrosion penetration x_{corr} is calculated from Eq. 3.51 as an average value in the nodes at the anode-cathode transition zone.

For each case, an average crack width is calculated and plotted as a function of x_{corr} in Figure 5.17c,d. Same as in the experiments (Fischer 2012), the crack width is calculated from the damaged finite elements on the exposed surfaces of the concrete specimen, as the sum of their averaged longitudinal crack widths. The dependence between the average crack width and the corresponding bond resistance is plotted in Figure 5.17e,f.

Comparing the cases for the first specimen (left column in Figure 5.17), it can be noticed that the results differ slightly from each other. Similarly to the comparison of the numerically obtained crack patterns, the type 1B shows the best agreement with the experimental results. In general the agreement is good, except for the relation between the crack width and the corrosion penetration depth, where even for case

1B, the crack width is slightly overestimated (see Figure 5.17c). However, having in mind the complexity of the problem, the magnitude of this overestimation is acceptable. For relatively small bar diameter (12 mm) and concrete cover (20 mm), the positions of anode and cathode do not significantly influence the bond resistance as a function of corrosion depth and crack width, respectively.

As expected, for the 16 mm bar diameter and 35 mm concrete cover (right column in Figure 5.17), the anode-cathode configuration has a greater influence on the bond resistance. The type 2C differs the most compared with the experimental results, since the corrosion-induced damage for this case is larger than in the experiment. Consequently, the reduction of bond resistance becomes overestimated. Similarly to the first specimen, the best agreement with the experimental results are obtained for half of the bar circumference being depassivated (type 2B). In the experiments, the free specimen surfaces were exposed to chlorides. Therefore, it is reasonable that the rebar region which is closer to these surfaces plays the most significant role in controlling the corrosion-induced damage of the concrete cover.

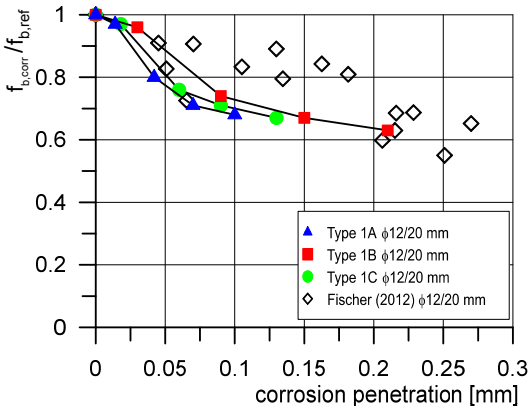

(a)

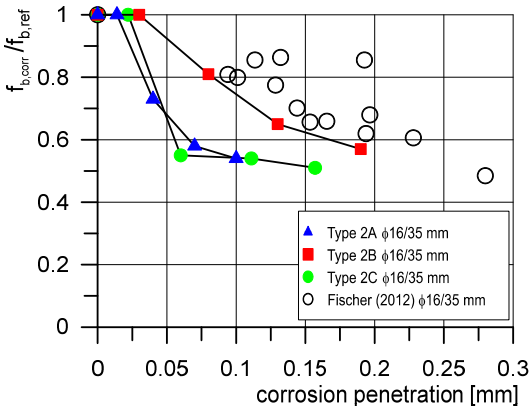

(b)

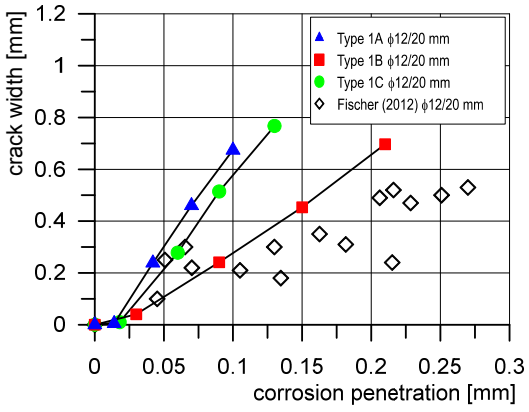

(c)

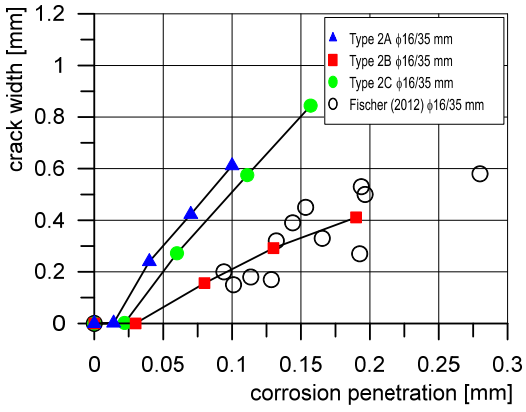

(d)

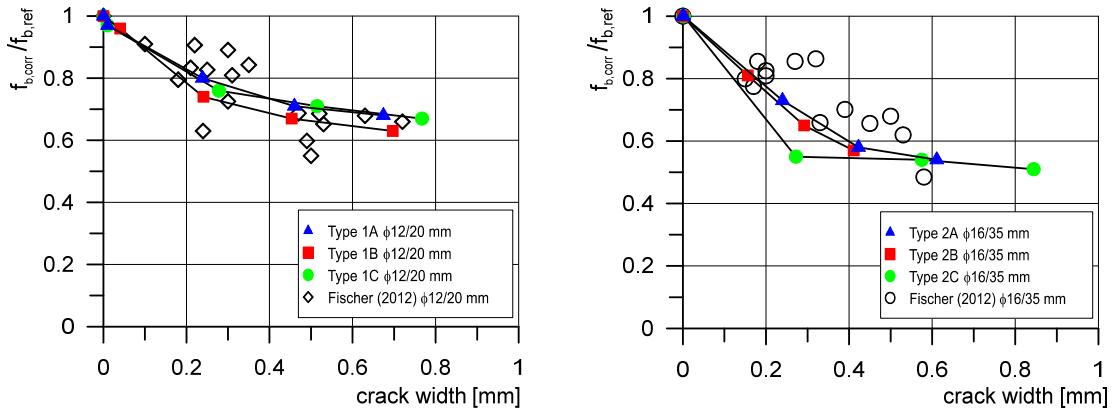

(e) (f)

Figure 5.17 Predicted and experimentally obtained results for both specimen types and all positions of anode and cathode: (a,b) Relative pull-out capacity as a function of average corrosion penetration; (c,d) Average crack width as a function of average corrosion penetration; (e,f) Relative pull-out capacity as a function of the average crack width

5.1.2.6 Influence of the transport of corrosion products through cracks

The above presented results show that the position of cathode and anode in the case 1B for the first specimen (ϕ12 / 20 mm) and in the case 2B for the second specimen (ϕ16 / 35 mm) gives the best agreement with the experimental results. Therefore, these two cases are chosen to study the effect of distribution of corrosion products through the cracks. For each specimen type, two cases are considered: (a) transport of rust is neglected and (b) transport is accounted for. Similarly as before, the beams are exposed, for each case, to the corrosion processes over the period of 7 years.

The damage (cracking) due to the expansion of corrosion products after 1, 3 and 7 years, respectively, for the type 1B is shown in Figure 5.18. The damage without the influence of the transport of rust is shown on the left, whereas the cracks produced when accounting for the distribution of rust are shown on the right hand side. The numerical results indicate a significant influence of the rust distribution on the corrosion-induced damage for the studied type of chloride-induced corrosion, with intermediate saturation. It reduces the damage and compared with the experience from the engineering practice (Thoft-Christensen 2000), there is a more realistic prediction of the first visible crack. For the type 1B, without and with transport of rust, the crack width of w = 0.05 mm is observed after 170 and 280 days, respectively. For the type 2B, the same crack width is observed after 300 and 540 days, respectively. The maximal crack widths and the average rust thickness around the investigated bar for type 1B are summarized in Table 5.5. The thickness of the rust is calculated as the sum of the average corrosion penetration x_{corr} and the inelastic radial expansion Δl_r.

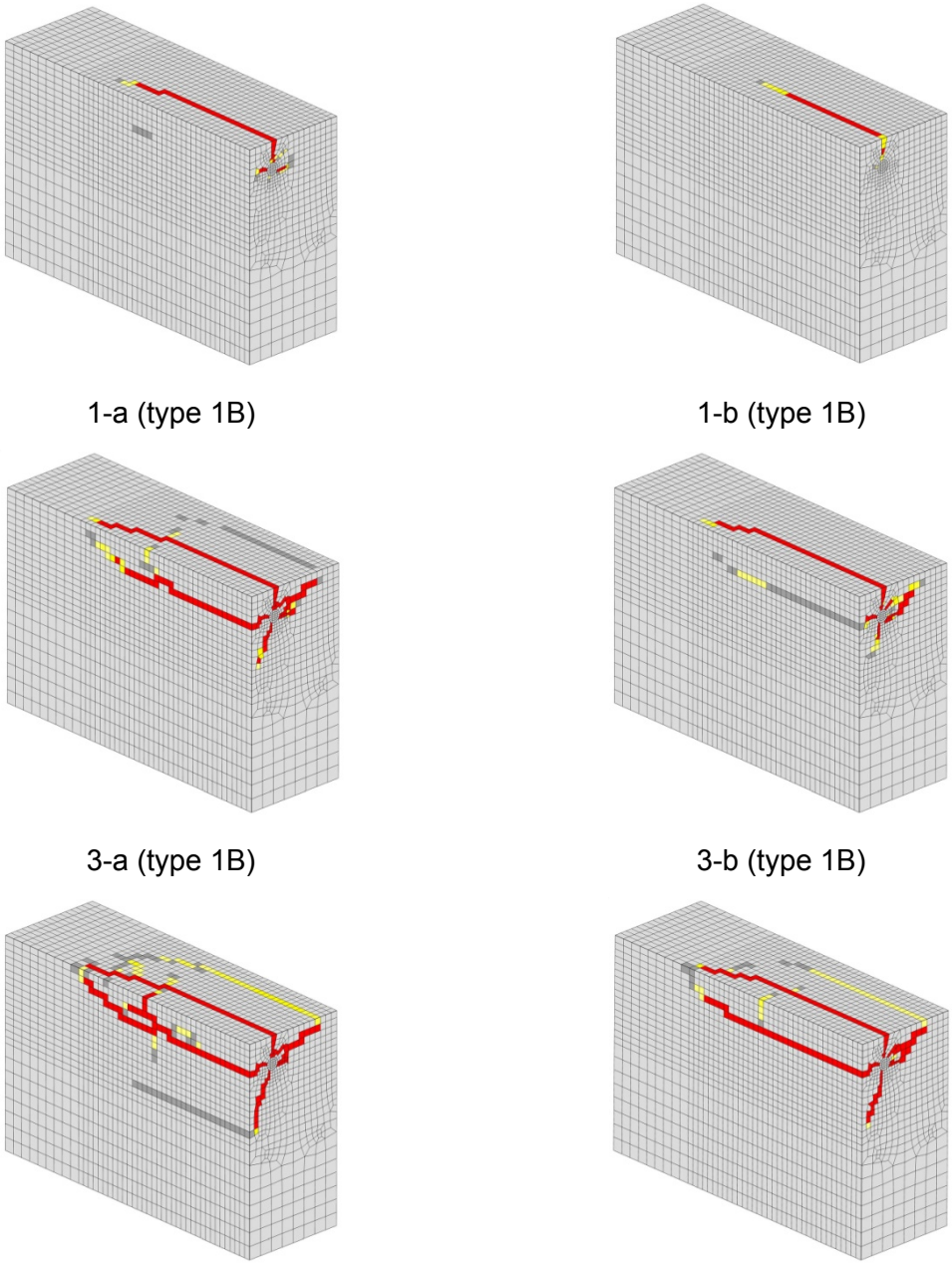

Figure 5.18 Predicted crack patterns due to corrosion induced damage, 1, 3 and 7 years after depassivation for: (a) without and (b) with accounting for the rust transport (b)

Similar crack patterns were obtained in the experiments (Fischer 2012), however, in the tests the corrosion was accelerated with the rate that was approximately 5 times higher than a nominal natural corrosion rate. Therefore, the development of corrosion-induced damage in time cannot be directly compared with the numerical analysis, in which the natural corrosion conditions are simulated.

Table 5.5. Thickness of the rust and maximum crack width for the type 1B

Time after depass. [year]	**Rust thickness *a* [mm]**				**Max. crack width [mm]**	
	WOT*		WT*		WOT	WT
	Aver.	Max.	Aver.	Max.		
1	0.11	0.26	0.06	0.13	0.24	0.09
2	0.23	0.52	0.11	0.25	0.53	0.28
3	0.34	0.78	0.17	0.38	0.73	0.45
4	0.46	1.04	0.23	0.52	0.91	0.60
5	0.58	1.30	0.28	0.66	1.10	0.72
7	0.82	1.84	0.40	0.92	1.46	0.94

*WOT= without transport of rust, WT= with transport of rust

To demonstrate the influence of corrosion products transport through cracks on bond resistance, the reinforcement bar is pulled out from the concrete specimens (type 1B and 2B) at t =0 (reference), 1, 2, 3, 4, 5 and 7 years, respectively. The predicted and experimentally measured (average) pull-out capacities and average crack widths are shown in Figure 5.19 as a function of the average corrosion penetration. Moreover, for the specimen type 1B (ϕ12 / 20 mm), the predicted and measured results are summarized in Table 5.6.

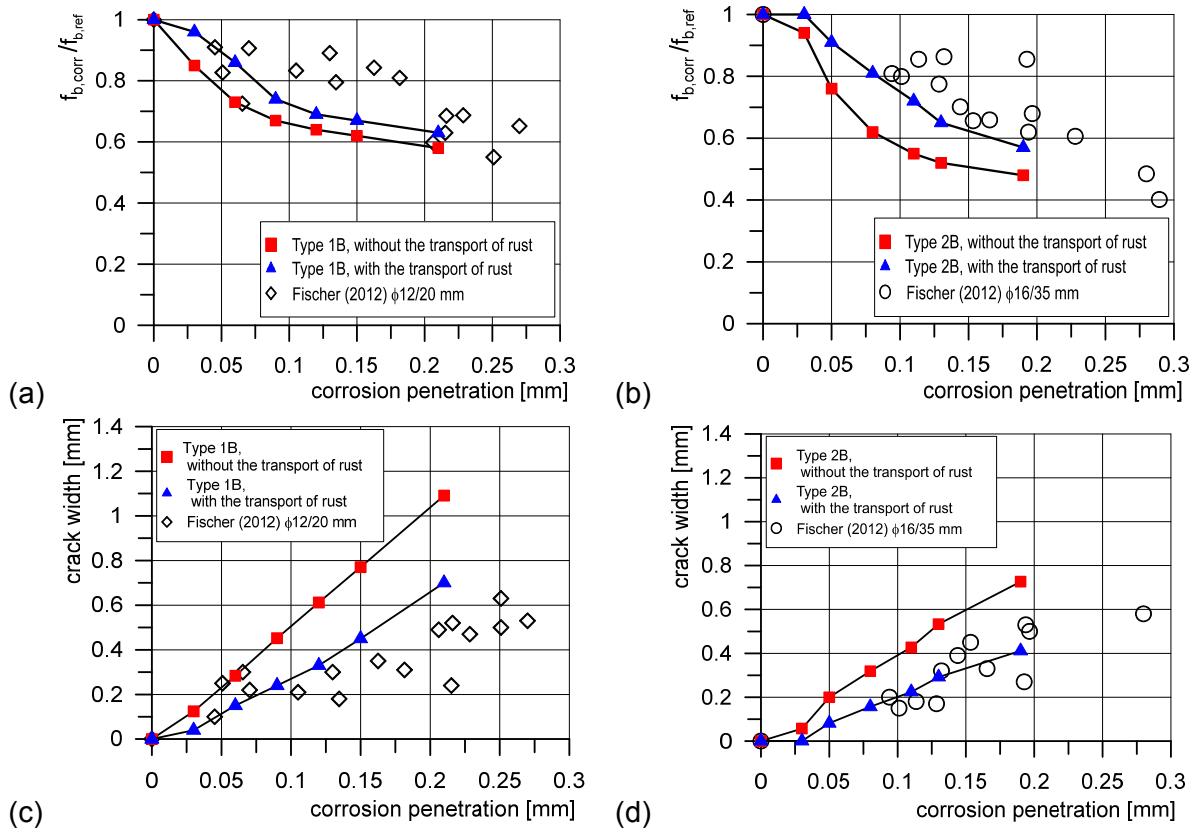

Figure 5.19 Predicted and measured results for specimen 1B and 2B: (a,b) The relative pull-out capacity as a function of the average corrosion penetration and (c,d) average crack width as a function of the average corrosion penetration

Table 5.6 Numerical and experimental results of the pull-out resistance for type 1B

Time after depass. [years]	**x_{corr} [mm]**	**Pull-out resistance [MPa]**			**Fischer 2012 ***	
		WOT	WT	Ref. model	x_{corr} [mm]	Pull.resistance [MPa]
0	-	-	-	6.22	-	6.29
1	0.03	5.29	5.98	-	0.045	5.70
2	0.06	4.54	4.98	-	0.070	5.72
3	0.09	4.17	4.60	-	0.105	5.24
4	0.12	3.98	4.42	-	0.135	5.00
5	0.15	3.86	4.18	-	0.182	5.09
7	0.21	3.67	4.04	-	0.210	4.10

*Time development cannot be directly compared with experiments in which the corrosion rate was accelerated approximately by factor of 5

In spite of the high complexity of the problem, it can be seen that the numerical prediction (for type 1B and 2B) in the case where the transport of corrosion products is accounted for, exhibits good agreement with the experimental data. Due to the larger crack widths (damage), the decrease of the pull-out capacity is higher if no transport of corrosion products is accounted for. As mentioned before, the numerical results encompassing the transport of rust through the cracks should be directly compared with the test data. Namely, in the experiments (Fischer 2012), a significant transport of rust through the cracks was observed, i.e. approximately 50% of generated rust was transported through cracks.

Finally, comparing the reduction of the pull-out capacity with respect to the average corrosion penetration for both specimen types (ϕ12 / 20 mm; ϕ16 / 35 mm), it can be seen that the experimental and numerical results confirm a higher reduction of the pull-out capacity in the case of a thicker concrete cover and a large bar diameter.

5.2 Single-rebar case with the influence of stirrups

Numerical results from the previous section show that the 3D chemo-hygro-thermo-mechanical model realistically predicts the corrosion induced damage in the case of concrete specimen with a single reinforcement bar. It is also important to investigate the application and robustness of the model for reinforced concrete elements with stirrups. By validating the numerical results with the experimental data for these cases, the model can be applied to investigate a wide spectrum of corrosion induced damage in RC structures.

5.2.1 Beam-end specimens with stirrups

5.2.1.1 Specimen geometry and test setup

In the beam-end experiments performed by Fischer (2012), described in the previous section, the specimens with stirrups were also investigated. The cross-sections of the concrete specimens and the position of the main rebars ϕ16 and ϕ12 correspond to the geometry without the stirrups (Section 5.1.2.1). The stirrups with the diameter ϕ6 mm were chosen with spacing of 90 mm (Figure 5.20). Two additional series were also studied, in which the direct electric contact with the main rebar was prevented by isolating the stirrup corners with tape. All investigated types of specimens with stirrups and their main characteristics are summarized in Table 5.7. Types 1 and 3 without stirrups, i.e. ϕ12/20 mm and ϕ16/35 mm respectively, are discussed in the previous section.

Table 5.7 Investigated specimen types with stirrups from the experiments by Fischer (2012)

Types	Diameter, d [mm]	Con. cover, c [mm]	c/d	Stirrups [mm]	Stirrup - el. contact
2	12	20	1.67	6/90	yes
4	16	35	2.19	6/90	yes
5	12	20	1.67	6/90	no
6	16	35	2.19	6/90	no

The specimens were exposed to the same aggressive conditions as mentioned in Section 5.1.2.1 and the corresponding pull-out capacity of the embedded reinforcement bars was subsequently investigated. Thus, these sets of experimental data offer a convenient tool not only for investigating the model ability to capture the influence of stirrups on the corrosion induced damage, but also for comparing the results with the ones presented in Section 5.1 (without stirrups).

In the following sections only the conditions from the series 5 and 6 are simulated, with the stirrups not being in the direct contact with the main reinforcement. This is

chosen to compare the results more easily with the ones from the previous section without the stirrups.

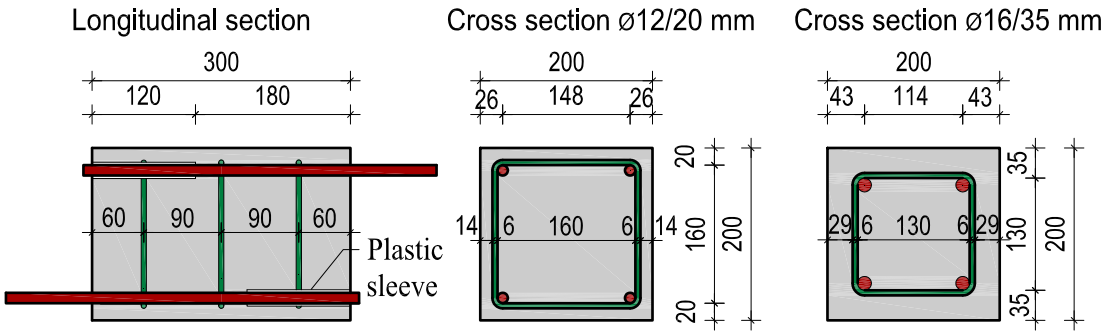

Figure 5.20 Geometry of the specimen with stirrups used in experiments by Fischer (2012)

5.2.1.2 Numerical model

Symmetry conditions are used to model only half of the specimen for the types 5 and 6. Similarly as in Section 5.1.2.2, the width of the modelled section for the type 6 is taken 10 mm wider than the symmetry plane to accommodate for a bigger bar diameter and a deeper concrete cover while analyzing the pull-out resistance (Figure 5.21a). Eight node solid elements are used to model the main reinforcement bar and the stirrups (Figure 5.21b). To avoid a contact problem between the main rebar and stirrups, their position is offset 2 mm towards the upper and side concrete surfaces. The 0.1 mm thick interface layer is placed around the steel reinforcement and modelled with eight node solid elements. Corresponding 1D corrosion contact elements are placed in the interface layer. Due to the presence of the curved stirrup geometry, the concrete is discretized by using the tetrahedral solid elements.

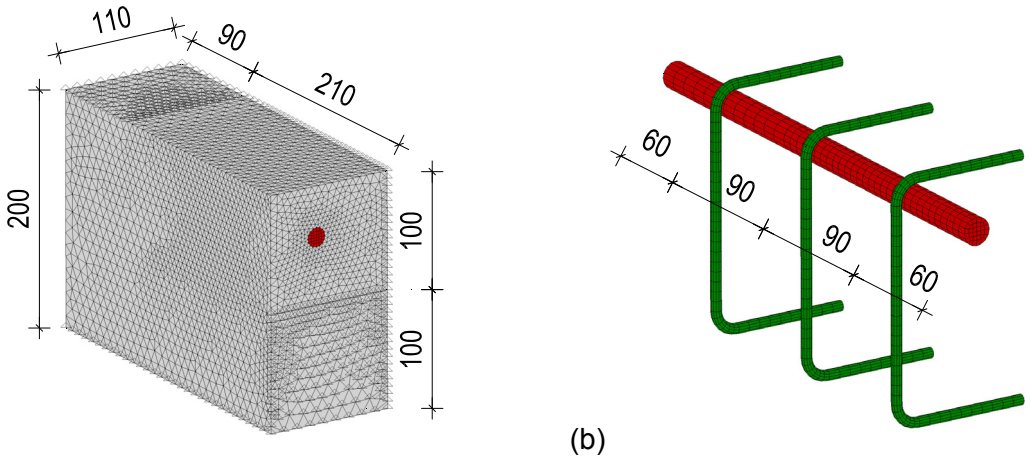

(a) (b)

Figure 5.21 Model geometry (in mm) with the finite element discretization of the specimen-type 6 (a) and the used main rebar and stirrups (b)

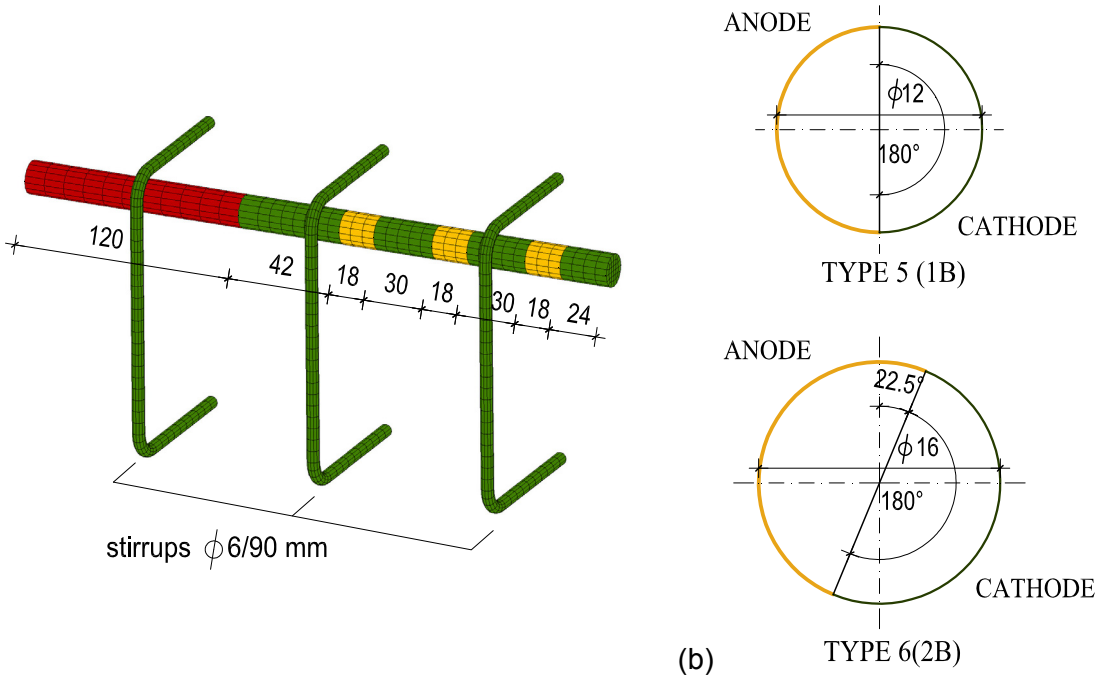

Figure 5.22 Distribution of the anodic and cathodic regions along the rebar and stirrups (a) and over the rebar's circumference for types 5 and 6 (b)

The same distribution of the anodic and cathodic regions along the rebar length is taken from the Section 5.1.2.2 (Figure 5.22a). The results from Section 5.1.2.3 show that the type 1B and 2B configurations for ϕ12/20 mm and ϕ16/35 mm, respectively, give the most realistic crack patterns compared to the ones from the experiment (Fischer 2012). Hence, the same anodic-cathodic distribution in the rebar's cross section is chosen (Figure 5.22b) for type 5 and type 6, respectively. The anodic-cathodic regions are kept unchanged.

Due to the stirrups being electrically isolated from the rebar in the experiment (Fischer 2012), it is assumed that the whole stirrup area is acting as a cathode. Type 2 and 4 specimens, where the electrical contact was enabled, show similar results regarding the corrosion induced damage and the behaviour of the pull-out capacity as compared to type 5 and 6 (Fischer 2012).

The steel stirrups are modelled as linear elastic material with the Young's Modulus of 200000 N/mm^2 and Poisson's ratio of 0.33. Further mechanical and electrochemical parameters used in the analysis are the same as mentioned in Section 5.1.2.2. Likewise, the boundary and initial conditions correspond to the conditions defined in the Section 5.1.2.2 for the specimens ϕ12/20 mm and ϕ16/35 mm, without the stirrups.

The importance of modelling the distribution of corrosion products into the pores and cracks is shown in Section 5.1.2.6. Therefore the transport of rust is accounted for in the following numerical simulations.

In the numerical analysis the specimen types 5 and 6 are exposed to natural corrosion conditions over 7 years. Subsequently, for different levels of corrosion induced damage, i.e. after 1, 2, 3, 4, 5 and 7 years of active corrosion, the pull-out capacity of the rebar is calculated.

5.2.1.3 Numerically predicted corrosion induced damage

As mentioned in the previous section, the corrosion induced damage is simulated for a period of 7 years. The numerically obtained crack patterns for the specimen type 6 after 2, 3, 5 and 7 years of active corrosion processes are shown in Figure 5.23.

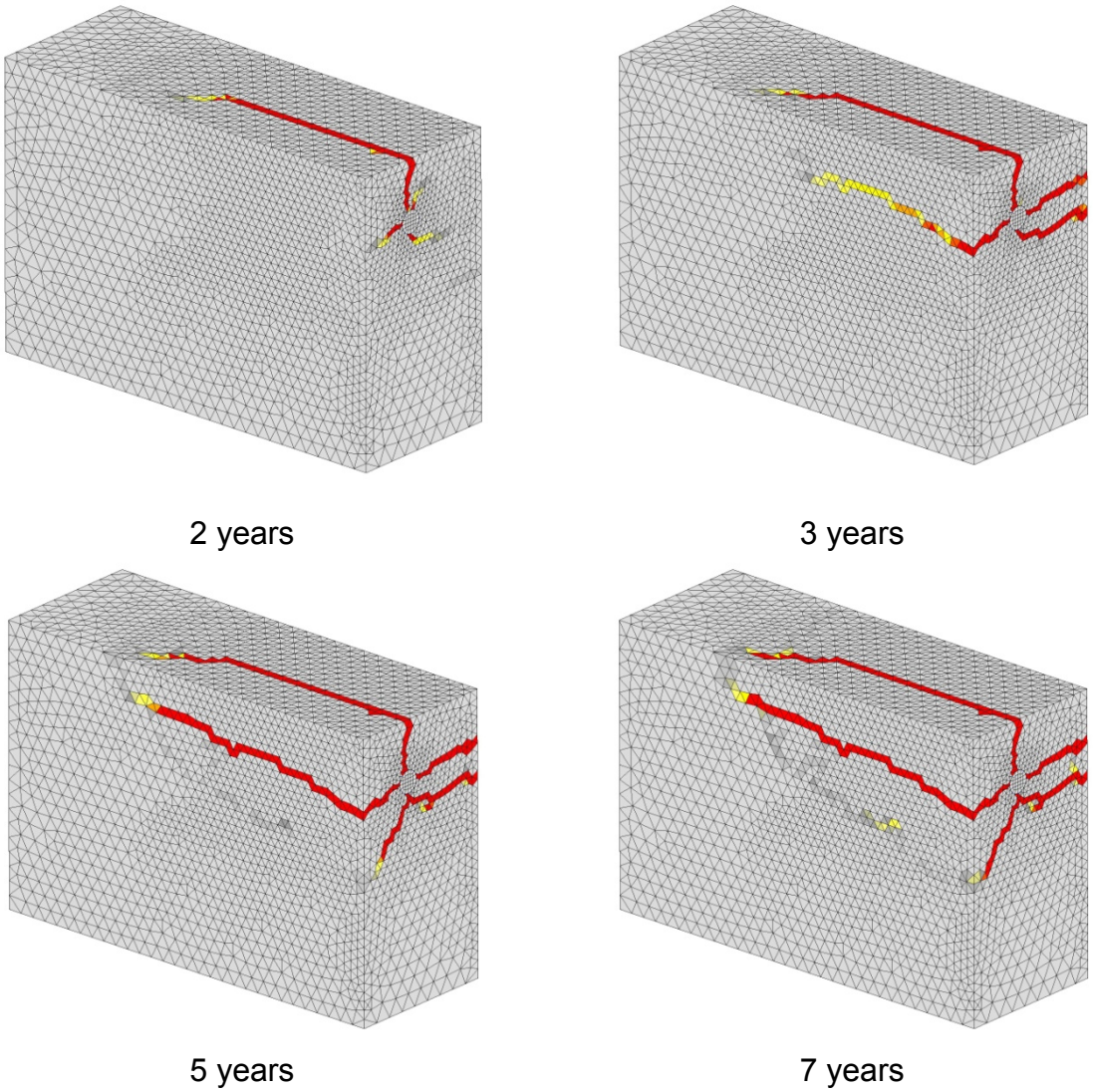

Figure 5.23 Numerically predicted crack patterns for the specimen type 6 after 2, 3, 5 and 7 years of active corrosion processes

To validate the numerical results, sum of average crack widths on the upper and side concrete surface is plotted as a function of the average corrosion penetration on the anodic-cathodic transition zone, for the specimen type 5 and 6. These results are then compared with the experimental data and presented in Figure 5.24. It can be

seen that for both cases a good agreement is obtained with the experimental data (Fischer 2012), showing that the corrosion induced damage (cracks) are developing realistically with the active corrosion process.

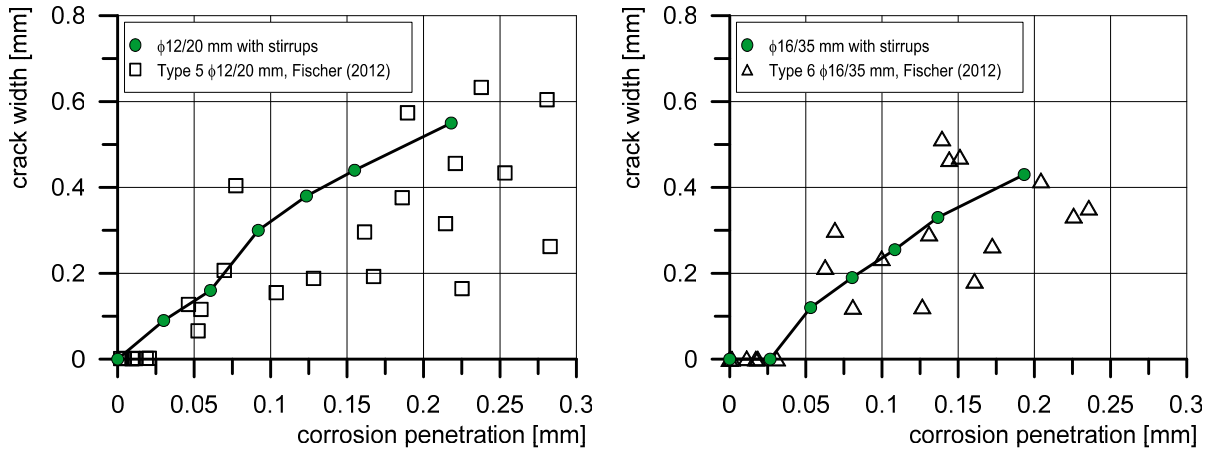

Figure 5.24 Sum of average crack widths on the concrete surfaces as a function of the average corrosion penetration for the type 5 (left) and type 6 (right)

5.2.1.4 Numerical analysis of the pull-out capacity for different corrosion levels

For each level of corrosion induced damage, i.e. 1, 2, 3, 4, 5 and 7 years after the depassivation, the corresponding pull-out capacity is calculated. The pull-out failure mode for different levels of corrosion damage for the specimen type 6 is shown in Figure 5.25. Experimentally obtained failure mode (Fischer 2012) due to the cracking of the concrete cover is replicated by the numerical results .

To validate the influence of the corrosion damage level on the corresponding pull-out capacity of the rebar, the relative values of the bond resistance are plotted in Figure 5.26 as a function of the average corrosion penetration of the rebar, x_{corr}. Comparison with the experimental results shows that in the case of the specimen type 6 (ϕ16/35 mm with stirrups), the same trend of a slowly decreasing pull-out capacity is realistically captured by the model (Figure 5.26b).

In the case of the specimen type 5 (ϕ12/20 mm with stirrups), the model is not able to simulate a slight increase of the bond resistance with the ongoing corrosion (Figure 5.26a), although the predicted decrease is relatively low and kept constant after reaching the relative value of 0.93 of the reference pull-out resistance (without corrosion).

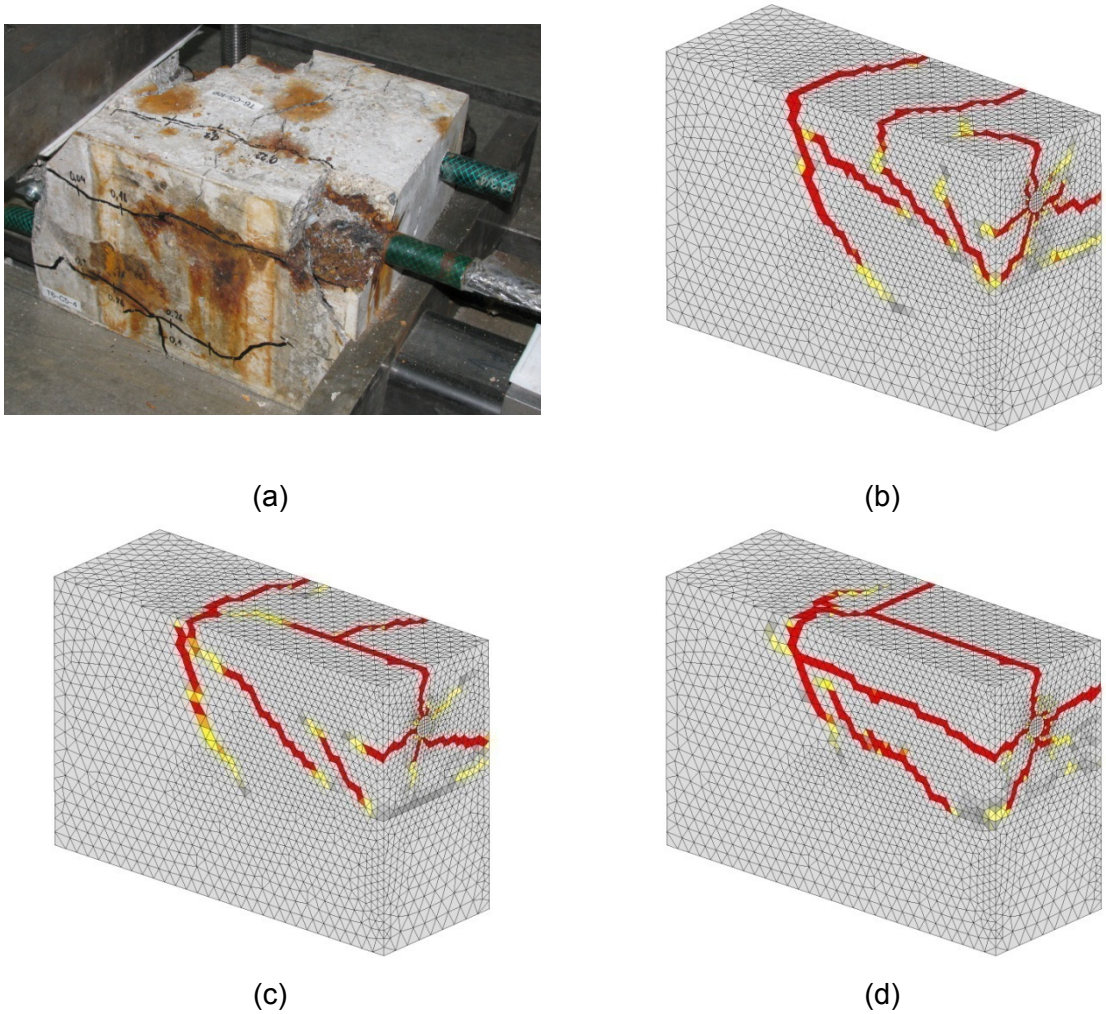

(a) (b)

(c) (d)

Figure 5.25 Pull-out failure mode obtained for the specimen type 6: (a) Fischer (2012), corresponds approximately to t = 7 years of the analysis (b) analysis (reference) t =0; (c) analysis, t = 2 years and (d) analysis, t = 7 years

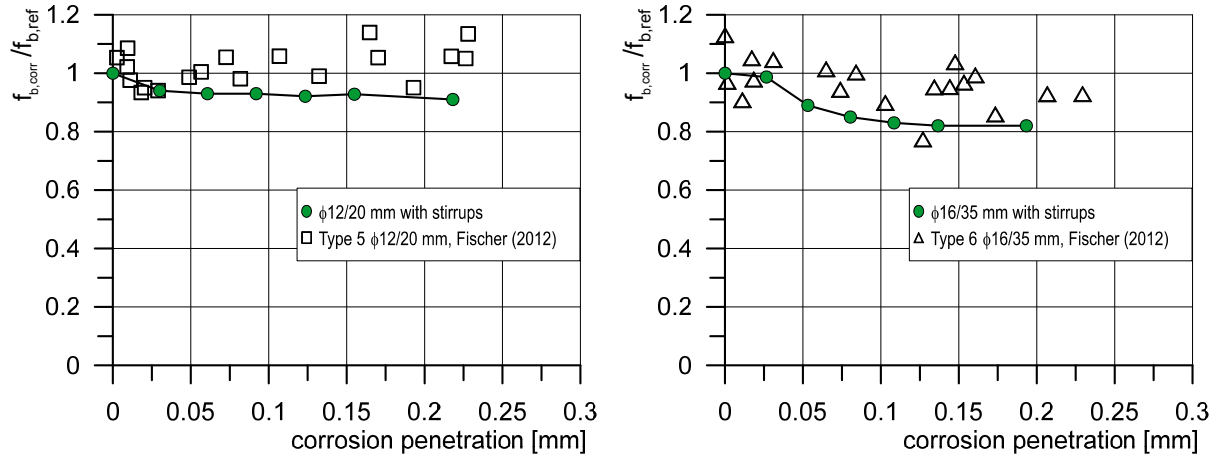

(a) (b)

Figure 5.26 Predicted and measured values of the relative pull-out capacity as a function of the average corrosion penetration of the rebar, for the specimen type 5 (a) and type 6(b)

The relative values of the pull-out capacity are also plotted as a function of the corresponding sum of average crack widths on the upper and side concrete surfaces. The average crack widths are calculated for each level of corrosion induced damage, i.e. from 1 to 7 years after depassivation. The predicted values are compared with the experimentally obtained data (Fischer 2012) in Figure 5.27. It can be seen that in the case of a larger concrete cover and larger bar diameter (Type 6) the predicted decrease of bond resistance is realistically following the slight decrease of the pull-out capacity (Figure 5.27b). In the case of a smaller bar diameter and concrete cover (Type 5), the minor relative increase of the pull-out force is not obtained (Figure 5.27a). Nonetheless, the decrease is relatively small at the beginning of the active corrosion process, i.e. with the onset of the visible corrosion induced damage (cracks) and is afterwards following a relatively constant trend line, same as in the experiments .

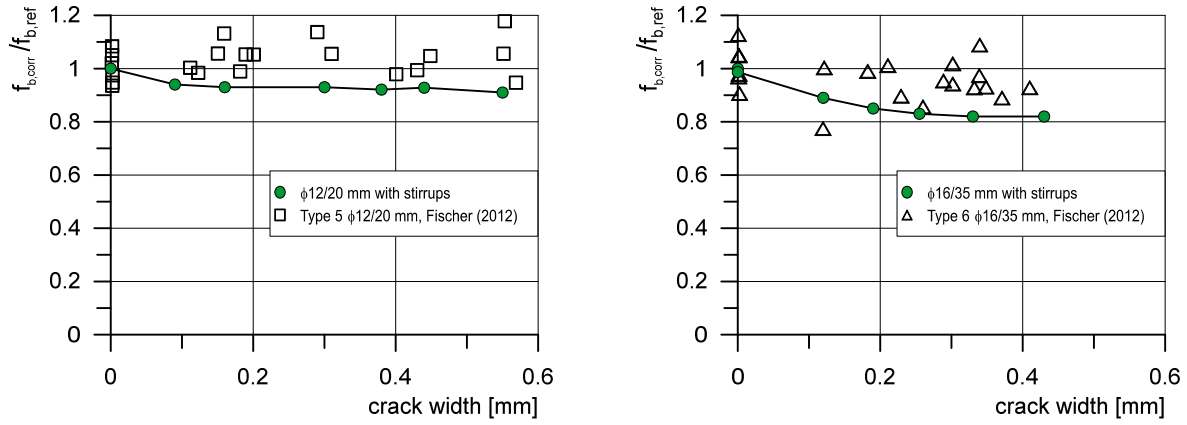

(a) (b)

Figure 5.27 Predicted and measured values of the relative pull-out capacity as a function of the average crack widths for the specimen type 5 (a) and type 6 (b)

5.2.1.5 Comparison of numerical results for the specimens with and without stirrups

Experimental data and numerical analysis show a significant influence of stirrups on the pull-capacity of rebars in the case of beam-end specimen due to corrosion induced damage. The numerically predicted results in the previous section and in section 5.1.2.5, show that the model is able to realistically capture the trend regarding the bond resistance with the ongoing corrosion process. To investigate the effect of stirrups, the relative pull-out capacity is plotted as a function of time (1, 2, 3, 4, 5 and 7 years) for specimen types ϕ12/20 mm and ϕ16/35 mm, with and without stirrups (Figure 5.28). It can be seen that with time, i.e. with the progressing corrosion damage, the relative bond resistance is decreasing much moderately for specimens with stirrups. After reaching a certain level of corrosion, the rebar is exhibiting approximately constant value of pull-capacity for specimen types 5 and 6, i.e. ϕ12/20 mm and ϕ16/35 mm with stirrups, respectively.

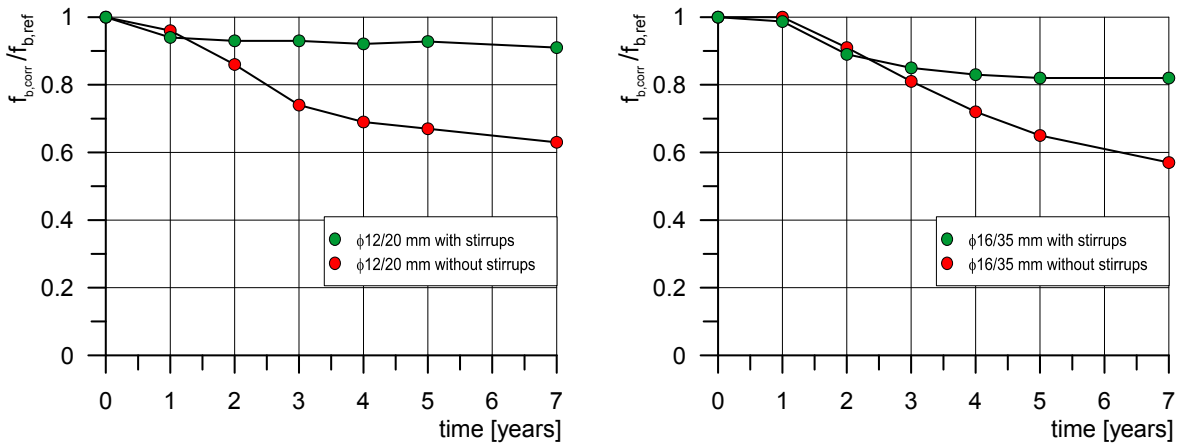

Figure 5.28 Relative pull-out capacity as a function of time (years) for specimens ϕ12/20 mm (left) and ϕ16/35 mm (right), with and without stirrups

To demonstrate the influence of the stirrups on corrosion induced crack patterns and crack widths, the damage after 1, 3 and 7 years is shown in Figure 5.29 for specimen ϕ12/20 mm, without (Type 1B - left column) and with stirrups (Type 5 - right column). Correspondingly, experimental and numerical average crack widths as a function of average corrosion penetration of the main rebar are given for all investigated specimens in Figure 5.30. It can be concluded, that for smaller levels of corrosion induced damage and for the assumed anodic-cathodic positions along the bar, the crack widths and crack patterns for the stirrup cases differ only slightly compared to the specimens where the stirrups are not present. Nonetheless, the experimental data by Fischer (2012) showed that the difference becomes more pronounced for higher levels of corrosion penetration, i.e. the crack widths for cases with stirrups were smaller compared to the cases where the shear reinforcement was not present.

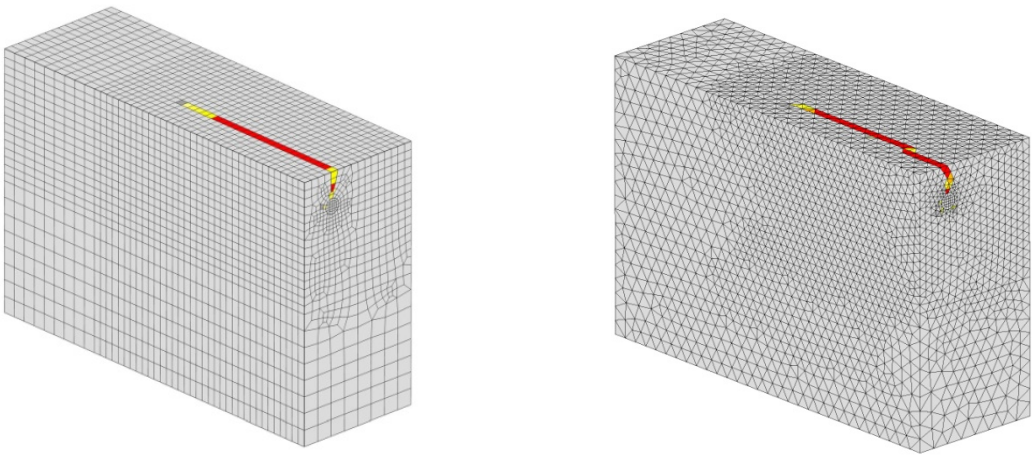

1-a (type 1B) 1-b (type 5)

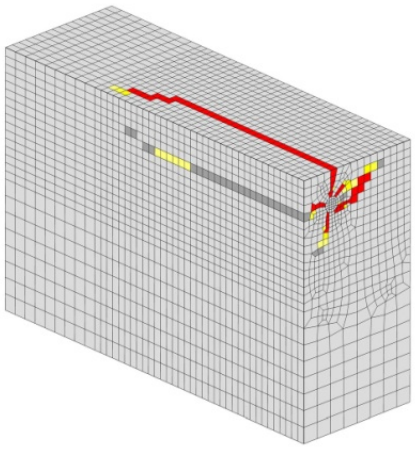

3-a (type 1B)

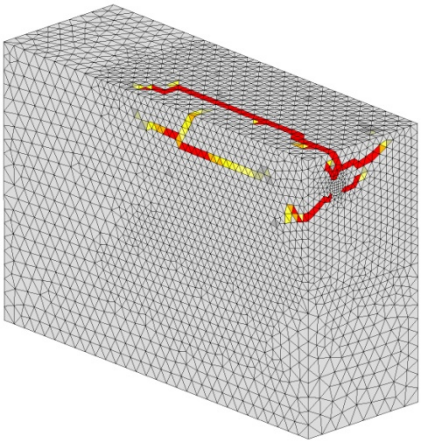

3-b (type 5)

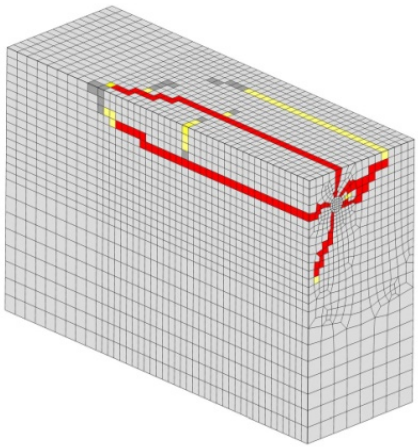

7-a (type 1B)

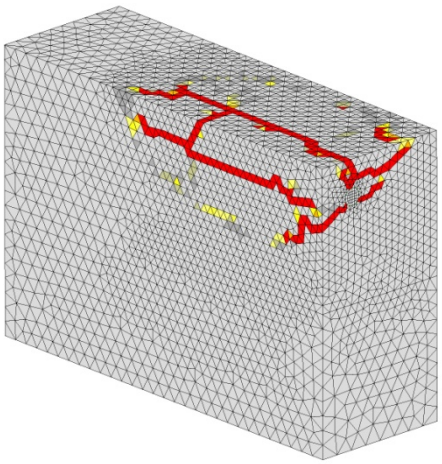

7-b (type 5)

Figure 5.29 Predicted crack patterns due to corrosion induced damage, 1, 3 and 7 years after depassivation for: (a) without (Type 1B) and (b) with stirrups (Type 5)

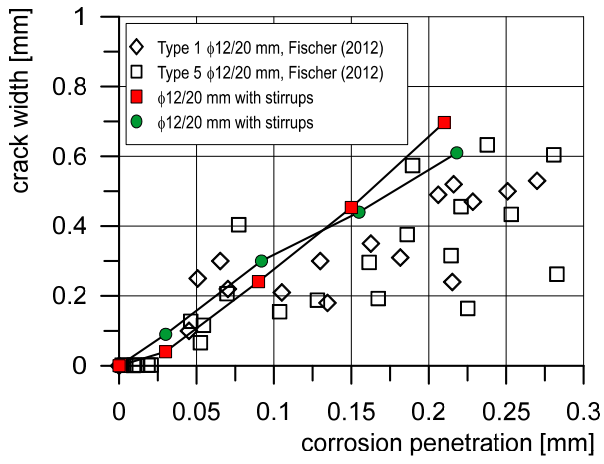

(a)

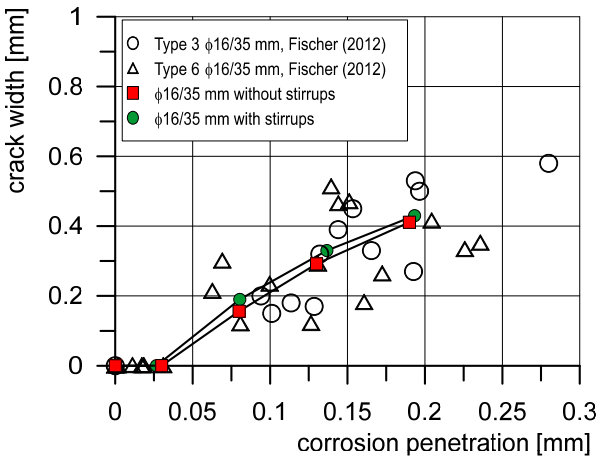

(b)

Figure 5.30 Predicted and measured values of the average crack width as a function of the average corrosion penetration for the specimens ϕ12/20 mm, with and without stirrups (a) and for the specimens ϕ16/35 mm, with and without stirrups (b)

Furthermore, the average values of the principle tensile stresses for the stirrup section, shown in Figure 5.31a, are monitored for types 5 and 6. Two cases are considered for each specimen: the average principle tensile stress calculated after a certain period (1, 2 ,3 ,4, 5 and 7 years) of active corrosion and the corresponding principle tensile stress obtained when the maximum bond capacity is reached in the subsequent pull-out of the main rebar. The results are shown in Figure 5.32 as relative values to the average principle tensile stress for the reference pull-out case (no corrosion damage), $\sigma_{11,ref}$.

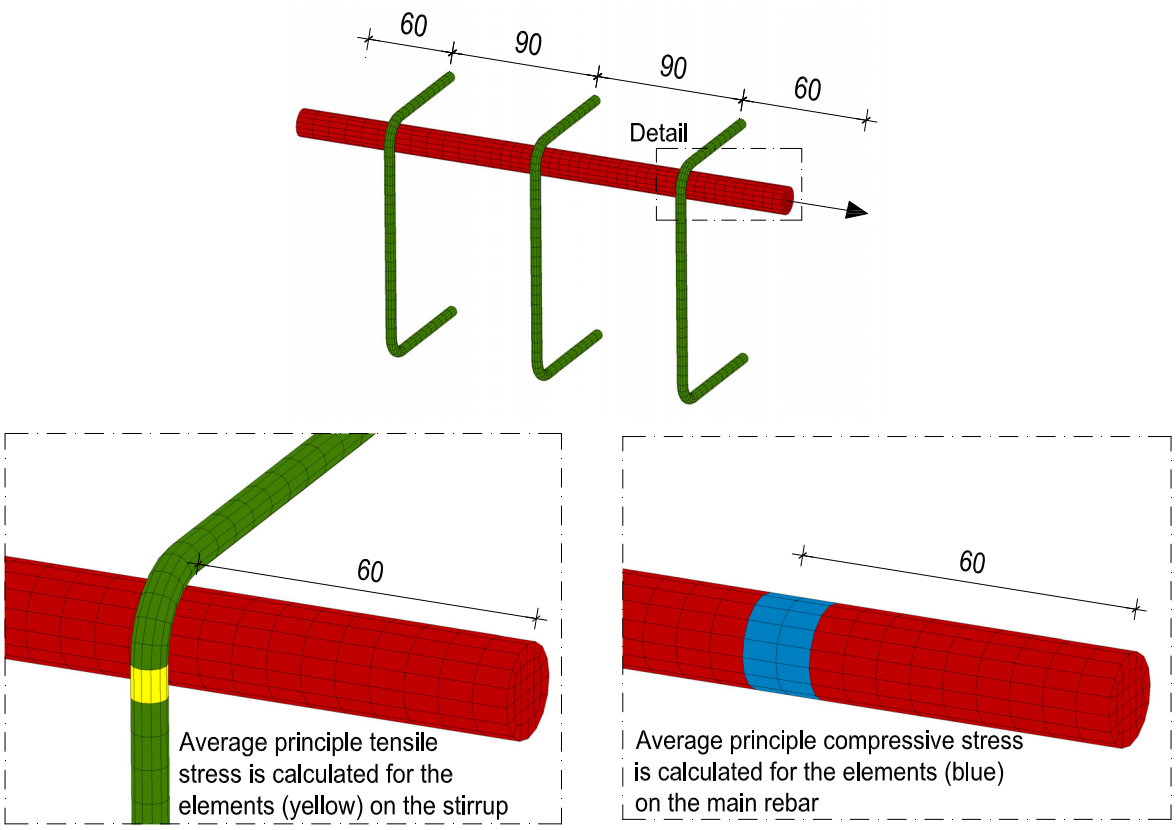

Figure 5.31 (a) Detail of the stirrup's elements (yellow) used to calculate the average values of the principle tensile stresses; (b) Detail of the rebar's elements (blue) used to calculate the average values of the principle compressive stresses

It can be seen that for the specimen type 5 (ϕ12/20 mm), the expansion of the corrosion products around the reinforcement bar activates the tensile stresses in the stirrup, which imposes confined conditions on the main rebar. Therefore, with the pull-out of the rebar the principle tensile stress in the investigated section at the peak load continuously rises and reaches almost 2,5 higher value after 7 years (Figure 5.32a). Due to a smaller bar and a smaller concrete cover, the confined conditions are already reached after 1 year of active corrosion and the relative bond resistance is afterwards kept approximately constant (Figure 5.26a). On the other hand, in the case of the larger bar diameter and concrete cover, i.e. in the case of type 6 (ϕ16/35 mm) the confined conditions are reached 3 years after the start of corrosion. This is clearly seen from the Figure 5.32b with a sudden jump of the principle tensile stress at the

peak load. Further on, this also explains a relatively larger decrease of the pull-out capacity at lower levels of corrosion induced damage for the specimen type 6 (Figure 5.26b) compared to type 5.

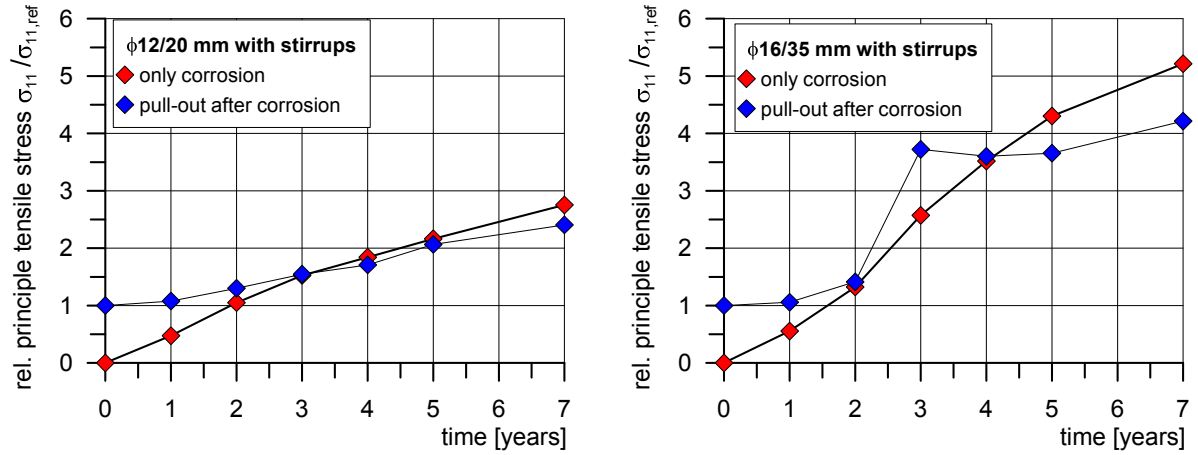

(a) (b)

Figure 5.32 Relative average principle tensile stresses in a stirrup section (during corrosion and after reaching a peak load during the pull-out of the rebar) plotted as a function of time for type 5 (a) and type 6 (b)

To illustrate the effect of stirrups with the ongoing expansion of the corrosion products, the average values of the principle compressive stresses in the rebar cross section, located under the stirrup for type 5 and in the corresponding position on the bar for type 1B (Figure 5.31b), are plotted in Figure 5.33 as a function of time. The values are numerically obtained after 1-7 years of active corrosion processes, before calculating the bond resistance. It can be seen that in both cases (with and without stirrups), the compressive forces are exerted on the rebar due to the expansion of corrosion products. In the case where the stirrups are present, confined conditions contribute to higher compressive stresses which have a positive effect of minimizing the reduction of the pull-out capacity with the ongoing corrosion damage.

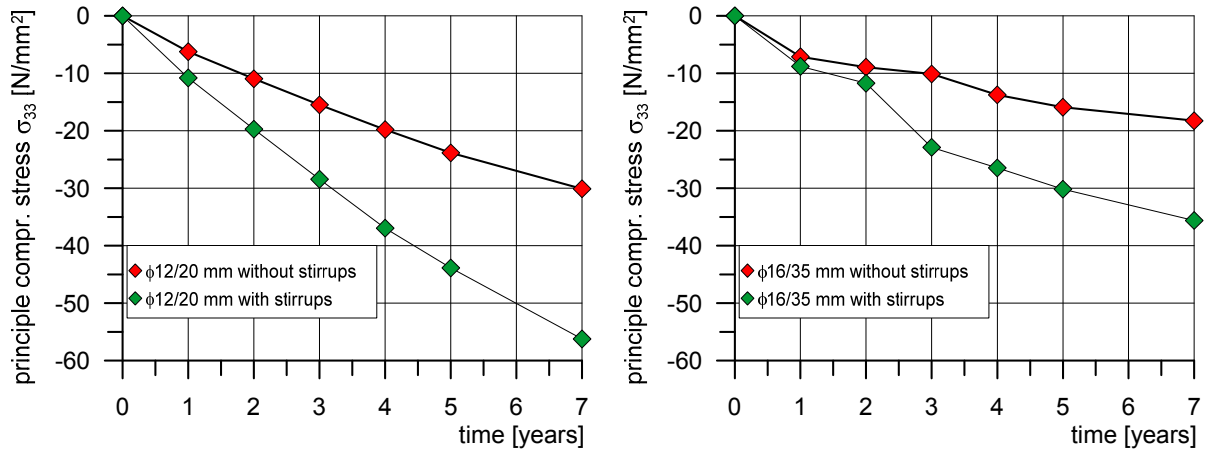

(a) (b)

Figure 5.33 Average values of the principle compressive stresses in the rebar cross-section (with and without stirrups) as a function of time for type ϕ12/20 mm (a) and ϕ16/35 mm (b)

In the case of the specimen ϕ16/35 mm with stirrups (type 6), the principle compressive stress is slowly increasing for a period between the first and the second year and then has a sudden increase after 3 years of active corrosion. From Figure 5.23 and 5.34a it can be concluded that the slower increase is contributed to the opening of the crack towards the upper surface for the period up to 2 years of active corrosion, which subsequently leads to a decrease of pressure with the corrosion products being transported into the opening crack. This is can also be observed by plotting the radial pressure on the surrounding concrete (Figure 5.34b). at the anode-cathode transition zone, 138 mm from the pull-out surface.

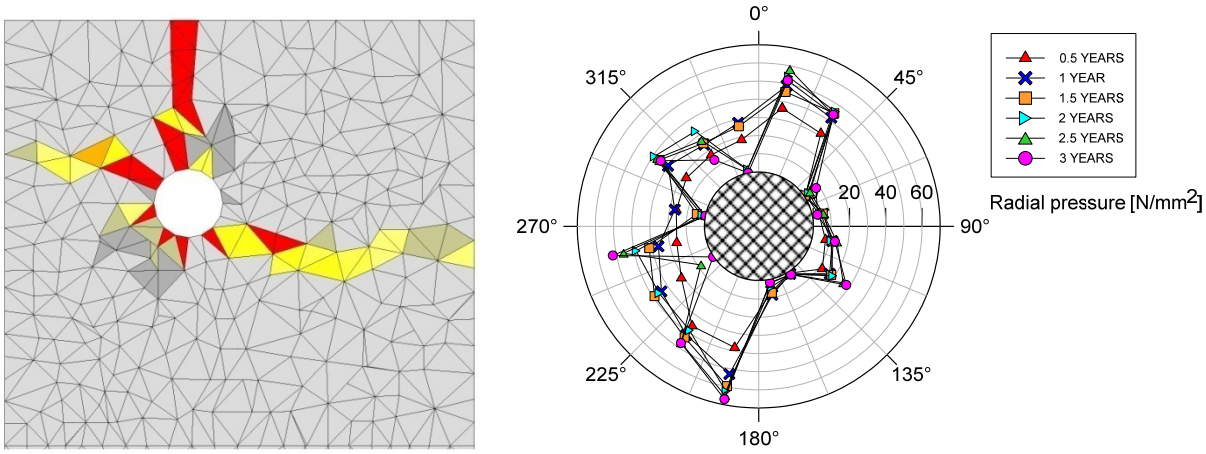

(a) (b)

Figure 5.34 Predicted crack pattern after 2 years (a) and the corresponding distribution of the radial pressure up to 3 years of active corrosion (b) for a cross section at the anode-cathode transition zone, 138 mm from the pull-out surface

5.3 Conclusions

The application of the developed 3D chemo-hygro-thermo-mechanical model for simulating corrosion induced damage in concrete specimens with a single embedded rebar is investigated. In the first part of the analysis, the qualitative validation of the model is shown on a simple reinforced concrete beam-end specimen. The inelastic strains of the implemented 1D corrosion contact elements, which correspond to the expansion of rust around the rebar, cause the cracking of the surrounding concrete. It is shown that the radial distribution of pressure is not symmetrically distributed over the depassivated surface. Moreover, the transport of rust into the cracks reduces the pressure on the surrounding concrete.

To further quantitatively verify and calibrate the 3D CHTM model, the experiments on the beam-end specimens by (Fischer 2012) are analysed. The cases without and with stirrups are studied and the effect of the shear reinforcement on the corrosion damage is investigated. The specimens are first exposed to aggressive environmental conditions and subsequently, the pull-out capacity of the rebar is predicted for different levels of corrosion.

The numerical results of the beam-end specimens (ϕ12/20 mm and ϕ16/35 mm) without stirrups yields the following conclusions:

For the assumed environmental conditions and material properties, the predicted corrosion-induced crack pattern depends on the geometry (bar diameter and concrete cover), position of anode and cathode, and on the transport of corrosion products through cracks.

The comparison with experimental results shows that the most realistic crack pattern is obtained for the case where the half of the bar surface, which is closer to the free concrete surface, is assumed to be the anode.

It is shown that the corrosion-induced radial pressure over the circumference of the reinforcement bar is not axial-symmetric. The highest pressure is observed in radial directions that coincide with the directions of crack propagation.

Active corrosion phase and consequently, the corrosion-induced damage, have a strong influence on the distribution of oxygen in the concrete specimen. The consumption of oxygen reaches a maximum at anode-cathode transition zones soon after depassivation of the reinforcement. However with the onset of corrosion-induced damage, the flow of oxygen rises in generated cracks causing an increase of the oxygen concentration along the reinforcement bar.

The numerical results show a very good agreement with experimental tests in which, for the assumed environmental conditions, approximately 50 % of corrosion products

were transported into the cracks. Due to the fact that a relatively large amount of corrosion products is distributed over the cracks, the corrosion-induced damage is less pronounced in the case when the transport of rust is accounted for.

The pull-out failure is due to the failure of concrete cover (splitting) and not to the pull-out of the bar from the concrete. As the results of numerical analysis show, corrosion-induced damage significantly reduces the pull-out capacity. The reduction is higher if the transport of rust through cracks is not accounted for. The predicted and experimentally measured pull-out capacity show a good agreement.

The numerical analysis of the beam-end specimens reinforced with stirrups shows that the model is capable to predict the corrosion induced damage for these cases. The increase of the average crack width with the ongoing corrosion penetration of the rebar is verified by comparing the results with the experimental data.

The model is able to realistically account for the influence of stirrups on the bond resistance for the ongoing corrosion damage. It is shown that the expansion of the corrosion products around the rebar activates the tensile forces in the stirrups. Therefore, the additional confinement through the stirrups minimizes the reduction of the pull-out capacity. By comparing the two investigated cases (ϕ12/20 mm and ϕ16/35 mm), it can be concluded that, for the constant stirrup diameter, the effect of the confinement conditions depends on the depth of the concrete cover and the size of the rebar. For a smaller cover and a smaller bar diameter, the confinement effect is reached sooner with the ongoing corrosion process and hence a lower decrease of the pull-capacity is obtained.

6 VALIDATION OF THE 3D CHTM MODEL: MULTI-REBAR CASE

Previous section shows a good agreement of the predicted corrosion induced damage using the 3D CHTM model with the experimental results. However, only one main reinforcement bar (without and with stirrups) was exposed to aggressive environmental conditions. For the engineering practice it is also important to verify the ability of the model to simulate the corrosion induced damage in the case of rebars placed close to each other, i.e. for the multi-rebar case. Numerical simulation for a group of reinforcement bars is a challenging task not only for simulating electrochemical processes, but for capturing specific crack patterns leading to delamination of the concrete cover. Moreover, the presence of stirrups in the case of the multi-rebar corrosion has a significant effect on the development of damage and needs to be taken into account.

The application of the 3D chemo-hygro-thermo-mechanical model is verified for the multi-rebar cases with and without stirrups and the results are presented in the following sections. Same as in the previous section, the water content is assumed to be uniformly distributed and constant in the investigated specimens. Hence, the hysteretic moisture behaviour of concrete is not taken into account.

6.1 Multi-rebar case without the influence of stirrups

6.1.1 Experimental setup

The main objective of the experiments performed by Dong et al. (2011) was to investigate the influence of stirrups spacing and anchorage performance on residual strength of corroded RC beam. Simultaneously, a reference series without the arranged stirrups across the beam length was also investigated. Specimens were firstly exposed to accelerated corrosion conditions. Subsequently, they were tested under four-point static bending test and the residual load capacity was measured.

The experiments present a valuable source for validating the numerical results for multi-rebar case and also for comparing the effect of stirrups on the corrosion induced damage. To verify the 3D CHTM model ability to simulate the corrosion induced damage for such cases, only the corrosion induced damage, i.e. the generated crack patterns from the experiments are compared with the numerical results.

The investigated specimens (Dong et al. 2011) were rectangular beams, marked as the series S0. The beams were 2100 mm long, with the cross-section size of 240x200 mm (Figure 6.1). Three rebars with the diameter of 16 mm were arranged 40 mm from the lower part of the beam in 60 mm spacing. The concrete cover was

32 mm for all three rebars, while the outer bars had a cover of 52 mm measured from the side surfaces (Figure 6.1b).

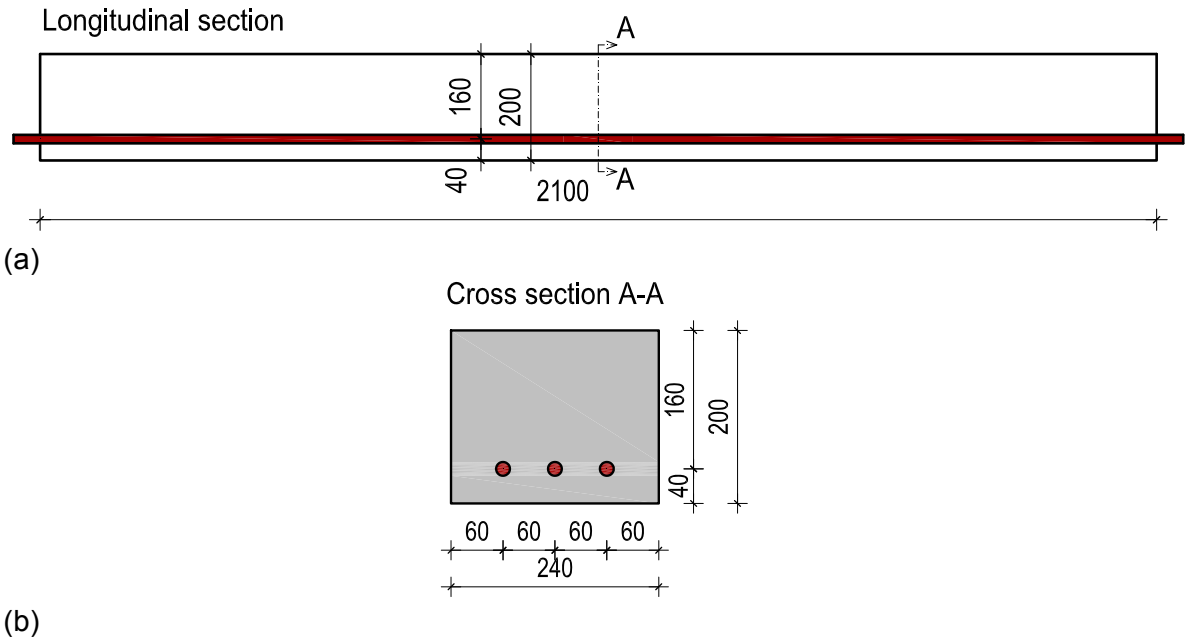

Figure 6.1 Longitudinal section (a) and cross section (b) of the investigated beams from the series S0 without stirrups (Dong et al. 2011)

Five percent sodium chloride solution was added to the concrete mixture, which acted as a corrosion catalyst, i.e. it increased the electrical conductivity of concrete. To achieve damage due to expansion of corrosion of rust products in a reasonable time period, the beams were exposed to accelerated corrosion conditions and the galvanic corrosion testing method was used (Murakami et al. 2006).

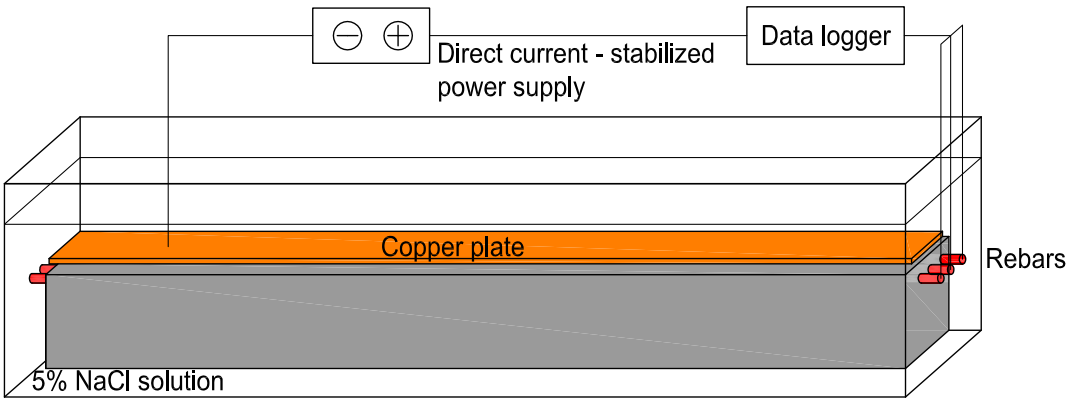

Figure 6.2 Accelerated corrosion test used by Dong et al. (2011)

The beams were placed in a water tank filled with 5% sodium chloride solution. The rebars were connected in an electrical circuit with a copper plate placed on the concrete surface near the bars (Figure 6.2). The direct current flowed through the circuit until a given amount of electricity was achieved, representing an expected corrosion ratio.

6.1.2 Numerical model and input parameters

To simulate the corrosion induced damage only a segment of 130 mm length of the beam is modelled (Figure 6.3a). Note that the here presented model simulates the natural corrosion conditions. Therefore, the actual experimental development of damage under accelerated corrosion cannot be directly compared with the simulated results in time.

The eight node solid elements are used to model the concrete, steel reinforcement and the interface layer. The 1D corrosion contact elements are radially placed in the interface layer with the thickness of 0.1 mm. Reinforcement bar circumference is discretized with 16 nodes, i.e. 16 corrosion contact elements are defined in each cross-section of the rebar.

The emphasis of the analysis is on the processes after depassivation of steel, therefore distribution of cathodic and anodic regions along the bar length and the circumference are assumed upfront. The processes before depassivation of steel are not simulated in this case, but their application is explained and verified in Ožbolt et al. (2010). Two anodic regions of 20 mm length each are defined along the reinforcement bar with the surrounding three cathodic regions, 30 mm each (Figure 6.3b).

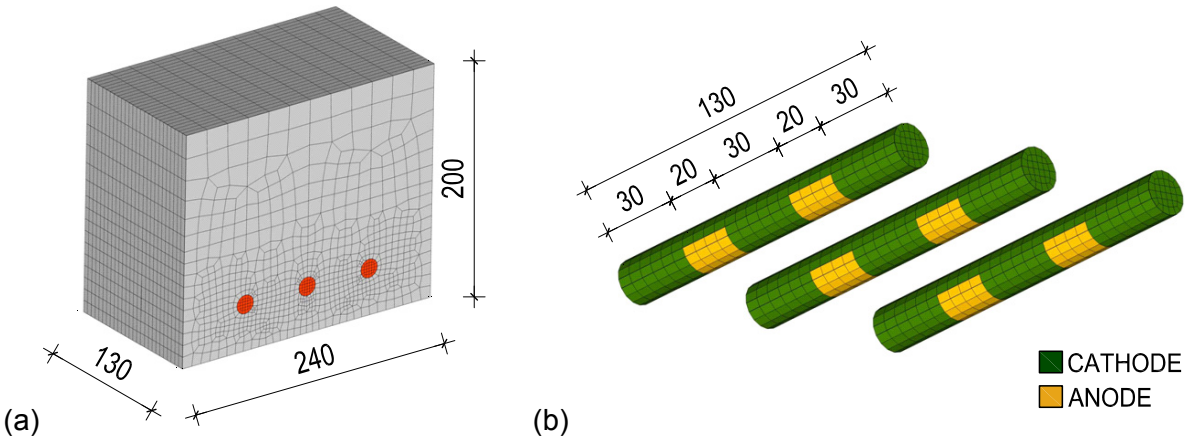

Figure 6.3 Model geometry (a) and the assumed distribution of the anodic and cathodic region along the rebar length (b), (all in mm)

The results from subsection 5.1.2.3 demonstrated a significant effect of the anodic-cathodic distribution along the bar circumference in the case of a single rebar. Therefore, to analyse this influence in the case of the multi-rebar specimen, three configurations are investigated. For the case A, it is assumed that a quarter of the circumference is depassivated in respect to the vertical axis of symmetry. The case B has a larger anodic surface corresponding to an angle of 135°, while for the case C half of the circumference is assumed as anode (Figure 6.4).

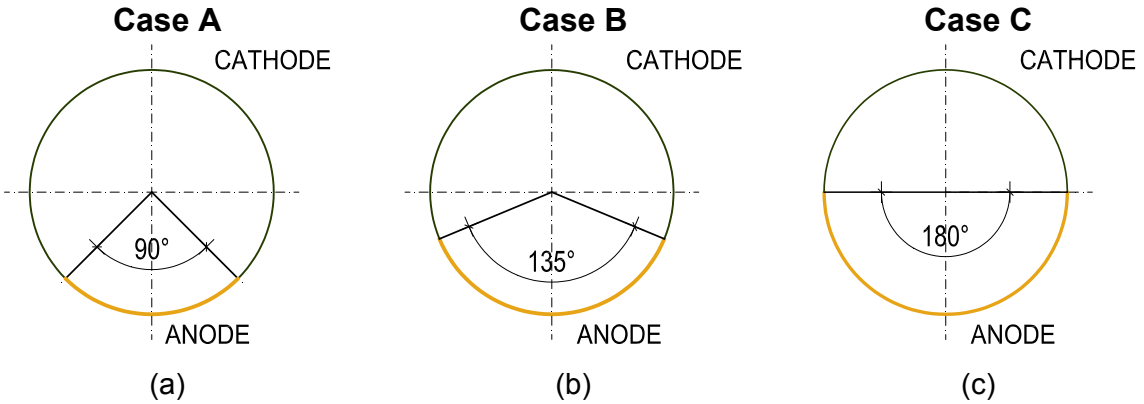

Figure 6.4. Assumed cases for the distirbution of the anodic and cathodic regions in the rebar's cross-section: (a) quarter of the circumference depassivated -Case A, (b) depassivated circumference length corresponding to an angle of 135° - Case B and (c) half of the circumference depassivated - Case C

The mechanical properties of the concrete and steel used in the model are listed in Table 6.1. The analysis is performed for initially un-cracked, good quality concrete (w/c = 0.4) assuming a constant water saturation of 50% and a constant temperature of 20 ºC. Therefore, the values for the electric conductivity and oxygen diffusivity coefficient are taken from Table 2.1 and 2.2., respectively. The boundary conditions for oxygen transport are taken the same as the initial conditions with a value of 0.0085 kg/m^3. These boundary conditions correspond approximately to severe splash conditions. Parameters used for the calculation of non-mechanical processes after depassivation of steel are listed in Table 6.2.

Table 6.1 Mechanical parameters used in the model

Parameter	Value
Modulus of elasticity of concrete, E_c (N/mm^2)	26200.0
Poisson's ratio of concrete, ν_c	0.18
Tensile strength of concrete, f_t (N/mm^2)	1.92
Uniaxial compressive strength of concrete , f_c (N/mm^2)	31.0
Fracture energy of concrete, G_f (J/m^2)	40.0
Modulus of elasticity of steel, E_s (N/mm^2)	200000.0
Poisson's ratio of steel, ν_s	0.33
Modulus of elasticity of rust, E_r (N/mm^2)	100.0
Volume expansion factor of rust, $\alpha_r = \rho_s / \rho_r$	4.0

Table 6.2. Parameters used for the calculation of non-mechanical processes

Parameter	Value
Faraday's constant, F (C/mol)	96486.7
Anodic exchange current density, i_{0a} (A/m^2)	1.875×10^{-4}
Cathodic exchange current density, i_{0c} (A/m^2)	6.25×10^{-6}
Anodic equilibrium potential, Φ_{0a} (V vs. SCE)	-0.780
Cathodic equilibrium potential, Φ_{0c} (V vs. SCE)	0.160
Tafel slope for anodic reaction, β_a (V/dec)	0.06
Tafel slope for cathodic reaction, β_c (V/dec)	0.160
Diffusivity coefficient of rust, D_r (m^2/s)	2.2×10^{-16}

The results from Section 5.1.2.6 show a great importance of incorporating the distribution of corrosion products through the cracks. Therefore, the case without the influence of rust transport is not investigated in this analysis. The calculation of non-mechanical processes (oxygen distribution, electrical potential, electric current density and distribution of corrosion products) and the corresponding mechanical damage is performed for a time period of 6 years.

6.1.3 Results and discussion

Predicted corrosion induced damage for all three investigated cases of the anode-cathode distirbution (A-C) are shown in Figure 6.5 for 1.5, 2, 3 and 6 years after depassivation. The crack is plotted in terms of maximal principal strains on undeformed specimens. The red (dark) zone corresponds to the crack opening of 0.10 mm or larger.

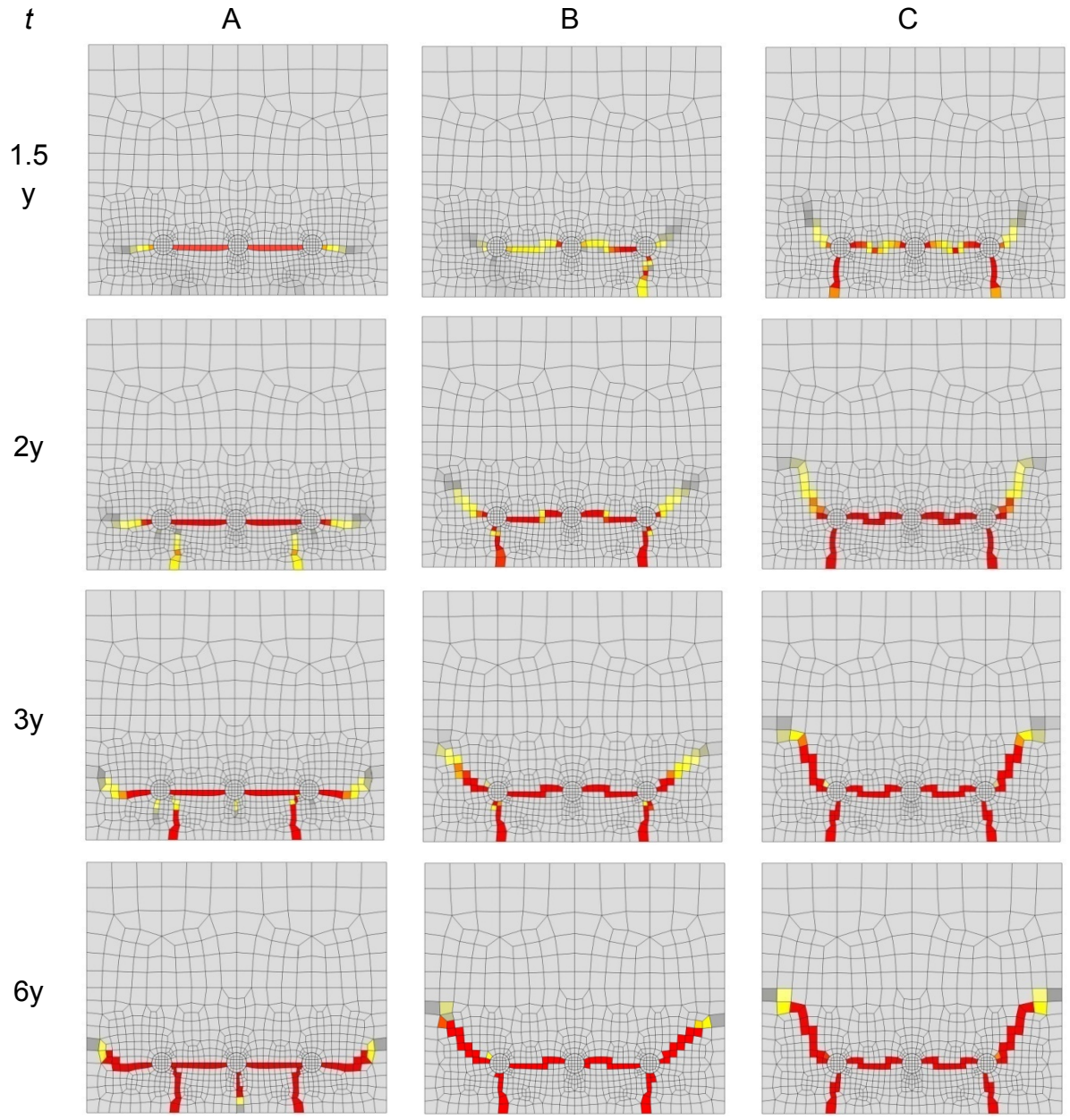

Figure 6.5 Predicted corrosion induced crack patterns in the beam's cross-section, 1.5, 2, 3 and 6 years after depassivation for all three cases of anode-cathode positions (A, B, C)

Comparing the predicted crack patterns of the beam cross-section (see Figure 6.5), it can be seen that with the increase of the anodic surface, the cracks propagating towards the specimen side surface tend to be more inclined. The corrosion induced damage for the case B gives the best agreement with the crack pattern observed in the experiment (Figure 6.6). This leads to the conclusion that the anode-cathode position in the experiment approximately coincides with the case B. From the evaluation of experimental results it can also be seen that the most corroded part of the cross-section of the reinforcement bar was close to the bottom concrete surface of the beam. Further on, the predicted crack pattern for the case B at the bottom surface of the concrete specimen agrees nicely with the experimentally observed cracks (Figure 6.7).

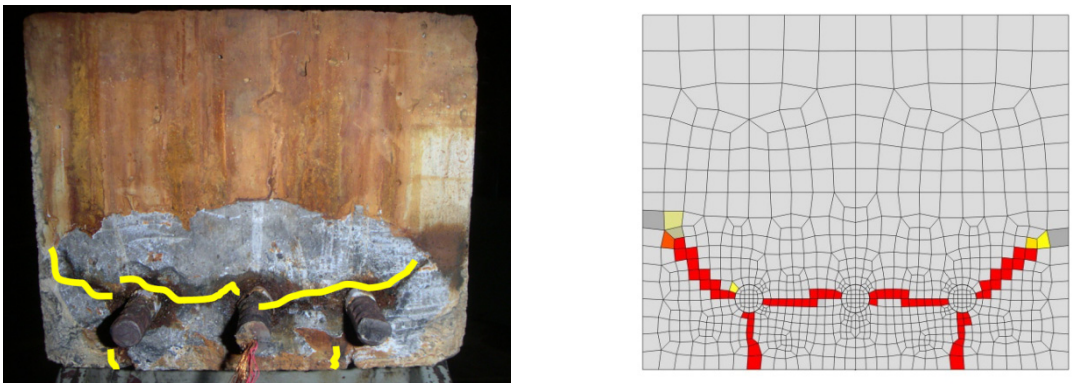

Figure 6.6 Experimentally (Dong et al. 2011) observed (left) and numerically predicted crack patterns at the beam's end for case B after 6 years (right)

The damage is characterised by the internal cracks propagating first between the rebars, with the surface cracks reaching the bottom and side surfaces later on. This can lead to delamination of the whole sections of the concrete cover which was also observed by other researchers in the case of multi-rebar specimens (Tran 2012). The numerical results (case B) show that the critical crack opening of 0.15 mm correlates to the total rust production of 0.0091 kg/m of reinforcement bars. The critical crack forms approximately 2.7 years after start of the corrosion process. This prediction is in good agreement with the statistical evaluation of measurements on structural elements under severe natural conditions (Thoft-Christensen 2000).

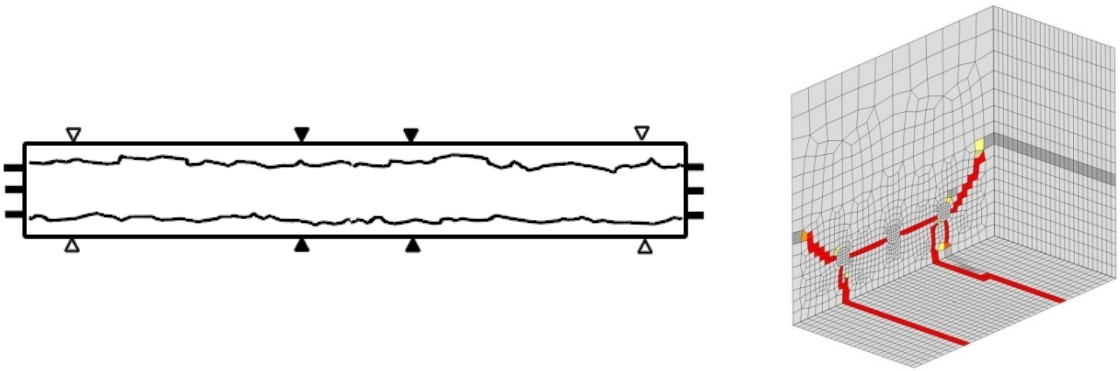

Figure 6.7 Experimentally (Dong et al. 2011) observed crack pattern (left) and numerically obtained corrosion damage on the bottom surface (right)

The importance of modelling the transport of corrosion products into the corrosion induced cracks is illustrated by the Figure 6.8a. It can be seen, same as in the numerical simulations (Figure 6.8b), that the ingress of the rust products into the cracks is obvious, even reaching the side surface. The pressure on the surrounding concrete is therefore less pronounced, which finally leads to a more realistic prediction of the corrosion induced damage.

(a) (b)

Figure 6.8 Evidence of rust products reaching the side surface of the specimen S0 in the experiments by Dong et al. (2011) (a) and numerically predicted distribution of corrosion products into the cracks for case B after 6 years (b)

6.2 Multi-rebar case with the influence of stirrups

6.2.1 Experimental setup

As mentioned in Section 6.1.1 the experiments performed by Dong et al. (2011) investigated the influence of stirrups on the residual strength of corroded RC beams. Therefore, the results of corrosion induced damage obtained for the series S80 (Dong et al. 2011) are closely studied to verify the predicted corrosion induced damage in the multi-rebar case with stirrups. For the series S80, stirrups of diameter 6 mm with spacing of 80 mm were used. The longitudinal and the cross-section are shown in Figure 6.9.

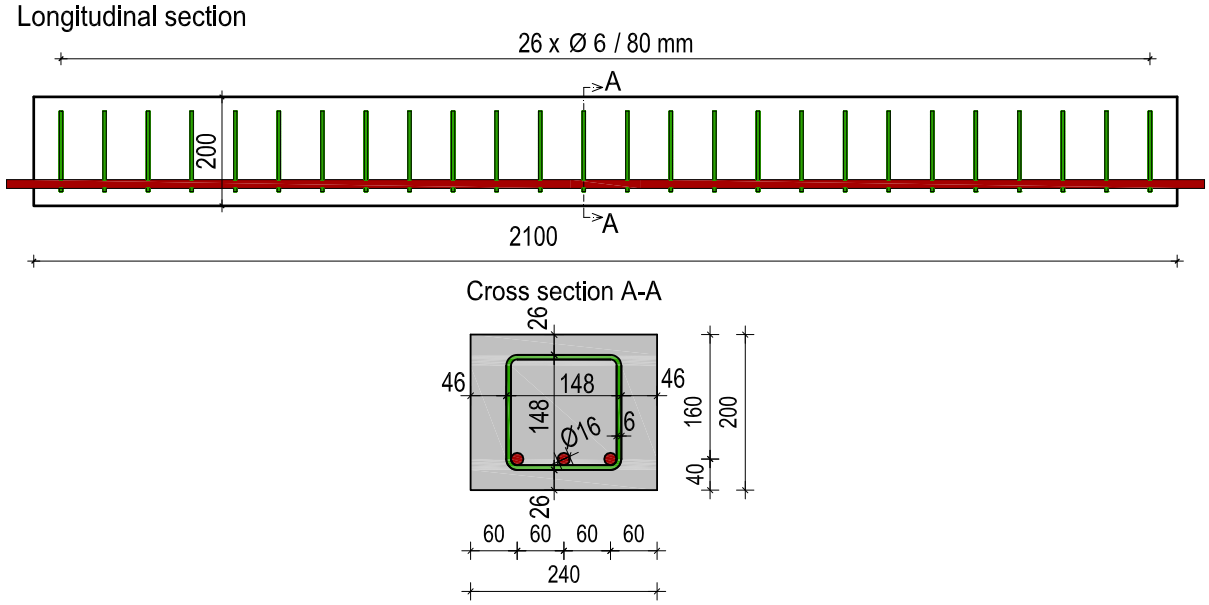

Figure 6.9 Geometry of the investigated beams from the series S80 with stirrups in experiments by Dong et al (2011)

The same conditions and the test setup for the accelerated corrosion described in 6.1.1 were used in the case of the series S80.

6.2.2 Numerical model

Same as in the previous section, only a 130 mm segment of the total beam length is modelled (Figure 6.10a). The main reinforcement bars (ϕ16 mm) are arranged axially 60 mm from each other and 40 mm from the lower concrete surface. Two additional stirrups with a diameter of 6 mm are placed at a distance of 80 mm from each other (Figure 6.10b). The direct contact with the main reinforcement is avoided by offsetting the stirrups 2 mm towards the lower and side concrete surfaces (Figure 6.10c). They are modelled the same as the main rebars, i.e. using eight node solid elements. The interface layer, with the addition of 1D corrosion contact elements, is

added around the stirrups and main bars. Due to the complex geometry, concrete is modelled with tetrahedral elements.

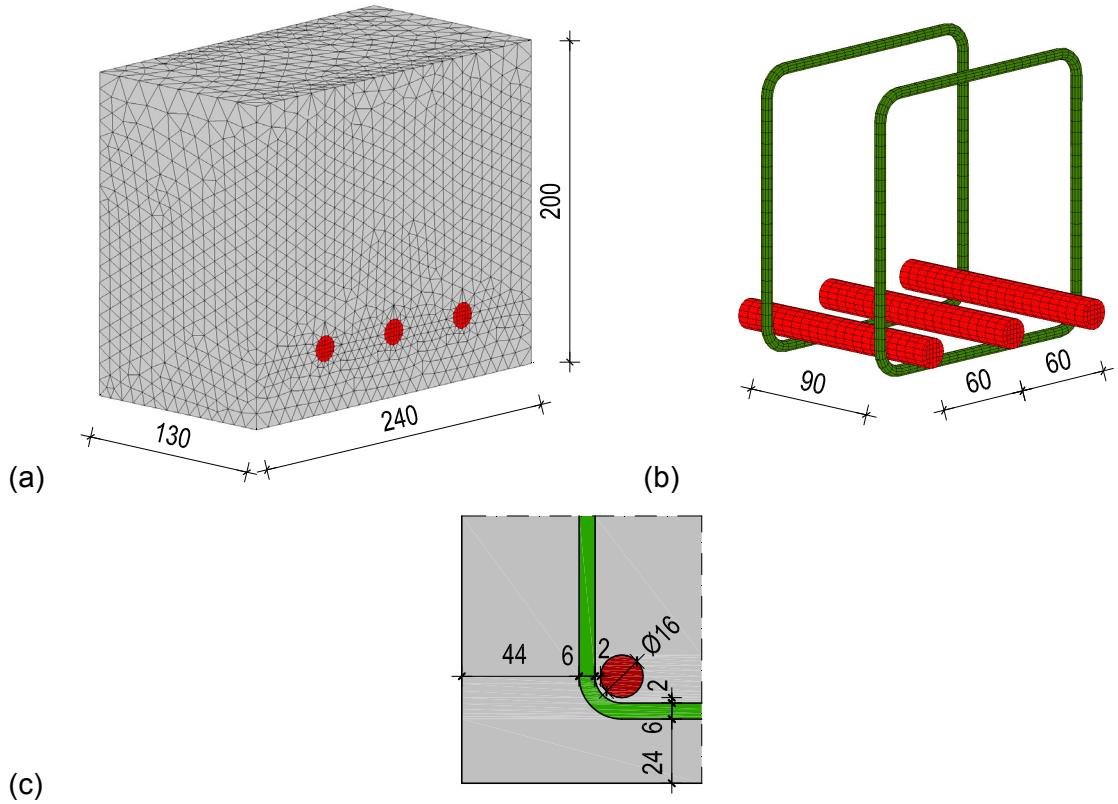

Figure 6.10 Finite element discretization of the beam's segment (a) and main rebars and stirrups (b) ; Detail of the stirrup and rebar contact (c)

As mentioned before, the anodic and cathodic regions on the stirrups and main rebars are assumed upfront. Therefore, only the processes after depassivation of steel are calculated and the anodic-cathodic regions are kept constant.

Three anodic regions of 12 mm in length are assumed on the stirrup lower arm. Their position corresponds to the position of the main rebars, i.e. they are chosen to be right below them. Two additional anodic regions of same length are also defined on each of the stirrups side arms, however only on the lower half of the side arm (Figure 6.11). Such configuration is chosen with the assumption that the depassivation occurs in the region close to the main reinforcement bars. It is also assumed that in the case of the stirrups the whole circumference is depassivated (Figure 6.11) due to a diameter of only 6 mm and also, in comparison with the main rebars, due to a closer position to the concrete surface.

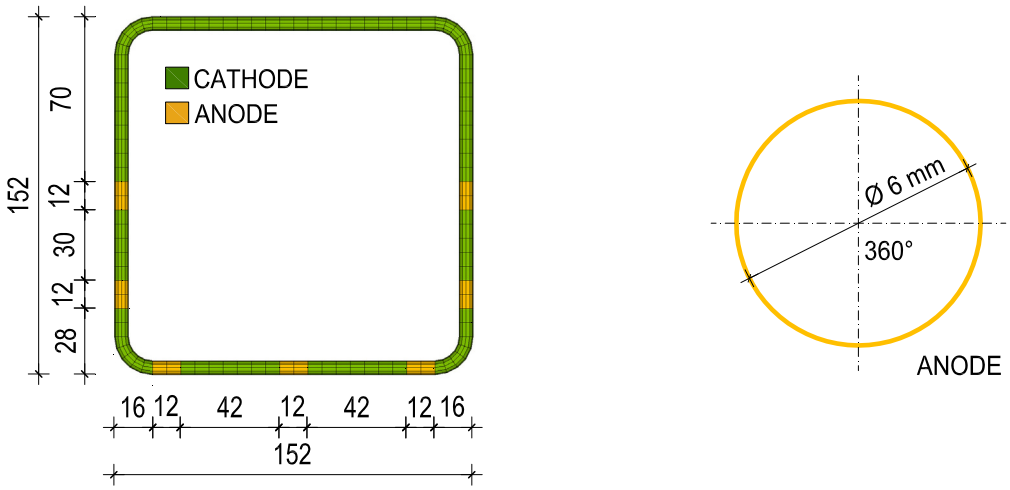

Figure 6.11 Assumed anodic-cathodic regions along the stirrups (left) and along the stirrup's circumference (right)

The position of the anodic and cathodic regions along the length of the main rebars is assumed to be directly dependent on the position of the stirrups. Therefore, two anodic regions along each bar length are defined and shown in Figure 6.12. For the distribution of depassivated regions in the bar cross section, two different configurations are chosen, one for the middle bar, denoted with M, and one for the side bars, marked with S. In the case of the middle bar (M) the same configuration from Section 6.1.2, which gives the best correspondence with the experimental results for specimens without stirrups, is assumed (Figure 6.12). For the side bars, only a half of this configuration is chosen for the side not facing the stirrup arm (Figure 6.12).

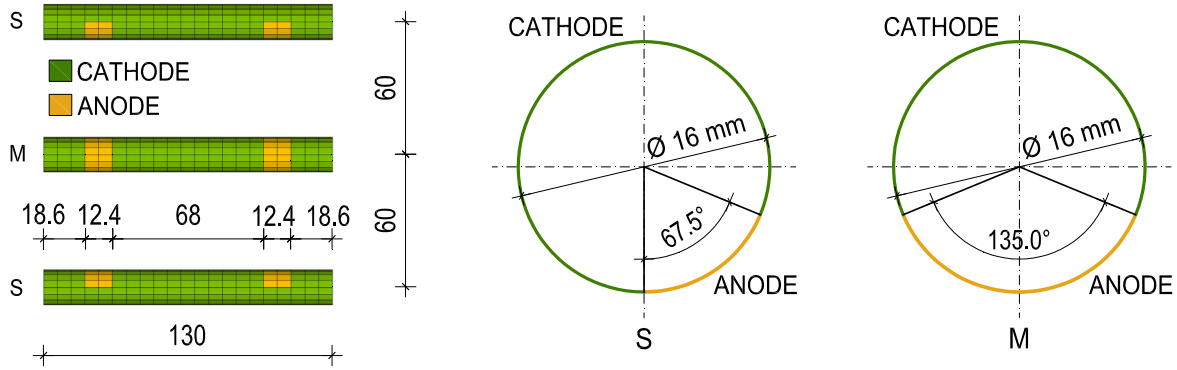

Figure 6.12 Assumed anodic-cathodic regions along the main rebars (left) and along the rebar's circumference for the side bar (S) and the middle bar (M) (right)

The material properties for the rebars and concrete are the same as defined in Section 6.1.1. The steel stirrups are modelled as linear elastic material with the Young's Modulus of 200000 N/mm^2 and Poisson's ratio of 0.33. The parameters which are relevant for modelling the non-mechanical processes, including the boundary and initial conditions, are chosen the same as shown in Section 6.1.1. The corrosion induced damage is investigated for a period of 6 years.

6.2.3 Numerically predicted corrosion induced damage

Predicted corrosion induced damage, for the assumed anode-cathode configuration given in Section 6.2.2, is shown in Figure 6.13 for 1.5, 2, 3 and 6 years after depassivation. The crack is plotted in terms of maximum principal strains on undeformed specimens with the red (dark) zone corresponding to the crack opening of 0.10 mm or larger. The internal cracks between the rebars are formed first, followed by a later damage which is characterized by two cracks under the side rebars (S) reaching the bottom surface and subsequently by two vertical cracks propagating to the upper surface.

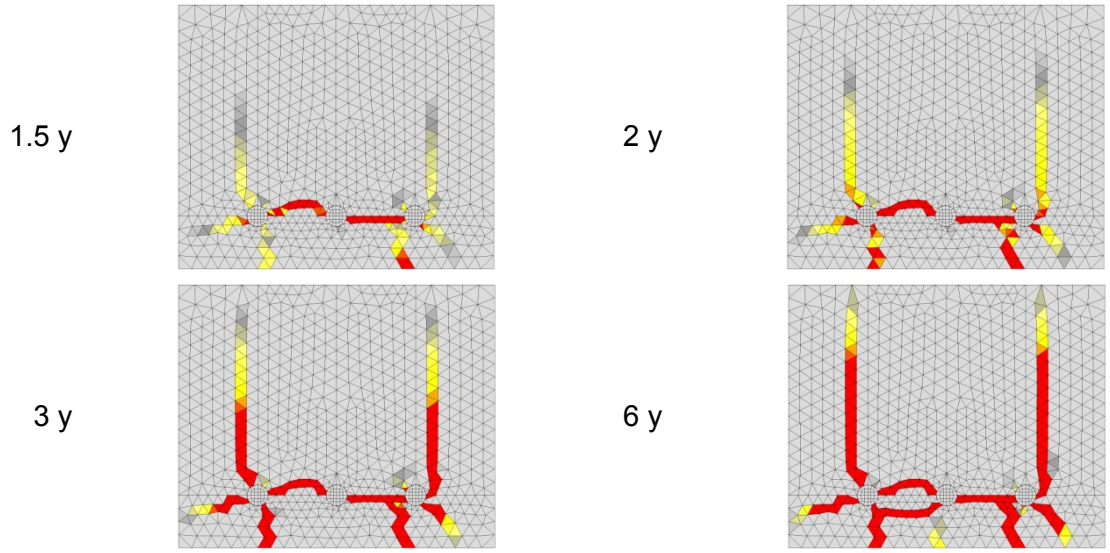

Figure 6.13 Predicted corrosion induced crack patterns in the beam's cross-section, 1.5, 2, 3 and 6 years after depassivation

The experimentally obtained and numerically predicted crack pattern, 6 years after depassivation, are shown in Figure 6.14. The simulated corrosion damage corresponds nicely to the damage after 6 years of active natural corrosion processes. It can be seen that the model is able to realistically replicate the development of corrosion induced cracks in the case of specimens with stirrups.

Figure 6.14 The crack pattern obtained from the experiments (Dong et al. 2011) (left) and from the numerical simulation, 6 years after depassivation (right)

By comparing the here predicted damage with the case without stirrups, shown in Figure 6.6, it can be seen that the crack pattern differs significantly. In the presence of stirrups, the two cracks propagate to the upper concrete surface parallelly with the side surfaces. As it is mentioned by Dong et al. (2011), due to expansion of corrosion products around the main rebars, the stirrup is under tensile stress which activates bond stresses between the stirrup and concrete. In this way, the compressive stress in concrete surrounding the stirrup arm is restricting the development of the corrosion induced crack to the side surface and the crack propagates towards the upper surface.

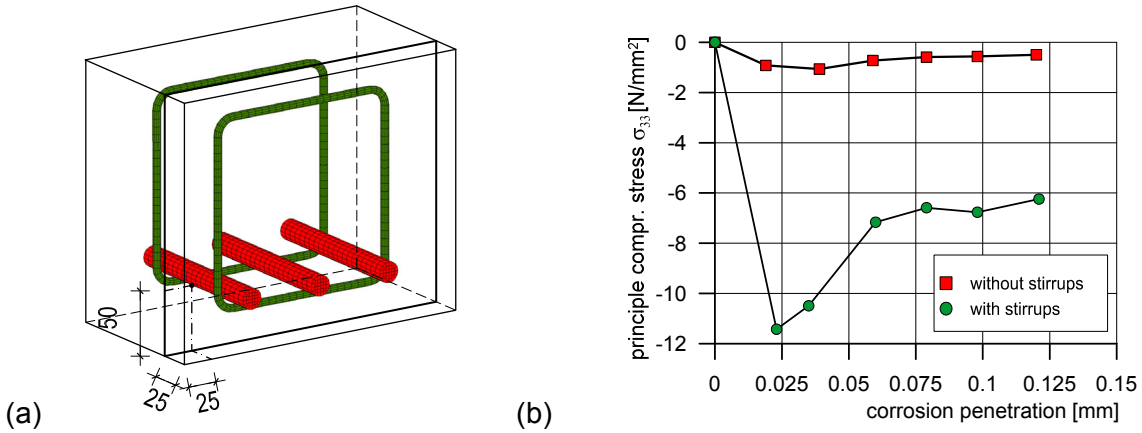

Figure 6.15 Position of the chosen concrete element (a) and calculated principle compressive stresses as a function of the average corrosion penetration (b)

The principle compressive stresses of a chosen concrete element near the side stirrup arm (position shown in Figure 6.15a) are plotted in Figure 6.15b as a function of the average corrosion penetration of the rebars at the anode-cathode transition zone, for the case without and with stirrups. The confined conditions in this concrete region due to the presence of stirrups, prevent the crack from reaching the side surface. After the crack propagates vertically, the compressive stresses start to decrease with the ongoing corrosion induced damage (Figure 6.15b).

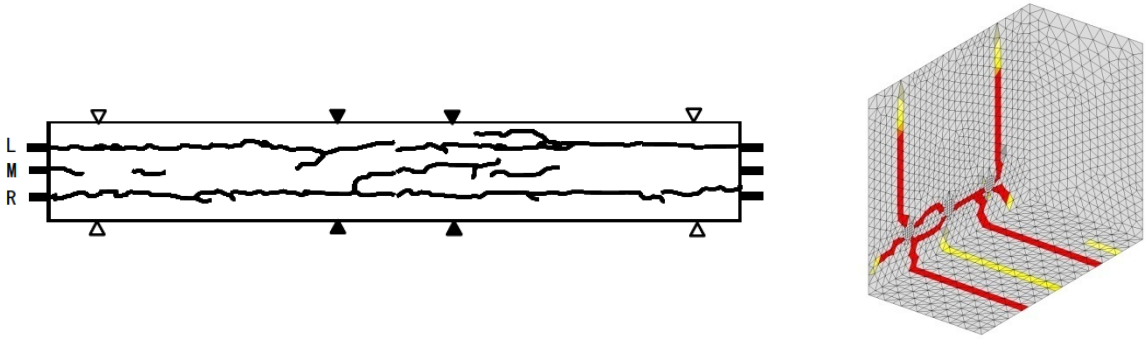

Figure 6.16 The corrosion induced damage on the bottom surface for the specimen (a)experimentally (Dong et al. 2011) and (b) numerically obtained after 6 years after depassivation

Simultaneously, the tensile stress in the lower stirrup arm reduces the confined conditions in concrete around the middle rebar (M), which are present due to the expansion of rust around the side bars (S) (Dong et al. 2011). This allows for an additional smaller crack to propagate from the middle rebar to the lower concrete surface (Figure 6.16). The principle tensile stresses of a chosen concrete element below the middle rebar (position shown in Figure 6.17a) are plotted in Figure 6.17b as a function of the average corrosion penetration of the rebars at the anode-cathode transition zone, for the case without and with stirrups. It can be seen that at the beginning of the corrosion process the tensile stresses increase for both cases, until the opening of the cracks under the side bars (S) (Figure 6.14). Afterwards, the stresses are decreasing, but in the presence of stirrups they start to rise again (Figure 6.17b) due to the influence of the lower stirrup arm .

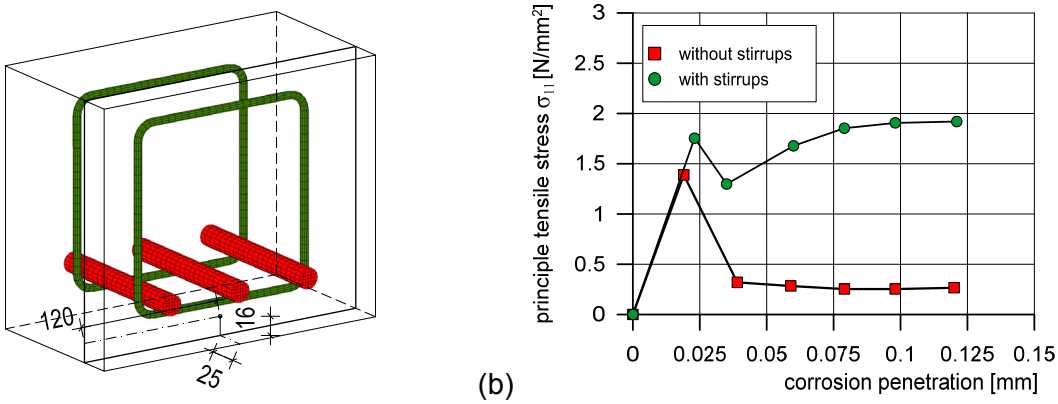

Figure 6.17 Position of the chosen concrete element (a) and calculated principle tensile stresses as a function of the average corrosion penetration (b)

Average calculated widths of the cracks along the bottom surface of the concrete specimen for cases without and with stirrups, are plotted in Figure 6.18 as a function of the average corrosion penetration of the rebars at the anode-cathode transition zone. It can been seen that the presence of stirrups reduces the crack widths and therefore the extent of the corrosion induced damage.

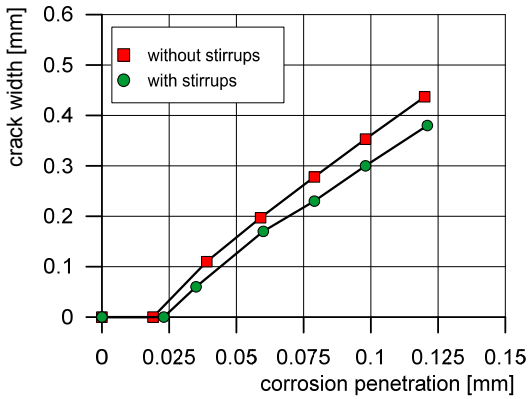

Figure 6.18 Average crack width (at the bottom surface) as a function of average corrosion penetration of the rebars for the case without and with stirrups

6.3 Conclusions

The corrosion induced damage of concrete elements with multiple arranged reinforcement bars is simulated using the 3D chemo-hygro-thermo-mechanical model. The cases without and with stirrups are analysed and the numerically obtained results are compared with the experimental data of Dong et al. (2011).

The model is able to predict the development of damage (cracks) in the concrete specimens, for both cases, with the expansion of corrosion products around the rebars in the vicinity of each other. The crack pattern is characterized with the forming of the internal crack between the rebars, followed by the development of the visible surface cracks. This can lead to delamination of larger sections of the concrete cover and subsequently to direct exposure of rebars to aggressive environmental conditions, which considerably reduces the mechanical properties of reinforced concrete elements. Furthermore, in the multi-rebar case without stirrups it is shown that the anodic-cathodic configuration on the rebar surface has a strong influence on the development of the corrosion induced damage. With the increase of the rebar anodic surface, the cracks towards the specimen side surfaces propagate in a more inclined manner.

The effect of stirrups on the corrosion induced damage of multi-rebar specimens is realistically captured by the 3D CHTM model. The confined conditions, in the concrete region around the stirrup arms, prevent not only the cracks from reaching the sides of the investigated specimen, but also contribute to smaller widths of the visible cracks on the bottom surface. Therefore, the presence of stirrups has a positive effect on the corrosion induced damage.

7 VALIDATION OF THE IMPLEMENTED HYSTERETIC MOISTURE BEHAVIOUR OF CONCRETE IN CHTM MODEL

7.1 Validation of the scanning curves

The experimental data by Baroghel-Bouny (2007) are used to verify the implemented empirical model for determining the scanning curves between the main adsorption and desorption isotherm. The experiments are focused on obtaining the desorption-adsorption characteristics for a wide range of normal and high-performance hardened cement pastes and concrete mixtures. Further on, hysteretic behaviour is also investigated by measuring and plotting the scanning isotherms within various relative humidity ranges. Only the experimentally obtained scanning curves for the concrete specimens with the w/c ratio of 0.27 and 0.43 are used for the here presented validation.

7.1.1 Description of the experimental setup and data

The water vapour desorption and adsorption experiments by Baroghel-Bouny (2007) were performed by using the salt solution method (Aimin 1989; Baroghel-Bouny 1994), at a constant temperature and atmospheric pressure. For this reason a sealed cell (desiccator) was used to place the specimens in conditions of controlled relative humidity by using a saturated salt solution. The specimens were exposed to stepwise changes in the RH and the corresponding mass water content was obtained by weighing the specimens for the equilibrium state. This is obtained by assuming that the specimen mass is stabilized after a longer period of time, up to several weeks or months, with the measurement precision of 0.001 g. The temperature of the enclosed cells was kept constant at 23 ºC and it was assumed that the gas pressure inside the cell was equal to the atmospheric pressure during the whole experiment.

Concrete specimens were 3 mm thick, with a diameter within a range of 70-110 mm and a mass between 20 and 40 g. For the here presented numerical simulation only the experimental results obtained for concrete specimens of the series BO (w/c ratio 0.43) and BH (w/c ratio 0.27) are used (Baroghel-Bouny 2007).

The specimens were initially exposed to stepwise decrease of RH inside of the cell, which subsequently gives the first desorption curve from 100% to 3% of RH. The first adsorption curves were then determined in the similar way by raising the cell's relative humidity in a step-by-step manner up to 100%. Likewise, first adsorption curves were measured starting from different RH values, i.e. RH=12%, 33%, 44%, 54% and 72%. In this way the scanning adsorption curves were obtained. Due to the lack of experimental data, only one scanning desorption curve is simulated starting from a relatively high value of 97% RH on the adsorption curve.

7.1.2 Numerical model

A simple finite element discretization of the concrete specimen is performed to validate the empirical model for the scanning curves. Using the symmetry conditions, only a quarter of the 3mm thick cylindrical specimen with a radius of 35 mm, is modelled with eight node solid elements (Figure 7.1). The boundary conditions, i.e. the changing relative humidity of the surrounding air is defined only in the nodes on one side of the model.

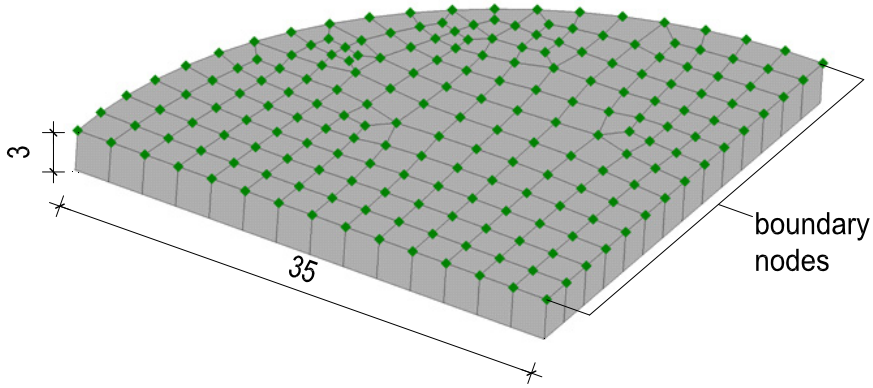

Figure 7.1 Model geometry (all in mm)

The experimentally obtained first desorption curve from 100% to 3% RH and first adsorption curve from 3% to 100 % are taken as the input data for the main desorption and adsorption isotherm. They are acting as envelopes for the calculated scanning curves. The values of the water vapour permeability and the surface transfer coefficient are taken relatively high as the numerical analysis is focused on the behaviour of the scanning curves with the corresponding change of relative humidity and not on the distribution of the RH and water content along the specimen depth. Therefore, the nodes on the "unloaded" side of the specimen have approximately same RH as the boundary nodes, for the same time step.

Initial value of the water content for the investigated scanning curve is dependent on the starting value of the RH, i.e. on the position on the main adsorption or desorption curve. The values of the simulated RH range and the corresponding initial conditions are given in Table 7.1. Temperature is taken as constant and is equal to 23 ºC. The rate of increase, i.e. decrease of relative humidity for the boundary condition is taken as 0.5 % of RH per day.

Table 7.1 The initial values of relative humidity and water content for the simulated scanning curves

Concrete series BO (w/c = 0.27)		
Scanning curve - RH range	Initial value of RH [%]	Initial value of water content [kg_{H_2O}/kg_{con}]
ads.curve from 12% - 100%	12	0.006
ads.curve from 33% - 100%	33	0.010
ads.curve from 54% - 100%	54	0.018
Concrete series BH (w/c = 0.43)		
Scanning curve -RH range	Initial value of RH [%]	Initial value of water content [kg_{H_2O}/kg_{con}]
ads.curve from 12% - 100%	12	0.006
ads.curve from 33% - 100%	33	0.010
ads.curve from 72% - 100%	72	0.027
des.curve from 97% - 3%	97	0.031

7.1.3 Numerical analysis of the scanning curves

The comparison of numerically calculated scanning curves with the experimentally obtained results is shown in Figure 7.2 and Figure 7.3, for the w/c ratio of 0.27 and 0.43, respectively. The main adsorption and desorption curves which are used as model input data, corresponding to the change of RH from 3% to 100% for the former and to the change of RH from 100% to 3% for the later, are also shown.

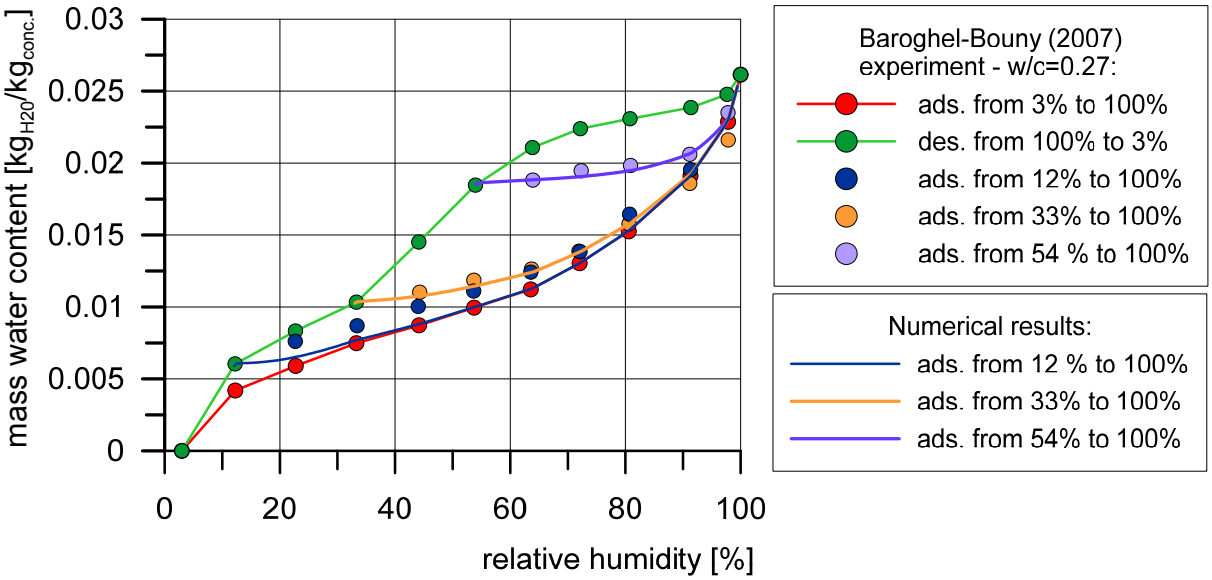

Figure 7.2 Results of the numerical simulations for the concrete series BH (w/c=0.27) compared with the experimental results by Baroghel-Bouny (2007)

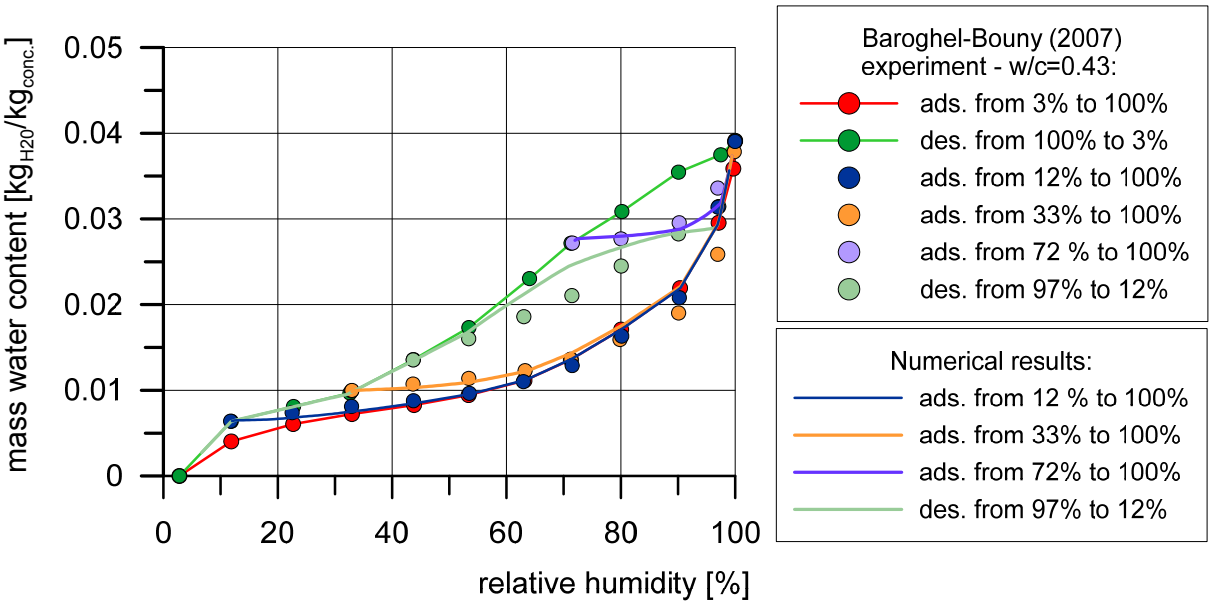

Figure 7.3 Results of the numerical simulations for the concrete series BO (w/c=0.43) compared with the experimental results by Baroghel-Bouny (2007)

The numerical results give a good agreement with the experimental results obtained by Baroghel-Bouny (2007), especially in the case of adsorption scanning curves. The experimental values on the scanning adsorption curves (33% to 100% for the series BH; 33% to 100% and 72% to 100% for the series BO) in the RH range above 80% are slightly lower than the corresponding values on the assigned main adsorption curves. This is not captured by the model due to the fact that the main isotherms serve as envelopes for describing the behaviour of the scanning curves.

Simulated desorption scanning curve for the range of 97% to 3 % RH, in the case of the series BO (Figure 7.3), has a slight deviation from the experimental data. This can be explained by relatively high RH initial conditions on the main adsorption curve, i.e. for the range of 95% to 100% RH. This is often regarded as a transition zone between the hygroscopic and over-hygroscopic ranges and can therefore produce great variability in measuring mass of water content (Baroghel-Bouny 2007).

7.2 Distribution of water content in concrete

Results of the experimental investigation by Ryu et al. (2011) are used to verify the hysteretic moisture model for concrete and its ability to predict the water content and relative humidity distribution in concrete specimens. The experimental results cover not only the concrete exposure to constant environmental conditions (constant temperature and RH), but also to cyclic humidity changes (with constant air temperature), cyclic temperature changes (with constant air humidity) and to combined cyclic humidity and temperature conditions. In the following numerical analysis the distribution of the moisture content in concrete specimens is investigated for two cases: (a) for constant drying conditions and (b) for cyclic humidity conditions with a constant air temperature.

7.2.1 Experimental setup

The specimens investigated by Ryu et al. (2011) were concrete prisms with the dimensions of 300x300x100 mm (Figure 7.4). Two concrete mixes were used to cast the prisms, one with the water-cement ratio of 0.3 and another with the ratio of 0.6. After casting, the specimens were water cured for 30 days at temperature of 60 ºC and subsequently left to cool in water at 20 ºC, for additional 10 days. To ensure that the exchange of moisture and heat occurs through only one exposed surface, 5 other surfaces were coated with epoxy resin and additionally covered with polystyrene.

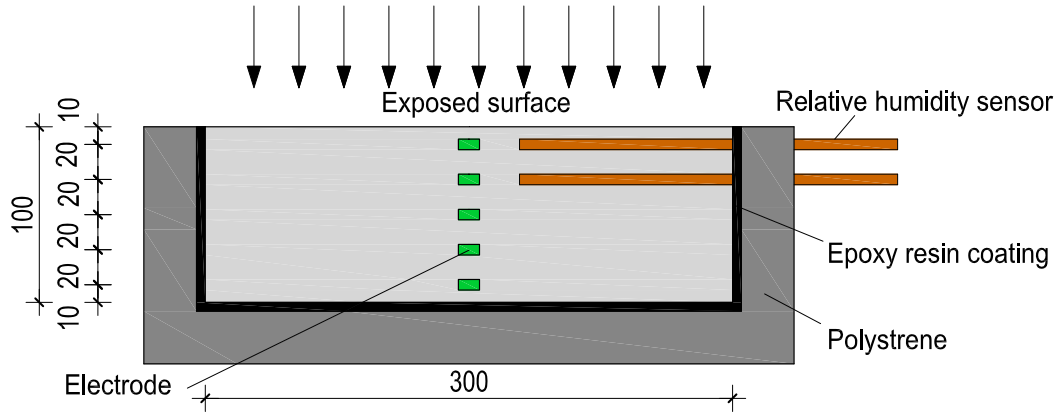

Figure 7.4 Cross-section geometry (all in mm) of the investigated concrete specimen (Ryu et al. 2011)

Electrodes calibrated for measuring the mass water content, were placed at 10, 30, 50, 70 and 90 mm depth and additional relative humidity sensors were installed at the depth of 10 and 30 mm (Figure 7.4).

At the first stage of the experiment, the specimens were placed in a room with a constant temperature of 20 ºC and constant relative humidity of 60%. They were kept under constant thermo-hygro drying conditions for 45 days while the change of the mass water content, at different depths, was measured. Afterwards, one group of

specimens was exposed to cyclic humidity changes with the constant temperature of 20 ºC. One cycle lasted for a day and corresponded to a daily change of relative humidity in Tokyo (Ryu et al. 2011), with the minimum and maximum value being 53.6% and 90.2%, respectively (Figure 7.5). The mass water content and relative humidity was measured in concrete at different depths for exposure time of total 4 cycles.

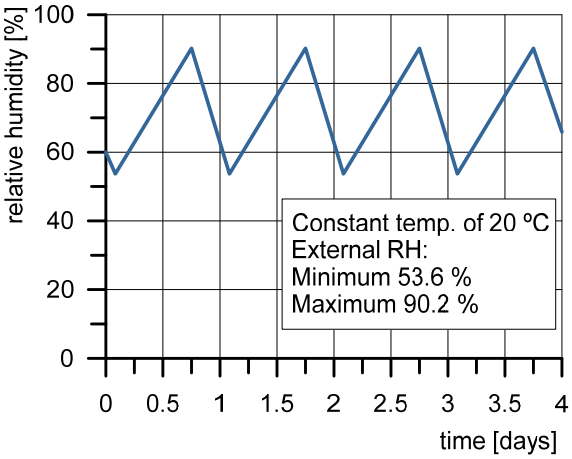

Figure 7.5 Cyclic change of relative humidity at a constant temperature of 20°C in experiments by Ryu et al. (2011)

7.2.2 Numerical model

Only one side of the concrete prism is exposed to the changing relative humidity, while the other surfaces are isolated from the influences of the outside environment. Hence, it is reasonable to assume that the transport process is one-dimensional and the change is occurring only along the axis perpendicular to the boundary surface. Therefore, only a smaller segment of the concrete prism is modelled with the full depth of 100 mm. The first 30 mm from the exposed surface is discretized with 2 mm eight node solid elements, while the rest of the segment is modelled with 5 mm elements. The geometry and the used discretization is shown in Figure 7.6.

Due to the insufficient information from the experiments (Ryu et al. 2011), the main adsorption and desorption isotherms are taken from the literature to correspond approximately to the investigated water-cement ratios. Therefore, the main sorption isotherms from the experiments by Baroghel-Bouny (2007) (w/c = 0.27) and Nielsen (2007) (w/c = 0.66) are used as input data to investigate specimens with w/c = 0.30 and w/c = 0.60, respectively. The sorption curves are shown in Figure 7.7.

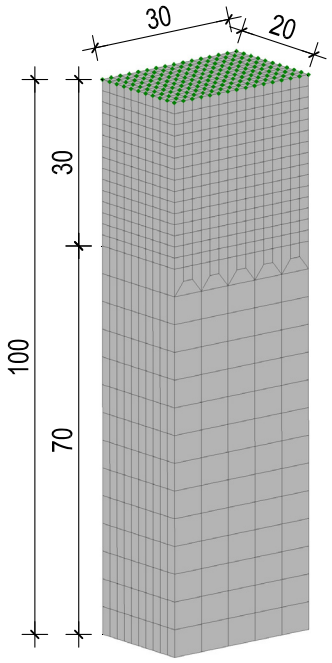

Figure 7.6 Model geometry (in mm) with the finite element discretization

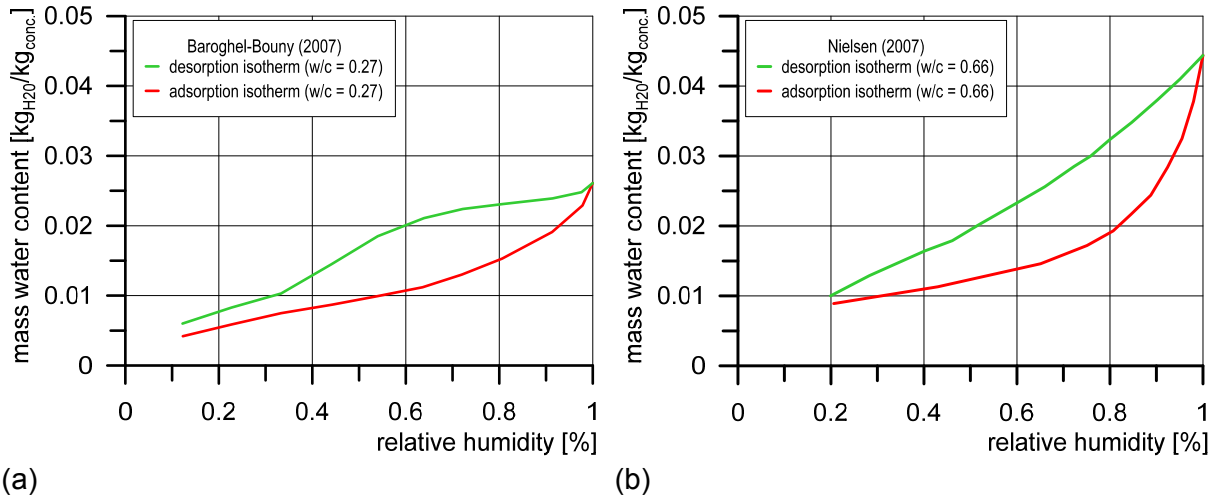

Figure 7.7 Input main adsorption and desorption curves from the experiments by Baroghel-Bouny (2007) (a) and Nielsen (2007) (b) used for specimens with w/c=0.3 and 0.6, respectively

The parameters needed for the analysis with the hysteretic moisture model for concrete are listed in Table 2.1. They are calibrated to obtain the most realistic distribution of the moisture content in the concrete specimens after 45 days of drying. For the initial conditions, it is assumed that the both specimens are completely saturated with water. The behaviour under constant drying conditions is investigated in the first part of the analysis. Therefore, the value of 60% of the ambient RH is defined in the boundary nodes on the upper surface (marked green in Figure 7.4) for the time period of 45 days. Afterwards, the specimens are analysed under cyclic wetting and drying conditions for 4 days, with the air relative humidity changing according to the Figure 7.5. The temperature is kept constant throughout the calculation at 20 ºC.

Table 7.2 Used model parameters

	w/c = 0.3	w/c = 0.6
Sorption isotherms	w/c =0.27(Baroghel-Bouny 2007)	w/c = 0.66 (Nielsen 2007)
Water vapour permeability [s]	7.0×10^{-12}	0.5×10^{-10}
Surface humidity transfer coefficient [m/s]	1.1×10^{-7}	4.5×10^{-6}

7.2.3 Numerical results for the constant drying conditions

The numerical results of the water saturation distribution for the first 45 days of exposure to drying conditions are shown in Figure 7.8 and Figure 7.9, for w/c ratio of 0.6 and 0.3, respectively. They are compared to the experimentally obtained values at depths of 10, 30 and 50 mm and for different time periods, from 5 to 45 days.

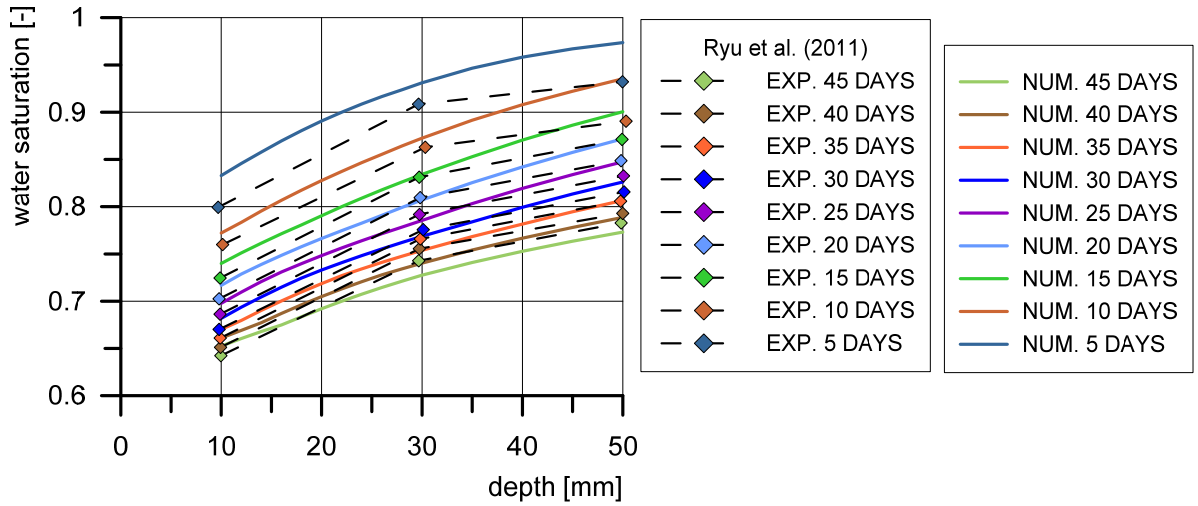

Figure 7.8 Experimentally measured and numerically obtained values of the water saturation distribution during drying for different time periods in the case of the concrete specimen w/c = 0.6

It can be seen that the prediction of the water saturation distribution along the depth of the specimen corresponds nicely with the measured values for different time periods. Same as in the experiment (Ryu et al. 2011), the concrete specimen with a higher water-cement ratio, exhibits faster drying behaviour than the high quality concrete. This is controlled in the analysis not only by the input isotherm, where the slope of the desorption curve is much steeper at higher RH values for the w/c ratio of 0.6 (Figure 7.7), but also with higher values of the water vapour permeability and surface humidity transfer coefficient listed in Table 7.2.

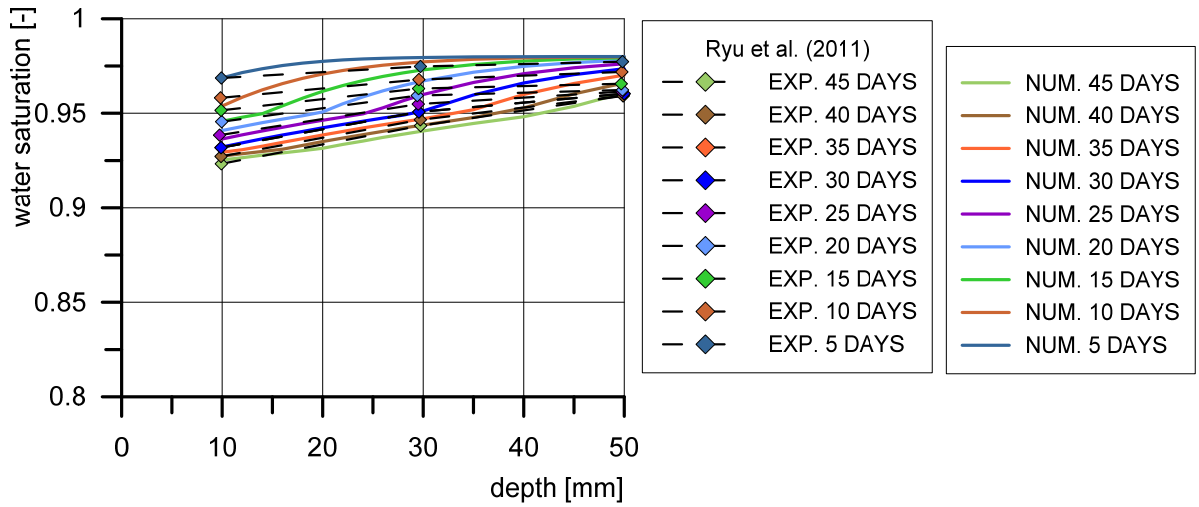

Figure 7.9 Experimentally measured and numerically obtained values of the water saturation distribution during drying for different time periods in the case of the concrete specimen w/c = 0.3

7.2.4 Numerical results for the cyclic wetting and drying conditions

Numerical and experimental values of water saturation (at depths of 10, 20 and 30 mm) and relative humidity (at depths of 10 and 30 mm) during the exposure to cyclic moisture conditions are plotted as a function of time in Figure 7.10 and Figure 7.11 for the specimens with the w/c ratio of 0.6 and 0.3, respectively.

In the case of a higher water cement ratio of 0.6 (Figure 7.10), the values of water saturation are predicted nicely compared with the experimental results. As expected, with the increasing depth the influence of the cyclic humidity conditions on the change of water content is decreasing. For the low quality concrete the water content remains unchanged already at a depth of 30 mm, during a relatively short cyclic period of four days.

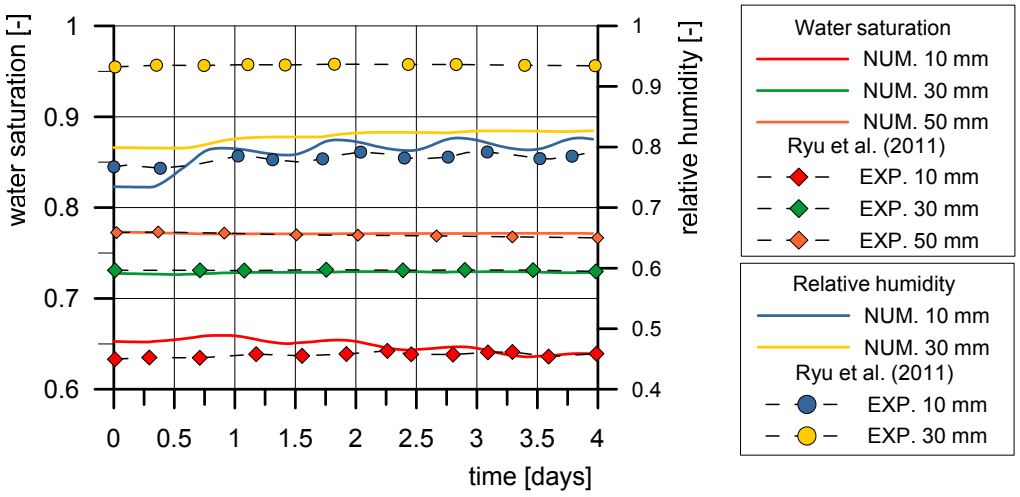

Figure 7.10 Experimentally measured and numerically obtained values of water saturation and relative humidity distribution for different time periods in the case of the concrete specimen (w/c = 0.6)

The values of the relative humidity at the depth of 10 mm show a nice agreement with the experimentally obtained data. The effect of the changing environmental conditions can be observed in the shape of the curve which mirrors the boundary conditions defined by Figure 7.5. On the other hand, the values of the internal relative humidity at the depth of 30 mm differ from the measured data. The difference between the numerical and experimental values of the relative humidity can be explained by using the substitute main adsorption and desorption curve from the literature, which corresponds approximately with the experimentally investigated concrete.

Similarly, for the specimen with w/c ratio of 0.3 the values of the relative humidity differ from the measured values at the depth of 10 mm, while the discrepancy is much lower at the depth of 30 mm (Figure 7.11). These results emphasize the influence of the model input data, i.e. the influence of the main isotherm input data which are taken from the literature due to the lack of material information from the experiment. On the other hand, the experimentally measured values of RH at the depth of 30 mm exhibit a rather large and unrealistic change of almost 30 % compared to the RH values at 10 mm depth, while the corresponding values of the water content differ approximately 3% (Figure 7.11).

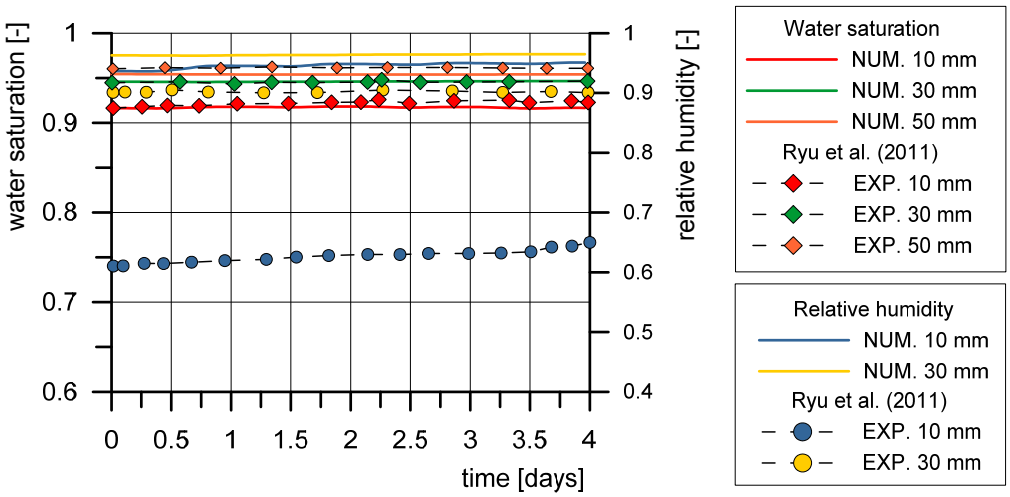

Figure 7.11 Experimentally measured and numerically obtained values of water saturation and relative humidity distribution for different time periods in the case of the concrete specimen (w/c = 0.3)

The values of the water saturation in Figure 7.11 show a good agreement with the experimental data at all depths. Due to a lower porosity, the effect of the humidity variations at the concrete surface on the saturation values decreases with depth. This can be clearly seen by plotting the scanning curves for depth of 4 and 10 mm in Figure 7.12a. The scanning curves for the concrete specimen with the w/c ratio of 0.6 are plotted for comparison in Figure 7.12b, for the same depths. It can be seen that due to a higher porosity, the effect of the cyclic wetting and drying is more pronounced with the increasing depth.

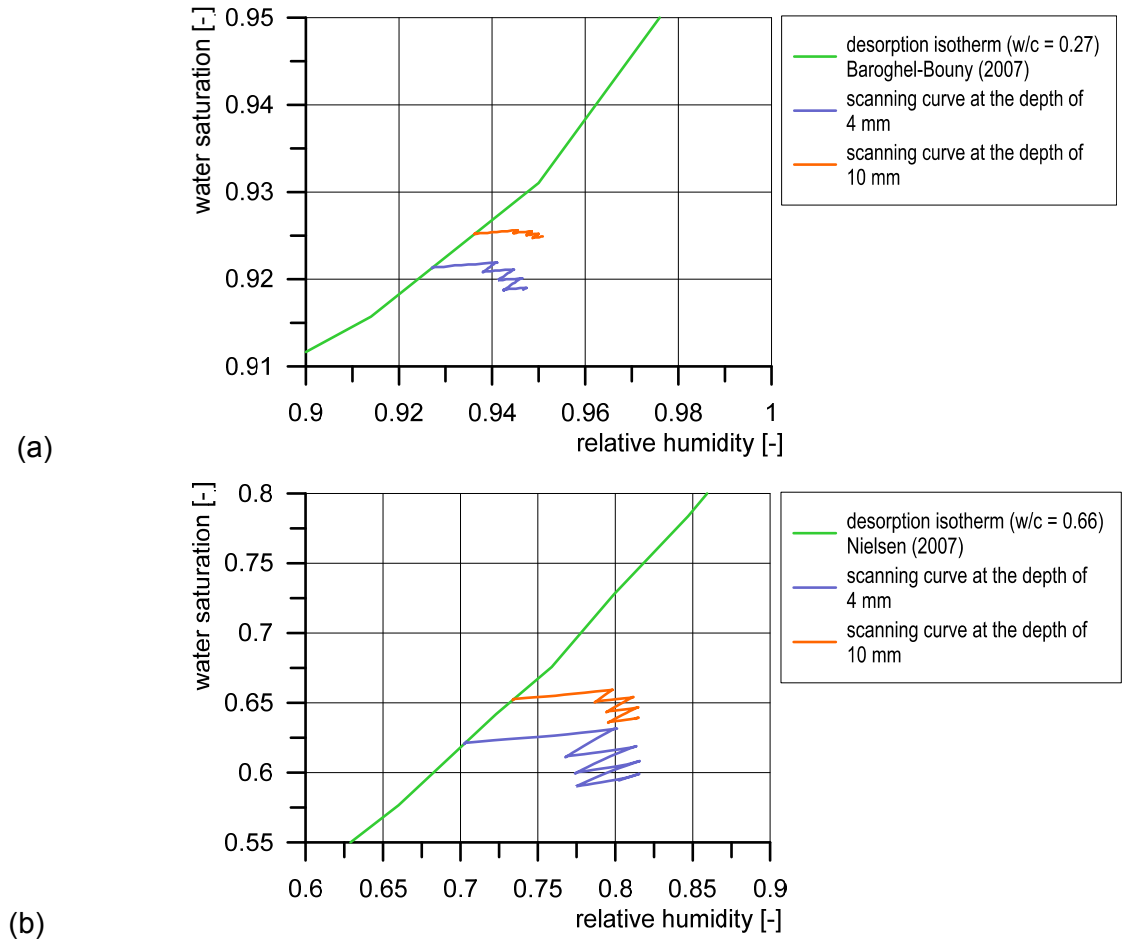

Figure 7.12 Numerically obtained scanning curves during the cyclic wetting and drying conditions at different depths (4 mm and 10 mm) for concrete specimen (a) w/c=0.3 and (b) w/c=0.6

7.3 Distribution of chloride ions in unsaturated concrete

As mentioned before, exposure of concrete specimens to cyclic wetting and drying conditions has strong implications on the transport processes important for the corrosion induced damage. Among others, transport of chloride ions responsible for depassivation of steel is strongly influenced by the hysteretic moisture behaviour of concrete. In such cases, distribution of chloride ions along the concrete depth exhibits characteristic "peak" profile shapes. Due to a pronounced moisture gradient, convective transport of ions becomes activated and at certain periods even more dominant than diffusion. Therefore, experiments in which the chloride profiles were measured in concrete under cyclic moisture conditions present an indirect way to validate a numerical hysteretic moisture model. To verify the here presented model, experiments by Polder & Peelen (2002) are numerically simulated.

7.3.1 Experimental setup and chloride measuring method

The tested concrete specimens were prisms with dimensions of 100x100x300 mm, with the total of 12 different concrete mixes prepared. In here presented numerical analysis only 3 mixes with the Portland cement are investigated and they are listed in Table 7.3.

Table 7.3 Investigated concrete mixes with Portland cement (Polder & Peelen 2002)

Mix code	Cement type	w/c	Cem.cont. [kg/m^3]	Agg.cont. [kg/m^3]	Water cont. [kg/m^3]
1400	CEM I Port. cement	0.40	338	1780	143
1450		0.45	318	1790	149
1550		0.55	287	1827	163

After casting specimens were first kept in a fog room for six days and afterwards stored in a climate room with a constant temperature of 20 ºC and constant humidity of 80% for 21 days. In the experiments, only one surface of each specimen was exposed to 26 weekly cycles. One cycle consisted of 24 hours exposure to 3% NaCl solution, which corresponds to chloride concentration of 18 kg/m^3, followed by drying for 6 days under temperature of 20 ºC and relative humidity of 50%. One cycle with the corresponding exposure conditions at the specimen surface is shown in Figure 7.13.

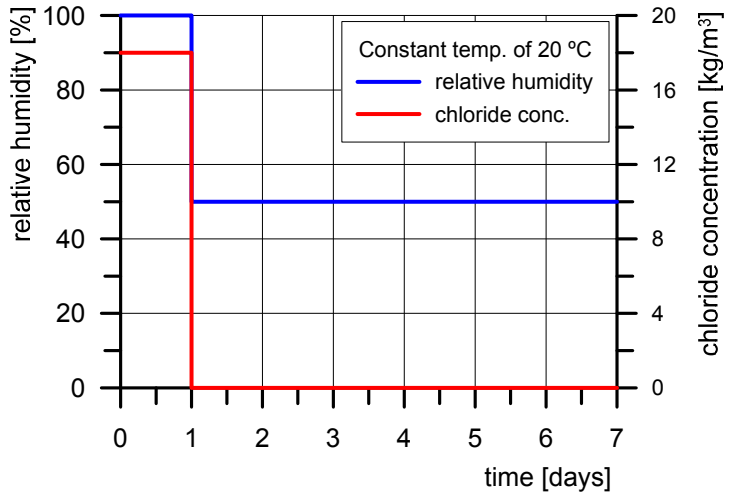

Figure 7.13 Change of relative humidity at a constant temperature of 20 °C for one exposure cycle in experiments by Polder & Peelen (2002)

Chloride penetration profiles were obtained after the finished exposure of 26 wet and dry cycles. The total chloride amount, as the percentage of the cement content, was measured in drilled increments of 2 mm up to the depth of 20 mm. The 2 mm thick concrete samples were firstly ground off and then dissolved in a hot nitric acid. Subsequently, the chloride amount was determined by using the Volhard's titration (Polder & Peelen 2002).

7.3.2 Numerical model

It is assumed that the transport processes are occurring only in one direction, along the depth of the concrete specimen. Therefore, only one column of eight node solid elements is modelled with the total depth of 100 mm. Due to the numerical stability reasons, which arise from the pronounced convective transport of chloride ions, a very fine mesh of 0.1 mm is chosen for the segment from the exposed surface and up to 5 mm of depth. For the depths up to 20 mm and finally 100 mm, the element size is taken as 0.5 mm and 1 mm, respectively (Figure 7.14).

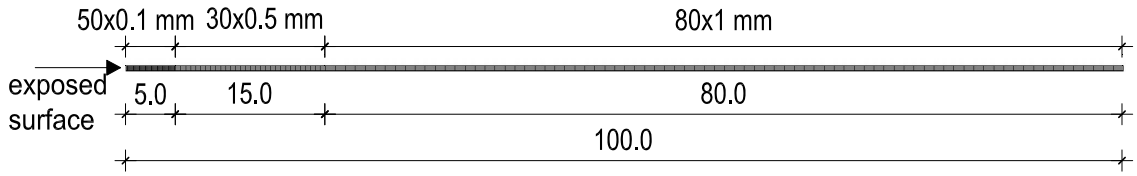

Figure 7.14 The model geometry (all in mm)

As mentioned in the previous section, three types of concrete specimens corresponding to the water cement ratios of 0.40, 0.45 and 0.55 are investigated. Corresponding parameters needed for the analysis of relative humidity, i.e. moisture content distribution and transport of chloride ions in the concrete specimen are given in Table 7.4.

Table 7.4 Used model parameters for the numerical analysis of the relative humidity and chloride ions distribution

Hysteretic moisture model for concrete			
	w/c = 0.40	w/c = 0.45	w/c = 0.55
Sorption isotherms	w/c =0.43 (Baroghel-Bouny 2007)	w/c =0.48 (Hansen 1986)	w/c=0.55 (Hansen 1986)
Water vapour permeability [s]	2.0×10^{-11}	7.0×10^{-11}	1.0×10^{-10}
Surface humidity transf. coeff. [m/s]	8.0×10^{-7}	1.0×10^{-6}	2.0×10^{-6}
Transport of chloride ions			
	w/c = 0.40	w/c = 0.45	w/c = 0.55
Initial chlor. diffusion coefficient [m^2/s]	2.0×10^{-11}	6.0×10^{-11}	2.0×10^{-10}
Chloride binding rate coefficient [s^{-1}]	1.5×10^{-7}	5.0×10^{-7}	2.0×10^{-6}

Data for the main adsorption and desorption isotherms were not obtained in the experiments of Polder & Peelen (2002). Hence, the sorption curves are chosen from the literature to approximately correspond with the investigated water cement ratios. The curves for w/c ratio of 0.43, measured by Baroghel-Bouny (2007), are used as alternate curves in the case of the specimen with w/c = 0.40 (Figure 7.15a). Similarly, the curves obtained by Hansen (1986) for w/c 0.48 and 0.55 are taken as substitute input curves for the w/c ratio of 0.45 and 0.55, respectively (Figure 7.15b,c).

The initial water content is determined from the corresponding desorption curve, with the assumption that the initial relative humidity in the specimen is constant and equal to 80 %. This relates to the experimental preconditioning procedure mentioned in the section 7.3.1. The initial chloride concentration values are taken as 0 kg/m^3 for all three types. The temperature is kept constant throughout the analysis and is equal to 20 ºC.

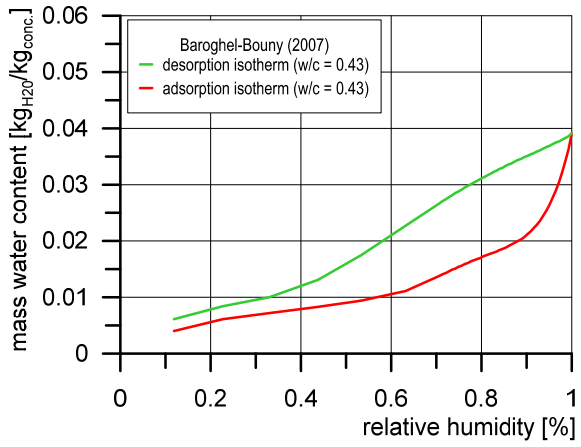

(a)

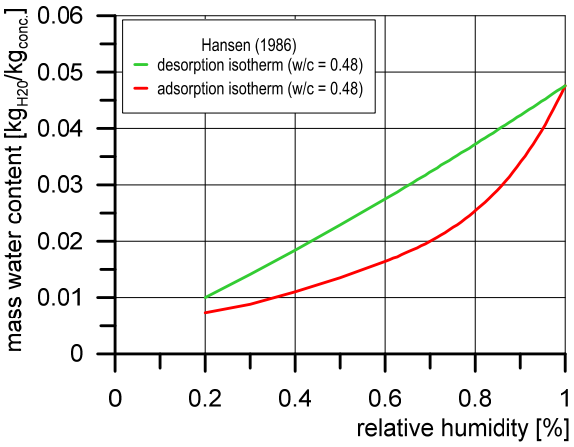

(b)

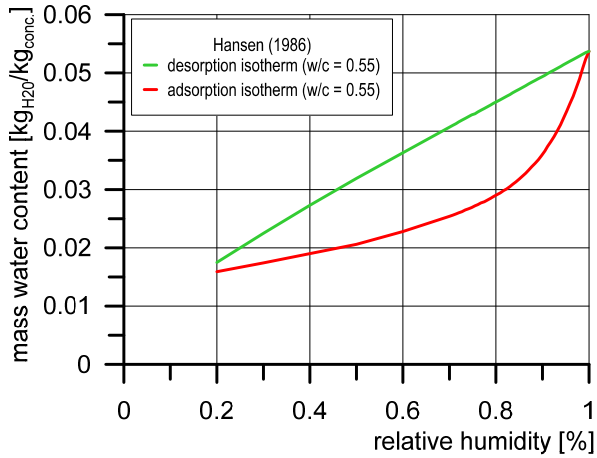

(c)

Figure 7.15 Input main adsorption and desorption curves from the experiments by (a) Baroghel-Bouny (2007) and (b,c) Hansen (1986) used for specimens with the w/c ratio of 0.40, 0.45 and 0.55, respectively

The boundary conditions are defined for the nodes on the exposed surface (Figure 7.14). Same as in the experiment, a total number of 26 weekly cycles with wetting and drying phases is simulated. The varying values of the relative humidity and chloride concentration for one cycle are taken as in Figure 7.14. For calculating the distribution of relative humidity, the mixed boundary conditions are defined as mentioned in Section 4.1.1. In the wetting phase of the cycle, during which the specimen is exposed to the 3% sodium chloride solution, the Dirchlet boundary conditions are implemented for calculating the transport of chloride ions. During the drying period, the exposed surface is treated as an insulated area with the flux of chloride ions being equal to zero at the boundary nodes.

7.3.3 Comparison of the numerically and experimentally obtained chloride profiles

The distribution of the total chloride content along the specimen depth for all three investigated cement mixes is given in Figure 7.16. The total chloride amount, containing the free chloride ions expressed in kg per m^3 of pore solution and bound chloride ions in kg per m^3 of concrete, is presented as a percentage of the cement content. The corresponding values of the cement amount in the mixes are given in Table 7.3.

It can be seen that the experimental and numerical results give a characteristic peak of the chloride ions near the exposed surface. The numerical results indicate that the exposure to wetting and drying conditions is one of the governing mechanisms for obtaining characteristic peak shapes of the chloride profiles along the concrete depth. The increase of the w/c ratio is followed not only by a more prominent translation of the profile peak, but also with higher values of the total chloride content

along the whole depth. This is accounted for by increasing the model parameters for the moisture and chloride transport with the w/c ratio (Table 7.2).

It must be noted that the position of the peaks in the case of the numerical results is closer to the concrete surface compared to the experimental data (Figure 7.16). The current analysis does not account for the carbonation processes occurring in the concrete, which can have a significant influence on reducing the chloride binding properties of the hydration products. In the experiments (Polder & Peelen 2002) it was observed that the carbonation depths varied from 2 to 3 mm, which can reduce the chloride content in affected region and therefore push the peaks further away from the exposed surface.

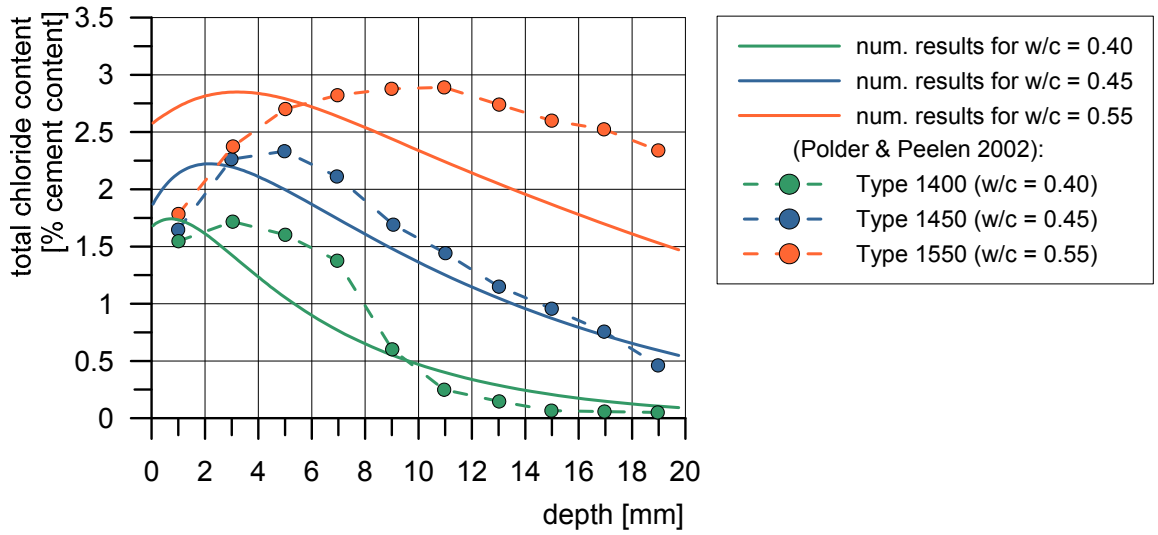

Figure 7.16 Experimental and numerical results of the chloride profiles obtained after 26 weekly cycles of wetting and drying, for concrete specimens with w/c ratios of 0.40, 0.45 and 0.55

To investigate the influence of the hysteretic moisture behaviour on the shape of the chloride profiles, the distribution of the total chloride content for the specimen with w/c of 0.45 is calculated for two cases: with and without accounting for the hysteretic moisture model for concrete (see Figure 7.17). For the latter case, the model parameters with the boundary and initial conditions are assumed the same as in Section 7.3.2. Furthermore, the moisture content is obtained from the calculated relative humidity values by using only the desorption isotherm curve (Figure 7.15b). Hence, the hysteretic moisture model and the subsequent scanning curves are not accounted for. It can be seen (Figure 7.17) that the hysteretic moisture behaviour has a strong influence on predicting the characteristic peak profile obtained in the experiments of Polder & Peelen (2002). In the case without the hysteresis, a relatively small maximum in the chloride content is calculated near the surface, but the overall shape corresponds more to a diffusive dominant environment in which the chloride amount slowly decreases along the depth from the exposed surface.

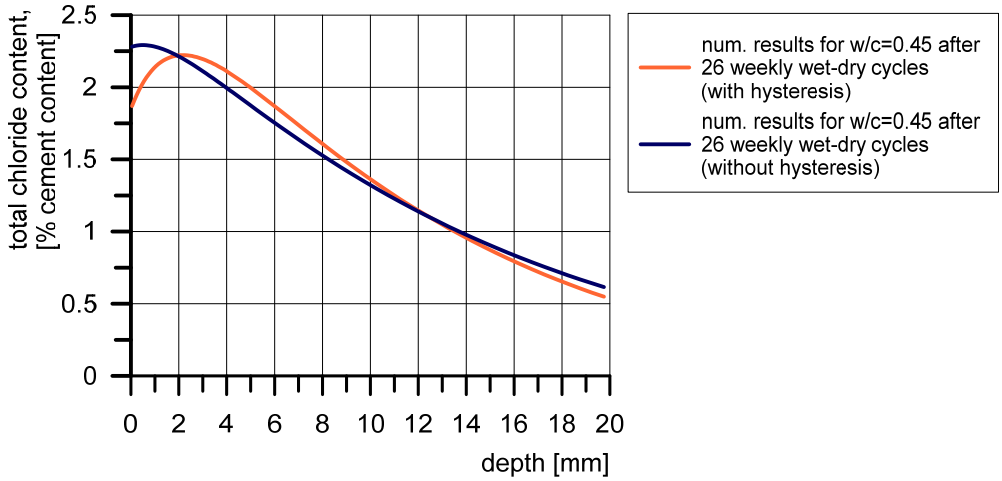

Figure 7.17 Numerical results of the chloride profiles obtained after 26 weekly cycles of wetting and drying for concrete specimen with w/c ratio of 0.45, with and without accounting for the hysteretic moisture behaviour of concrete

7.3.4 Influence of the wetting phase on the chloride distribution

To investigate the influence of the wetting conditions on the distribution of chlorides in the concrete specimen, the relative humidity and the corresponding chloride profiles are shown in Figure 7.18 for the w/c ratio of 0.45 and 0.40. The profiles are presented for the 5., 10., 15. and 26. cycle after the finished wetting phase and up to the depth of 20 mm.

It can be seen that during the wetting phase the chlorides are pushed inwards in both cases. Subsequently, they are added to the existing amount of chlorides near the exposed surface from the previous cycles, which leads to an appearance of a peak in the profile shape for the type w/c 0.45 (Figure 7.18a). Also the influence of the relative humidity gradient becomes higher in later cycles, causing for the larger amounts of ions being transported inside the specimen.

In the case of the w/c ratio of 0.40, the appearance of the peak is not pronounced during the wetting phase at later cycles, which can be explained by the lower value of the water vapour permeability corresponding to a lower porosity concrete. From equation 6.20 it can be seen that the values of the permeability coefficient strongly influence the convective part of the chloride transport and therefore the ingress of chlorides. The distribution of ions in the drying phase is also a significant factor for the appearance of the peak during the wetting stage and it is addressed in the next section.

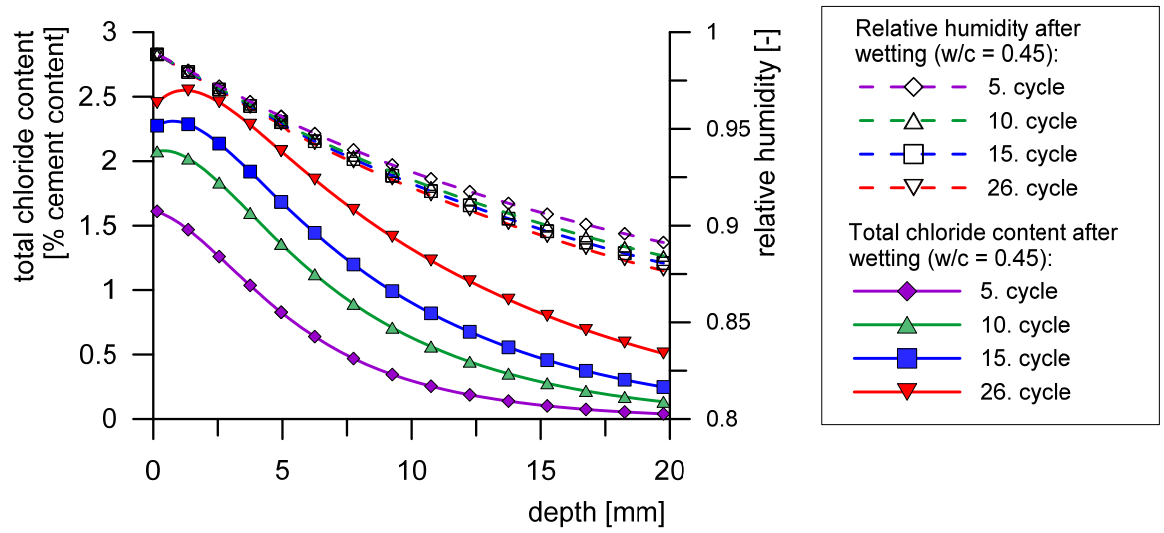

(a)

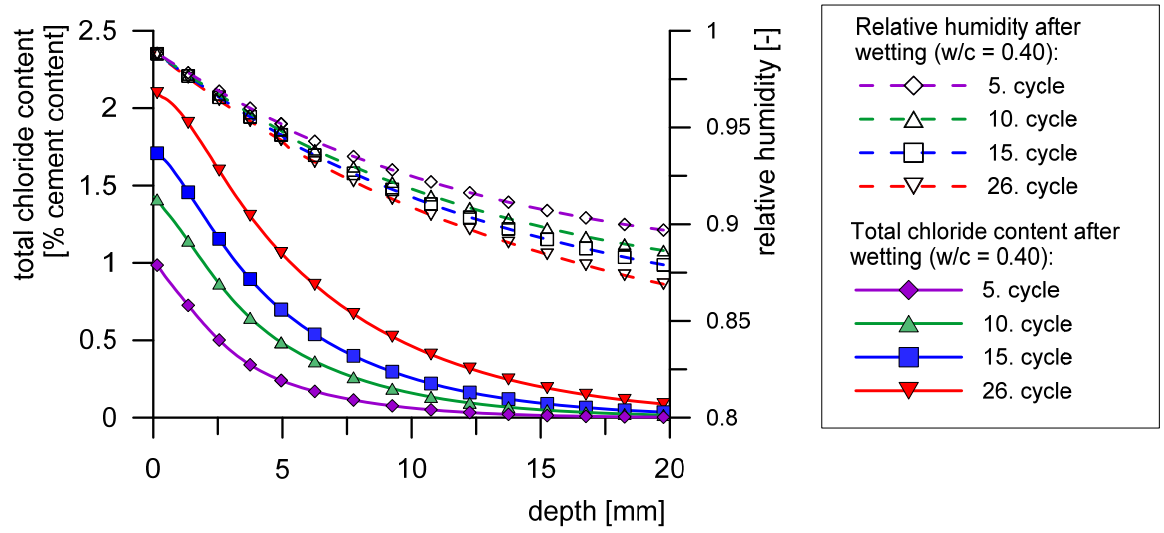

(b)

Figure 7.18 Numerical results for the relative humidity and chloride profiles obtained after the wetting phase for the 5. 10., 15. and 26. cycle in the case of concrete specimens with w/c ratios of 0.45 (a) and 0.40 (b)

The extent of the chloride ingress during the wetting phase is highly dependent on the convective component of the transport process. To illustrate the influence of the relative humidity gradient, chloride profiles for the type w/c = 0.45 are shown in Figure 7.19 after first 24 hours of exposure to the sodium chloride solution. Five different initial relative humidities (60%, 70%, 80%, 90 and 99% RH) are assumed and the corresponding RH distribution after wetting is plotted in Figure 7.19. It can be seen that in the case of the dominant diffusive conditions, i.e. for the initial RH of 99%, chlorides are penetrating the concrete in a less progressive manner compared to the lower initial humidities. With the increase of the relative humidity gradient, the chlorides are entering through the cover in much larger extent and the profile shapes are changing from a concave to an S shape curve.

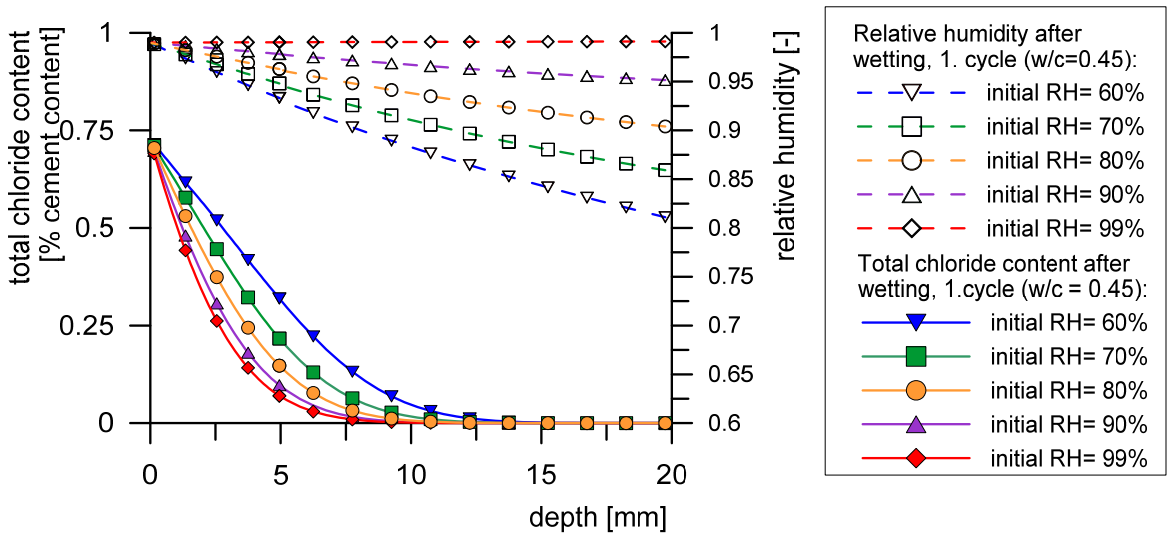

Figure 7.19 Chloride profiles and the corresponding RH distribution after the first wetting phase, for different initial RH conditions (w/c=0.45)

7.3.5 Influence of the drying phase on the chloride distribution

The relative humidity and the corresponding chloride profiles after the finished drying phase for the 5., 10., 15. and 26. cycle are shown in Figure 7.20. The profiles are plotted up to the depth of 20 mm and for w/c ratios of 0.45 and 0.40.

During drying which lasts for 6 days, the relative humidity is decreasing on the exposed surface. The decreasing value is dependent on the surface humidity transfer coefficient and the water vapour permeability. To better understand the influence of drying on the chloride distribution, the relative humidity, mass water content and chloride profiles are depicted in Figure 7.21 for different stages of the drying phase during the 15. cycle (w/c= 0.45).

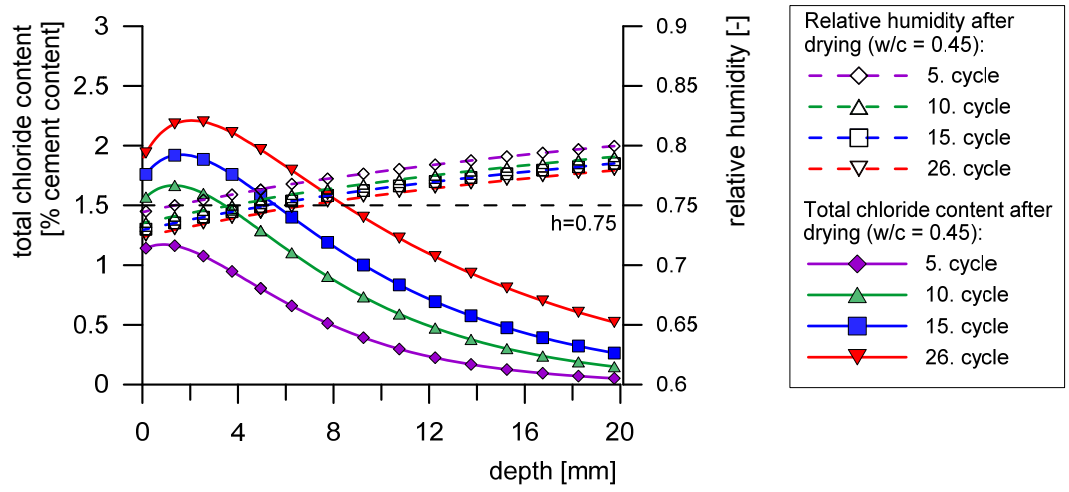

(a)

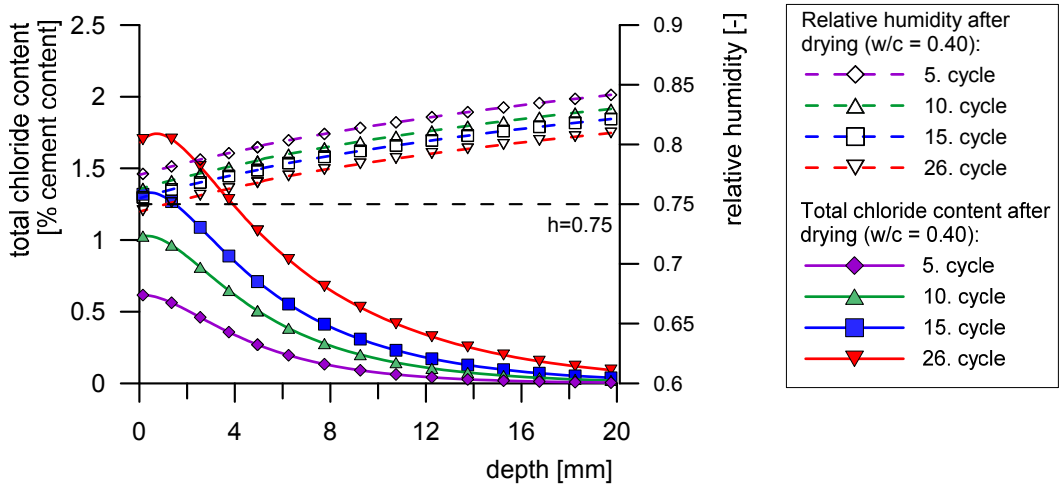

(b)

Figure 7.20 Numerical results for the relative humidity and chloride profiles (total chloride content) obtained after the drying phase for the 5. 10., 15. and 26. cycle in the case of concrete specimens with w/c ratios of 0.45 (a) and 0.40 (b)

In Figure 7.21c it can be seen that at the beginning of the drying phase the chlorides are still being transported inside the concrete specimen with the relative humidity gradient oriented away from the exposed surface (Figure 7.21a). The RH in the boundary nodes is slowly decreasing with the ongoing drying. From 5 to 50 hours after the start of drying, it can be observed that the gradient of RH, which is now oriented towards the surface, is relatively small as the values along the depth are following the decreasing trend on the surface. The diffusion contribution to the total chloride flux has a stronger influence during this period and in this way the chlorides and the profile peak are pushed even further inside.

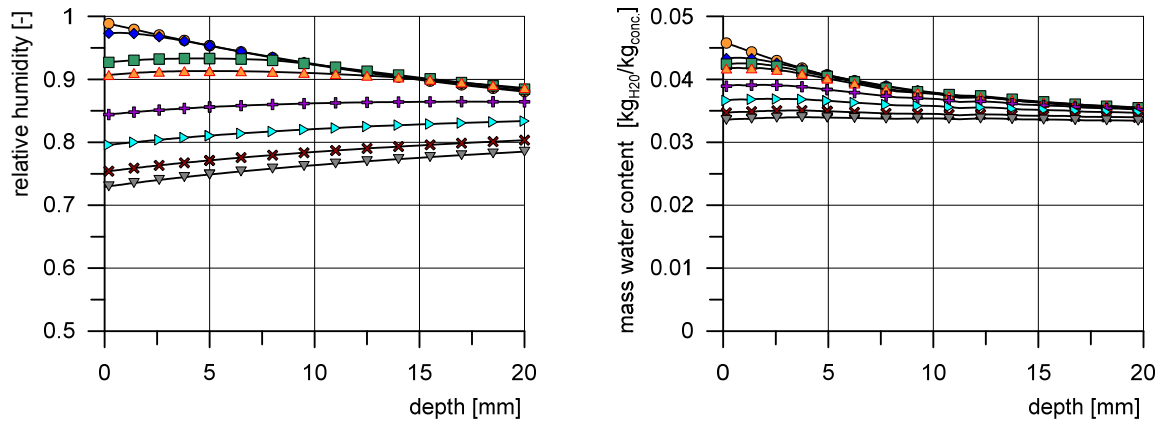

(a) (b)

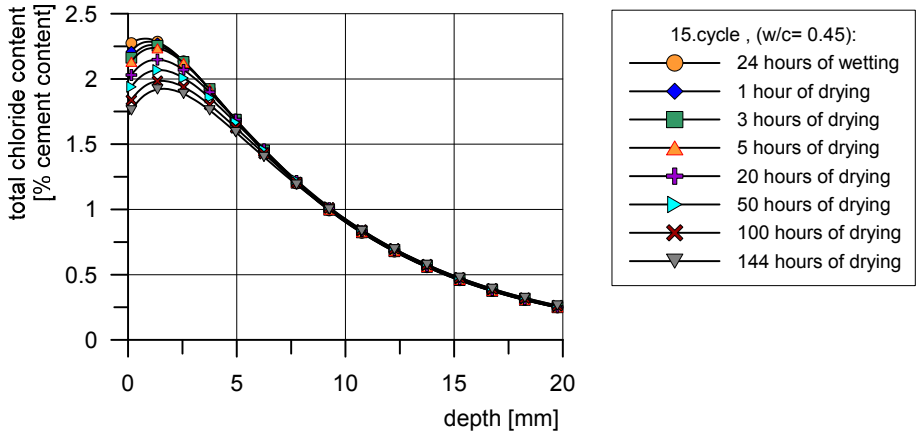

(c)

Figure 7.21 Numerical results for the relative humidity (a), water saturation (b) and chloride distribution (c) obtained during the drying phase of the 15. cycle, for the type w/c= 0.45

Relative humidity gradient which is orientated towards the exposed surface is increasing in the later phase of drying, but in the concrete region with the values of RH being under 80 % (Figure 7.21a). The relatively low RH values affect not only the convective, but also the diffusive flux as shown in Equations 5.20 and 5.22. By plotting the values of the reduction factor $f_1(h)$ explained in section 4.1.2 (Figure 7.22), it can be seen that the value of the vapour permeability and the chloride diffusion coefficient starts to significantly decrease after 90% of RH and reaches only 50 % of its value at 75 %. Hence, the total flux of chloride ions near the surface is reduced compared to the diffusion dominated flux at higher depths.

Comparing the relative humidity distribution at the end of the drying phases for w/c 0.45 and 0.40 in Figure 7.20, it can be seen that the value of 75% RH (near the exposed surface) is reached more rapidly with the increase of w/c. Therefore, the mitigation of the chloride ions in this region is more pronounced with a higher w/c ratio.

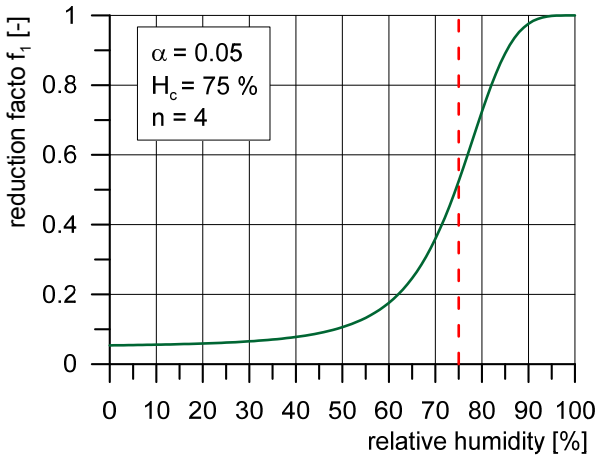

Figure 7.22 Dependence of the reduction factor f_1 on the relative humidity values

7.3.6 Scanning curves behaviour during the wetting and drying cycles

To illustrate the change of relative humidity and water content during 26 weekly cycles of wetting and drying, the scanning curves for all three w/c ratios are plotted in Figure 7.23. The water content is expressed in terms of mass water content and the numerical data is taken for the depth of 10 mm from the exposed surface. Figure 7.23 illustrates that for cement mixes with a lower w/c ratio, the scanning curves are covering a relatively small RH range. As the values of water vapour permeability and surface humidity coefficient increase with a higher w/c ratio, the scanning curves are stretched over a larger relative humidity range.

Further on, the corresponding total change of the mass water content during 26 cycles is also increasing with the w/c ratio. It can be concluded that with a higher w/c ratio, the moisture hysteretic behaviour of concrete (the scanning loops) is more pronounced with the exposure to cyclic wetting and drying conditions. Therefore, the position of the chloride profile peak gets translated further away from the surface as the w/c ratio increases (Figure 7.16). It is important to note that the scanning loops become less prominent with depth as shown in Section 7.2.4.

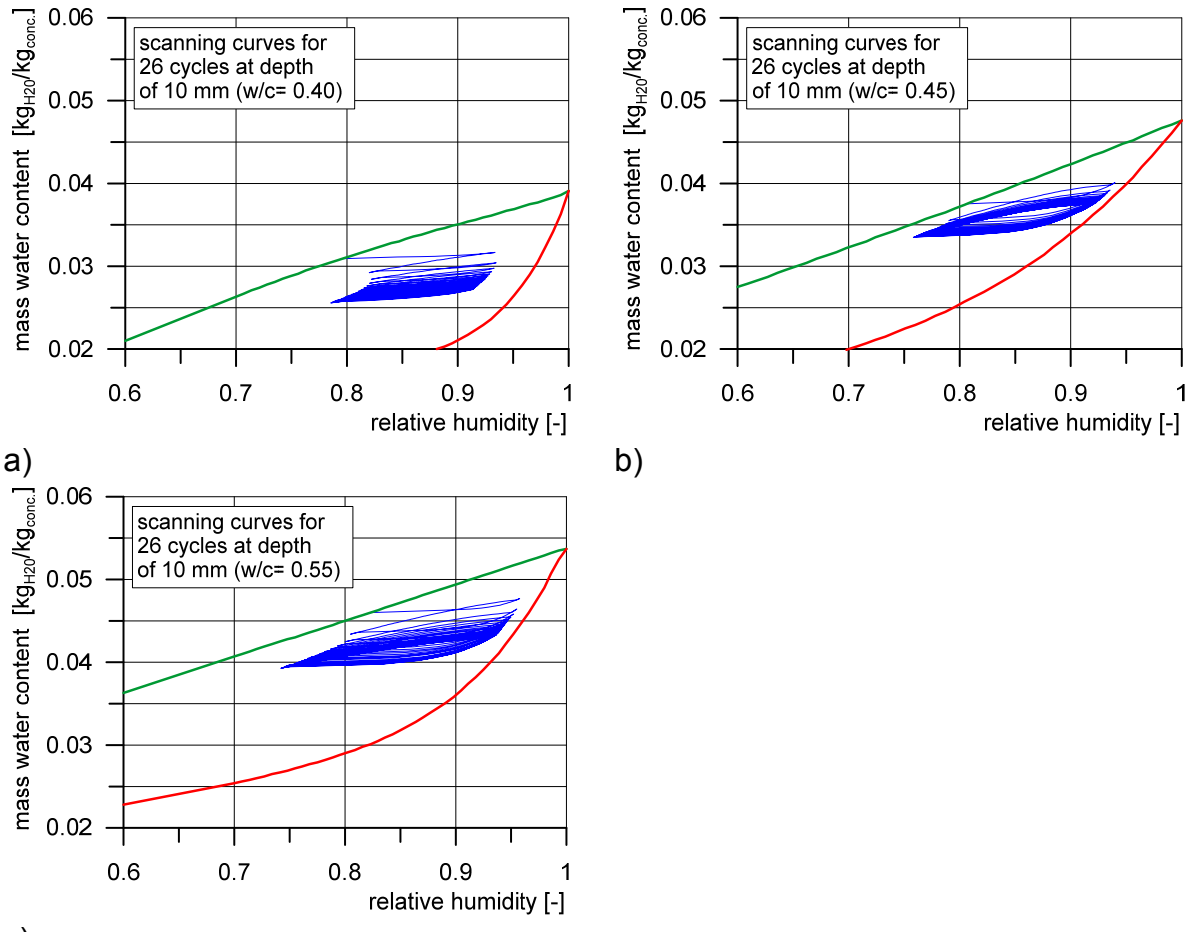

Figure 7.23 Scanning curves during the 26 weekly cycles of wetting and drying at the depth of 10 mm for specimen types w/c 0.40 (a), 0.45 (b) and 0.55 (c)

7.4 Conclusions

The hysteretic moisture model for concrete, as a further extension of the 3D chemo-hygro-thermo-mechanical model, is validated through three numerical examples.

The model ability to simulate the shapes of the scanning curves is addressed in the first example by using the experimental data by Baroghel-Bouny (2007). It is shown that the empirical model is capable of predicting the behaviour of scanning curves between the main adsorption and desorption isotherms for different RH ranges.

Further on, the application of the hysteretic moisture model for simulating the distribution of relative humidity and moisture content in concrete is verified on the experiments performed by Dong et al. (2011). The calculated distribution of the moisture content after 45 days of drying shows a good agreement with the experimental data for two investigated concrete specimens (w/c ratio of 0.3 and 0.6). The shape of the input main adsorption - desorption curve, the values of the water vapour permeability coefficient and the surface humidity transfer coefficient have a significant influence on the predicted values. With the increase of the w/c ratio, the corresponding values of the coefficients are also increasing which is related to the increase of concrete porosity. The distribution of RH and moisture content in concrete after 4 wet and dry cycles, corresponds nicely with the experimental measurements. By plotting the scanning curves for two investigated concrete mixtures, it can be seen that the effect of the cyclic change of the ambient RH at the exposed surface is more pronounced along the depth for a higher porosity, i.e. higher w/c ratio of concrete.

In the third numerical example the chloride distribution in concrete under dynamic moisture conditions is investigated by simulating the experimental conditions from Polder & Peelen (2002). The predicted chloride profiles for different concrete mixtures show a good agreement with the experimental data and therefore validate the definition of the convective flux of chloride ions due to the moisture transport. The profiles are characterized with a peak which is translated away from the exposed surface. The appearance of the profile maximum in the total chloride content is explained by a complex interaction of the cyclic wetting and drying conditions and can only be predicted by taking the hysteretic moisture behaviour of concrete into account. The hysteretic behaviour is more pronounced with the increase of the w/c ratio which results in a more prominent translation of the profile peak further away from the surface and in higher values of the total chloride content along the specimen depth.

8 CONCLUSIONS AND OUTLOOK

Here presented work is a further development of the 3D chemo-hygro-thermo-mechanical model, focused on predicting the rate of rust production and the corresponding damage of the concrete cover surrounding the embedded steel bars. The extent of the damage and its progress in time are highly dependent on the ingress of corrosion products into pores and cracks. Therefore, the transport of rust is incorporated into the model as a convective diffusion process. The expansion of rust and the subsequent compressive pressure on the cover is taken into account by developing one-dimensional corrosion contact elements. To ensure a realistic simulation of the corrosion induced damage, the mechanical processes are coupled with the non-mechanical processes, and vice versa. The model is implemented into a finite element code and its application is verified through a transient 3D finite element analysis of a series of numerical examples.

The application of the model in simulation of corrosion induced damage of concrete specimens with a single embedded rebar is investigated in the first part of the study. The qualitative validation is shown on a simple unloaded beam-end specimen. The inelastic strains of the implemented 1D corrosion contact elements, which correspond to the expansion of rust around the rebar, cause the cracking of the surrounding concrete. It is shown that the radial distribution of pressure is not symmetrically distributed over the depassivated surface. Further on, the defined transport of rust into the cracks reduces the pressure on the surrounding concrete.

The experiments on the beam-end specimens (Fischer 2012) are used to quantitatively verify and calibrate the 3D CHTM model. The cases without and with stirrups are investigated. The specimens are first exposed to aggressive environmental conditions and subsequently, the pull-out reduction of the rebar is investigated for different levels of corrosion.

The numerical analysis of the beam-end specimens (ϕ12/20 mm and ϕ 16/35 mm), without stirrups, shows that the predicted corrosion-induced crack pattern is significantly affected by the geometry configuration of the specimen (bar diameter and concrete cover), distribution of the anodic and cathodic regions in the rebar cross-section, and by the transport of corrosion products into cracks. Further on, the corrosion-induced radial pressure over the circumference of the reinforcement bar is not constant. The highest pressure is observed in radial directions which coincide with the directions of cracks.

From the analysis of the corresponding non-mechanical process it can be concluded that the consumption of oxygen reaches maximum values at anode-cathode transition zones soon after depassivation of reinforcement. However, with the onset

of corrosion-induced damage the flow of oxygen increases in generated cracks causing an increase of the oxygen concentration along the reinforcement bar.

The influence of distribution of rust into the corrosion induced cracks is additionally studied in the case of the beam-end specimens without stirrups. Numerical results show a very good agreement with experimental tests in which, for assumed environmental conditions, approximately 50 % of corrosion products were transported into cracks. Due to the fact that a relatively large amount of corrosion products is distributed over the cracks, the corrosion-induced damage is less pronounced when the transport of rust is accounted for.

The pull-out capacity of embedded rebar is calculated for different levels of corrosion induced damage. The pull-out failure is due to the cracking and splitting of the concrete cover and not due to the pull-out of the bar from the concrete. Corrosion-induced damage significantly reduces the pull-out capacity with the reduction being higher if the transport of rust through cracks is not accounted for. The predicted and experimentally measured values of the pull-out capacity show a good agreement.

The calculated corrosion induced damage and the pull-out capacity of the beam-end specimens with stirrups correspond realistically with the experimental results. It is shown that the expansion of the corrosion products around the rebar activates the tensile forces in the stirrup arms. Therefore, the additional confinement through the stirrups minimizes the reduction of the pull-out capacity. The effect of the confinement conditions depends on the depth of the concrete cover and the size of the rebar, for a constant stirrup diameter. For a smaller cover and a smaller bar, the confinement effect is reached sooner with the ongoing corrosion process and therefore a minimized reduction of the pull-capacity is obtained.

In the framework of the present work, the corrosion induced damage of concrete elements with multiple arranged rebars is also studied. The cases without and with stirrups are analysed and the numerically obtained results are compared with the experimental data of Dong et al. (2011). The model is able to predict the development of damage (cracks) for both cases. The crack pattern is characterized with the forming of the internal cracks between the rebars, followed by the development of the visible surface cracks. This can lead to delamination of larger sections of the concrete cover which presents a significant damage effect on the structural bearing capacity. Furthermore, the predicted crack patterns are dependent on the arrangement of the anode-cathode regions in the cross section of the rebars.

The effect of stirrups on the corrosion induced damage of multi-rebar concrete specimens is realistically captured by the 3D CHTM model. The confined conditions, in the concrete region around the stirrup arms prevent the cracks from reaching the sides of the specimen. They also contribute to smaller widths of the visible cracks on

the specimen surface. Hence, the presence of stirrups has a positive effect on reducing the extent of corrosion induced damage.

Although all of the presented numerical studies give a good agreement with the experimental data, further work is needed to quantify the parameters related to transport of corrosion products. This requires a comprehensive and detailed experimental study for different climate conditions, focused on determining the types of generated rust products and their corresponding amount distributed in the corrosion induced cracks and pores. Further on, it is shown that the anodic-cathodic configuration on the steel bar surface has a significant influence on the development of the corrosion induced damage. Currently, the position of the anodic regions is assumed in advance. This requires that a set of possible anode-cathode spatial distributions on the steel surface is investigated, which presents a time consuming effort. Therefore, a numerical algorithm based on the maximum entropy of the related electrochemical reactions should be developed to determine the most optimal configuration of the depassivated regions.

The hysteretic moisture model for concrete, as a further development of the 3D chemo-hygro-thermo-mechanical model, is also presented. The hysteretic behaviour of concrete is characterised by the ability to contain different degrees of water saturation for the same value of relative humidity, at a constant temperature. The implemented empirical definition of the scanning curves is verified by simulating the experiments of Baroghel-Bouny (2007).

Further on, the application of the model for predicting the distribution of relative humidity and moisture content in concrete is tested on experiments of Dong et al. (2011). The calculated distribution of water after drying and subsequent exposure to wet and dry cycles agree well with the experimental data. It is shown that the shape of the input isotherm curves, the values of the water vapour permeability coefficient and the surface humidity transfer coefficient have a strong effect on the predicted behaviour. With the increase of the w/c ratio, the corresponding values of the coefficients are also rising which relates to the increase of the concrete porosity. By plotting the scanning curves for the investigated concrete mixtures, it can be seen that the effect of the cyclic RH change is more pronounced in concrete with a higher porosity, i.e. higher w/c ratio.

The chloride distribution in concrete under dynamic moisture conditions is investigated by simulating the experiments of Polder & Peelen (2002). The predicted chloride profiles show a good agreement with the experimental results and therefore validate the influence of the moisture transport on the total flux of chloride ions. The profiles exhibit a characteristic peak in the total chloride content values which is translated away from the exposed surface. This is contributed to a complex interaction of the cyclic wetting and drying conditions and can only be predicted by taking the hysteretic moisture behaviour of concrete into account. The hysteretic

behaviour is more pronounced with the increase of the w/c ratio which results in a more significant translation of the profile peak further away from the surface and in higher chloride content along the specimen depth.

The hysteretic moisture model for concrete is verified on examples of uncracked specimens. Therefore, the moisture distribution and its influence on other transport processes needs to be investigated for cases of damaged concrete exposed to wet and dry cycles. Further on, the values of the anodic and cathodic current densities and the corresponding rust production under dynamic moisture conditions should be analysed and verified with experimental data.

BIBLIOGRAPHY

Ababneh, A., Benboudjema, F. & Xi, Y. (2003). Chloride penetration in nonsaturated concrete. *Journal of Materials in Civil Engineering*, *15*(2), 183–191.

ACI-222. (2001). Protection of Metals in Concrete Against Corrosion.

Ahmed, S. F. U., Maalej, M. & Mihashi, H. (2007). Cover cracking of reinforced concrete beams due to corrosion of steel. *ACI materials journal*, *104*(2).

Åhs, M. (2007). *Moisture Redistribution in Screeded Concrete Slabs*. Lund Institute of Technology, Lund University, Lund Institute of Technology, Lund University.

Aimin, X. (1989). Water desorption isotherms of cement mortar with fly ash. *Nordic concrete research*, (8), 9–23.

Aldea, C. M., Ghandehari, M., Shah, S. P. & Karr, A. (2000). Estimation of water flow through cracked concrete under load. *ACI Materials Journal*, *97*(5).

Al-Harthy, A., Stewart, M. & Mullard, J. (2011). Concrete cover cracking caused by steel reinforcement corrosion. *Magazine of Concrete Research*, *63*(9), 655–667.

Alonso, C., Andrade, C., Rodriguez, J. & Diez, J. M. (1998). Factors controlling cracking of concrete affected by reinforcement corrosion. *Materials and Structures*, *31*(7), 435–441.

Anderberg, A. (2004). Moisture properties of self-levelling flooring compounds. *Report TVBM 3120*, *3120*.

Andrade, C., Alonso, C. & Molina, F. J. (1993). Cover cracking as a function of bar corrosion: Part I-Experimental test. *Materials and structures*, *26*(8), 453–464.

Andrade, C., Díez, J. M. & Alonso, C. (1997). Mathematical modeling of a concrete surface “skin effect” on diffusion in chloride contaminated media. *Advanced Cement Based Materials*, *6*(2), 39–44.

Ang, A. H. S. & Chen, S. (2009). *Frontier Technologies for Infrastructures Engineering: Structures and Infrastructures Book Series* (Vol. 4). CRC Press.

Angst, U., Elsener, B., Jamali, A. & Adey, B. (2012). Concrete cover cracking owing to reinforcement corrosion-theoretical considerations and practical experience. *Materials and Corrosion*, *63*(12), 1069–1077.

Apostolopoulos, C. A. & Papadakis, V. G. (2008). Consequences of steel corrosion on the ductility properties of reinforcement bar. *Construction and Building Materials*, *22*(12), 2316–2324.

Bentz, D. P., Garboczi, E. J., Lu, Y., Martys, N., Sakulich, A. R. & Weiss, W. J. (2013). Modeling of the influence of transverse cracking on chloride penetration into concrete. *Cement and Concrete Composites*, *38*, 65–74.

Balabanić, G., Bićanić, N. & Đureković, A. (1996a). The influence of w/c ratio, concrete cover thickness and degree of water saturation on the corrosion rate of reinforcing steel in concrete. *Cement and concrete Research*, *26*(5), 761–769.

Balabanić, G., Bićanić, N. & Đureković, A. (1996b). Mathematical modeling of electrochemical steel corrosion in concrete. *Journal of engineering mechanics*, *122*(12), 1113–1122.

Balafas, I. & Burgoyne, C. J. (2010). Environmental effects on cover cracking due to corrosion. *Cement and Concrete Research*, *40*(9), 1429–1440.

Baroghel-Bouny, V. (1994). Characterization of cement pastes and concretes—Methods, analysis, interpretations. *LCPC, Paris*.

Baroghel-Bouny, V. (2007). Water vapour sorption experiments on hardened cementitious materials: part I: essential tool for analysis of hygral behaviour and its relation to pore structure. *Cement and Concrete Research*, *37*(3), 414–437.

Bažant, M. Z. & Bažant, Z. P. (2012). Theory of sorption hysteresis in nanoporous solids: Part II Molecular condensation. *Journal of the Mechanics and Physics of Solids*, *60*(9), 1660–1675.

Bažant, Z. P. (1975). Pore pressure, uplift, and failure analysis of concrete dams. *Int. Commission on Large Dams*.

Bažant, Z. P. (1979). Physical model for steel corrosion in concrete sea structures—theory. *Journal of the Structural Division*, *105*(6), 1137–1153.

Bažant, Z. P. (1979). Physical model for steel corrosion in concrete sea structures-application. *Journal of the structural division*, *105*(ASCE 14652 Proceeding).

Bažant, Z. P., Adley, M. D., Carol, I., Jirásek. M., Akers, S. A., Rohani, B., Cargile, J. D. & Caner, F. C. (2000). Large-strain generalization of microplane model for concrete and application. *Journal of engineering mechanics*, *126*(9), 971–980.

Bažant, Z. P. & Bažant, M. Z. (2012). Theory of sorption hysteresis in nanoporous solids: Part I: Snap-through instabilities. *Journal of the Mechanics and Physics of Solids*, *60*(9), 1644–1659.

Bažant, Z. P. & Kaplan, M. F. (1996). *Concrete at high temperatures*. Longman Essex, UK.

Bažant, Z. P. & Najjar, L. J. (1972). Nonlinear water diffusion in nonsaturated concrete. *Matériaux et Construction*, *5*(1), 3–20.

Bear, J. & Bachmat, Y. (1990). *Introduction to modeling of transport phenomena in porous media* (Vol. 4). Springer.

Bentur, A. and B. N. & Diamond, S. (2005). *Steel corrosion in concrete: fundamentals and civil engineering practice*. CRC Press.

Bertolini, L., Elsener, B., Pedeferri, P., Redaelli, E. & Polder, R. B. (2004). *Corrosion of steel in concrete*. John Wiley \& Sons.

Bhargava, K., Ghosh, A. K., Mori, Y. & Ramanujam, S. (2005). Modeling of time to corrosion-induced cover cracking in reinforced concrete structures. *Cement and Concrete Research*, *35*(11), 2203–2218.

Broomfield, J. P. (2002). *Corrosion of steel in concrete: understanding, investigation and repair*. CRC Press.

Browne, R. D. (1980). Mechanisms of corrosion of steel in concrete in relation to design, inspection, and repair of offshore and coastal structures. *ACI Special Publication*, *65*.

Brunauer, S. (1943). *Adsorption of gases and vapors*. Princeton : Princeton University Press.

Brunauer, S., Emmett, P. H. & Teller, E. (1938). Adsorption of gases in multimolecular layers. *Journal of the American Chemical Society*, *60*(2), 309–319.

Burkan Isgor, O. & Razaqpur, A. G. (2004). Finite element modeling of coupled heat transfer, moisture transport and carbonation processes in concrete structures. *Cement and Concrete Composites*, *26*(1), 57–73.

Böckris, J. O. M., Reddy, A. K. N. & Gamboa-Aldeco, M. E. (2000). *Modern Electrochemistry, 2A: Fundamentals of Electrodics*. Kluwer New York.

Cairns, J. (1998). *State of the art report on bond of corroded reinforcement*. Tech Rep No. CEB-TG-2/5, CEB.

Cairns, J., Plizzari, G. A., Du, Y. and L. D. W. & Franzoni, C. (2005). Mechanical properties of corrosion-damaged reinforcement. *ACI materials journal*, *102*(4).

Callister, W. D. & Rethwisch, D. G. (2012). *Fundamentals of materials science and engineering: an integrated approach*. John Wiley \& Sons.

Caré, S., Nguyen, Q. T., L'Hostis, V. & Berthaud, Y. (2008). Mechanical properties of the rust layer induced by impressed current method in reinforced mortar. *Cement and Concrete Research*, *38*(8), 1079–1091.

Castellote, M., Andrade, C. & Alonso, C. (1999). Characterization of transport of caesium, strontium, cobalt and iron ions through concrete by steady-state migration and natural diffusion tests. *Advances in cement research*, *11*(4), 161–168.

Chana, P. S. (1990). A test method to establish realistic bond stresses. *Magazine of Concrete Research*, *42*(151), 83–90.

Chernin, L. & Val, D. V. (2011). Prediction of corrosion-induced cover cracking in reinforced concrete structures. *Construction and Building Materials*, *25*(4), 1854–1869.

Chi, J. M., Huang, R. & Yang, C. C. (2002). Effects of carbonation on mechanical properties and durability of concrete using accelerated testing method. *Journal of marine science and technology*, *10*(1), 14–20.

Cook, R. D., Malkus, D. S. & Plesha, M. E. (1998). *Concepts and applications of finite element analysis*. Wiley.

Cornell, R. M. & Schwertmann, U. (1996). *The iron oxides: structure, properties, reactions, occurrences and uses*. Wiley.

Derluyn, H., Derome, D., Carmeliet, J., Stora, E. & Barbarulo, R. (2012). Hysteretic moisture behavior of concrete: Modeling and analysis. *Cement and Concrete Research*, *42*, 1379–1388.

Dong, W., Murakami, Y., Oshita, H., Suzuki, S. & Tsutsumi, T. (2011). Influence of Both Stirrup Spacing and Anchorage Performance on Residual Strength of Corroded RC Beams. *Journal of Advanced Concrete Technology*, *9*(3), 261–275.

El Maaddawy, T. & Soudki, K. (2007). A model for prediction of time from corrosion initiation to corrosion cracking. *Cement and concrete composites*, *29*(3), 168–175.

Eurocode 1992: DIN EN 1992 1-1: Bemessung un Konstruktion von Stahlbeton- und Spannbetontragwerken - Teil 1-1: Allgemeine Bemessungsregeln und Regeln für den Hochbau. *Detusche-Fassung EN*

Espinosa, R. M. & Franke, L. (2006). Inkbottle Pore-Method: Prediction of hygroscopic water content in hardened cement paste at variable climatic conditions. *Cement and concrete research*, *36*(10), 1954–1968.

Everett, D. H. (1955). A general approach to hysteresis. Part 4. An alternative formulation of the domain model. *Transactions of the Faraday Society*, *51*, 1551–1557.

Fagerlund, G. (1999). Om hysteresis mellan porvattentryck och fukthalt: konsekvenser för uttorkningskrympning och frostbeständighet. *Rapport TVBM (In swedish)*.

Feldman, R. F. & Sereda, P. J. (1964). Sorption of water on compacts of bottle-hydrated cement. I. The sorption and and length-change isotherms. II. Thermodynamic considerations and theory of volume change. *Journal of applied Chemistry*, *14*, 87–104.

Feldman, R. F. & Sereda, P. J. (1968). A model for hydrated Portland cement paste as deduced from sorption-length change and mechanical properties. *Matériaux et Construction*, *1*(6), 509–520.

Fenaux, M. (2013). *Modelling of chloride transport in non-saturated concrete. From microscale to macroscale*. Universidad Politecnica de Madrid.

fib (2006). *Model code for service life design* (Vol. 34). Fédération internationale du béton.

Fichtner, S. (2011). *Untersuchungen zum Tragverhalten von Gruppenbefestigungen unter Berücksichtigung der Ankerplattendicke und einer Mörtelschicht*. Universität Stuttgart.

Fischer, C. (2012). *Auswirkungen der Bewehrungskorrosion auf den Verbund zwischen Stahl und Beton*. Universität Stuttgart.

Foley, R. T. (1975). Complex Ions and Corrosion. *Journal of The Electrochemical Society* , *122*(11), 1493–1494.

Gjørv, O., Vennesland, Ø. & El-Busaidy, A. (1977). Electrical resistivity of concrete in the oceans. *Offshore Technology Conference*.

Glass, G. K. & Buenfeld, N. R. (1995). Chloride threshold levels for corrosion induced deterioration of steel in concrete. *Chloride Penetration into concrete: proceedings of the RILEM international workshop* (pp. 429–440).

Glass, G. K. & Buenfeld, N. R. (2000). The influence of chloride binding on the chloride induced corrosion risk in reinforced concrete. *Corrosion Science*, *42*(2), 329–344.

Glassstone, S. (1964). An introduction to electrochemical behaviour of steel in concrete. *ACI Journal*, *61*(177-88).

Grassl, P., Fahy, C., Wheeler, S. & Gallipoli, P. (2014). A 2D hydro-mechanical lattice approach for modelling corrosion induced cracking of reinforced concrete. *Computational modelling of concrete structures : proceedings of Euro-C 2014, St. Anton Am Arlberg*, 759-764

Hall, C., Hoff, W. D., Taylor, S. C., Wilson, M. A., Yoon, B., Reinhardt, H., Sosoro, M., et al. (1995). Water anomaly in capillary liquid absorption by cement-based materials. *Journal of Materials Science Letters*, *14*(17), 1178–1181.

Hansen, K. K. (1986). *Sorption Isotherms - A catalogue*. The Technical University of Denmark.

Harker, A. H., Sharland, S. M. & Tasker, P. W. (1987). A Mathematical Model of Uniform Corrosion of Intermediate Level Radioactive-Waste Canisters in Concrete. *Radioactive Waste Management and Environmental Restoration*, *8*(1), 65–85.

Huet, B., L'hostis, V., Santarini, G., Feron, D. & Idrissi, H. (2007). Steel corrosion in concrete: Determinist modeling of cathodic reaction as a function of water saturation degree. *Corrosion science*, *49*(4), 1918–1932.

Hussain, R. R. & Ishida, T. (2010). Development of numerical model for FEM computation of oxygen transport through porous media coupled with micro-cell corrosion model of steel in concrete structures. *Computers \& structures*, *88*(9), 639–647.

Isgor, O. B. (2001). *A durability model for chloride and carbonation induced steel corrosion in reinforced concrete members*. Carleton University, Ottawa, Canada.

Isgor, O. B. & Razaqpur, A. G. (2006). Advanced modelling of concrete deterioration due to reinforcement corrosion. *Canadian Journal of Civil Engineering*, *33*(6), 707–718.

Ishida, T., Iqbal, P. O. & Anh, H. T. L. (2009). Modeling of chloride diffusivity coupled with non-linear binding capacity in sound and cracked concrete. *Cement and Concrete Research*, *39*(10), 913–923.

Ishida, T., Maekawa, K. & Kishi, T. (2007). Enhanced modeling of moisture equilibrium and transport in cementitious materials under arbitrary temperature and relative humidity history. *Cement and concrete research*, *37*(4), 565–578.

Jacob, A. (2008). Composite bridge decks cut life cycle costs. *Reinforced Plastics*, *52*(9), 30–32.

Jamali, A., Angst, U., Adey, B. & Elsener, B. (2013). Modeling of corrosion-induced concrete cover cracking: A critical analysis. *Construction and Building Materials*, *42*, 225–237.

Jennings, H. M. (2000). A model for the microstructure of calcium silicate hydrate in cement paste. *Cement and Concrete Research*, *30*(1), 101–116.

Kobayashi, K. & Shuttoh, K. (1991). Oxygen diffusivity of various cementitious materials. *Cement and concrete research*, *21*(2), 273–284.

Kranc, S. C. & Sagüés, A. A. (1997). Modeling the Time-Dependent Response to External Polarization of a Corrosion Macrocell on Steel in Concrete. *Journal of The Electrochemical Society*, *144*(8), 2643–2652.

Kumar, A. (2010). *Water flow and transport of chloride in unsaturated concrete.* University of Saskatchewan, Saskatoon, Canada

Kušter, M. (2013). *Service life prediction of reinforced concrete bridges exposed to chlorides*. University of Zagreb, Croatia

Kwiatkowski, J., Woloszyn, M. & Roux, J.J. (2009). Modelling of hysteresis influence on mass transfer in building materials. *Building and Environment*, *44*(3), 633–642.

Langmuir, I. (1916). The constitution and fundamental properties of solids and liquids. part I. solids. *Journal of the American Chemical Society*, *38*(11), 2221–2295.

Leech, C., Lockington, D. & Dux, P. (2003). Unsaturated diffusivity functions for concrete derived from NMR images. *Materials and Structures*, *36*(6), 413–418.

Lettow, S. (2006). *Ein Verbundelement für nichtlineare Finite Elemente Analysen-Anwendung auF Übergreifungsstößе*. Universität Stuttgart.

Liu, Y. (1996). *Modeling the time-to-corrosion cracking of the cover concrete in chloride contaminated reinforced concrete structures*. Virginia Polytechnic Institute and State University.

Liu, Y. & Weyers, R. E. (1998). Modeling the time-to-corrosion cracking in chloride contaminated reinforced concrete structures. *ACI Materials Journal*, *95*(6).

Lu, C., Jin, W. & Liu, R. (2011). Reinforcement corrosion-induced cover cracking and its time prediction for reinforced concrete structures. *Corrosion Science*, *53*(4), 1337–1347.

Maekawa, K., Ishida, T. & Kishi, T. (2008). *Multi-scale modeling of structural concrete*. CRC Press.

Marsavina, L., Audenaert, K., De Schutter,. G., Faur. N. & Marsavina, D. (2009). Experimental and numerical determination of the chloride penetration in cracked concrete. *Construction and Building Materials*, *23*(1), 264–274.

Martinez, I. & Andrade, C. (2009). Examples of reinforcement corrosion monitoring by embedded sensors in concrete structures. *Cement and Concrete Composites*, *31*(8), 545–554.

Martin-Perez, B. (1999). *Service life modelling of RC highway structures exposed to chlorides*. University of Toronto.

Maruya, T., Takeda, H., Horiguchi, K., Koyama, S. & Hsu, K. (2007). Simulation of steel corrosion in concrete based on the model of macro-cell corrosion circuit. *Journal of Advanced Concrete Technology*, *5*(3), 343–362.

Mayergoyz, I. D. (1985). Hysteresis models from the mathematical and control theory points of view. *Journal of Applied Physics*, *57*(8), 3803–3805.

McArthur, H. & Spalding, D. (2004). *Engineering materials science: Properties, uses, degradation, remediation*. Elsevier.

McCafferty, E. (2010). *Introduction to corrosion science*. Springer.

Meijers, S., Bijen, J., De Borst, R. & Fraaij, A. (2005). Computational results of a model for chloride ingress in concrete including convection, drying-wetting cycles and carbonation. *Materials and structures*, *38*(2), 145–154.

Michel, A.; Pease. B. J., Geiker, M. R., Stang, H. & Olesen, J. F. (2011). Monitoring reinforcement corrosion and corrosion-induced cracking using non-destructive x-ray attenuation measurements. *Cem.and Concrete Research*, *41*(11), 1085–1094.

Molina, F. J., Alonso, C. & Andrade, C. (1993). Cover cracking as a function of rebar corrosion: part 2—numerical model. *Materials and Structures*, *26*(9), 532–548.

Morinaga, S. (1990). Prediction of service life reinforced concrete buildings based on the corrosion rate of reinforcing steel. *Durability of Building Materials and Components, Proceedings of the Fifth International Conference* (pp. 5–13).

Mualem, Y. (1974). A conceptual model of hysteresis. *Water Resources Research*, *10*(3), 514–520.

Murakami, Y., Kinoshita, T., Suzuki, S., Fukumoto, Y. & Oshita, H. (2006). Study on the residual strength for corroded RC reinforced beam. *Concrete Research and Technology* , *17(1)*, 61–74 .

Müller, H:S & Bohner, E: (2012). *Rissbildung infloge Bewehrungskorrosion. Teilprojekt B1*. Dauerhaftigkeitsbemessung von Stahlbetonbauteilen auf Bewehrungskorrosion. Tl.2: Dauerhaftigkeitsbemessung. Deutscher Ausschuss für Stahlbeton. Berlin

Neville, A. M. (1973). Properties of concrete. *Pitman, London*.

Newman, J. & Thomas-Alyea, K. E. (2004). *Electrochemical systems*. John Wiley & Sons.

Nielsen, L. F. (2007). Moisture Sorption in Porous Materials: a best fit description from experimental data. *Moisture Sorption in Porous Materials*, *1*, 36–01.

Ochs, F., Heidemann, W. & Müller-Steinhagen, H. (2008). Effective thermal conductivity of moistened insulation materials as a function of temperature. *International Journal of Heat and Mass Transfer*, *51*(3), 539–552.

Oh, B. H. & Bažant, Z. P. (1983). Crack band theory for fracture of concrete. *Materials and Structures, January-February*, 155–177.

Osterminski, K., Polder, R. B. & Schießl, P. (2008). Long term behaviour of the resistivity of concrete. *Heron*, *53*(1), 59–78.

Osterminski, K: & Schieβl, P: (2012). *Voll-probabilistische Modellierung von Bewehrungskorrosion. Ein Beitrag zur Dauerhaftigkeitsbemessung. Projekt D.* Dauerhaftigkeitsbemessung von Stahlbetonbauteilen auf Bewehrungskorrosion. Tl.2: Dauerhaftigkeitsbemessung. Deutscher Ausschuss für Stahlbeton. Berlin

Otieno, M. B., Beushausen, H. D. & Alexander, M. G. (2011). Modelling corrosion propagation in reinforced concrete structures-A critical review. *Cement and Concrete Composites*, *33*(2), 240–245.

Ožbolt, J., Balabanić, G. & Kušter, M. (2011). 3D Numerical modelling of steel corrosion in concrete structures. *Corrosion science*, *53*(12), 4166–4177.

Ožbolt, J., Balabanić, G., Periškić, G. & Kušter, M. (2010). Modelling the effect of damage on transport processes in concrete. *Construction and Building Materials*, *24*(9), 1638–1648.

Ožbolt, J., Eligehausen, R. & Reinhardt, H. (1999). Size effect on the concrete cone pull-out load. *Fracture Scaling* (pp. 391–404).

Ožbolt, J., Li, Y. & Kožar, I. (2001). Microplane model for concrete with relaxed kinematic constraint. *International Journal of Solids and Structures*, *38*(16), 2683–2711.

Ožbolt, J., Oršanić, F. & Balabanić, G. (2014). Modeling pull-out resistance of corroded reinforcement in concrete: Coupled three-dimensional finite element model. *Cement and Concrete Composites*, *46*, 41–55.

Ožbolt, J., Oršanić, F., Balabanić, G. & Kušter, M (2012a). Modeling damage in concrete caused by corrosion of reinforcement: coupled 3D FE model. *International journal of fracture*, *178*(1-2), 233–244.

Ožbolt, J., Oršanić, F., Kušter, M. & Balabanić, G. (2012b). Modelling bond resistance of corroded reinforcement . *Bond in Concrete 2012. Proceedings of the international conference*, 437–44.

Ožbolt, J. & Reinhardt, H. (2002). Numerical study of mixed-mode fracture in concrete. *International journal of fracture*, *118*(2), 145–162.

Page, C. L., Short, N. R. & El Tarras, A. (1981). Diffusion of chloride ions in hardened cement pastes. *Cement and concrete research*, *11*(3), 395–406.

Page, C. L. & Treadaway, K. W. J. (1982). Aspects of the electrochemistry of steel in concrete. *Nature Publishing Group*, *297*, 109 – 115.

Pedersen, C. R. (1990). *Combined heat and moisture transfer in building constructions* (Vol. 214). Thermal Insulation Laboratory, Technical University of Denmark.

Polder, R. B. & Peelen, W. H. A. (2002). Characterisation of chloride transport and reinforcement corrosion in concrete under cyclic wetting and drying by electrical resistivity. *Cement and Concrete Composites*, *24*(5), 427–435.

Powers, T. C. & Brownyard, T. L. (1946). Studies of the physical properties of hardened Portland cement paste. *ACI Journal Proceedings* (Vol. 43).

Poyet, S. (2009). Experimental investigation of the effect of temperature on the first desorption isotherm of concrete. *Cement and Concrete Research*, *39*(11), 1052–1059.

Preisach, F. (1935). Über die magnetische Nachwirkung. *Zeitschrift für physik*, *94*(5-6), 277–302.

Ranaivomanana, H., Verdier, J., Sellier, A. & Bourbon, X. (2011). Toward a better comprehension and modeling of hysteresis cycles in the water sorption-desorption process for cement based materials. *Cement and Concrete Research*, *41*(8), 817–827.

Rao, S. S. (2005). *The finite element method in engineering*. Butterworth-Heinemann.

Raupach, M. (1996). Chloride-induced macrocell corrosion of steel in concrete—theoretical background and practical consequences. *Construction and building materials*, *10*(5), 329–338.

Raupach, M. & Gulikers, J. (1999). A simplified method to estimate corrosion rates—A new approach based on investigations of macrocells. *Durability of Building Materials and Components 8: Service life and durability of materials and components*, *1*, 376.

Richards, L. A. (1931). Capillary conduction of liquids through porous mediums *Journal of Applied Physics*, 1, 318-333

Rodriguez, J., Ortega, L. M., Casal, J. & Diez, J. M. (1996). Corrosion of reinforcement and service life of concrete structures. *Durability of Building materials and components*, *7*(1), 117–126.

Rosenberg, A., Hansson, C. M. & Andrade, C. (1989). Mechanisms of corrosion of steel in concrete. *Materials science of concrete*, *1*, 285–314.

Ryu, D., Ko, J. & Noguchi, T. (2011). Effects of simulated environmental conditions on the internal relative humidity and relative moisture content distribution of exposed concrete. *Cement and Concrete Composites*, *33*(1), 142–153.

Saetta, A. V., Scotta, R. V. & Vitaliani, R. V. (1993). Analysis of chloride diffusion into partially saturated concrete. *ACI Materials Journal*, *90*(5).

Sandberg, P., Peterson, K., Sarensen, H. & Arup, H. (1995). Critical chloride concentrations for the onset of active reinforcement corrosion. *Chloride Penetration into concrete: proceedings of the RILEM international workshop* (pp. 435–439).

Scott, A. N. (2004). *The influence of binder type and cracking on reinforcing steel corrosion in concrete*. University of Cape Town.

Sleiman, H., Amiri, O., Ait-Mokhtar, A. & Loche, J.-M. (2012). Chloride transport through unsaturated concrete: chloride profile simulations and experimental validation. *Magazine of Concrete Research*, *64*(4), 351–359.

Stern, M. & Geary, A. L. (1957). Electrochemical polarization I. A theoretical analysis of the shape of polarization curves. *Journal of the electrochemical society*, *104*(1), 56–63.

Stolten, D. (2010). *Hydrogen and fuel cells: fundamentals, technologies and applications*. John Wiley & Sons.

Suda, K., Misra, S. & Motohashi, K. (1993). Corrosion products of reinforcing bars embedded in concrete. *Corrosion Science*, *35*(5), 1543–1549.

Sudjono, A. S. & Seki, H. (2000). Experimental and analytical studies on oxygen transport in various cementitious materials. *ACI Special Publication*, *192*.

Šavija, B., Pacheco, J. & Schlangen, E. (2013a). Lattice modeling of chloride diffusion in sound and cracked concrete. *Cement and Concrete Composites*, *42*(Complete), 30–40.

Šavija, B., Luković, M. & Pacheco, J. and S. E. (2013b). Cracking of the concrete cover due to reinforcement corrosion: A two-dimensional lattice model study. *Construction and Building Materials*, *44*, 626–638.

Taylor, G. (1938). Plastic strain in metals. *Journal of the Institute of Metals,*, (62), 307–324.

Thoft-Christensen, P. (2000). *Modelling of the deterioration of reinforced concrete structures*. Dept. of Building Technology and Structural Engineering.

Thomas, M. D. & Bamforth, P. B. (1999). Modelling chloride diffusion in concrete: effect of fly ash and slag. *Cement and Concrete Research*, *29*(4), 487–495.

Tran, K. K. (2012). *Study on cracking behavior of concrete due to rebar corrosion*. Nagoya University, Japan.

Tran, K. K., Nakamura, H., Kawamura, K. & Kunieda, M. (2011). Analysis of crack propagation due to rebar corrosion using RBSM. *Cement and Concrete Composites*, *33*(9), 906–917.

Tuutti, K. (1982). *Corrosion of steel in concrete. Swedish Cement and Concrete Institute*. CIB, Research Report.

Tuutti, K. (1993). The Effect of Individual Parameter on Chloride Induced Corrosion. *Chloride Penetration into Concrete Structures. Götenborg, Sweden*, 18–25.

Van Mier, J. G. (1996). *Fracture processes of concrete* (Vol. 12). CRC press.

von Greve-Dierfeld, S. & Gehlen, C. (2012). *Lebensdauerbemessung - Anwendung und Validierung. Teilprojekt A4.* Dauerhaftigkeitsbemessung von Stahlbetonbauteilen auf Bewehrungskorrosion. Tl.2: Dauerhaftigkeitsbemessung. Deutscher Ausschuss für Stahlbeton. Berlin

Walton, J. C. & Sagar, B. (1986). A corrosion model for nuclear waste containers. *MRS Proceedings* (Vol. 84).

Wang, K., Jansen, D. C., Shah, S. P. & Karr, A. F. (1997). Permeability study of cracked concrete. *Cement and Concrete Research*, *27*(3), 381–393.

Williamson, S. J. & Clark, L. A. (2000). Pressure required to cause cover cracking of concrete due to reinforcement corrosion. *Magazine of Concrete research*, *52*(6), 455–467.

Wong, H. S., Zhao, Y. X., Karimi, A. R., Buenfeld, N. R. & Jin, W. L. (2010). On the penetration of corrosion products from reinforcing steel into concrete due to chloride-induced corrosion. *Corrosion Science*, *52*(7), 2469–2480.

Xi, Y., Bažant, Z. P. & Jennings, H. M. (1994). Moisture diffusion in cementitious materials Adsorption isotherms. *Advanced Cement Based Materials*, *1*(6), 248–257.

Yalcyn, H. & Ergun, M. (1996). The prediction of corrosion rates of reinforcing steels in concrete. *Cement and concrete research*, *26*(10), 1593–1599.

Zhang, T. & Gjørv. O. E. (1996). Diffusion behavior of chloride ions in concrete. *Cement and Concrete Research*, *26*(6), 907–917.

Zhao, Y., Dai, H., Ren, H. & Jin, W. (2012). Experimental study of the modulus of steel corrosion in a concrete port. *Corrosion Science*, *56*, 17–25.

Lebenslauf

23/09/1984	geboren in Karlovac (Kroatien)
09/1999-06/2003	Gymnasium in Karlovac, Abschluss Abitur
10/2003-12/2008	Studium des Bauingenieurwesens an der Universität Zagreb, Abschluss Diplom
03/2009-01/2011	Assisstent in der Abteilung Brückenbau der Fakultät für Bauwesen, Universität Zagreb
02/2011- 03/2014	wissenschaftlicher Mitarbeiter am Institut für Werkstoffe im Bauwesen, Universität Stuttgart